Investigation of Intrinsic Rotation Dependencies in Alcator C-Mod Using a New Data Analysis Workflow

By

Daniel (Joowon) Kwak

B.S., Nuclear Engineering and Radiological Sciences (2013)

University of Michigan

SUBMITTED TO THE DEPARTMENT OF NUCLEAR SCIENCE
AND ENGINEERING
IN PARTIAL FULFILLMENT OF THE REQUIREMENTS FOR THE DEGREE OF

MASTER OF SCIENCE IN NUCLEAR SCIENCE AND ENGINEERING
AT THE
MASSACHUSETTS INSTITUTE OF TECHNOLOGY

June 2015

Signature of Author: Signature redacted

Daniel (Joowon) Kwak
Department of Nuclear Science and Engineering
May 19th, 2015

Certified by: Signature redacted

Anne E. White
Cecil and Ida Green Associate Professor of Nuclear Science and Engineering
Thesis Supervisor

Certified by: Signature redacted

John E. Rice
Senior Research Scientist of the MIT Plasma Science and Fusion Center
Thesis Reader

Accepted by: Signature redacted

Mujid S. Kazimi
TEPCO Professor of Nuclear Engineering
Chair, Department Committee on Graduate Students

Investigation of Intrinsic Rotation Dependencies in Alcator C-Mod Using a New Data Analysis Workflow

By

Daniel (Joowon) Kwak

Submitted to the Department of Nuclear Science and Engineering
On May 19th, 2015 in partial fulfillment of the
Requirements for the degree of
Master of Science in Nuclear Science and Engineering

Abstract

Toroidal rotation, important for suppressing various turbulent modes, mitigating MHD instabilities, and preventing locked modes that cause disruptions, may not be sufficiently generated by external devices in larger devices i.e. ITER. One possible solution is intrinsic rotation, self-generated flow without external momentum input, which has been observed in multiple tokamaks. More specifically, rotation reversals, a sudden change in direction of intrinsic rotation without significant change in global plasma parameters, have also been observed and are not yet fully understood. Studying this phenomenon in ohmic L-mode plasmas presents a rich opportunity to gain better understanding of intrinsic rotation and of momentum transport as a whole. The literature presents many different hypotheses, and this thesis explores three in particular. The first two hypotheses each posits a unique parameter as the primary dependency of reversals – the dominant turbulent mode, or the fastest growing turbulent mode(TEM/ITG), and the local density and temperature profile gradients, especially the electron density gradient, respectively. Other studies state that neoclassical effects cause the reversals and one study in particular presents a 1-D analytical model. Utilizing a new data analysis workflow built around GYRO, a gyrokinetic-Maxwell solver, hundreds of intrinsic rotation shots at Alcator C-Mod can be processed and analyzed without constant user management, which is used to test the three hypotheses. By comparing the rotation gradient u', a proxy variable indicative of the core toroidal intrinsic rotation velocity, to the parameters identified by the hypotheses, little correlation has been found between u' and the dominant turbulence regime and the ion temperature, electron temperature, and electron density profile gradients. The plasma remains ITG-dominated based on linear stability analysis regardless of rotation direction and the local profile gradients are not statistically significant in predicting the u'. Additionally, the experimental results in C-Mod and ASDEX Upgrade have shown strong disagreement with the 1-D neoclassical model. Strong correlation has been found between u' and the effective collisionality ν_{eff}. These findings are inconsistent with previous experimental studies and suggest that further work is required to identify other key dependencies and/or uncover the complex physics and mechanisms at play.

Thesis Supervisor: Anne E. White
Title: Cecil and Ida Green Associate Professor of Nuclear Science and Engineering

Acknowledgements

I'd like to thank my adviser, Professor Anne White, who has always provided me with inspiration, guidance, and motivation when needed most during my time at MIT, and reader, Dr. John Rice, who has provided his expertise, guidance, and knowledge countless times. I also owe a great thanks to Chi Gao, Dr. Nathan Howard, Dr. Matt Reinke, Dr. Greenwald, Dr. Clemente Angioni, Dr. Rachel McDermott, Dr. Choongki Sung, Mark Chilenski, and Paul Ennever, each of whom contributed to this research effort. I am also very grateful to the entire Alcator C-Mod staff and the PSFC and C-Mod administrative staff for everything they've done to make this research possible. Lastly, I thank my family, friends, and my officemate Juan Ruiz Ruiz for their encouragement and advice.

This research and the second year of my Research Assistantship were funded by the Alcator C-Mod Department of Energy contract (DE-FC02-99ER54512-CMOD). The first year of my Research Assistantship was funded partially by the MITEI-Lockheed Martin fellowship with the remainder coming from the MIT Department of Nuclear Science and Engineering.

Contents

List of Figures

List of Tables

1 Introduction

Faced with a rapidly growing population and increases in energy consumption per capita, the world is in need of more effective and abundant sources of energy. Nuclear fusion has the potential to revolutionize the world by utilizing reactions over a million times more powerful than those of oil or gas with a virtually unlimited supply base. Researched as a source of energy starting in the early 1950s, nuclear fusion is a reaction in which two light nuclei combine, or "fuse", to create a larger nucleus and release energy over one million times that of typical chemical reactions. However, for nuclei to become energetic enough to overcome the Coulomb barrier of charge repulsion to fuse, the nuclei must be at temperatures over 100 million Kelvin. At these temperatures, the electrons are stripped from the fuel atoms and the fuel becomes a plasma, which must be confined and controlled such that a sustainable number of fusion reactions occur to generate power. Many devices to accomplish this have been designed and tested, but the most successful device is called a tokamak, which is a toroidal chamber that uses toroidal and poloidal magnetic fields to confine the highly energetic plasma. A simplified diagram of a tokamak is shown below in Figure 1.

To improve the performance of tokamaks for power generation, a better understanding of plasma momentum transport is necessary to maximize the confinement time. Also, the plasma confined in the tokamak demonstrate various turbulent modes that negatively affect confinement. Intrinsic rotation, a phenomenon in which the plasma rotates inside the torus without any external momentum input, has been observed in multiple tokamaks and addresses both issues as it provides an opportunity to study momentum transport and is a possible method of mitigating turbulence in future devices. More specifically, the plasma has been observed to change the rotation direction upon certain changes in plasma parameters and poses an important issue in understanding what truly drives these direction reversals. There have been multiple viewpoints attempting to determine the dominant parameter related to these rotation reversals of which the most notable is the transition of the dominant turbulent regime from the trapped electron mode (TEM) to the ion temperature (ITG) mode. However, there have been seemingly contradictory experimental observations and simulations in previous work. Therefore, these contradicting view points instigates the question: does the TEM/ITG transition really play an important role in rotation reversals? If so, how? If not, what other parameters are the dominant players?

This thesis aims to answer this question through providing further validation for one of the viewpoints or possibly identifying new parameters that play important roles in ohmic L-mode rotation reversals, a subset of rotation reversals that remains especially difficult to understand. To test whether the dominant turbulent regime plays an important role, linear stability analysis using GYRO will be performed on a collection of many ohmic L-mode rotation reversal shots from Alcator C-Mod, the tokamak at the MIT Plasma Science and Fusion Center (PSFC). An analysis workflow will be created that processes a large number of shots from its initial state of diagnostic measurements to determining the dominant turbulent regime and the growth rates of every rotation reversal shot to find correlations with rotation reversals. Error and sensitivity analysis will also be implemented to generate robust linear stability results that account for experimental and analysis errors. Additionally, these shots will be used to study the correlation of various other plasma parameters to reversals to validate current viewpoints or possibly identify new ones. By analyzing a large number of

ohmic L-mode shots, which has not been done in previous work, the objective is to probe several hypotheses for the driving mechanism in rotation reversals, especially focused on probing the role of the TEM/ITG transition.

This chapter is broken down as follows: Section 1.1 will cover the motivation behind this study, Section 1.2 provides a brief description of Alcator C-Mod, the high field tokamak used at MIT, and Section 1.3 provides a short background on intrinsic rotation and momentum transport. Section 1.4 provides an overview of the rotation reversal phenomenon and the three hypotheses that are being tested, Section 1.5 states the problem statement, and Section 1.6 provides a thesis summary.

1.1 Motivation

For fusion energy to become viable, the confinement time for the plasma must exceed a certain threshold at a given plasma density and temperature, given by the Lawson criteria. However, unstable turbulent modes result in disruptions inside the plasma that result in loss of confinement, rapid dissipation of energy, and ultimately, the loss of the hot plasma required for nuclear fusion reactions. Additionally, computationally modeling these modes to predict their behavior is incredibly difficult as the underlying physics issues are not well understood and simplified models are rarely accurate in application. Therefore, it is critical to tokamak performance and commercialization of fusion energy to suppress the presence and growth of turbulence, which toroidal rotation of the plasma can do within a wide range of performance regimes.

Velocity shear resulting from plasma flow is known to improve confinement by suppressing turbulence [1, 2, 3, 4, 5, 6] and plasma rotation can increase stability against a variety of MHD modes, such as resistive wall modes [6, 7, 8] and neoclassical tearing modes [9, 10]. These resistive wall modes (RWMs) and tearing modes have deleterious effects on tokamak performance, so plasma rotation offers one possible method of mitigating some of the turbulent modes plaguing tokamak performance.

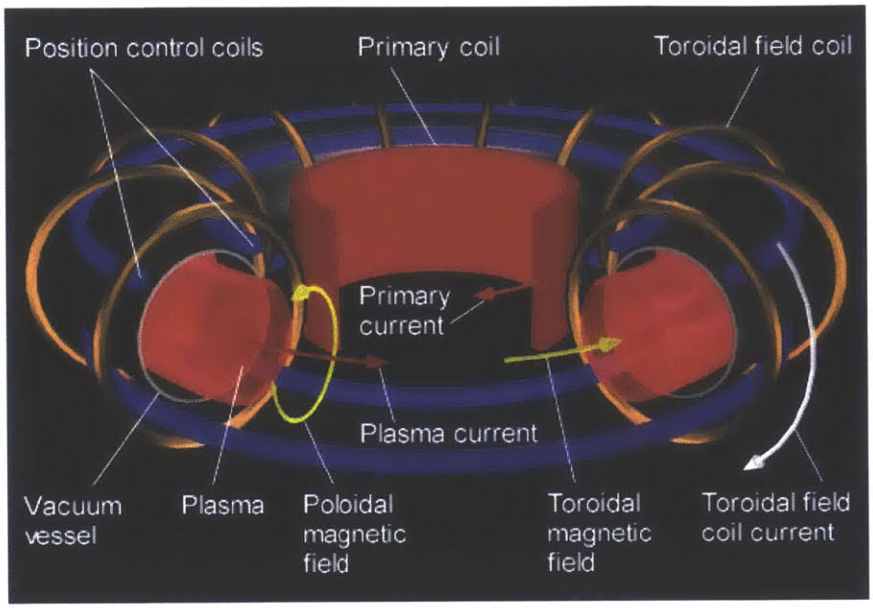

Figure 1: Illustrative diagram of the major components of a tokamak in confining the plasma torus [Courtesy of the Univ. of Illinois - Urbana Champaign]

In current devices, toroidal rotation is primarily generated through neutral beam injection, which injects neutral particles toroidally into the plasma to spin the plasma as shown in Figure 1. However, momentum contribution from external devices will not be sufficient to generate adequate rotation in future devices, such as ITER. More importantly, ITER will be highly susceptible to locked modes (plasma with V_Φ=0) in low-torque plasmas, which can lead to disruptions, rapid dispersion of the plasma energy into the tokamak walls [11]. These two factors threaten the plasma confinement and performance of ITER, so methods to generate rotation must be investigated. One source of rotation is from the plasma itself; intrinsic rotation, self-generated flow present in the absence of external momentum input, has been observed in multiple tokamaks [11]. However, intrinsic rotation and what drives it must be better understood in order to both predict the level of rotation in future devices and hopefully control it. Also, improved understanding of rotational and momentum transport is necessary to improve fusion device performance, which can be provided by studying intrinsic rotation [12].

More specifically, rotation reversals, the change in direction of the core toroidal rotation as a result of small changes in various plasma parameters, have been observed in intrinsically rotating tokamak plasmas [13]. With specific changes to certain plasma parameters, the plasma has been observed to stop and change its rotation direction in the core without affecting other plasma parameters and without additional external momentum input. A sample shot of a rotation reversal for Alcator C-Mod is shown in Figure 2.

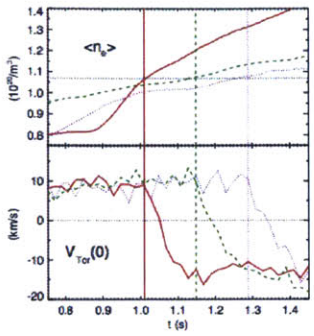

Figure 2: Rotation reversal evident by the change in core toroidal velocity $V_{Tor}(0)$ from positive to negative for a shot in the Alcator C-Mod tokamak [14].

This phenomenon is not only an interesting problem to study but also an opportunity to gain understanding about intrinsic rotation and momentum transport by attempting to discover the driving mechanisms for reversals. There have been multiple explanations for this rotation reversals in the literature. Rotation reversals were first observed in TCV and to depend on electron density [15]. Later, a correlation between rotation reversals and the dominant turbulence regime, or the most unstable turbulent mode, was identified through experimental observations [12, 13, 14, 16]. The two types of dominant turbulence regimes would be classified as Ion Temperature Gradient (ITG), where turbulence is driven primarily by the ion temperature radial gradient, or by Trapped Electron Mode (TEM), where turbulence is driven primarily by trapped particle effects, and electron temperature and density gradients. The term dominant refers to the turbulent mode fluctuations that have the greatest growth rates and therefore are the fastest growing, or most unstable.

In contrast to these results, other experiments found that reversals are most dependent on density gradients rather than the dominant mode of the turbulence [17] and others have observed no strong correlation between rotation reversals changes in the dominant turbulence mode [18, 19]. The discrepancies in observations and interpretations of the results leaves an open question that must be answered with further analysis of new data.

Additionally, comparison of theory to experimental observations of rotation reversals is still an open area of research. Because studying rotation reversals can shed more light on what drives intrinsic rotation, identifying the key dependencies of rotation reversals and studying the underlying physics of the phenomena is critical in improving our understanding of momentum generation and transport.

Therefore, this thesis aims to utilize a vast database of ohmic L-mode shots with strong rotation reversals and intrinsic rotation in Alcator C-Mod to validate/invalidate previous work and further characterize rotation reversals by using multi-variable regression methods to possibly identify new dependencies. More specifically, linear stability analysis using GYRO will be performed to look for for TEM/ITG linear stability boundaries in C-Mod, which will be compared to rotation reversals to locate possible correlations between momentum transport and turbulence. In addition, error and sensitivity analyses will be used to provide further transparency and demonstrate the potential effects of experimental and analysis uncertainties in the characterization of rotation reversals. Therefore, this project will provide

a large and highly analyzed database of Alcator C-Mod shots, and possible next steps would be to continue contributing to the international rotation reversal database and perform cross-tokamak and cross-shot type analysis.

1.2 Alcator C-Mod

Alcator C-Mod is the tokamak at the Massachusetts Institute of Technology as an integral part of the Plasma Science and Fusion Center. The device was upgraded from Alcator C, following Alcator A constructed in the early 1970s. Alcator C-Mod is a compact, high-field, diverted tokamak with major radius R = 0.67m, minor radius a = 0.21m, and a magnetic field B_T<8 T. The design parameters are listed below.

Table 1: Design and plasma parameters for Alcator C-Mod [20].

Parameter	Typical Values
Major radius (R)	0.67 m
Minor radius (a)	0.21 m
Volume	1 m^3
Toroidal magnetic field (B_T)	$\leq$ 8 T
Plasma current (I_P)	$\leq$ 2.0 MA
Plasma electron density (n_e)	$\leq$ 1 x 10^{21} m^{-3}
Electron temperature (T_e)	$\leq$ 10 keV
Ion temperature (T_i)	$\leq$ 10 keV
Plasma pressure (P)	$\leq$ 1.8 x 10^5Pa
ICRF heating power	$\leq$ 8 MW, 50 to 80 MHz
LHCD power	$\leq$ 3 MW, 4.6 GHz

It can be seen from the table that the ion cyclotron range frequencies (ICRF) heating power and (lower hybrid current drive) LHCD input power are very substantial. These are used exclusively for auxiliary heating and current drive for Alcator C-Mod. With its relatively small radius and compact design, Alcator C-Mod can create extremely strong magnetic fields which allows for a very high plasma pressure. These characteristics make the tokamak optimal for research in plasma transport, ICRF heating, external current drive, plasma-material interactions, and confinement regimes, especially the I-Mode [21].

Alcator C-Mod utilizes a wide array of diagnostics. To study intrinsic rotation and rotation reversals, the high resolution x-ray spectrometers (HIREX) are used to measure both the time-resolved core rotation velocity and ion temperature profiles and charge exchange recombination spectroscopy (CXRS) is used to measure the edge rotation velocity profiles [22]. Thomson scattering systems are used to measure both electron density and temperature [23, 24]. Phase contrast imaging (PCI) with gas puff imaging and reflectometer systems are utilized to make sensitive density fluctuation measurements [23], which are used to determine various plasma turbulent modes, and electron cyclotron emission (ECE) diagnostics are used to make electron temperature profile and fluctuation measurements [25]. The diagnostics measurements used for analysis will be described in further detail in Appendix A.

Accurate density and temperature measurements are essential for energy transport calculations and linear stability analysis, which will be covered in later sections; therefore, the error bars of these diagnostic measurements are used both for evaluating the quality of C-Mod shots for the database and for the error and sensitive analysis performed throughout the study.

1.3 Intrinsic Rotation

Intrinsic rotation, or spontaneous rotation, began to be studied after researchers attempted to understand the torque scans while measuring toroidal velocity profiles in the core of the JFT-2M tokamak [26]. Through this analysis of transport of toroidal momentum, researchers discovered the existence of a non-diffusive term in the transport matrix, which resulted in a spontaneous source of toroidal momentum. This discovery followed the discovery of a non-diffusive inward electron heat flux term in the DIII-D tokamak [27] and a non-diffusive inward flux of momentum transport in JT-60U [28]. It was observed that this non-diffusive flux term resulted in a finite and significant toroidal plasma velocity, especially in the core, without any external momentum input. This phenomenon has also been observed in Alcator C-Mod [11, 29, 30], DIII-D [31], TCV [32], and many other devices and in different confinement modes and configurations, such as in H-mode [11], I-mode, ion transport barrier (ITB) [33, 34, 35, 36], L-mode [14], and various others.

All of these different configurations result in variations in the observed intrinsic rotation. However, the focus of this section will primarily be on intrinsic rotation observed in H-mode and L-mode confinement regimes, as they represent the two most common confinement modes for Alcator C-Mod and will be consist of ohmic and RF plasma discharges. Also, the study of intrinsic torque was utilized partially to understand the intrinsic rotation in H-mode plasmas, which was observed to be triggered at L-H transitions [11, 30]. Therefore, intrinsic rotation in L-mode, H-mode, and L-H transitionary plasmas are very important and can be used to reveal the underlying physics behind this phenomenon, especially starting from the 'Rice scaling' for H-mode plasmas [11, 37]. This empirical scaling was derived from inter-machine comparisons of intrinsic rotation in JET, Alcator C-Mod, Tore Supra, COMPASS-D, DIII-D, TCV, and JT-60U and is expressed as

$$\triangle V \sim \frac{\triangle W}{I_p}$$

where V is the toroidal rotation velocity, W is the total plasma internal energy, and $I_p$is the plasma current. It has been well-observed that the core rotation velocity increases linearly with the total internal energy, or plasma pressure, and is also inversely proportional to the plasma current when the plasma is in the H-mode. This scaling was similarly observed for I-mode plasmas as well [21, 38], where I-mode called the "improved mode" is the confinement regime with high energy confinement like H-mode but very weak particle confinement. Figure

3 shows a plot of measurements showing how the Rice scaling fits the velocity measurements for various devices.

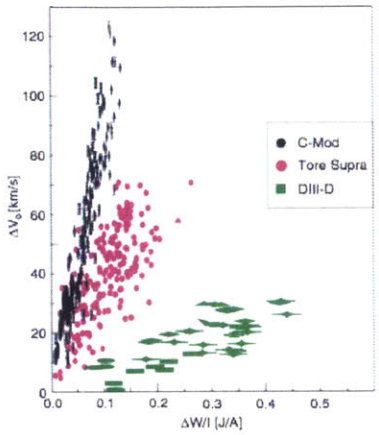

Figure 3: Intrinsic rotation velocity (difference between the L-mode velocity and the H-mode value) vs. the change in store energy over the plasma current for three tokamaks [11].

As shown, H-mode and I-mode intrinsic rotation is primarily in the co-current direction. It can be also seen that the difference in the enhanced confinement velocity and the L-mode velocity is linearly proportional to the change in stored energy normalized to the plasma current. However, it can also be seen that the coefficients of those scalings, or the slope, are different, which leads to the conclusion that the coefficients of the Rice scaling are dependent on the device characteristics, possibly size, plasma geometry, primary heating method, etc. Therefore, to normalize for device-specific characteristics, the size, magnetic field strength, and other parameters were included in a regression analysis and the best fit is expressed as

$$\triangle V = CB^{1.1} \triangle < P >^{1.0} I_p^{-1.9} R^{2.2}$$

with B as the magnetic field, <P> as the volume averaged plasma pressure, and R as the major radius of the tokamak. Although there still an additional coefficient, the value range among devices is much smaller and can be seen from Figure 4 that the velocity of all devices, even the future ITER tokamak, are still within error bars [11].

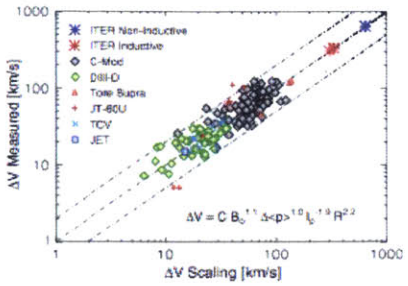

Figure 4: Measured difference in the rotation velocity as a function of the scaling shown above for various tokamaks [11].

Although this empirical scaling does not provide clear insight into the underlying physics and driving mechanism of intrinsic rotation in enhanced confinement regimes, the scaling can provide clues about what is happening. The core toroidal rotation is also well known to respond to changes at the plasma edge due to momentum diffusivity with a delay for the momentum transport from the edge [30, 39]. Additionally, this scaling worked regardless of whether the plasma was ohmic H-modes and ICRF H-modes. This implies that the ion temperature is not a driving mechanism of intrinsic rotation. Also, it was observed in many studies that rotation is independent of the normalized gyroradius ρ^* and the normalized collisionality ν^*, which implies that certain types of turbulence are not involved in the creation or maintenance of the toroidal rotation [11]. As mentioned previously, I-mode has high energy confinement similar to H-mode but has weak particle confinement; yet, I-mode and H-mode plasmas exhibit similar intrinsic rotation behaviors in similar parameter spaces. Therefore, it can be suggested that the temperature gradient, not density gradients, plays an important role in driving intrinsic rotation in enhanced confinement regimes [40].

With the existence of the universal Rice scaling and strong dependencies on several plasma parameters, intrinsic rotation in H-mode and I-modes has very simple dependencies on macroscopic and global plasma parameters. The physics cannot be extracted from these scalings and correlations, but it has been strongly suggested that turbulence, temperature gradients, plasma pressure, and plasma current play important roles in determining the rotation velocity. The theory behind this phenomenon will be covered later in the chapter.

In contrast to H-mode and I-mode plasmas, L-mode plasmas exhibit very complex dependencies on plasma parameters [41, 42, 43, 44]. The velocity strongly depends on electron density, magnetic field, field configuration, distance between primary and secondary separatrices (SSEP), and plasma current in non-linear ways and the velocity can be both counter and co-current.. To illustrate the complex dependencies of L-mode rotation velocities, a plot of the rotation velocity as a function of the electron density is shown in Figure 5.

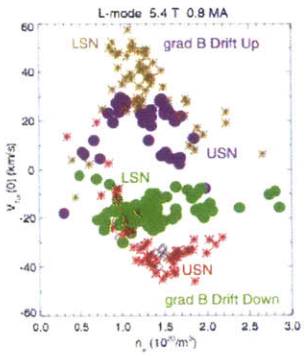

Figure 5: Toroidal rotation velocity at the core vs. electron density for various magnetic configurations in Alcator C-Mod [43].

At first glance, it can be seen from the figure that the dependence of the toroidal rotation velocity V_{Tor} on the electron density is non-monotonic for almost all of the configurations. Lower single null (LSN) and upper single null (USN) indicate where the magnetic fields cross to form the x-point, an area in which the plasma can exit from, and are two magnetic configurations. Unlike the strong linear relationships observed in Figure 3, the velocity can not only be co-current or counter-current depending on the magnetic field configuration but also can change directions depending on the value of the density. For example, for the USN plasma in the grad B drift down configuration, the rotation gets more counter-current until it hits a certain threshold and then becomes less counter-current. This change in rotation with increasing density has also been observed in multiple tokamaks [42].

For double null plasmas, the separation distance between the primary and secondary separatrices were found to have a significant effect on the intrinsic rotation velocity for L-mode plasmas. A separatrix is the boundary between open and closed magnetic field lines in which closed field lines confine the plasma and open ones allow the plasma to be diverted out of the bulk plasma. Figure 6 below illustrates a double null plasma and the presence of the primary and secondary separatrix.

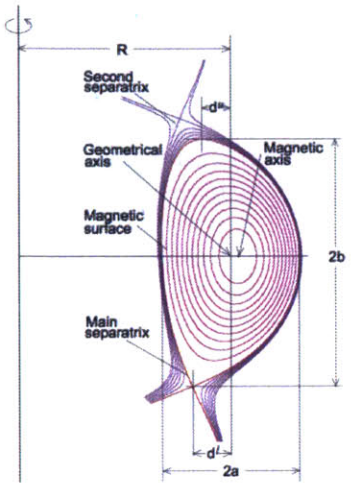

Figure 6: Diagram of the magnetic field lines in a double null magnetic configuration

It can be seen that the separatrix serves as a boundary between the bulk plasma and exterior and effectively acts as a plasma edge. Therefore, the strong dependence of the L-mode rotation velocity at the core on the SSEP, the distance between the separatrices associated with the upper and lower x-points as shown in Figure 6 suggests that the edge physics is important in determining the rotation at the core. A sample correlation between the velocity and SSEP is shown below in Figure 7.

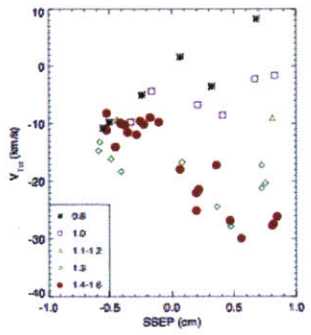

Figure 7: Core toroidal rotation velocity vs. SSEP, the distance between the separatrices associated with the upper and lower x-points, arranged by line averaged plasma density[43].

For a given density, the rotation velocity has a monotonic dependence on the SSEP. However, the fact that the velocity decreases more and more with increasing SSEP, the distance between the separatrices associated with the upper and lower x- points, at higher densities suggests that the plasma edge is important in defining the behavior of intrinsic rotation at the core, but the plasma density also plays a vital role in determining how the rotation will behave to changing parameters. From Figure 5 and 7, it can be seen that the

rotation velocity has a very complex and interdependent relationship with various parameters at once and this is true of the dependencies of the magnetic field and plasma current as well. Therefore, unlike those of enhanced confinement regimes, it is difficult to characterize the intrinsic rotation of L-mode plasmas empirically, so it must be attempted to be understood fundamentally from the physics of momentum transport. This difficulty in characterizing and understanding L-mode intrinsic rotation is the motivation for using ohmic L-mode shots as the basis for this study.

To understand the physics behind intrinsic rotation, the first step is the turbulent momentum flux, which provides an expression for the mean field momentum flux in the plasmas driven by electrostatic turbulence and can be studied in-depth using [45] as reference. The expression is given as

$$\Pi_{r,\phi} =< n >< \tilde{v}_r \tilde{v}_\phi > + < \tilde{v_r} \tilde{n} >< v_\phi > + < \tilde{n} \tilde{v_r} \tilde{v_\phi} > \tag{1}$$

where the first term is the toroidal Reynolds stress, the second is the convective flux, and the third term represents the nonlinear flux, which is often driven by processes such as mode-to-mode coupling and turbulence spreading and is not well understood. Although the last term might play a vital role as it has been suggested that strongly nonlinear processes could be at work in generating flows, the focus will be on the Reynolds stress term [46]. This Reynolds stress term, can be decomposed as

$$< \tilde{v}_r \tilde{v}_\phi >= -\chi_\phi \frac{\partial < v_\phi >}{\partial r} + V < v_\phi > + \Pi^R_{r,\phi} \tag{2}$$

where $\chi_\Phi$is the turbulent viscosity, or momentum diffusivity, V is the momentum convection velocity or momentum pinch, which is covered in detail in [47], and $\Pi^R{}_{r,\Phi}$is the residual stress, which will be the focal point of this section. The residual stress term is the one piece of the expression that is not directly proportional to $<v_\Phi>$ or $\partial<v_\Phi>/\partial r$ and can be seen as a 'driving term' for intrinsic rotation. The residual stress term is proportional to $\nabla P_{i,e}$, $\nabla T_{i,e}$, or ∇n and is a term for the process in which free energy from part of the driving heat flux Q is converted into toroidal rotation by turbulence [45]. The residual stress term is known to generate a local intrinsic rotation torque $-\partial_r \Pi^R_{r,\phi}$ which creates the rotation, but the exact mechanism that converts energy into the torque is still not well understood. As a simplified model used in general theories [40, 45], the residual stress term can be viewed as part of a heat engine, which converts heat flux into net momentum in the plasma, and the goal is to uncover how the engine works.

Despite the early stage of intrinsic rotation theory, it is well understood that the rotation is driven by parallel and perpendicular Reynolds stresses and that the parallel Reynolds stress requires symmetry breaking to become a residual stress term [48]. These symmetry breaking mechanisms essentially convert inhomogeneities of wave momentum in the radial plane of the

tokamak into asymmetry parallel to the current, which creates an intrinsic torque. Because various symmetry-breaking mechanisms exist, including the electric field shear, intensity gradient, and polarization stress [48, 49, 50], finding the contributions of each to driving intrinsic rotation is another important question to be answered. Nonetheless, it can be seen that the primary focus of research is on the residual stress term of the momentum flux and discovering its driving mechanisms.

1.4 Rotation Reversal

While investigating intrinsic rotation, multiple types of transport bifurcations were observed in which the plasma exhibits two very different behaviors in terms of momentum transport. One interesting phenomenon that has been observed in ohmic and RF L-mode plasmas is the rotation reversal, when the plasma spontaneously changes its intrinsic rotation flow direction without significant affecting other macroscopic plasma parameters. Similar to the background section on intrinsic rotation, the previous knowledge on rotation reversals are highly empirical, driven primarily by observations and simulations done on various tokamaks, and empirical scalings are used to provide insight into the underlying physics by highlighting the parameters and transport mechanisms that seem to highly affect reversals. Out of these studies, three different hypotheses about the key dependencies of rotation reversals have arose and are driven by different sets of observations and simulations and assumptions that lead to their conclusions. After a brief introduction into rotation reversals, these three hypotheses will be explored in detail and how they compare to each other.

Rotation reversals have been first studied in detail in the TCV [15] and Alcator C-Mod [14] Here, the reversal is observed as a change of sign in rotation (reversed direction) at the core, as shown in Fig. 1. The rotation reversal occurs when the plasma density exceeds a critical threshold density n_{sat}or other parameters such as magnetic field and plasma current. Various experiments have been done on multiple devices, where the density is ramped up during a single shot to induce rotation reversals. A sample shot from C-Mod demonstrating the change in rotation direction with increasing density is shown in Figure 8.

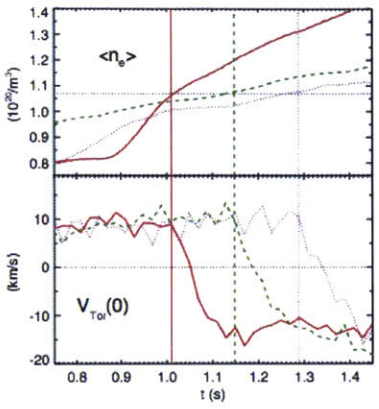

Figure 8: Rotation velocity and line averaged electron density as function of time to locate critical density for rotation reversal in Alcator C-Mod [14].

As the density is gradually increased at the beginning of the shot, the toroidal velocity remains reasonably constant. However, at a certain density, marked as the vertical red line close to t = 1.0 s, the toroidal velocity in the core begins to decrease dramatically and actually is negative, indicative of counter-current rotation. However, even though the density continues to increase, the velocity peaks at a specific counter-current value and remains relatively stable. Because of the temporal relation, the rotation reversals can be said to have been "caused" by the density approaching the critical density, observing how this critical reversal density changes with various plasma parameters has been a way of uncovering the dependencies of rotation reversals.

Two parameters that have been observed to highly affect the critical reversal density are the magnitudes of the magnetic field B and plasma current I_p[16, 40]. Sample plots illustrating those correlations are shown in below in Figure 9.

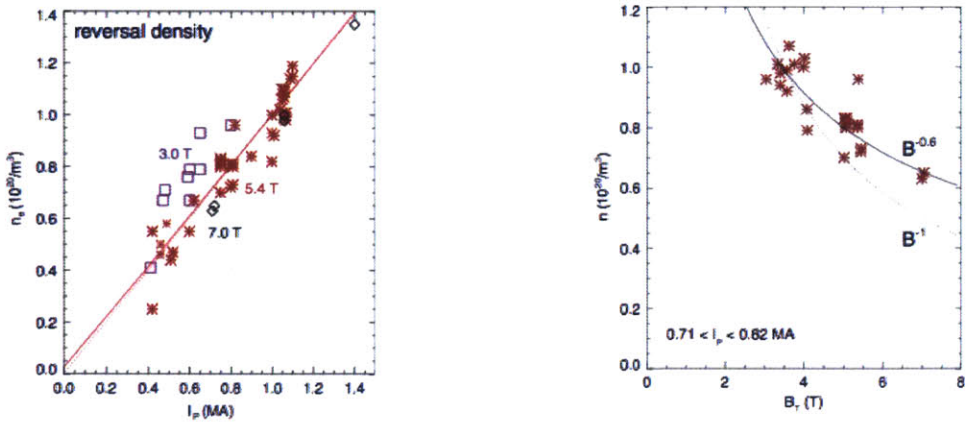

a) b)

Figure 9: Plots of the rotation reversal density vs. a) plasma current and b) toroidal magnetic field in ohmic plasmas in Alcator C-Mod [14].

From Fig. 9a, it can be seen that the critical density scales linearly with plasma current and that the reversal densities at lower magnetic fields tend to be higher than what is predicted and those of higher magnetic fields tend to be lower. This can also be seen in Fig. 9b, where the reversal densities are inversely proportional to the magnetic field approximately by $1/B^{0.6}$. Therefore, with increasing magnetic field at a fixed current, the critical density decreases. It has also been observed that reversal densities are proportional to the safety factor $q = \frac{rB_\Phi}{RB_\theta}$ and the normalized collisionality $\nu_\star \equiv 0.0118\frac{qRZ_{eff}n_e}{T_e^2\epsilon^{1.5}}$, the ratio of the collision frequency to the bounce frequency, but these are directly proportional to the plasma current and density, respectively. Therefore, those correlations are not novel and either can be used when deemed appropriate.

In addition to how the toroidal rotation velocity changes at the core, seeing how the velocity profile evolves during a rotation reversal can provide further clues to its driving mechanism. A plot of the rotation velocity profile and the corresponding electron temperature and electron density profiles from Alcator C-Mod are shown in Figure 10.

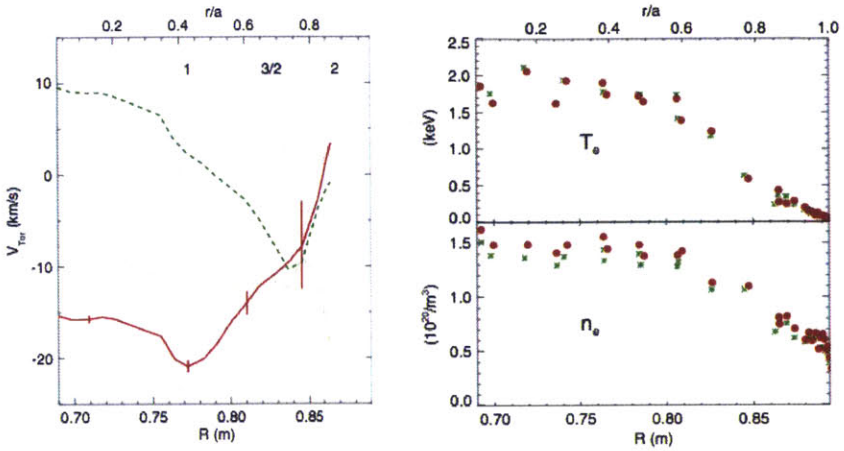

Figure 10: Rotation velocity, electron temperature, and electron density profiles at various times in a single ohmic plasma discharge (Green dotted line corresponds to the green asterisks and the red solid line corresponds to the red circles) [14].

For the green and red lines on the velocity plot, it can be seen that despite one being largely co-current and one being largely counter-current, the velocities are anchored at q = 3/2, as shown on Figure 10. This has been observed not only in Alcator C-Mod but in various devices, such as ASDEX Upgrade [12]]. Outside of q = 3/2, the velocity profile at the edge seem alike. Also, it seems that most of the velocity change is done between the q = 1 and 3/2 region. Inside q=1, the velocity profile is relatively flat and stable, due to sawteeth oscillations, which has been observed in multiple devices and well-explained [15, 32]. Despite the large difference in magnitude and sign, the temperature and density profiles are relatively the same. This observation suggests that the electron temperature and density may not have a strong effect on rotation reversals.

Because rotation reversals can analytically be thought of as a change in sign of the Reynolds stress, the same momentum flux expression that was used to explain intrinsic rotation can be used to understand reversals. The decomposed Reynolds stress term, expressed in Equation 2 as

$$< \tilde{v}_r \tilde{v}_\phi >= -\chi_\phi \frac{\partial < v_\phi >}{\partial r} + V < v_\phi > + \Pi^R_{r,\phi}$$

is believed to be what drives the intrinsic rotation; therefore, one or more of these terms must change sign when the density hits the critical density for the rotation velocity to be decreased and eventually reversed [45]. The momentum diffusivity $\chi_\Phi$is always positive and the radial rotation velocity gradient does not change signs in observed shots. V, the velocity pinch, is always directed inwards and it is made up of three separate pinch mechanisms: turbulent equipartition pinch [51], thermoelectric pinch [51], and the Coriolis pinch [49]. The first does not change sign unless the density gradient changes as well, the second is dependent on large temperature gradients, and the sign of the third can only change sign if the density profile gradient changes sign. However, from Fig. 10. it can be seen that within this regime, the

density and temperature gradients are relatively small and never change sign. Therefore, it can be seen that the velocity pinch term cannot be a strong driver of changing the sign of the Reynolds stress.

The remaining term, the residual stress, $\Pi^{R}{}_{r,\Phi}$ is a collection of momentum flux mechanism that are not directly related to the plasma rotation (convective) or to the rotation gradient (diffusive) terms, such as the perpendicular velocity shear [50, 52, 54], up/down asymmetries [53], and profile shearing [55]. Therefore, it is highly likely that the residual stress term changes signs if one or more of these mechanisms changes sign and dominates. These residual mechanisms have different dependencies on plasma parameters, so previous studies have attempted to locate dependencies and correlations of rotation reversals to identify exactly what mechanisms could be the dominant drivers. This thesis explores three major hypotheses, each stating that the dominant parameter in rotation reversals is:

1. the **dominant turbulence mode**, especially the TEM/ITG transition [12, 14]
2. the **density and temperature local profile gradients**, especially the electron density gradient, indirectly related to the TEM-dominated regime [13, 17]
3. the **neoclassical corrections** to the equilibrium ion distribution [56, 57].

1.4.1 Dominant Turbulence Regime

The first hypothesis suggests that the change in rotation direction is caused by the change in the turbulence mode propagation direction when the dominant turbulence regime of the plasma transitions from the trapped electron mode (TEM) to the ion temperature gradient (ITG) mode [14], which is also believed to be the driving mechanism for the transition in the global energy confinement regime in ohmic plasmas [59]. The idea stemmed from observations of rotation reversals within proximity of the transition in the energy confinement regime from linear Ohmic confinement (LOC) to saturated Ohmic confinement (SOC) in Alcator C-Mod [14, 42, 43] and ASDEX Upgrade [12].

The LOC/SOC transition can be briefly explained as the point in which the energy confinement time of the tokamak no longer increases with an increase in electron density. In various devices, the energy confinement time $\tau_E$scales linearly with electron density, which is appropriately called the linear Ohmic confinement (LOC) regime, but at a certain threshold density, the confinement time seems to remain relatively flat, which is called the saturated Ohmic confinement (SOC) regime. This transition with increasing density is shown below in Figure 11a.

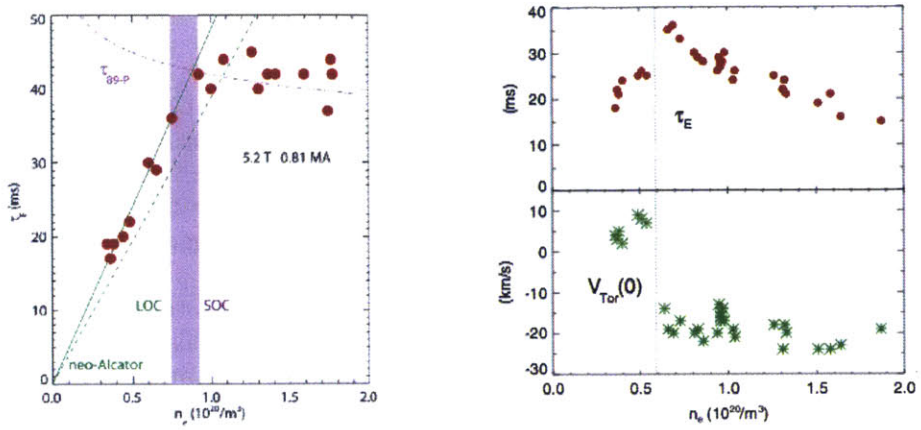

(a) (b)

Figure 11: (a) Energy confinement vs. electron density showing the LOC/SOC transition for Alcator C-Mod [Rice, Phys. Plasmas, 2012] and (b) Rotation reversal and energy confinement time vs. electron density [14].

Figure 11a and 11b can be compared to see that at a specific density, the energy confinement time no longer continues to increase. At the LOC/SOC transition (marked as the purple bar in Fig. 11a and dotted line in Fig. 11b), the rotation reversal was also observed. which suggests that both phenomena are related and share the same driving mechanism - the dominant turbulence regime [58, 59, 60]

These observations are qualitatively consistent with the physics behind the residual stress, which can change signs based on the change in the mode propagation direction. In the TEM-dominated regime, the propagation direction is the electron diamagnetic direction, but ITG-dominated, the plasma propagation direction is in the ion diamagnetic direction, which is a change in sign. This same mechanism has been used to explain the LOC/SOC transition in global energy confinement and has been well supported [61]. Therefore, the concomitant shift in the energy confinement mode, dominant turbulent mode, and intrinsic rotation direction after a critical density observed repeatedly in Alcator C-Mod are suggestive of strong connections among the three phenomena.

Significant changes in density fluctuation measurements were observed during rotation reversals that support this idea. Because density fluctuations are indicative of various turbulent modes [62]., significant changes of this parameter during reversals is important to study. A sample shot of the dispersion plot of these fluctuations, measured using the phase contrast imaging (PCI) diagnostic, before (top in Fig. 12a) and after (bottom in Fig. 12b) the rotation reversal are shown below in Figure 12.

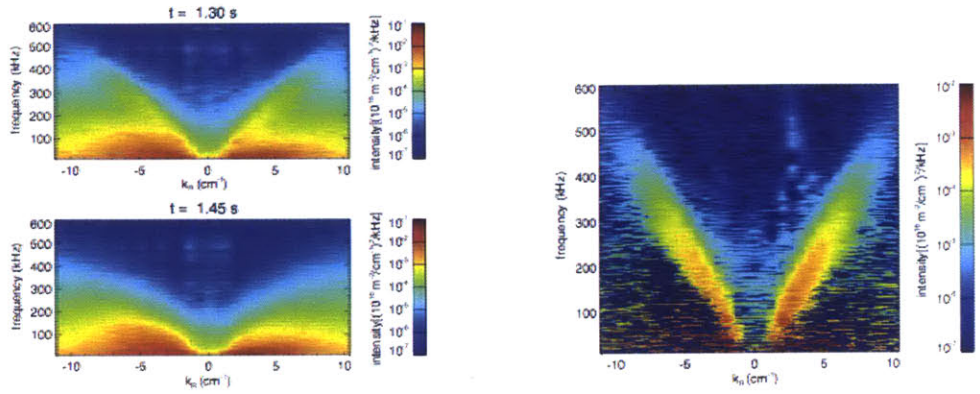

(a) (b)

Figure 12: (a) Dispersion plot of density fluctuations before and after the rotation reversal [14] (b) Difference between the two dispersion plots [14].

It can be seen that there are two distinct figures that originate from k_R= -2 $cm^{-1}$and 2 cm^{-1}in the top picture of Fig. 12a which extend from approximately f= 100 Hz to between 400 Hz where $k_R$is the wavenumber component and f is the frequency of the fluctuations. . However, after the rotation reversal at t = 1.45 s, the "lobes" have disappeared, which indicates a fundamental change that altered the mechanism driving density fluctuations in the plasma. To better observe the difference before and after the reversal, the difference dispersion plot is shown in Fig. 12b, which clearly shows the existence of two nodes extending from -2 and 2 cm^{-1}up to -10 and 10 cm^{-1}. It can also be seen that the right node with the positive $k_R$has a greater intensity, and also, these nodes were not able to be detected at the plasma edge, suggesting that the changes in density fluctuations, and therefore the turbulence, occur within the core. The phase velocities, which are the slopes of those nodes in Fig. 12b, are very similar which indicates that these features must occur where flux surfaces are symmetric, which is in the plasma interior. Also, the $k_R\rho_s$, where ρ_s is the normalized gyroradius, is between 0.15 and 0.7, which are typical values of TEMs. However, ITG modes can also exist in this range. Although the direction of propagation of these fluctuations or of the mode propagation cannot be determined experimentally in C-Mod, the discernible changes after rotation reversals does provide support that turbulence may play an important role in intrinsic rotation .

To develop this hypothesis, other parameters have been studied with respect to rotation reversals, especially those commonly known to have correlations with turbulence and confinement regime. A plot of these parameters for one C-Mod shot, which aims to show the correlations, is shown below in Figure 13.

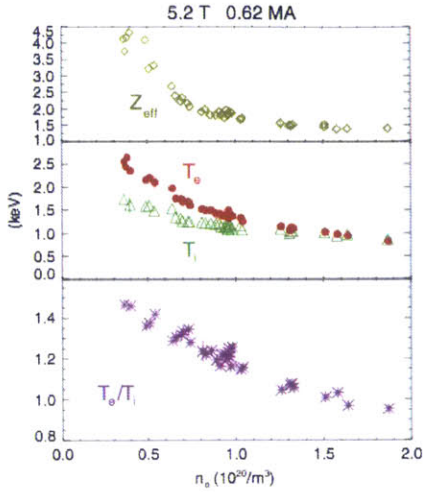

Figure 13: Plot of Z_{Jeff}(ion effective charge), $T_{e,i}$(electron and ion temperatures), and the temperature ratios vs. density. Vertical dotted line represents the critical density for rotation reversal [14].

In contrast to the sudden changes in the global energy confinement regime and densitiy fluctuations, other parameters such as the effective ion charge Z_{eff}, temperatures, and the temperature ratio $\frac{T_e}{T_i}$ all drop monotonically and gradually without any noticeable changes at the critical reversal density. Therefore, this suggests that these parameters do not play important roles in the underlying physics of rotation reversals, which potentially eliminates these parameters as part of the primary dependencies.

In terms of the physics and more specifically, the Reynolds stress term, it was shown that reversals can occur when one or more of the three terms change sign at the critical density and are larger in magnitude than the others to become a dominant term(s) [45]. These three terms are written as

$$< \tilde{v}_r \tilde{v}_\phi >= -\chi_\phi \frac{\partial < v_\phi >}{\partial r} + V < v_\phi > + \Pi^R_{r,\phi}$$

where the first is the diffusive term, second is the convective term, and the last is the residual stress term. The momentum diffusivity $\chi_\Phi$is always positive and cannot change sign, and the momentum pinch term is made of various mechanisms that are not likely to change sign in both TEM and ITG-dominated plasmas. This eliminates the diffusive and convective terms as potential drivers [14]. As a result, the residual stress term must change sign, which can occur depending on the underlying turbulence through the change in the mode propagation direction [14, 61]. One possible way the TEM/ITG transition causes the rotation reversal is that the transition of the dominant turbulence regime and the turbulent mode propagation direction. The change in wave propagation from the electron diamagnetic direction corresponding to the TEM-dominated regime to the ion drift direction due to

the ITG-dominated regime can cause a change in sign of the residual stress. However, the magnitude and sign of the turbulent mode propagation direction has not been measured experimentally in C-Mod, which is essential in validating this hypothesis. Therefore, to test this hypothesis, the dominant turbulence regime for the plasma must be identified and compared to the intrinsic rotation direction to verify whether the TEM/ITG bifurcation exists for co-current and counter-current plasmas, respectively.

1.4.2 Local Profile Gradients

Rather than the dominant turbulence regime, the second hypothesis identfies the local density and temperature profile gradients, most notably the electron density profile, as the primary parameter for determining the strength and sign of the residual stress torque, which determines the rotation, and states the effective collisionality $\nu_{eff}$and the electron and ion temperature gradients are also important contributions [13, 17]. This hypothesis is developed based upon observations from the ASDEX Upgrade tokamak of the rotation reversal occurred concomitantly with electron density peaking past a critical threshold rather than during the TEM/ITG transition observed in Alcator C-Mod. These observations were further supported upon discovery of a phenemon referred to as a "double reversal" in ASDEX Upgrade, in which the plasma rotation would switch from co-current to counter-current as density was increased, and then change back from counter-current to co-current again with increasing density. This phenomenon can be seen in Figure 14b. Because the dominant turbulence regime does not also change from TEM to ITG and then ITG back to TEM upon the second reversal while significant changes are observed in the density gradient, these observations suggest that both of the observed rotation reversals are not caused by the ITG/TEM transition and other dependencies and mechanisms must be identified.

A series of plots of plasma parameters as a function of the effective collisionality ν_{eff}based on measurements at ASDEX Upgrade are shown below in Figure 14.

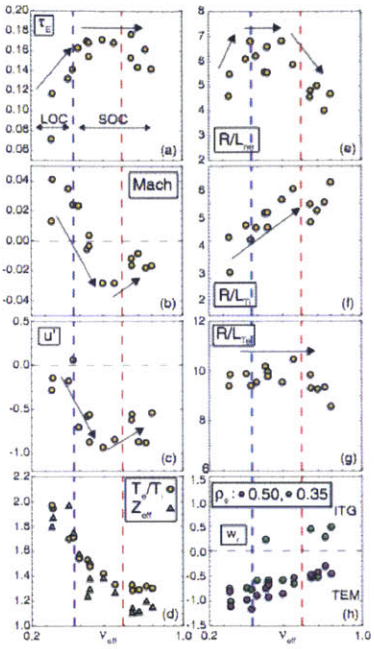

Figure 14: Plot of (a) energy confinement, (b) Mach number, (c) normalized toroidal velocity gradient, (d) temperature ratio and ion effective charge, (e) normalized electron density gradient, (f) normalized ion temperature gradient, (g) normalized electron temperature gradient, and (h) dominant turbulent mode vs. effective collisionality of ASDEX Upgrade time slices of one ohmic L-mode plasma discharge at various collisionalities [17].

Similar to the observations at Alcator C-Mod, the energy confinement regime transitions from LOC to SOC at a critical effective collisionality, which is proportional to density and expressed as $\nu_{eff} = 0.00279(15.94 - 0.5log\frac{n_e}{T_e^2}) \times \frac{n_e}{T_e^2} R\sqrt{m_A} Z_{eff}$ where m_A is the mass of the main ion and Z_{eff} is the effective nuclear charge. The Mach number, given as $M = \frac{V_\phi}{V_{thi}}$ where $V_{thi} = \sqrt{\frac{2T_i}{m}}$ is the ion thermal velocity, is effectively a normalized toroidal velocity and can be seen to change direction at the first dotted line, which is when the LOC/SOC transition occurs in Fig. 14b. Additionally, the temperature ratios and Z_{eff} monotonically decrease as a function of ν_{eff}, which was also observed in C-Mod and shown in Figure 14. However, as ν_{eff} increases and the plasma goes deeper into the saturated ohmic confinement regime, the rotation velocity begins to transition from counter-current to the co-current direction. This double reversal can be seen for a single shot in Figure 14b. In Figure 15a, a weak sign of a double reversal can be seen in the plot, which shows the u' of 190 intrinsic rotation shots as a function of ν_{eff} and will be explained in detail later in this section. Past $\nu_{eff} \sim 0.45$, several shots show the u' becoming positive again. However, this result is not conclusively and no such observation has been found in C-Mod. If the double reversal can be identified in C-Mod, it provides an excellent opportunity to identify strong dependencies due to the fact that finding a parameter that significantly changes or phenomenon that alters its behavior upon both rotation reversals is a clear indicator of an underlying relationship between the two.

By using this method on the parameters shown in Fig. 14, it can be seen that the normalized density gradient R/L_{n_e} where L_{n_e} the density gradient scale length is expressed as $L_{n_e} = \frac{n_e}{\nabla n_e}$, changes along with the Mach, number. R/L_{T_i} and R/L_{T_e} monotonically increase and remain constant, respectively, with increasing collisionality, which indicates that the ion temperature gradient may play an important role, but not to the degree of the density gradient. The density gradient becomes greater with initial increase in effective collisionality, an indicator of density peaking, which is consistent with the dominant turbulence regime transitioning from TEM to ITG.

In addition to a single-shot analysis shown in Figure 14, past work from ASDEX Upgrade used a database of 190 ohmic L-mode rotation reversal/intrinsic rotation shots to identify similar correlations between u' and collisionality and local profile gradients. These multi-shot plots are shown below in Figure 15.

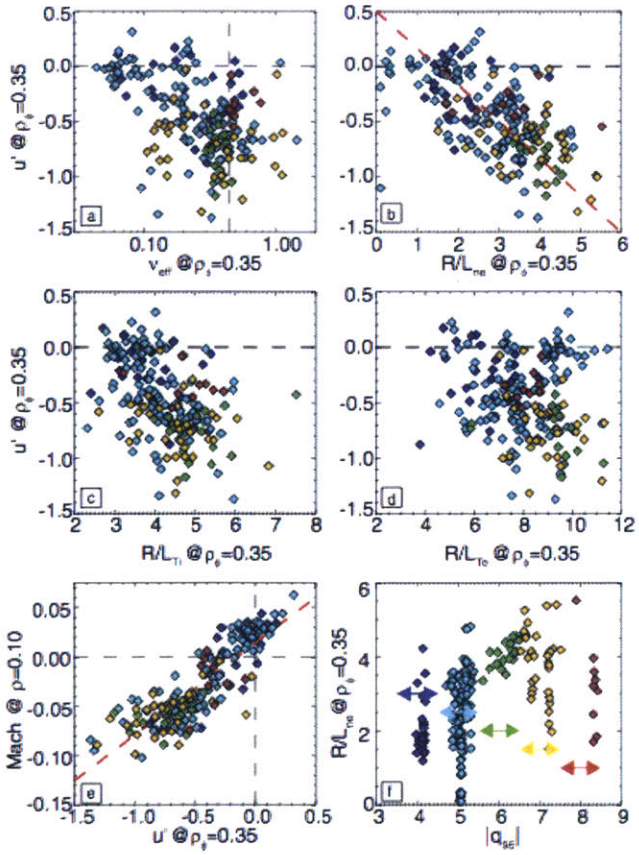

Figure 15: Plots of ASDEX Upgrade ohmic L-mode profiles at $\rho_\phi = 0.35$ of (a) u' vs. ν_{eff}, (b) u' vs. $\frac{R}{L_{n_e}}$, (c) u' vs. $\frac{R}{L_{T_i}}$, (d) u' vs. $\frac{R}{L_{Te}}$, (e) Mach number vs. u', and (f) $\frac{R}{L_{n_e}}$ vs. q_{95}. Colors of shots are used to refer to specific q_{95} as shown in (f) [17].

From Figure 15, it can be seen that the time slices of the single ohmic L-mode discharge

and the large set of ohmic L-mode shots in ASDEX Upgrade display similar correlations between u' and the profile gradients. It can also be seen from Figure 15e that u' near the core is highly correlated to the Mach number very close to the core at $\rho_\phi = 0.1$. This strong correlation suggests that the rotation gradient u' may be a good indicator of the rotation velocity at the core and supports the link between the residual stress term and rotation reversals. A multi-variable regression of u' for the density and temperature profile gradients ($\frac{R}{L_{n_e}}$, $\frac{R}{L_{T_e}}$, $\frac{R}{L_{T_i}}$) along with the effective collisionality ν_{eff} was performed for this database at $\rho_\phi = 0.3$ and the expression is given in Equation 3 below.

$$u' = -(0.12 \pm 0.02)\frac{R}{L_{n_e}} - (0.09 \pm 0.04)ln(\nu_{eff}) - (0.06 \pm 0.03)\frac{R}{L_{T_i}} - (0.028 \pm 0.014)\frac{R}{L_{T_e}} \quad (3)$$

The expression had a root mean square error (RMSE) of 0.27. From this regression expression, it can be seen that the most statistically significant parameter out of the four is the electron density gradient followed by the effective collisionality, ion temperature gradient, and the electron temperature gradient. The study also found little correlation between u' and q_{95}, the safety factor, and $\rho^\star$, the normalized Larmor radius.

As seen in Alcator C-Mod, the critical density of rotation reversals at ASDEX Upgrade were also linearly dependent on the current but its relationship with magnetic field could not be verified due to lack of wide range of magnetic field in the database. Also, it has been stated in past work from ASDEX Upgrade that the rotation gradient u' is more correlated with the effective collisionality than the electron density. The plots of various parameters from Figure 15 are shown as functions of both electron density and collisionality for comparison in Figure 16.

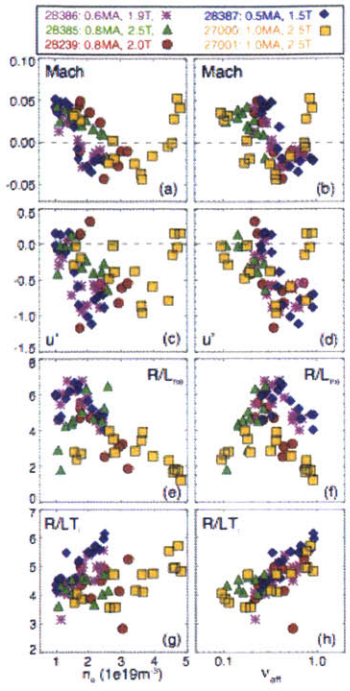

Figure 16: Plots from ASDEX Upgrade intrinsic rotation database analysis of Mach number, rotation gradient, normalized electron density gradient, and the normalized ion temperature gradient as a function of electron density $n_e$and effective collisionality ν_{eff}[17].

The study suggests that the correlations are apparent in both sets of plots, but some parameters, such as the profile gradients, are more correlated with the effective collisionality as the independent variable [17]. Because rotation reversals occur within a very narrow range of effective collisionality while the critical density can vary more widely due to other parameters, such as current and magnetic field, the work suggests collisionality could be a more effective parameter to use in consolidating many shots [17, 61]. It can also be seen from Fig. 16b and 16f that the Mach number and u' are the lowest when the density gradient is at its maximum, suggesting that they are all linked and are highly dependent on the effective collisionality. From these plots, it can be seen that the rotation is co-current with flat electron density profiles and counter-current at highly peaked profiles

These observations are further supported by a database of linear gyro-kinetic simulations done at ASDEX Upgrade to study the effective density gradient as functions of effective collisionality and the real frequency of the dominant turbulent mode, or the most unstable linear mode, which is plotted below in Figure 17.

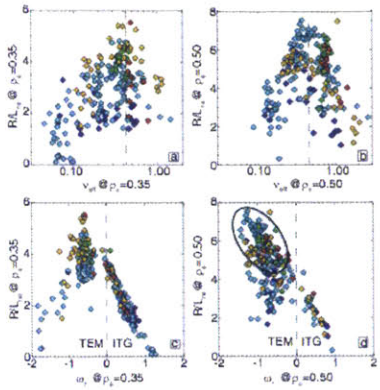

Figure 17: Plots from the ASDEX Upgrade rotation database of the normalized electron density gradient vs. effective collisionality and frequency of the dominant turbulent mode at ρ_Φ=0.35 and 0.5 [17].

As seen from Figure 17, the density gradient peaks are indicative of the rotation reversals and these gradients are non-monotonic as they increase and decrease, corresponding to the double reversal. For the dominant turbulence regime to be the primary determinant in rotation reversals, these density gradients should also achieve their maximum at the TEM/ITG transition, marked at ω_r= 0 and demarcated by the dashed line. However, for both$\rho_\phi = 0.3$ and $\rho_\phi = 0.5$, the maximum density gradient occurs well within the TEM regime between $\omega_r = -1$ and -0.5 for both locations. It can be seen from Fig. 17d that almost the full range of density gradients, corresponding to rotation in both the co-current and counter-current direction, are in the TEM-dominated regime. This density peaking in the TEM regime has been observed and reproduced by gyro-kinetic simulations multiple times [13, 63, 64].

These results from ASDEX Upgrade further suggest that rotation reversals are not driven by the dominant turbulent regime transition and by profiles, primarily by the local electron density profiles [13, 17]. This in combination with the observed double reversals that cannot be explained by the one-time turbulence transition from TEM to ITG supports the idea that the electron density gradient, as well as the effective collisionality and temperature gradients, are the primary parameters behind determining the residual stress term driving rotation reversals. Although the TEM regime might play an indirect role in rotation reversals due to the density profile, this hypothesis, based on studies at ASDEX Upgrade, identifies the local density and temperature profile gradients to be the primary dependencies of rotation reversals.

1.4.3 Neoclassical Corrections

The first two hypotheses believe that the dominant turbulence regime play a role in rotation reversals, either directly (TEM/ITG transition) or indirectly (TEM through electron density gradients), but other work suggest that rotation reversals cannot be tracked by a simple linear transition from the TEM to ITG-dominated regime or profile gradients [18, 19]. The hypothesis attributes the change in momentum transport in rotation reversals to other sources, such as higher gyrokinetic terms or neoclassical corrections [56, 57, 65]. In current

gyrokinetic simulations, only three sources of residual stress are included: diffusion from ion fluid parallel velocity shear, the Coriolis pinch, and the E x B shear pinch. However, there are many more possible sources of residual stress that can drive intrinsic rotation that are not taken into account. Therefore, these unrealized turbulent mechanisms or higher order terms not included in simulations can be potential causes for reversals and reasons why the correct mechanism has not been identified. One specific theory that suggests the mechanism driving reversals to be neoclassical corrections to the equilibrium ion distribution that modifies the turbulent transport will be the focus of this hypothesis [56, 57].

Previous work in C-Mod have shown that neither the TEM/ITG transition nor the local profile gradients play an important role in determining the rotation reversal and intrinsic rotation. Multiple plots on the parameters for one co-current and one counter-current ohmic L-mode shots at C-Mod are shown below in Figure 18.

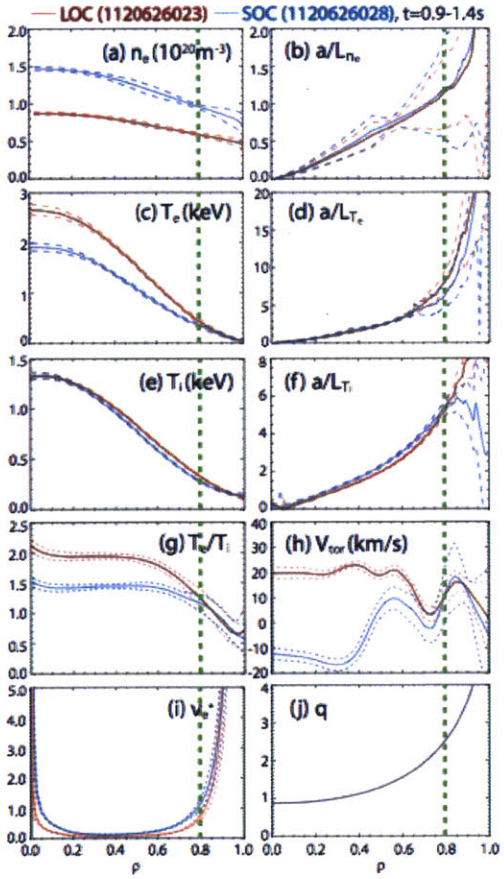

Figure 18: Time-average parameter profiles for a LOC (co-current: 1120626023) and SOC (counter-current: 1120626028) ohmic L-mode C-Mod shots. Solid lines show the time-averaged values and the dotted lines show the error [19].

It can be seen from Figure 18h that the shot in the linear ohmic confinement (LOC)

regime has a strong co-current rotation profile at 20 km/s and the shot in the saturated ohmic confinement (SOC) regime has a strong counter-current rotation profile at -10 km/s at the core. For both shots, the profiles of the normalized electron density gradient (Fig. 18b), normalized electron temperature gradient (Fig. 18d), and the ion temperature gradient (Fig. 18f) are almost identical, despite the rotation differing by almost 30 km/s at the core. This suggests that the local profile gradient might not be the primary parameter that determines the strength and direction of the intrinsic rotation. Using the same LOC and SOC shots from C-Mod, linear stability analysis results from an earlier study is shown below in Figure 19.

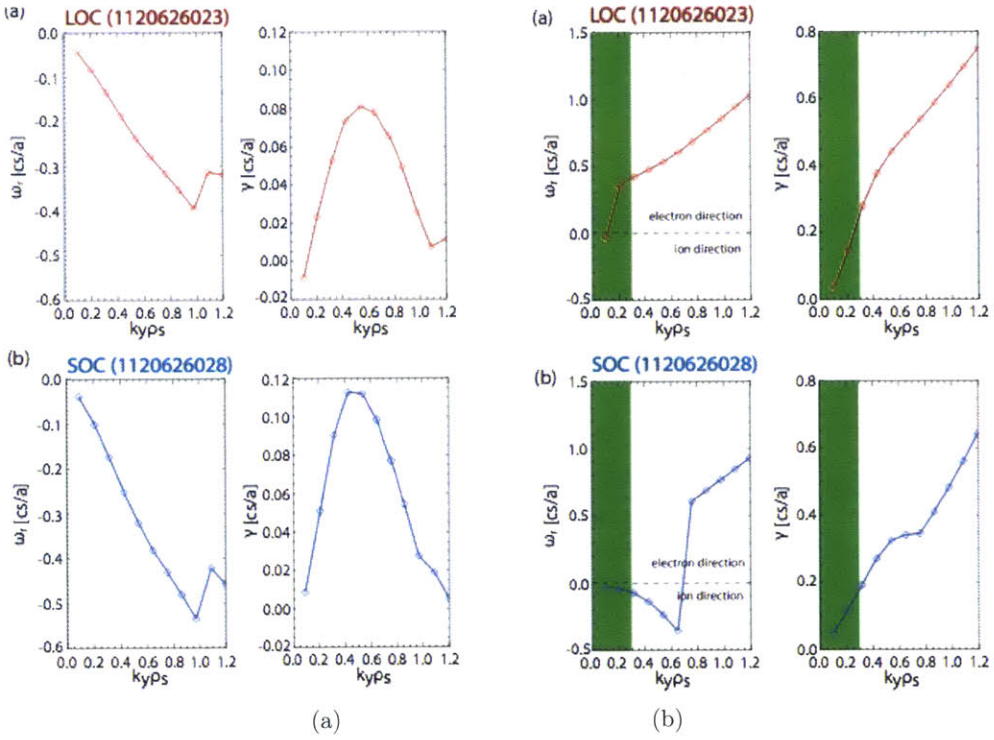

(a) (b)

Figure 19: Linear stability analysis results from GYRO simulation for a LOC (1120626023) and SOC (1120626028) C-Mod plasma at (a) ρ_ϕ~ 0.5 and (b) ρ_ϕ~ 0.8 [19].

It can be seen from Fig. 19a that the real frequency and growth rates of the dominant turbulence are almost identical for both co-current and counter-current rotating plasmas near the core. Only far from the core, atρ_ϕ~ 0.8 , the co-current plasma is in the TEM-dominated regime while the counter-current remains in ITG-dominated, and this is has been observed repeatedly in experiments. Contrary to the first two hypotheses, which were supported by observations of the co-current rotating plasma being in the TEM-dominated regime and switching to ITG at some point, both plasmas shown in Figure 19 are strongly in the ITG-dominated regime. This is a vastly different result and were repeated various times to be ITG-dominated during both LOC and SOC confinement regimes at ρ_ϕ~ 0.5 [19]. Additionally, correlate electron cyclotron emission (CECE) measurements at the edge were used to support the linear stability results shown in Fig 19. Both fluctuation measurements

and gyrokinetic simulations demonstrate that the ohmic L-mode C-Mod plasma is firmly in the ITG-dominated regime insideρ_ϕ~ 0.8 for both co-current and counter-current plasma discharges. Density fluctuations, which are indicative of the turbulence, were measured insideρ_ϕ~ 0.8 by PCI diagnostics. The same 'nodes' identified previously and shown in Fig. 12 were observed but earlier works suggest that these originate not from the rotation reversal itself but the change in Doppler shift as the rotation direction and magnitude changed. However, this effect was not able to be quantified through experimental measurements [18].

Additionally, through linear and non-linear gyrokinetic simulations, the hypothesis suggests using higher order gyrokinetic simulations to model the residual stress term, which results from symmetry breaking that cannot be directly incorporated into simple gyrokinetics. Local GYRO simulations include three symmetry-breaking mechanisms: the diffusion from ion fluid parallel velocity shear, Coriolis pinch, and the E x B shear pinch, as well as the profile shear for global simulations. However, modeling the residual stress must be exhaustive in that all mechanisms must be accounted for, such as neoclassical mechanisms [66, 67]. Although residual stress have been incorporated into linear gyrokinetic models by using a finite poloidal tilt angle [13, 17], the exact angle has to be determined by trial and error and can leave room for large discrepancies and is not a fully tested method. As a result, this hypothesis suggests that using a more comprehensive, high-order gyrokinetic simulations could provide more accurate modeling of the momentum transport[18].

One specific theory that supports this hypothesis suggests that one source of residual stress not accounted for in current local and global gyrokinetic simulations, the neoclassical mechanisms, plays a significant role in rotation reversals [Hillesheim 2014]. This theory, first stated by Hillesheim, suggests that neoclassical corrections to the equilibrium ion distribution function modifies the turbulent momentum transport. Because these corrections strongly depend on collisionality, this theory suggests that collisionality is the core parameter in determining rotation reversals and intrinsic rotation and presents a 1-D intrinsic rotation model. The theory is based on non-linear turbulence simulations that have shown change in sign of the momentum flux when a collision frequency threshold is crossed with no effect to the linear turbulence drive. [66, 67, 68, 69]. This collision threshold that is correlated to the reversal is crossed when the normalized collisionality given by

$$\nu_\star = \frac{qR_\psi \nu_{ii}}{v_{ti}\epsilon^{1.5}} \tag{4}$$

crosses the critical threshold $\nu_c \sim 1$ where $\epsilon$is the inverse aspect ratio of the flux surface, q is the safety factor, and ν_{ii} is the ion-ion collision frequency. Once the plasma transitions from a low collisionality (banana) regime to the intermediate collisionality (plateau) regime, the neoclassical distribution function changes, which drives and changes the turbulent momentum flux. The model is given by

$$\frac{v_{ti}}{R_\psi}\frac{\Pi_{int}}{Q_i} = \frac{B}{B_\theta}\frac{\rho_i}{L_{T_i}}\tilde{\Pi}(\nu_\star) \tag{5}$$

where $Q_i$is the turbulent energy flux, $\rho_i$is the ion gyroradius, and $L_{T_i}$is the ion temperature gradient scale length, and$\tilde{\Pi}$is the order unity function dependent on the normalized collisionality and is expressed as

$$\tilde{\Pi}(\nu_\star) = \frac{\tilde{\Pi}_0(\nu_\star/\nu_c - 1)}{1 + (\nu_\star/\nu_c)(\tilde{\Pi}_0/\tilde{\Pi}_\infty)} \tag{6}$$

which clearly shows that the function changes sign when the normalized collisionality $\nu_\star$ meets the critical collisionality threshold ν_c. $\tilde{\Pi}_0$, and $\tilde{\Pi}_\infty$are constants determined through turbulence simulations. By changing the sign of this unity function, it changes the sign of Π_{int},the intrinsic momentum flux. By assuming that the intrinsic momentum flux is balanced by the turbulent diffusion, the expression relates the momentum flux to the rotational gradient written as

$$m_i n_i \chi_\phi R_\psi^2 \frac{\partial \Omega_\phi}{\partial r} = \Pi_{int} \tag{7}$$

such that the change in sign changes the sign of the gradient, possibly resulting in a change in toroidal rotation velocity. This theory demonstrated strong agreement with experimental data from MAST. Figure 20 shows the experimental and theoretical co and counter-current toroidal velocity profiles using MAST data and the 1-D theory.

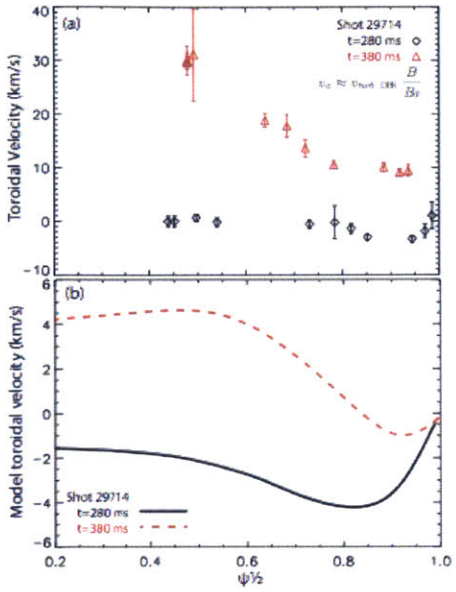

Figure 20: Comparison of (a) experimental rotational velocity data from MAST and (b) model prediction of rotational profiles using Hillesheim's 1-D model [57].

Although the magnitudes differ between the two plots, which can be modified by changing simulation-derived constants ν_c, $\tilde{\Pi}_0$, and $\tilde{\Pi}_\infty$, the shape of the profiles are similar. This theory offers one possible explanation for the effect of collisionality on rotation reversals and can be tested through comparing collisionality to C-Mod reversals. Testing this theory reveals insights into the effect of neoclassical corrections, a significant part of plasma transport, on the residual stress and ultimately the intrinsic rotation. Therefore, this 1-D model will be tested using the C-Mod dataset of intrinsic rotation/ reversal shots to verify whether the structure of the rotation profiles are accurately predicted and to quantify the discrepancy between the experimental and theoretical rotation velocities predicted from this model, as shown in Figure 20. Despite being a simplified 1-D model, this theory still captures the key physics of this idea and is a first step in investigating the role of neoclassical effects on intrinsic rotation and reversals.

1.5 Statement of the Problem and Proposed Method

The current status of research on rotation reversals leaves three fundamental questions that need to be answered. The first is identifying which of the three hypotheses (if any) are correct and to provide support of that theory with further observational evidence. Question 1 is:

1. **Is the TEM/ITG dominant turbulence regime the major factor in determin-**

ing ohmic L-mode rotation reversals and is it the primary driving mechanism for the change in sign of the residual stress? How do the measurement and analysis errors affect the linear stability analysis and resulting correlations?

With three observationally-driven explanations of rotation reversals, the need for validation is apparent. Measurement errors of the diagnostics systems of tokamaks and errors from the analysis tools used to run gyro-kinetic simulations (which will be touched upon later) [12, 14, 18, 19] or regression analysis [17] must be accounted for using sensitivity analysis to show how robust the analysis is in determining the main dependencies. This has not been done in previous studies but is essential in providing accurate and tenable results. Question 2 that must be answered is:

2. What role do neoclassical corrections play in intrinsic rotation and rotation reversals?

Previous work from Hillesheim, Barnes, and Parra suggest that neoclassical corrections modify the turbulent transport and causes the reversals rather than the linear turbulence drive and the TEM/ITG transition [56, 57, 65, 66]. If neither the linear turbulence drive and related turbulence mechanisms nor the neoclassical effects are the primary mechanisms behind rotation reversals, the final question that must be answered is:

3. Are there any new dependencies not identified in previous results, which can provide a better picture of the underlying physics of rotation reversals?

Although the study to identify dependencies has already been quite extensive, it can always benefit from a more exhaustive search and by using sensitivity analysis, the parameters and factors that are essential to rotation reversals can be identified or validated.

This thesis aims to answer all three questions through the use of an analysis workflow, a semi-autonomous process that analyzes a vast number of rotation reversal shots from Alcator C-Mod to provide further validation for one of the three hypotheses and/or identify new parameters that seem important in driving reversals. Within this process, sensitivity analyses will also be performed to quantify the impact that both measurement and analysis errors have on the results of linear stability and regression analysis used to identify the key dependencies.

1.6 Thesis Summary

This thesis is broken into 7 chapters with Chapter 1 as the introduction. Chapters 2 and 3 focus primarily on the methdology and process of preparing the data to test the hypotheses. Chapter 2 briefly covers the methodology of testing the three hypotheses. A more detailed methodology that explains the work and how to perform the analysis in great granularity is provided in Appendix A. The chapter focuses on how the workflow was built, the rationale behind it, and the specific routines and codes that were used, created, or modified. Those who hope to use, modify, replicate, or test the analysis workflow are recommended to read this

detailed methodology. Chapter 3 covers the information of the 76 ohmic L-mode shots from C-Mod that exhibit strong intrinsic rotation and reversals. The experimental parameters and the process of identifying shots is explained there. A full list of shots, time ranges, and rotatation directions can be found in Appendix C.

Chapter 4,5 and 6 focus on the testing of the three hypotheses. Chapter 4 presents the results of testing the dominant turbulence regime hypothesis and the sensitivity and error analysis. Chapter 5 presents the results of testing the local profile gradient hypothesis and how the data compares between Alcator C-Mod and ASDEX Upgrade. Chapter 6 tests the 1-D analytical neoclassical model against C-Mod experimental data. The conclusion of all of the results, discussion, and recommended future work can be found in Chapter 7.

2 Methodology

To test the three hypotheses presented in literature that is the focus of this thesis, rotational profile data from Alcator C-Mod must be identified, processed, analyzed, and stored. Multiple routines and programs must be used from analyzing a plasma discharge in order to verify that it is indeed a high-quality shot that clearly demonstrates co-current and counter-current intrinsic rotation prior to performing regression analysis and linear stability analysis. The current system, which will be explained step-by-step in the next section, is a chain of processes that requires the user to manually take each shot through all of the routines, ensuring accurate results at each step. Also, typical transport studies only include analysis of a handful of shots, at most. Consequently, a single tool that takes shots as inputs, runs through all of the routines, and generates the required outputs could be very beneficial for studying large data sets. Additionally, each shot could have significant measurement and analysis errors as well as user biases; there are many variables to control. By analyzing a large number of shots in the range of tens to over a hundred, these errors and biases could be reduced or "washed out". This provides a larger sample size in identifying possible correlations or lack thereof. Therefore, to process such a large number of shots, a single tool or workflow that does not require constant user monitoring and attention is a novel in this area of research and would be of great utility. This section aims to explain how the fundamental questions presented in the introduction will be answered and to show the utility of the workflow in comparison to the traditional process performed at C-Mod.

The primary goal of this thesis is to analyze as many rotation reversal shots as possible from Alcator C-Mod and find correlations between the reversal and various plasma parameters to identify the most important driving terms, focusing especially on the dominant turbulence regime and gradients, by using regression and sensitivity analysis. The results will be used to test the three hypotheses. This goal will be accomplished through three steps:

1) **A database of shot numbers will be used as inputs for the workflow, which will use this list to locate and read data from the C-Mod database using MDS-plus.**

2) **An analysis workflow is created, a semi-autonomous set of IDL routines with a single user interface that takes the C-Mod shots numbers as inputs, processes and performs linear stability analysis using GYRO, and outputs the type, frequencies, and growth rates of the dominant turbulent mode for each shot. To calculate gradients, the same workflow is used to fit profiles to estimate the gradients at various spatial coordinates. The workflow will also perform error and sensitivity analysis on linear stability results and fitting.**

3) **The results will then be analyzed using a simple multi-variable regression and qualitatively to find possible strong correlations for comparing against the primary dependencies suggested by the hypotheses as well as identifying new possible rotation reversal dependencies.**

The analysis workflow toolkit, an assembly of multiple analysis programs written in Inter-

active Data Language (IDL), allows for a streamlined process for performing linear stability analysis for tens to hundreds of shots without constant user input. A simplified diagram of the analysis workflow and the various routines used is shown below in Figure 21.

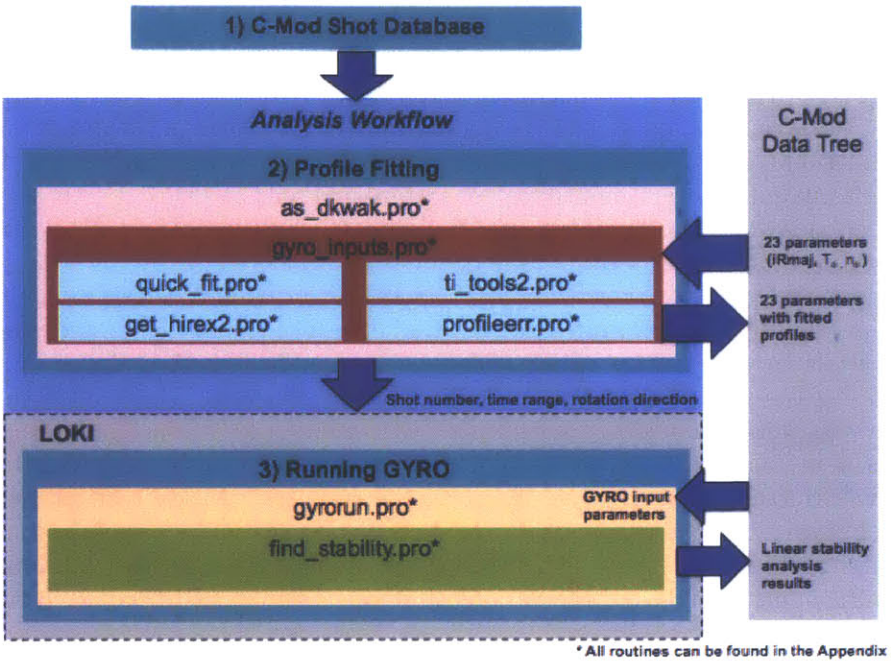

Figure 21: Diagram of the analysis workflow structure developed for this study including the IDL routines used.

To develop a database for the analysis workflow, a collection of many (76) C-Mod ohmic L-mode rotation reversal shots is collected. These shots will then need to be checked for quality of diagnostics measurements and development in time. The shots that meet these requirements will then be categorized depending on its confinement regime, current, etc. and then added to form the database that will be the input base for the analysis stream. This database is Step 1 of the workflow.

Before the analysis workflow is created, whether TRANSP, an analysis tool that performs power balancing and will be explained in a future section, needs to be used in the stream will be explained. For this study, the analysis workflow will exclude TRANSP for greater simplicity, as TRANSP requires user input and an automated method has not been throughly tested and finalized. To create the analysis workflow, the optimal fitting tools will need to be chosen (Quickfits, FIT, GPR, etc.), which has been decided upon discussions with researchers and testing various high-quality shots to determine the most accurate tool for electron density and temperature gradients. Then, this tool will be implemented into the gyro_inputs file created by Martin Greenwald, which will create the input files for GYRO, and the sensitivity analysis methods will be implemented as well. Before the stream is finalized, sample shots will be manually analyzed using all of these tools in the correct order to provide a control set for comparison. Then, the stream will be tested by analyzing the same sample shots and

comparing the results to the control set. Based on these results, the analysis workflow will be modified and corrected accordingly. The profile fitting is Step 2 of the workflow shown in Figure 21.

After the analysis workflow has been finalized, it will be used to run linear stability analysis for the entire database, which is Step 3 as shown in Figure 21. The outputs will be the real frequency and growth rate of the dominant turbulence regime, which can be used to attempt to identify a correlation between the turbulence regime and rotation reversals. This will provide evidence for the existence and magnitude of the correlation, which answers Question 1. With this database of the frequency and growth rates of the dominant turbulent mode, densities and density gradients, temperature and temperature gradients, safety factors, and other plasma parameters, multi-variable regression will be utilized to check previously identified dependencies and correlations (dominant turbulent mode and electron density gradient) and to identify new potential dependencies, which addresses Question 2.

Throughout this whole work-stream, error and sensitivity analysis will be implemented in the stream and used to demonstrate the potential effects of experimental and analysis errors on the outputs and correlations, which address Question 2. This step aims to provide more insight on the assumptions that go into identifying correlations between rotation reversals and to show the overall impact of these errors on the robustness of the results from the linear stability and regression analysis. By using this analysis stream with sensitivity analysis, this thesis can lend further support to verifying the correct key rotation reversal dependencies, possibly identify new dependencies, and provide transparency and greater accuracy in understanding the results of this study. A detailed description of how the three steps are executed from a tactical point of view and the various components analysis workflow shown in Figure 21 is provided in Appendix A.

3 C-Mod Rotation Database

A total of 76 ohmic L-mode C-Mod profiles are used to test the three hypotheses presented in the study and identify the key rotation reversal dependencies . Of the 76 profiles, 54 are classified as rotation reversal shots and the remaining 22 are classified as intrinsic rotation profiles within this study. Although all of these shots in C-Mod display intrinsic rotation because there is no external momentum input, the term 'intrinsic rotation profile' is used for profiles that either do not have a rotation reversal or ones that do but cannot be used as a rotation reversal shot for one or more reasons. One reason is when the rotation reversal is too weak and the velocity change is not large enough such that the post-reversal velocity is close to 0. Another reason is when the reversal occurs in a time range where the velocity HIREXSR measurements are not available or accurate, which happens toward the very end of the discharge. The term 'rotation reversal profile' refers to profiles that do display a strong rotation reversal. Because a rotation reversal shot contains both the co-current and counter-current regions before and after the reversal, each reversal shot can be used to generate two profiles, one co-current and one counter-current. Therefore, the 54 rotation reversal profiles are actually from only 27 unique C-Mod shots, each providing one co-current and one counter-current profile. Because intrinsic rotation shots can only provide one type of rotation profile, 22 unique C-Mod shots were used for the 22 intrinsic rotation profiles in the dataset. The list of these 49 shot numbers, time ranges, and rotation direction can be found in Appendix C.

Time traces for a typical rotation reversal shot and a typical intrinsic rotation shot are shown below in Figure 22a and 22b, respectively.

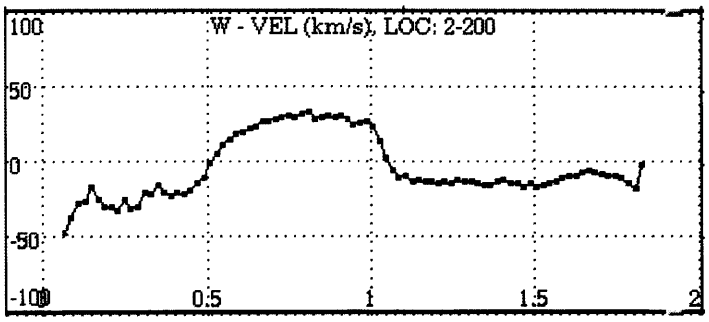

(a)

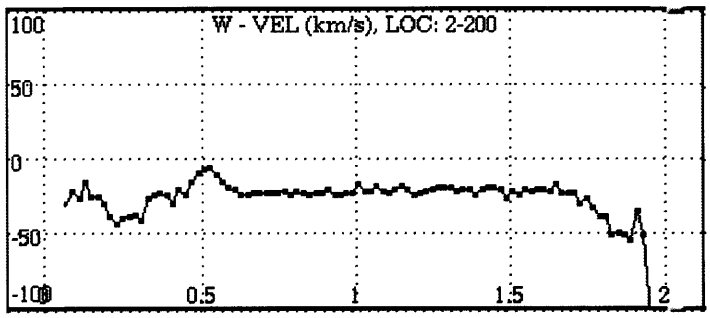

(b)

Figure 22: dwscope line-averaged toroidal rotation velocity (km/s) time traces in seconds for C-Mod (a) rotational reversal shot (1120626027), which provides two profiles, and (b) intrinsic rotation shot (1120210011), which provides only one profile, with positive velocity as co-current and negative velocity as counter-current from the HIREXSR w-channel that measures the w He-like argon emissions. Additional information on HIREXSR channels provided in Appendix A.

In Fig. 22a, a rotation reversal occurs from positive velocity to negative at approximately 1.1 s. With a velocity change of approximately 45 km/s within a span of 0.1-0.2 s, this shot is considered to display a strong rotation reversal. In determining the time ranges for the co-current and counter-current shots from this shot, a range between 0.05 and 0.2 s with a steady velocity is chosen. As an example, for shot 1120626027, the co-current time range is 0.7 - 0.9 s and the counter-current time range is 1.2 to 1.298 s. Each rotation reversal shot creates a shot-pair - one co-current and one counter-current. It can be seen in Fig. 46b that no reversal occurs and the velocity remains relatively stable at -25 km/s. Because the velocity is so stable in time, a time range can be taken anywhere within the large time range between t = 0.6s and 1.6s. For simplicity, time ranges near 1.0 s is chosen. Because each discharge lasts approximately 2 seconds, time range near 1.0 s ensures that it is near the middle of the discharge such that there is a high probability that all of the other plasma parameters, such as density, current, magnetic field, and heating are relatively stable in time and are not prone to huge fluctuations that might occur at the start and end of a discharge. As an example, the time range for this shot is 0.7 - 0.898 s.

The reason for using 0.898s rather than 0.9s is due to how data is stored into the tree using gyro_inputs. The output from each run of gyro_inputs.pro is named by the average of the time range used and the data is not deleted or overwritten to preclude the risk of accidentally overwriting previous analysis. Instead, the time range is simply shortened or lengthened by one millisecond to create a new set of outputs stored into the tree under a different name. Due to this process, many time ranges for these shots are ± 0.002 seconds from multiples of 0.1 s, as it took multiple attempts to get the most accurate profile fits using gyro_inputs.pro.

In the workflow, the rotation reversal shots and intrinsic rotation shots are separated in the analysis to identify any possible differences in parameter dependencies that may arise between the two. Because rotation reversals involve a sudden change in the rotation direction without a significant change in the global plasma parameters, this huge momentum distribution may cause or be the result of fundamentally different physics in comparison to a mono-directional intrinsic rotation discharge with no reversal. Because several intrinsic rotation shots actually display rotation reversals, the time ranges for these shots are chosen to be at least a minimum 0.3-0.4 s away from the rotation reversal to decrease the probability that the mechanisms triggering the rotation reversal are at play within the intrinsic rotation time range. In the results, both shots are plotted together but are marked differently so that both shot type-specific and overall trends and correlations can be identified if they exist.

The 76 C-Mod shots have a wide range of global plasma parameters, such as toroidal magnetic field $B_T$and current I_p. The ranges of various global plasma parameter ranges of rotation reversal and intrinsic rotation shots are listed in Table 2.

Table 2: List of global plasma parameter ranges for 54 rotation reversal shots and 22 intrinsic rotation shots in C-Mod.

Parameter (Units)	Rotation Reversal Shots	Intrinsic Rotation Shots
I_p(MA)	0.55 - 1.1	0.6 - 1.1
B_T(T)	3.0 - 5.5	5.4 - 5.6
q_{95}	3.2 - 4.8	3.4 - 6.1
T_e(keV)*	1.6 - 2.8	1.5 - 3.0
T_i(keV)*	1.1 - 1.5	1.1 - 1.5
$n_e(10^{20}m^{-3})$*	1.1 - 1.5	0.6 - 1.6
V_Φ(km/s)*	-40 - 45	-25 - 20

* line-averaged quantities

The ranges shown in Table 2 are the maximum and minimum values for the parameters within the time ranges of the various 76 shots. Discharges were operated in the lower single null (LSN), upper single null (USN), and inner wall limited magnetic field configurations with only ohmic heating in the low confinement regime. The rotation reversals are usually induced by ramping the density or plasma current up or down past a critical threshold and the magnetic field is fixed through the duration of all of the discharges used in this study [15, 32, 43].

The plasma current is usually in the counterclockwise direction from the top-down lab perspective of the tokamak and is used as the reference in determining the direction of the intrinsic rotation as co-current or counter-current. With this counterclockwise current

rotation, a positive toroidal velocity corresponds to co-current rotation and vice versa for the counter-current rotation. However, some cases exist in which the plasma current is in the clockwise direction even though the toroidal velocity direction is still referenced relative to the current regardless of the absolute direction. This results in a positive toroidal velocity actually corresponding a counter-current rotation, which can be problematic as the analysis workflow assumes positive velocities to correspond to co-current rotation. A solution to this issue is described in Appendix A.

The primary parameters used in calculating the localized profile gradients and collisionality and performing linear stability analysis are the electron density n_e, electron temperature T_e, ion temperature T_i, and toroidal rotation velocity V_Φ. The diagnostic systems used to make these profile measurements and the literature on these systems is listed below in Table 3.

Table 3: List of key parameters used for testing hypotheses, C-Mod diagnostic system used to make the profile measurements, and literature on these systems

Plasma Parameter	Diagnostic System
n_e	Thompson scattering [Hughes J.W. et al 2003 RSI 74 1667, Basse N.P. 2007 Fusion Sci. Tech. 51 476]
T_e	ECE grating polychrometer [Basse N.P. 2007 Fusion Sci.Tech. 51 476, O'Shea P.J. 1995 Proc 9th Joint] Thompson scattering [Hughes J.W. et al 2003 RSI 74 1667, Basse N.P. 2007 Fusion Sci. Tech. 51 476]
T_i	HIREXSR [Ince-Cushman 2008 RSI 79 10E302, Rice 1997 NF 37 421, Reinke 2012 RSI 83 113504]
V_Φ	HIREXSR [Ince-Cushman 2008 RSI 79 10E302, Rice 1997 NF 37 421, Reinke 2012 RSI 83 113504]

The typical integration time for the HIREXSR spectrometer system is 20 ms with a ~1 cm spatial resolution. Rather than an absolute calibration, each shot is calibrated by using locked modes as the benchmark shot, assuming $V_\Phi = 0$ in a given time range of the locked mode shot [11]

4 Testing the Dominant Turbulence Regime Hypothesis

The dominant turbulence regime hypothesis, based on experiments at C-Mod, identifies the fastest growing turbulent mode, more specifically the TEM/ITG transition, as a key parameter linked to the rotation reversal. This hypothesis was developed based on two key observations. The first was the observation of rotation reversals occurring simultaneously with the transition of the global confinement regime from linear ohmic confinement (LOC) to saturated ohmic confinement (SOC) [61]. A plot showing this observation is shown in Figure 23 and Figure 11b.

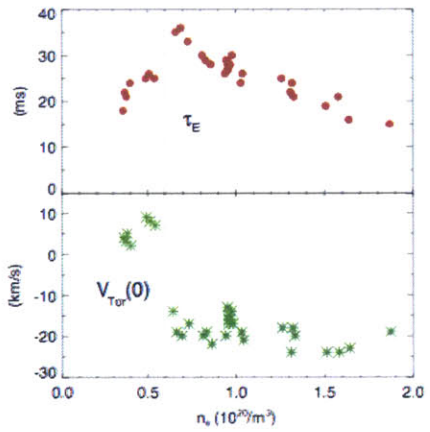

Figure 23: Energy confinement time and toroidal rotation velocity vs. electron density in Alcator C-Mod [14].

The second observation is the connection between the LOC/SOC transition and change in the core turbulence, based on measured turbulence changes at the LOS/SOC transition [14, 40, 70]. By combining these two, the hypothesis states that at low collisionality, the turbulence is dominated by trapped electron modes (TEM) and the ohmic energy confinement and density profile peaking increases with increasing collisionality. At a critical collisionality, the density profile peaking and increase in energy confinement stops, the ion temperature gradient (ITG) dominates over TEMs, as shown in Figure 24 below, and the rotation changes from the co-current to the counter current direction, as shown in Figure 23. For the rotation reversal to occur, the momentum flux must change sign, which requires that the residual stress term shown in Equation 2 change sign as well. The change in the turbulence mode propagation direction that happens with the TEM/ITG transition is a possible mechanism for changing the sign of the residual stress term and thus, causing the rotation reversal.

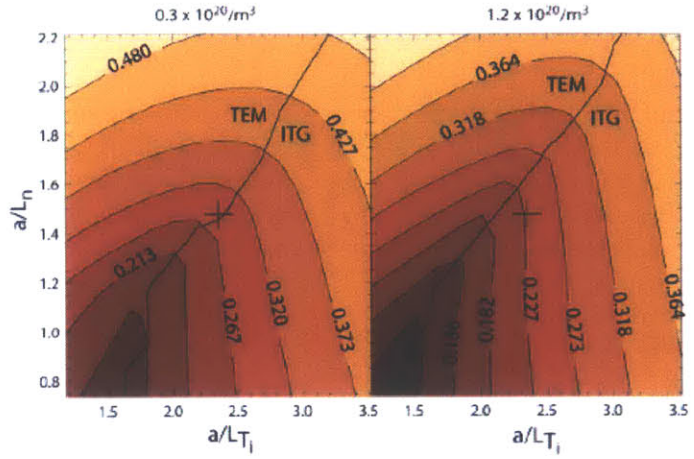

Figure 24: Contour plots of the linear growth rates of the fastest growing modes as a function of the electron density and ion temperature gradients at two densities indicative of co-current ($0.3 \times 10^{20}/m^3$) and counter-current rotation ($1.2 \times 10^{20}/m^3$) with + indicating the operational point [61].

From two contour plots shown in Figure 24 of the linear stability analysis results using GYRO, it can be seen that for the co-current shot before the reversal, the plasma remains TEM-dominated. The + sign shows the error bars, indicating that the plasma could actually be ITG-dominated. However, in the counter-current shot, the plasma is fully in the ITG-dominated regime These two plots show the transition from TEM-dominated to ITG-dominated after the rotation.

To test this hypothesis, linear stability analysis is performed on the time-averaged profiles of the 54 ohmic L-mode rotation reversal C-Mod shots to determine the fastest growing, the most unstable, turbulent mode. The output of each linear stability analysis is the real frequency ω_r and growth rates of the fastest growing turbulent mode as a function of the normalized wave number $k_\theta \rho_s$. The real frequency ω_r is used to determine whether the plasma is TEM or ITG-dominated. Because linear gyrokinetic simulations are relatively quick and computationally inexpensive, it is the ideal choice for testing this hypothesis and performing sensitivity analysis. Linear simulations provide information only on the fastest growing, or the most dominant, turbulent mode. It does not provide any information regarding sub-dominant modes, interactions between modes, and higher gyrokinetic terms. Nonetheless, for an initial testing of the link between TEM/ITG transitions and rotation reversals, linear stability analysis is fully sufficient. The outputs are compared with u', the rotation gradient and the motivation for using this variable for comparison is explained in the next section.

When each GYRO run is complete, the results are saved into individual .sav files for each of the 35 sensitivity cases for each C-Mod shot. These are then analyzed and plotted using combinedfiletest.pro. The IDL routines used for linear stability analysis, gyrorun.pro and find_stability.pro, are described in Section 2 and their locations can be found in the Appendix, and the analysis workflow used to generate these results is described in detail in Section 2.4. The input values used for GYRO are listed in Table 1,4, and 6 in Appendix A and the list of shots can be found in the Appendix C.

4.1 Use of the rotation velocity gradient (u')

The toroidal rotation velocity gradient, u', is used as the primary variable for identifying trends and testing the hypotheses. u' will be plotted vs. the key parameters suggested by the three hypotheses to identify correlations. The expression for u' is given as

$$u' = -\left(\frac{R^2}{v_{thi}}\right)\frac{d\omega}{dr} \tag{8}$$

where $v_{thi} = \sqrt{\frac{2T_i}{m_i}}$is the main ion thermal velocity and $\omega = \frac{V_\phi}{R}$is the toroidal rotation angular velocity. Thus, u' is the radial angular velocity gradient normalized to the ion thermal velocity to yield a unit-less metric that can be used across various tokamak experiments. The gradient rather than the toroidal velocity itself is used as the primary variable for three reasons - previous work suggests that u', not the velocity is directly proportional to the residual stress term, u' may be a better and earlier indicator of reversals, and u' has been used as the primary variable for rotation in previous work.

Within the momentum flux equation, it is suggested that the toroidal Reynolds stress term is the key physics quantity behind intrinsic rotation and reversals. The Reynolds stress term can be decomposed into

$$< \tilde{v}_r \tilde{v}_\phi >= -\chi_\phi \frac{\partial < v_\phi >}{\partial r} + V < v_\phi > + \Pi^R_{r,\phi}$$

as shown in Equation 2, where the right-hand terms are the diffusive, convective, and residual stress terms, respectively. The residual stress term represents the sum of turbulence mechanisms that are not diffusive or convective in nature and can be seen as a catch-all term for mechanisms that are not dependent solely on the velocity gradient and the velocity itself [45]. The residual stress term is the physical term in which free ion and electron energy is converted into toroidal velocity via turbulence, the main driver of intrinsic rotation [48]. Without external momentum, the momentum flux equation must be equal to zero, and assuming the other convective and non-linear flux terms in the momentum flux equation are negligible, which is supported by experimental studies, the Reynolds stress term must be equal to zero as well [45]. This means that the three terms shown in the equation above must equal to zero. It has been shown that the dominant pinch terms, most notably the the turbulent equipartition pinch, the thermoelectric pinch, and the Coriolis pinch, are negligible and do not create the sign change necessary for the rotation reversal [45, 49, 51]. Therefore, this implies that the intrinsic rotation behavior is determined by the balancing of the diffusive flux and the residual stress [17]. Because $\chi_\phi$is positive and does not change sign, the value and sign of the residual stress is directly proportional to the radial gradient of the toroidal rotation velocity, such that $\chi_\phi u' \sim \Pi^R_{r,\phi}$. Therefore, to understand how the

turbulence induced residual stress behaves and changes with various parameters, u' is the ideal term.

It has been shown in various experiments in C-Mod and ASDEX Upgrade that as the collisionality is increased in time, the rotation gradient u' changes signs earlier than the velocity [14, 17]. This can be seen from Figure 33b and 33c. This suggests that u' rather than the velocity may be the fundamental parameter that is changing and truly affected by the increasing collisionality. Thus, u' may be the more fundamental term for the underlying physics behind reversals and a better indicator of the phenomenon. Additionally, from Figure 34e in Chapter 5, it can be seen that the rotation velocity at $\rho_\phi = 0.1$is highly correlated with u' at $\rho_\phi = 0.35$. This allows for predicting what the rotation velocity is very close to the core where HIREXSR measurements may be very inaccurate by knowing the u' at a location farther from the core. Thus, by measuring the u' at at location where HIREXSR measurements are fairly accurate (~10% error), one can indirectly determine the rotation velocity at the core and its direction to an accurate degree and overcome the possible issue of large measurement errors.

Lastly, u' is used as the parameter for determining the rotation direction and magnitude for much of the earlier work in rotation reversals [13, 14, 17, 57]. As a consequence of the first two reasons, the strong correlations in support of the hypotheses described in this study are cast in terms of u'. Therefore, to make direct comparisons of the experimental data and its trends and to test the hypotheses in the most straightforward and simple way as possible, u' is used.

4.2 Correlations between u' and ω_r

To identify any trends between reversals and the dominant turbulence regime, u' is plotted as a function of the real frequency for three different wave numbers ($k_\theta \rho_s = 0.3$, 0.5, and 0.7) at three different spatial locations (ρ_ϕ= 0.3, 0.5, 0.7), where $\rho_\phi = \sqrt{(\psi_0 - \psi)(\psi - \psi_{sep})}$ - the normalized toroidal flux coordinates. These plots are shown in Figure 25.

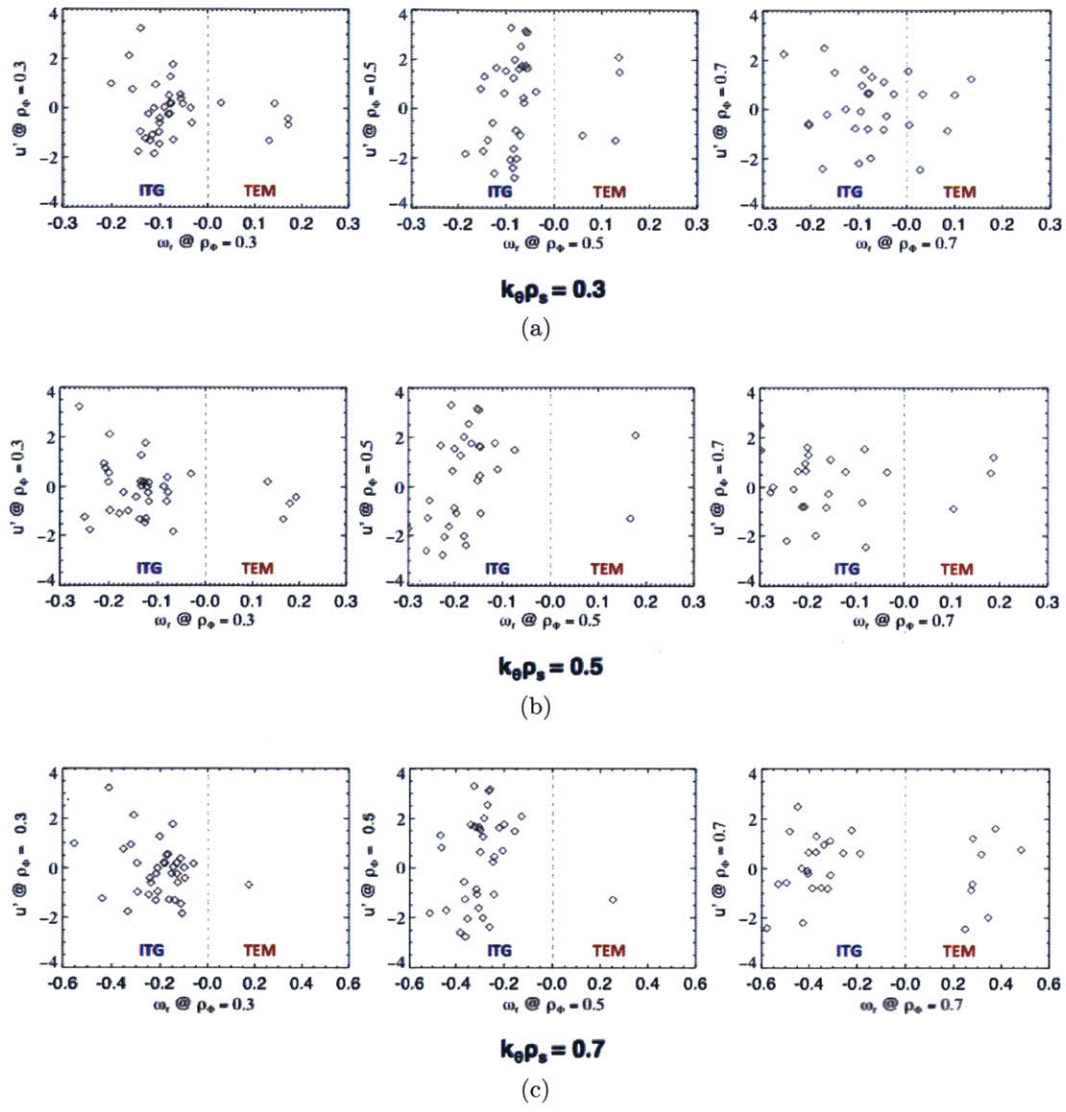

Figure 25: Plots of rotation gradient u' vs. real frequency ω_r for ohmic L-mode C-Mod shots at three spatial locations (ρ_ϕ= 0.3, 0.5, 0.7) for wavenumbers (a) $k_\theta \rho_s$ = 0.3, (b) $k_\theta \rho_s$= 0.5, and (c) $k_\theta \rho_s$ = 0.7.

These linear stability analysis results show that the plasma is mainly ITG dominated for both co-current and counter-current shots. Close to the core at ρ_ϕ= 0.3 for all three wavenumbers ($k_\theta \rho_s$ = 0.3, 0.5, and 0.7), it can be seen that for shots with positive and negative rotation gradients, corresponding to co-current and counter-current rotation, respectively, have negative real frequencies, indicative of ITG as the dominant turbulent mode. These results are inconsistent with this hypothesis, as one would expect the co-current shots with u' $>$ 0 to be TEM-dominated and the counter-current shots with u' $<$ 0 to be ITG-dominated. However, this bifurcation is not observed in these plots. Also, it can be seen

that with increasing wavenumbers, or decreasing wavelengths, the plasma becomes more ITG-dominated as the real frequency becomes more negative. For$k_\theta \rho_s = 0.3$, the $\omega_r$range is 0 to -0.2 and for $k_\theta \rho_s = 0.5$ and 0.7, the $\omega_r$range grows to 0 to -0.3 and then 0 to -0.6, respectively. This suggests that the turbulence at shorter wavelengths grows increasingly ITG-dominated.

The ITG-dominance and trend between frequency range and wave number can be seen in the other two wavenumbers, $k_\theta \rho_s = 0.5$ and 0.7, as well. Few exceptions to this pattern can be seen farther from the core at $\rho_\phi = 0.7$. For $k_\theta \rho_s = 0.3$ and 0.7 at this location, the plasma is not strongly ITG-dominated. At $\rho_\phi = 0.7$ and for $k_\theta \rho_s = 0.3$, as shown by the right-most plot in Figure 25a, the shots are evenly scattered and no dominance of either TEM or ITG can be clearly seen, although more shots at in the ITG regime. For $k_\theta \rho_s = 0.7$ as shown in the right-most plot in Figure 25c, a large number of shots are in the TEM-dominated regime. Normally, only 2-3 shots remain in this regime, so the large number is noticeable. Also, it can be seen from this plot that all of the shots are either strongly ITG-dominated or TEM-dominated, with no shots close to the TEM/ITG boundary. Although these shots are unique cases and unexpected, no plot in Figure 25 comparing u' vs. ω_r shows the strong bifurcation that separates co-current and counter-current shots that the hypothesis suggests. These linear gyrokinetic results are inconsistent with the hypothesis, which states that the dominant turbulent mode and the TEM/ITG transition plays an important role in the rotation reversal.

These C-Mod results can be compared with other linear stability results from earlier C-Mod studies and ASDEX Upgrade. Linear stability analysis results from two C-Mod shots, one with in the linear ohmic confinement (LOC) regime and the other in the saturated ohmic confinement (SOC) regime, are shown below in Figure 26.

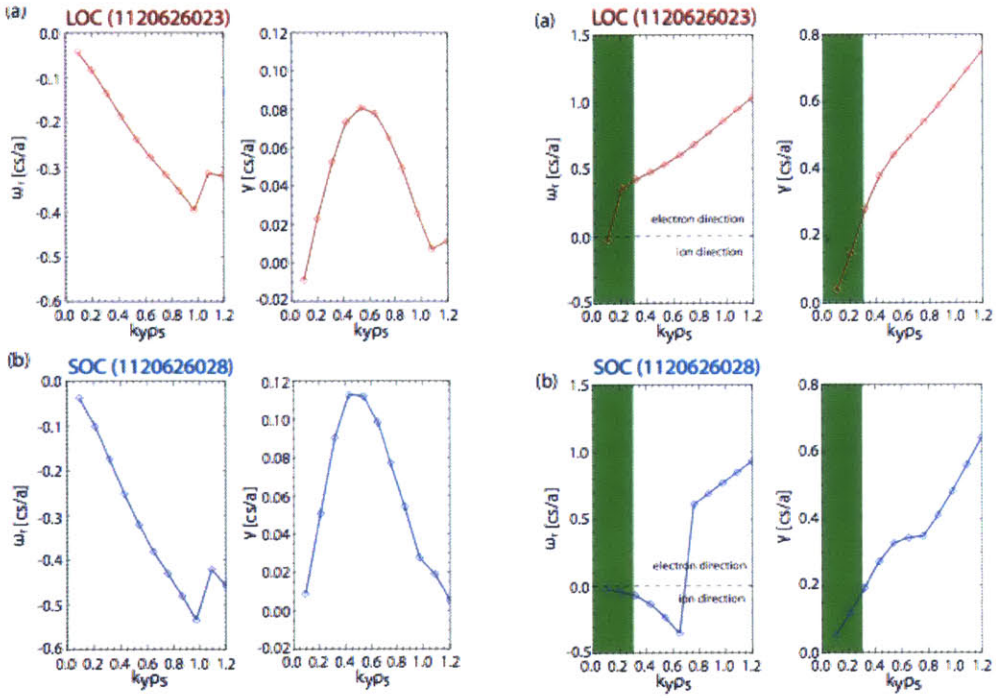

(a) (b)

Figure 26: Linear stability analysis results from GYRO simulation for a LOC (1120626023) and SOC (1120626028) plasma at (a) $\rho_\phi{}^{\sim}$ 0.5 and (b) $\rho_\phi{}^{\sim}$ 0.8 [19].

Similar to the results plotted in Figure 25, the negative frequency corresponds to the ion drift direction, which is due to the ITG mode and the positive frequency corresponds to the electron drift direction, which is driven by TEM. From Figure 26a, it can be seen that at $\rho_\phi{}^{\sim}$ 0.5, plasmas in the LOC and SOC regime are both strongly ITG-dominated. This is consistent with the intrinsic rotation/reversal results. However, at $\rho_\phi{}^{\sim}$ 0.8, the plasma becomes bifurcated, with the LOC plasma being TEM-dominated and the SOC plasma ITG-dominated at low wavenumbers and transitioning to TEM-dominated after $k_y\rho_s{}^{\sim}$ 0.6. These earlier results are consistent with what was observed in this study. Farther from core, the plasma is no longer strongly ITG-dominated for both co-current and counter-current shots, and that is evident in previous C-Mod results, as shown in Figure 26b.

In ASDEX Upgrade, linear stability analysis on an intrinsic rotation database showed a strongly TEM-dominated plasma for both co-current and counter-current shots. This is indirectly seen in the plots of $\frac{R}{L_{ne}}$vs. ω_r shown below in Figure 27.

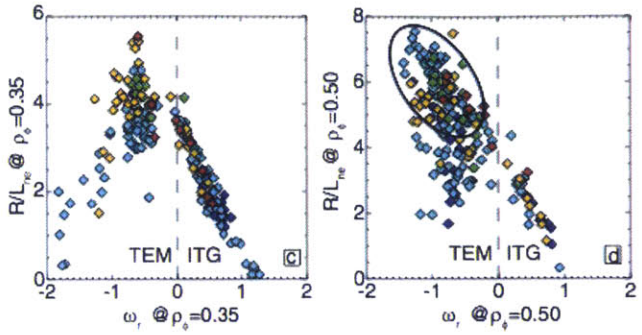

(a) (b)

Figure 27: Plots of the normalized electron density gradient $\frac{R}{L_{n_e}}$ vs. real frequency of the turbulence fluctuations ω_r for intrinsic rotation shots in ASDEX Upgrade at (a) ρ_ϕ= 0.35 and (b) ρ_ϕ= 0.5 [17].

In ASDEX Upgrade, electron density gradient has shown a strong correlation to the rotation gradient u' , as shown in Figure 34b. As the electron density gradient $\frac{R}{L_{ne}}$ increases, the u' decreases, signifying a more counter-current rotation. Therefore, using that correlation, it can be seen in earlier ASDEX Upgrade experiments, shown inFigure 27b at ρ_ϕ= 0.5, the plasma remains TEM-dominated for a large range of $\frac{R}{L_{ne}}$ that correspond to both co-current and counter-current shots. This is inconsistent with the findings of this study and previous C-Mod linear stability analysis results, which showed that the plasma was ITG-dominated. Closer to the core at ρ_ϕ= 0.35, the plasma with lower $\frac{R}{L_{ne}}$ were ITG-dominated and higher $\frac{R}{L_{ne}}$ were TEM-dominated. This shows that co-current plasmas in ASDEX Upgrade were ITG-dominated and counter-current were TEM-dominated, which is inconsistent with C-Mod observations. Rather than a TEM to ITG transition as the rotation switches from co-current to counter-current, the opposite is observed in ASDEX Upgrade, in which the co-current to counter-current transition signified by the increasing $\frac{R}{L_{ne}}$ corresponds to a ITG to TEM transition. The exact reason or mechanism for the discrepancy between C-Mod and ASDEX Upgrade linear gyrokinetic simulations is not known. Nonetheless, the ASDEX Upgrade results, previous C-Mod linear stability results, and this study's findings show that both co-current and counter-current plasmas remain dominated by a single mode rather than undergoing a TEM/ITG transition. Some results even suggest that the plasma actually undergoes a ITG to TEM transition near the core [17].

Because the real frequency that determines the dominant turbulent mode varies with the wavenumber, showing u' vs. ω_r at three wavenumbers may not the best way to demonstrate the linear stability results and testing this hypothesis. The wavenumbers $k_\theta \rho_s$ = 0.3, 0.5 and 0.7 were chosen due to the fact that previous work used these wavenumbers for comparing ω_r with various other parameters [13, 17]. As most longwave linear gyrokinetic simulations only solve the equations for wavenumbers ranging from 0 to 1.2 at most, 0.3, 0.5, 0.7 present a representative sample locations that are equidistant from each other. However, the goal of linear gyrokinetic simulations is to identify the the dominant turbulent mode, or the fastest growing mode, and sampling three wave numbers ($k_\theta \rho_s$ = 0.3, 0.5 and 0.7) could result in actually missing the mode of with the highest growth rate. For example, if the wavenumber with the highest growth rate was $k_\theta \rho_s$ = 0.75, which had a strong TEM-dominance, but

remained ITG-dominated for $k_\theta \rho_s$ between 0 and 0.7, then the dominant turbulence mode was not accurately shown by these plots. Earlier works show the full spectrum of ω_r vs. $k_\theta \rho_s$ plots for each results to preclude this risk [14, 19]. However, as this study has performed linear gyrokinetic simulations for a large number of shots, displaying each result is not a possibility. Therefore, a better test for identifying the dominant turbulent mode of these plasmas would be to display the real frequency ω_r that corresponds to the wavenumber $k_\theta \rho_s$ with the highest growth rate in a specific interval. To utilize this method, the u' was plotted against the ω_r corresponding to the wavenumber $k_\theta \rho_s$ with the highest growth rate γ between the range $k_\theta \rho_s$ of 0.25 and 0.80. These new plots at three different spatial locations (ρ_ϕ = 0.3, 0.5, and 0.7) is shown below in Figure 28.

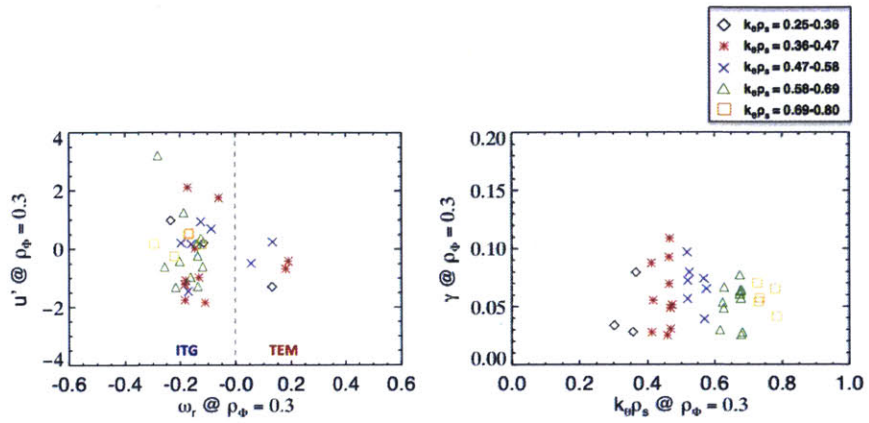

(a)

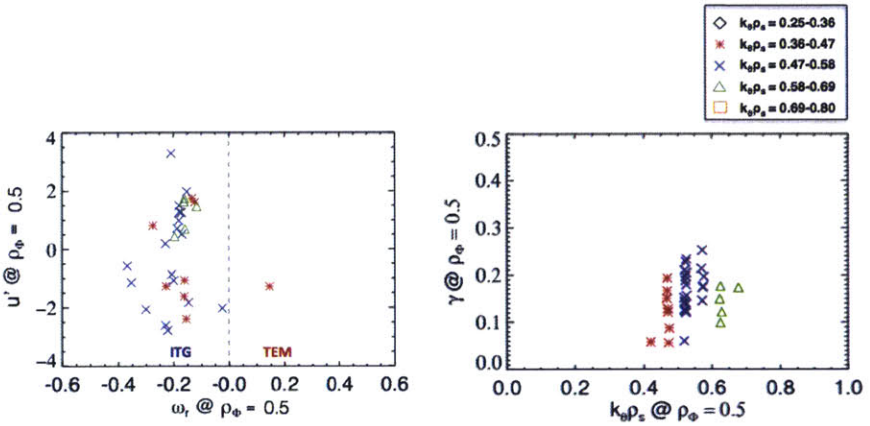

(b)

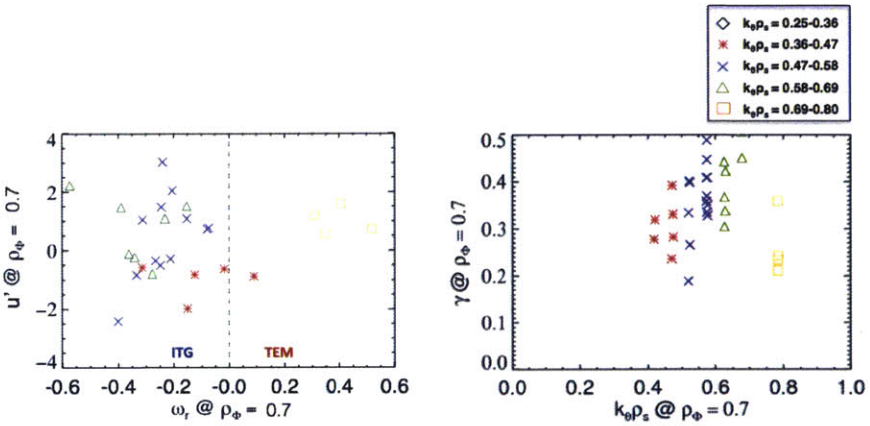

(c)

Figure 28: Plots of rotation gradient u' vs. real frequency ω_r of the fastest growing turbulent fluctuations and of growth rate γ vs. $k_\theta\rho_s$ from linear stability analysis of ohmic L-mode C-Mod shots at three spatial locations (a) ρ_ϕ= 0.3, (b) ρ_ϕ= 0.5, and (c) ρ_ϕ= 0.3. Symbols indicate the value of the $k_\theta\rho_s$ corresponding to the highest growth rate .

Each linear stability base case run generates the real frequency ω_r and growth rate γ of the fluctuations as a function of the wavenumber $k_\theta \rho_s$. For each shot, the $k_\theta \rho_s$ between 0.25 and 0.80 that corresponds to the highest growth rate was selected and the real frequency ω_r of the fluctuation with this wavenumber was chosen as the representative real frequency to determine the dominant turbulent mode for each shot. The right plots for Figure 28 show how the shots are separated into five buckets depending on the $k_\theta \rho_s$ of the fastest growing fluctuations. Each of the five buckets covered a $k_\theta \rho_s$ range of 0.11 between $k_\theta \rho_s$= 0.25 and 0.80 and are represented by symbols with different colors and shapes.

Close to the core at ρ_ϕ= 0.3, it can be seen for Figure 28a that the fastest growing modes are still ITG for both co-current and counter-current plasmas. Figure 54a looks very similar to the plots at ρ_ϕ= 0.3 in Figure 51, that used selected $k_\theta \rho_s$ rather than the one with the highest growth rate. This shows that the plasmas that showed strong ITG-dominance at $k_\theta \rho_s$ = 0.3, 0.5, and 0.7 were truly ITG-dominated. From the right plot in Figure 28a, which shows in which$k_\theta \rho_s$ range the fastest growing fluctuations fell into, it can be seen that it was a pretty uniform distribution between $k_\theta \rho_s$ = 0.25 and 0.75, with the most shots falling into the interval with $k_\theta \rho_s$ between 0.4 and 0.5.

Similar trends can be observed in the plots at ρ_ϕ= 0.3 and 0.5 in the figure. At both locations, the plasma remains ITG-dominated for a wide range of u'. These results are in agreement with those shown in Figure 25, suggesting that the TEM/ITG transition and the dominant turbulence regime is not a primary dependency of the rotation reversal. As seen in Figure 51, the range of the real frequency of the data set increases with increasing distance from the core. One unique observation is the TEM-dominance of shots with the highest growth rates at high $k_\theta \rho_s$. This is shown by the orange squares, which correspond to the highest growth rates in $k_\theta \rho_s$ between 0.65 and 0.75, in the TEM regime, as shown in Figure 28c. This peculiarity of only these shots being strongly TEM-dominated can be partly explained from single C-Mod shot analysis shown in Figure 26b. At $\rho_\phi \sim$ 0.8, the growth rates of the linear stability results increase monotonically rather than peaking at a $k_\theta \rho_s \sim$ 0.5 as shown in Figure 26a. For these four shots, the $k_\theta \rho_s$ of the fastest growing mode is simply the maximum of the $k_\theta \rho_s$ range, which is approximately 0.80, and this is seen in Figure 28c. Therefore, it could be possible that these shots have the similar growth rate profile as the one shown in Figure 26b. It can also be seen from Figure 26b that at these higher wave numbers, the plasma is TEM-dominated, even for counter-current rotating plasmas. If only these shots out of the C-Mod dataset are similar to the one shown in Figure 26b, it could explain why only they are strongly TEM-dominated compared to the rest of the shots. Although this is an observational and phenomenological answer, the specific underlying physics or reasons behind these results is unknown.

4.3 Correlations between R/L_{ne} vs. ω_r

In previous ASDEX Upgrade results shown in Figure 27, it can be seen that near the core, there is a bifurcation in the dominant turbulence regime with the increasing electron density gradient. At ρ_ϕ= 0.35 for $\frac{R}{L_{n_e}}$ below 3.5, the plasma is ITG-dominated. For shots with $\frac{R}{L_{n_e}}$ above, the plasma is TEM-dominated, and overlap between the two modes exist between

$\frac{R}{L_{n_e}}$ of 3.0 and 3.5. However, at ρ_ϕ= 0.5, the bifurcation is not as easily noticeable. Most shots in a wide range of $\frac{R}{L_{n_e}}$ are TEM-dominated rather than ITG-dominated although in C-Mod, most shots remained ITG-dominated. In these plots, $\frac{R}{L_{n_e}}$ is used as a parameter with strong correlations to u' and therefore as a proxy variable for u', but a more direct comparison can be beneficial. Therefore, the normalized electron density gradient $\frac{R}{L_{n_e}}$ was plotted as a function of the real frequency of the turbulence from linear stability analysis at three spatial locations (ρ_ϕ = 0.3, 0.5, and 0.7) for three wave numbers ($k_\theta \rho_s$ = 0.3, 0.5, and 0.7) and is shown below in Figure 29.

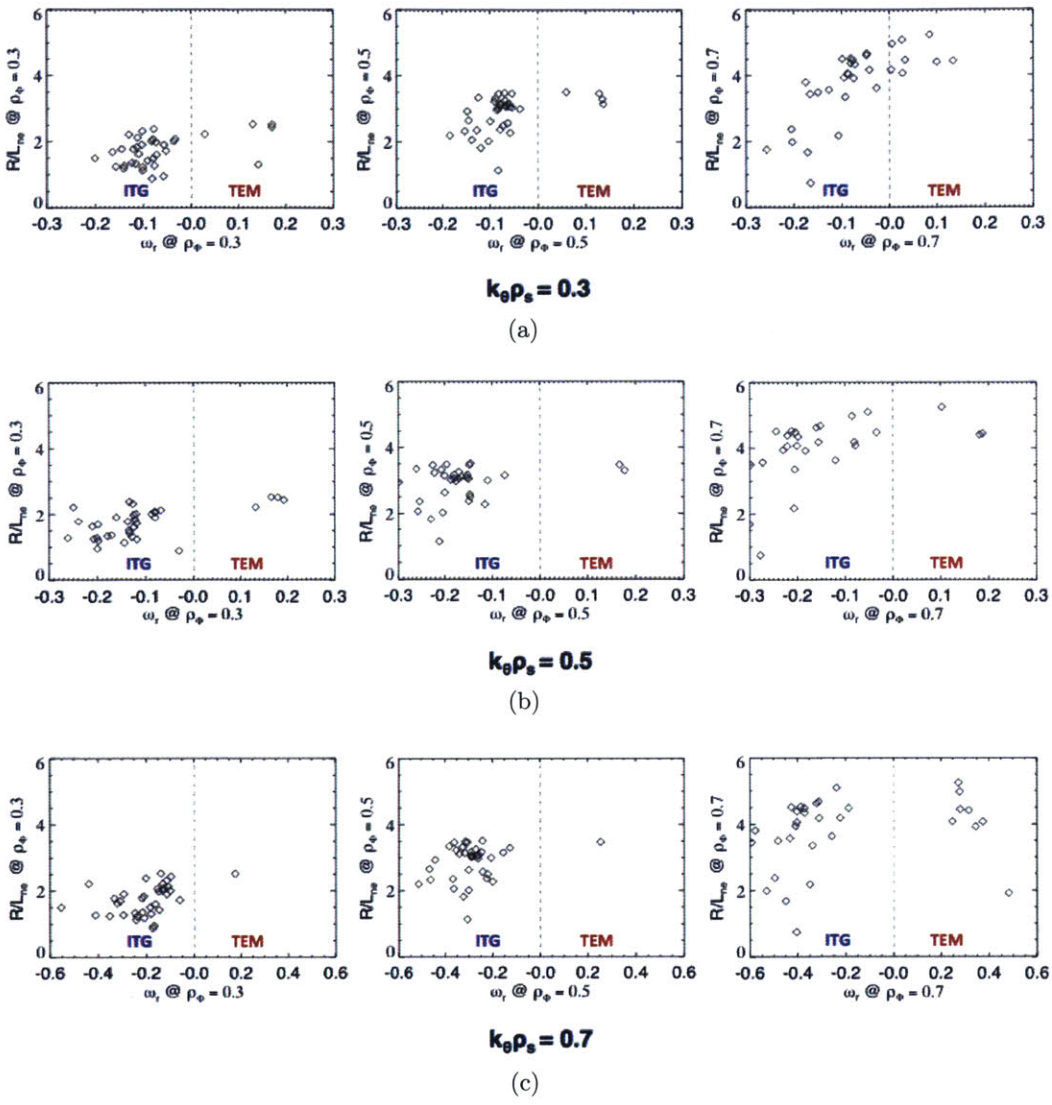

Figure 29: Plots of normalized electron density gradient $\frac{R}{L_{n_e}}$ vs. real frequency ω_r for ohmic L-mode C-Mod shots at three spatial locations (ρ_ϕ= 0.3, 0.5, 0.7) for wavenumbers (a) $k_\theta \rho_s$ = 0.3, (b) $k_\theta \rho_s$= 0.5, and (c) $k_\theta \rho_s$ = 0.7.

From Figure 29, it can be seen that the results at the various wavenumbers exhibit similar trends. Most of the shots remain ITG-dominated at all locations, which is consistent with results shown in Figure 52 and 54. It can also be seen that the range of $\frac{R}{L_{ne}}$ close to the core is limited, rarely exceeding 2. However, farther from the core, at ρ_ϕ= 0.5 and 0.7, the range of $\frac{R}{L_{ne}}$ increases significantly, ranging from 0 to 6 atρ_ϕ= 0.7. Also, it can be seen that there is no threshold $\frac{R}{L_{ne}}$ value at which the plasma becomes strongly TEM-dominated. Although a few shots exhibit this behavior, more data points are needed.

The limited range of $\frac{R}{L_{n_e}}$ near the core at ρ_ϕ= 0.3 and 0.5 precludes a complete comparison to the experiments at ASDEX Upgrade from being made. In ASDEX Upgrade experiments, as shown in Figure 27, at ρ_ϕ= 0.35, the plasma becomes TEM-dominated for shots with $\frac{R}{L_{n_e}}$ greater than 3. However, at ρ_ϕ= 0.3 in C-Mod, $\frac{R}{L_{n_e}}$ does not reach this threshold value and actually is consistent with the observations from ASDEX Upgrade. The same can be said for C-Mod results at ρ_ϕ= 0.5, which also has a limited $\frac{R}{L_{n_e}}$ range. In Figure 27b, the plasma is strongly TEM-dominated for $\frac{R}{L_{n_e}} > 2.0$ in ASDEX-Upgrade, but in C-Mod, this is not seen. One reason is the limited range of $\frac{R}{L_{n_e}}$, which prevents a complete comparison to be made to the bifurcation between $\frac{R}{L_{n_e}}$ and the dominant turbulence regime observed in ASDEX Upgrade. A larger number of shots and shots with higher density gradients are necessary to span a large enough $\frac{R}{L_{n_e}}$ to test the existence of a turbulent mode bifurcation as seen in Figure 27.

4.4 Sensitivity and Error Analysis

In linear gyrokinetic simulations, profile gradients play a significant role in determining the magnitude and type of the turbulent mode fluctuatios. However, exactly how much of an effect these density and temperature gradients can have on the linear stability results used in this study for intrinsic rotation shots are not well-known. By performing a sensitivity analysis in which one of the ion temperature, electron temperature, and electron density gradients is modified, the parameter with the largest effect can be identified and how much that effect is can be quantified. Therefore, in the analysis workflow, a sensitivity analysis was performed by gyrorun.pro for 1 base case and 6 sensitivity cases, as listed in Table 4.

Table 4: Descriptions of the sensitivity cases on gyro_run.pro for linear stability analysis using GYRO

Case Number	Description
1	No changes to normalized gradients (Base case)
2	Increase $\frac{a}{L_{T_i}}$ by 1-sigma error
3	Decrease $\frac{a}{L_{T_i}}$ by 1-sigma error
4	Increase $\frac{a}{L_{T_e}}$ by 1-sigma error
5	Decrease $\frac{a}{L_{T_e}}$ by 1-sigma error
6	Increase $\frac{a}{L_{n_e}}$ by 1-sigma error
7	Decrease $\frac{a}{L_{n_e}}$ by 1-sigma error

Rather than a fixed percentage increase/decrease, the errors due to fitting and experiment for the gradients were used. This was done for two purposes - to perform a more realistic sensitivity analysis and to perform a quick error analysis.

A sensitivity analysis by increasing the inputs by a fixed percentage is a simple method to observe how these changes affect the output. However, one may not accurately know how much the input would actually vary, especially for experiments with diagnostics systems that have very different measurement errors. If one input would rarely be expected to vary more

than 1-2% while the second can vary by 50-60%, performing a sensitivity analysis with a fixed 10% increase/decrease for both input parameters would be artificial, unrealistic, and provide little information about how the output would truly vary when the model is used for real cases. Using the 1-sigma errors of the gradients calculated from the workflow, as described in the Appendix, allows for a more realistic sensitivity analysis as each parameter is increased/decreased by a more accurate and experimentally significant amount. This is important in C-Mod, where the ion temperature, electron temperature, and electron density are measured using different systems that have varying measurement and systematic errors. Also, instead of using coarse estimates of how much each parameter would be expected to vary, by using the actual errors that incorporate fitting and measurement errors for the sensitivity cases, the results can also be used as a quick estimate of the errors of the linear stability results.

The sensitivity analysis was performed using 6 sensitivity cases for the C-Mod dataset, as listed in Table 4 above. Cases 2-3 correspond an increase/ decrease in the ion temperature gradient $\frac{a}{L_{T_i}}$by its 1-sigma error, referred to as the $\frac{a}{L_{T_i}}$ case, cases 4-5 correspond to an increase/decrease in the electron temperature gradient $\frac{a}{L_{T_e}}$, referred to as the $\frac{a}{L_{T_e}}$ case, and cases 6-7 correspond to an increase/decrease in the electron density gradient $\frac{a}{L_{n_e}}$, referred to as the $\frac{a}{L_{n_e}}$ case . All of the gradients are normalized to the minor radius a as it is the input used by GYRO. The process and methodology is described in detail in the Appendix. After the analysis was completed, an IDL routine sensetest.pro was written to compile all of the results and combinedfiletest.pro was used to generate the plots. The locations of these routines can also be found in the Appendix. Plots of the senstivitiy analysis results for two shots (1120222026 and 1120724015) are shown below in Figure 30 and 31.

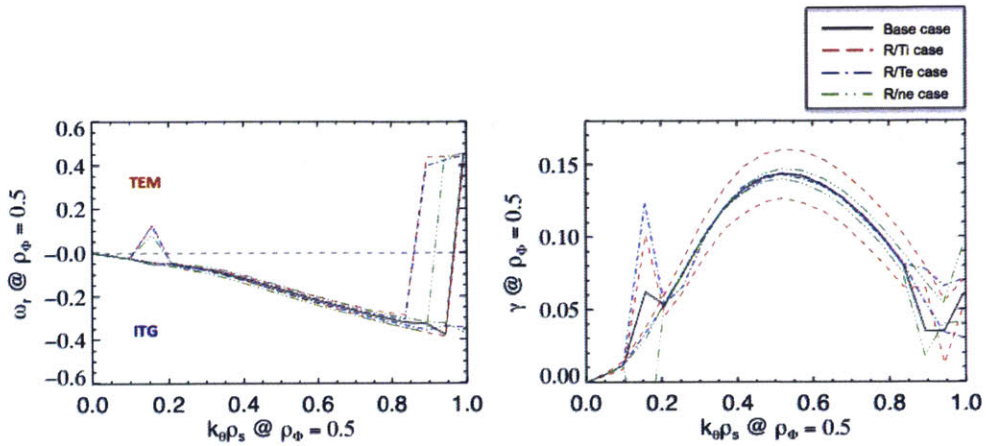

(a)

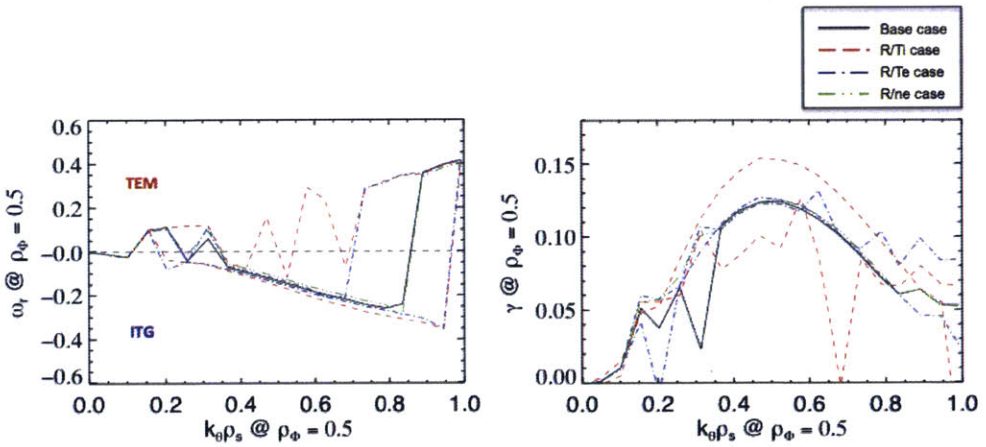

(b)

Figure 30: Plots real frequency ω_r and growth rate γ vs. $k_\theta\rho_s$ of the most unstable turbulent mode for a ohmic L-mode C-Mod shot 1120222026 at ρ_ϕ=0.5 in the (a) co-current direction and (b) counter-current direction with sensitivity cases increasing and decreasing the local T_i, T_e, and n_e profile gradients by its 1-sigma error (16%, 9%, 15%) as shown in Table 4.

The plots show the 6 sensitivity cases overlayed on the base case linear stability results. Each type of sensitivity case, depending on the parameter that is modified, is shown in the plots with a different color and line style.

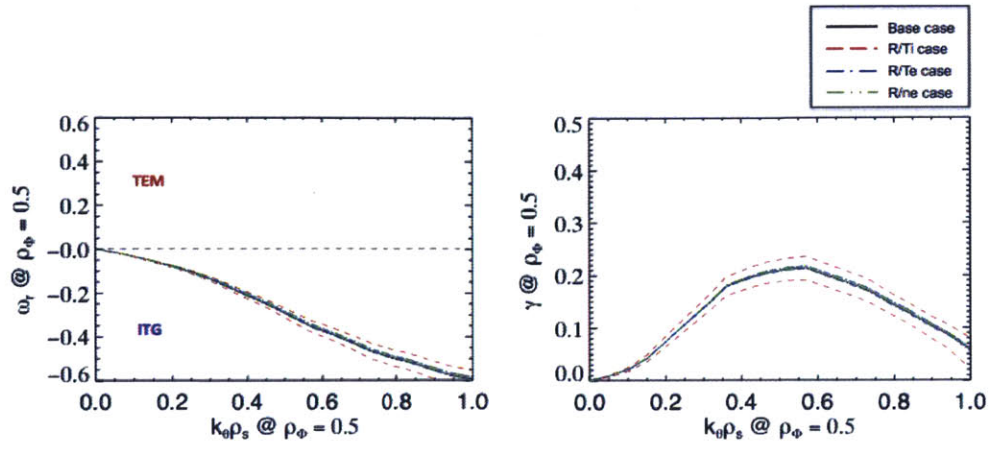

(a)

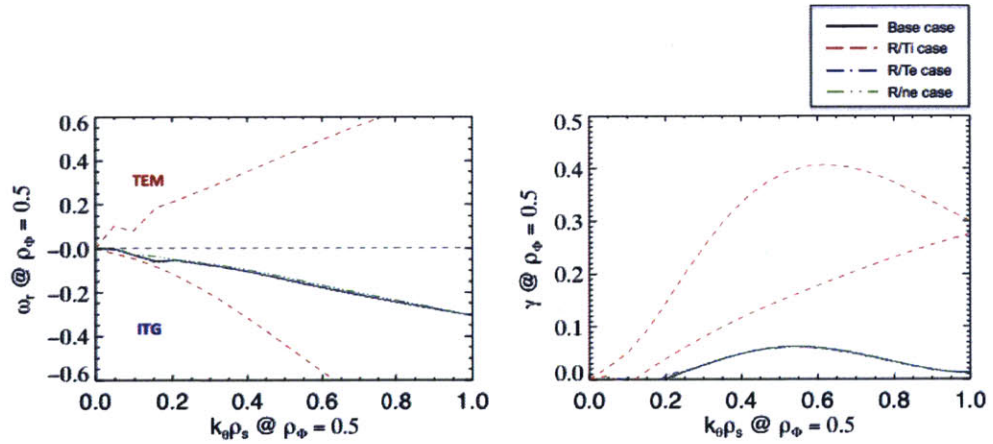

(b)

Figure 31: Plots real frequency ω_r and growth rate γ vs. $k_\theta \rho_s$ of the most unstable turbulent mode for ohmic L-mode C-Mod shot 1120724015 at ρ_ϕ=0.5 in the (a) co-current direction and (b) counter-current direction with sensitivity cases increasing and decreasing the local T_i, T_e, and n_e profile gradients by its 1-sigma error as shown in Table 4.

112022026 and 1120724015 were chosen as their sensitivity analysis exhibited the common traits seen for all of the other C-Mod shots. It can be seen that both shots remain strongly ITG-dominated for both the co-current and counter-current direction, as expected from the previous results. However, it can be seen from Figure 30b and 31b that for some of the sensitivity cases, the plasma is actually TEM-dominated. This can be seen primarily by red dashed line, indicating an increase in the ion temperature gradient $\frac{R}{L_{T_i}}$by the 1-sigma error calculated previously for each shot. In Figure 30b, the shot is predicted to be weakly TEM-dominated for two sensitivity cases as it oscillates near $\omega_r = 0$. In Figure 30a, the sensitivity cases do show noticeable effects but the plasma remains strongly ITG-dominated, suggesting

that even accounting for the expected errors, the shot is ITG-dominated. This is also seen in Figure 31a, in which the plasma is fully ITG-dominated within the entire wavenumber range shown in the plot. From these plots, which are indicative of the sensitivity analysis of the other shots, it can be seen that the increase/decrease to the gradients do have noticeable effects. One extreme example can be seen in Figure 31b, in which the $\frac{R}{L_{T_i}}$ case shows the plasma being very strongly TEM-dominated or very strongly ITG-dominated. Rather than due to the physics, this is most likely to a very large 1-sigma error due to poor profile fitting that resulted in such large ω_r values. This is evident in the growth rate plot in Figure 31b, which shows the $\frac{R}{L_{T_i}}$ case (red dash) having much larger growth rates than those calculated by the other cases.

From Figure 30 and 31, it can be seen that the $\frac{R}{L_{T_i}}$ changes seem to have the greatest effect on the real frequency ω_r and growth rates γ of the linear stability results. However, because these cases were run for 54 profiles, it is not feasible to show the ω_r vs. $k_\theta \rho_s$ and γ vs. $k_\theta \rho_s$ plots for each shot to identify any trends or behaviors. Therefore, the average % change of ω_r from each sensitivity case for each of the 54 shots is plotted for three wavenumbers ($k_\theta \rho_s$= 0.3, 0.5, and 0.7) and three spatial locations (ρ_ϕ= 0.3, 0.5, and 0.7) The nine plots are shown below in Figure 32.

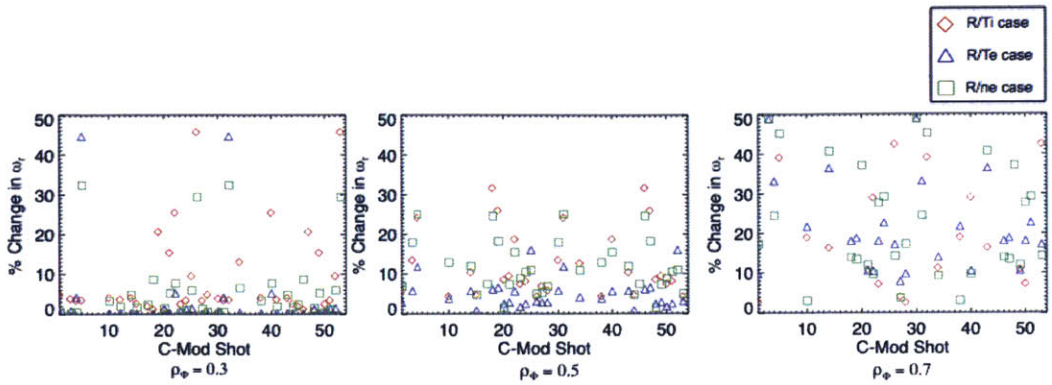

(a)

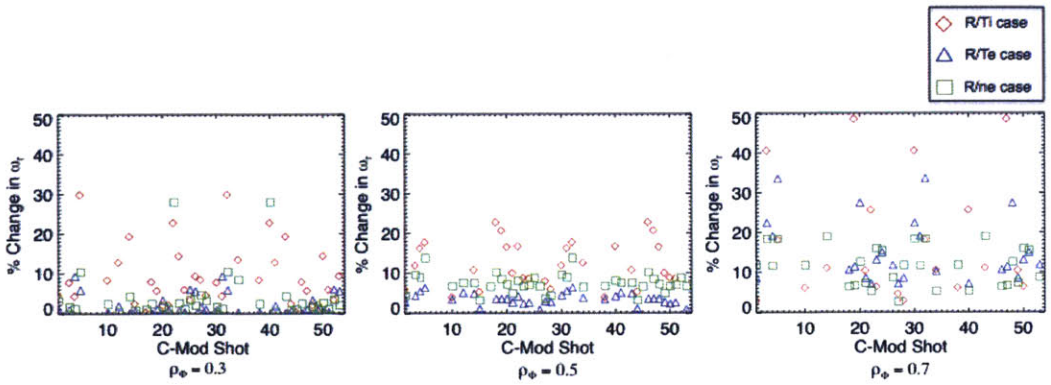

(b)

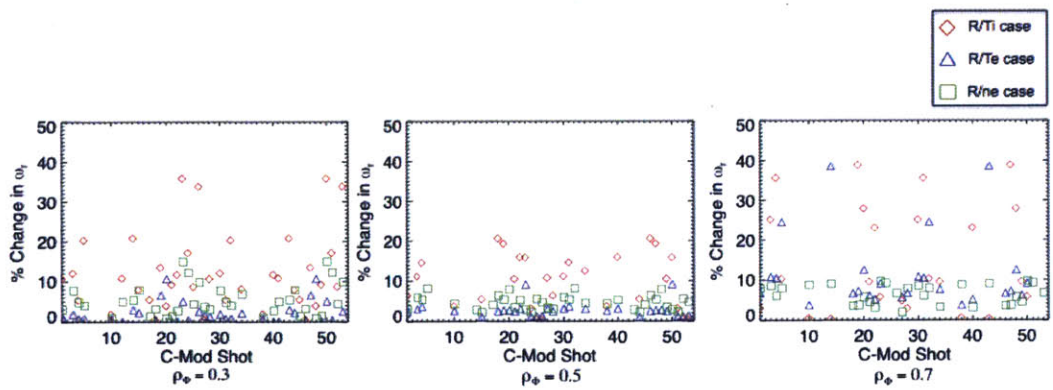

(c)

Figure 32: Sensitivity scan plots of real frequencyω_r vs. wavenumber $k_\theta \rho_s$ for ohmic L-mode C-Mod shots at three spatial locations (ρ_ϕ= 0.3, 0.5, 0.7) for wavenumbers (a) $k_\theta \rho_s = 0.3$, (b) $k_\theta \rho_s$= 0.5, and (c) $k_\theta \rho_s$ = 0.7. Scans performed by increasing and decreasing the local T_i, T_e, and n_e profile gradients by its 1-sigma error as shown in Table 4.

To calculate the average % change, the ω_r from the two sensitivity cases for each parameter was subtracted from that of the base case, divided by the base case ω_r to calculate a percentage, and then averaged. This was done for three wavenumbers at three spatial locations. In order to prevent outliers, such as the one seen in Figure 31b, from distorting the plots, all % changes that exceeded 50% were removed as they represented less than 10% of the 54 shots. From Figure 32, it can be seen that for the three $k_\theta \rho_s$ values and at ρ_ϕ= 0.3 and 0.5, the $\frac{R}{L_{T_i}}$ cases (red triangle) yield the largest change in the real frequency ω_r with an average 14% change and 11% change, respectively. At ρ_ϕ= 0.7, the % change vary widely due to large fitting errors and is therefore ignored, as it does not show an accurate picture of the sensitivity of the linear stability simulations. The cases with the second largest effect are the ones changing the electron density gradient $\frac{R}{L_{n_e}}$ (green square). At ρ_ϕ= 0.3 and 0.5, the average % change from the base case among all 54 reversal profiles are 6% and 4%, respectively. The $\frac{R}{L_{T_e}}$ cases (blue triangle) produced the least change overall, averaging less than a 2% change on average at ρ_ϕ= 0.3 and 2.5% change on average at ρ_ϕ= 0.5. These results are expected as it has been known that the dominant turublence regime is highly dependent on the ion temperature gradient $\frac{R}{L_{T_i}}$ and the electron density gradient $\frac{R}{L_{n_e}}$ [17, 62].

Because the sensitivity analysis was performed using the 1-sigma errors of these local profile gradients as the sensitivity factor, the results must be studied in the context of the 1-sigma errors that were used. Table 5 below lists the 1-sigma error at the three spatial locations (ρ_ϕ= 0.3, 0.5, and 0.7) for the density and temperature profile gradients.

Table 5: List of local density and temperature profile gradient errors used for the sensitivity analysis.

Parameter	ρ_ϕ= 0.3	ρ_ϕ= 0.5	ρ_ϕ= 0.7
$\frac{R}{L_{T_i}}$	15.7%	14.2%	21.7%
$\frac{R}{L_{T_e}}$	12.6%	11.2%	16.7%
$\frac{R}{L_{n_e}}$	8.3%	7.5%	13.3%

It can be seen that the ion temperature gradient $\frac{R}{L_{T_i}}$ has the largest errors, which is expected as HIREXSR has the largest measurement errors of diagnostics systems used to measure temperature and density. This can be used to partly explain why the $\frac{R}{L_{T_i}}$ cases have generated the large % changes in the sensitivity cases. However, it can also be seen that the results from the $\frac{R}{L_{T_i}}$ cases have yielded % changes over a factor of 2 or 3 greater than the $\frac{R}{L_{n_e}}$ cases even though $\frac{R}{L_{T_i}}$ has less than twice the errors. This suggests that the large effects modifying $\frac{R}{L_{T_i}}$ has on the linear stability analysis cannot be fully attributed to its larger error. Additionally, $\frac{R}{L_{T_e}}$ has a much larger error than $\frac{R}{L_{n_e}}$ yet modifying it by 11-12% for each sensitivity case has yielded changes less than 3% on average. Therefore, accounting for the varying 1-sigma errors used for the sensitivity cases, it can still be seen that the $\frac{R}{L_{T_i}}$ has the most significant effect on the ω_r of the linear stability analysis followed by $\frac{R}{L_{n_e}}$ with $\frac{R}{L_{T_e}}$ having the least effect, which was expected.

It has been shown that $\frac{R}{L_{T_i}}$ cases have yielded on average a 11-14% change, $\frac{R}{L_{T_e}}$cases have yielded a 4-6% change, and the $\frac{R}{L_{n_e}}$cases have had less than 3% change on the real frequency ω_r of the fastest growing modes. Because these results were calculated by using the error from fitting and measurements, they can also be used as a proxy for the error of the linear stability analysis. As a quick estimate for the error, the largest changes from the sensitivity analysis, which is 14%, can be assumed to be the errors for the ω_r for Figures 25, 28, and 29. Even with a 15-20% error assumed from the sensitivity cases, it can be seen from Figure 25 and 28 that both co-current and counter-current discharges remain strongly ITG-dominated rather than near the TEM/ITG threshold as shown in Figure 24.

4.5 Summary

The dominant turbulence regime hypothesis posits that the TEM/ITG transition and the rotation reversal, which have been observed to occur simultaneously in C-Mod, are linked and that the dominant turbulence mode is a key dependency of intrinsic rotation. This hypothesis is based on observations of the rotation reversal and transition of the global confinement regime from the linear ohmic confinement (LOC) regime to the saturated ohmic confinement (SOC) regime. Earlier studies have shown the LOC/SOC transition to be linked to the dominant turbulence regime and the TEM/ITG transition, thus suggesting that the rotation reversal and the transition of the dominant mode to be linked. Therefore, to test this hypothesis, linear stability analyis using GYRO was performed on 54 rotation reversal ohmic L-mode C-Mod profiles to determine the fastest growing, or the dominant, turublent mode to observe whether this mode transitions along with the change in the rotation direction.

To see how the rotation changes with the real frequency of the most unstable mode, the rotation gradient u', a proxy for the intrinsic rotation velocity, is plotted against the real frequency ω_r from the linear stability analysis results for three wavenumbers ($k_\theta \rho_s$= 0.3, 0.5, and 0.7) at three spatial locations (ρ_ϕ= 0.3, 0.5, and 0.7). At all locations and for all wavenumbers, both co-current and counter-current shots with u' ranging from -2 to 2 remained ITG-dominated. No bifurcation between TEM and ITG can be seen for the different directions. These plots are shown in Figure 51. It could be seen that farther from the core at ρ_ϕ= 0.7, several points were strongly TEM-dominated, although it showed no correlation to the rotation direction. This suggests that they were the result of large errors at the edge for various parameters used in the linear stability analysis rather than a key physics observation.

One significant fault with only plotting u' vs. ω_r for three values of $k_\theta \rho_s$is that these three areas could have very low growth rates, such that the plots would not truly capture the fastest growing mode. Therefore, to resolve this potential issue, the $k_\theta \rho_s$ that corresponds to the fluctuations with the largest growth rate γ, rather than the values 0.3, 0.5, and 0.7, were used for the u' vs ω_r plots, as shown in Figure 25 and 28. By doing so, the true fastest growing mode fluctuations would be used. Even from this method, it could be seen that both co-current and counter-current plasmas remained strongly ITG-dominated at all three spatial locations (ρ_ϕ= 0.3, 0.5, and 0.7), which supports the initial results. These findings also agree with earlier C-Mod linear stability results, which showed both co-current and counter-current and LOC and SOC shots to be strongly ITG-dominated within $\rho_\phi \tilde{}$ 0.8. Therefore, the comparisons suggest that the TEM/ITG transition is not a key parameter in

the rotation reversal and the rotation direction.

Conversely, it has been observed from gyrokinetic simulations in ASDEX Upgrade that both co-current and counter-current shots remain strongly TEM-dominated rather than ITG-dominated. Additionally, these results were plotted in terms of $\frac{R}{L_{ne}}$ vs. ω_r rather than u', as shown in Figure 27. Therefore, to make a direct comparison, the same $\frac{R}{L_{ne}}$ vs. ω_r plots were generated using C-Mod data, as shown in Figure 29. It can be seen that for all ranges of $\frac{R}{L_{ne}}$, the plasma remains ITG-dominated, rather than TEM-dominated. However, the $\frac{R}{L_{ne}}$ range in the C-Mod data is very limited such that a transition to the TEM-dominated regime would be not observed if it exists. Therefore, within this limited range of $\frac{R}{L_{ne}}$, the shots are strongly ITG-dominated, but shots with larger $\frac{R}{L_{ne}}$ need to be incorporated to ensure that the plasma is not TEM-dominated at higher values of $\frac{R}{L_{ne}}$ near 4-6. Although the disparity between C-Mod and ASDEX Upgrade linear stability results cannot be explained, both results show one dominant turbulent mode for both co-current and counter-current shots, which is inconsistent with this hypothesis. However, it has been observed experimental that rotation reversals and LOC/SOC transition occur simultaenously, which is consistent with the first observation used to develop this hypothesis. Therefore, further work is needed to uncover the discrepancy between linear gyrokinetic results and experimental observations.

Lastly, a sensitivity anaysis was performed using the ion temperature gradient, electron temperature gradient, and the electron density gradient as the parameters to be modified. 6 sensitivity cases and 1 base case were run, as listed in Table 4. This analysis was designed to see how varying the various gradients by their 1-sigma errors would affect the ω_r of the fastest growing mode. The results indicate that the $\frac{R}{L_{T_i}}$cases have the largest effect on the ω_r, averaging 11-14%. Although this is partly due to $\frac{R}{L_{T_i}}$ having the largest 1-sigma errors, the difference in the % change from the $\frac{R}{L_{T_i}}$ cases and the next largest case, $\frac{R}{L_{ne}}$, is too large for this to be the sole cause. Therefore, this suggests that $\frac{R}{L_{T_i}}$ has the most significant effect on the ω_r of the dominant turbulent mode, followed by $\frac{R}{L_{ne}}$, and the $\frac{R}{L_{Te}}$. This is expected as the ion temperature and electron density gradients are linked to the ITG modes and TEMs. This sensitivity analysis is also used as an ad-hoc error analysis for the linear stability results, showing the ω_r to have errors of 15-20%. Even accounting for these errors, it can be seen that the plasma is still strongly ITG-dominated according to linear gyrokinetic simulations for both co-current and counter-current shots, as the ω_r is much less than 0 for most of the shots, as shown by Figure 25. These results support the initial findings and show that even accounting for experimental and fitting errors, the results remain inconsistent with the hypothesis and show that the TEM/ITG transition is not directly linked to rotation reversals, as the plasma remains strongly ITG-dominated regardless of the intrinsic rotation direction, except near the edge.

5 Testing the Local Profile Gradient Hypothesis

From experiments at ASDEX Upgrade, density and temperature local profile gradients were observed to be strongly correlated with the rotation reversal, most notably the electron density gradient [13, 17], rather than the dominant turbulence regime and the TEM/ITG transition. These correlations are shown in Figure 33 and Figure 34 below and the expression from a multi-variable regression of ASDEX Upgrade profiles is given in Equation 4 and listed below.

$$u' = -(0.12 \pm 0.02)\frac{R}{L_{n_e}} - (0.09 \pm 0.04)ln(\nu_{eff}) - (0.06 \pm 0.03)\frac{R}{L_{T_i}} - (0.028 \pm 0.014)\frac{R}{L_{T_e}}$$

Using the 76 intrinsic rotation/reversal profiles from C-Mod, the correlations between these profile gradients and the rotation gradient will be calculated to test these observations. The list of shot numbers, times, and rotation direction of the C-Mod shots used for this analysis can be found in the Appendix C.

In addition to the density and temperature profile gradients, collisionality was identified to be a key parameter linked to reversals and intrinsic rotation from ASDEX Upgrade. It was observed that the effective collisionality ν_{eff} is highly correlated to reversals, suggesting that it is a more fundamental physics parameter than the electron density, as shown in Figure 16. Using the C-Mod database, the correlation between the rotation gradient and the effective collisionality is tested as well. To calculate the statistical significance of each of these four parameters, multi-variable linear regression was also performed to compare to the results from ASDEX Upgrade shown in the equation above.

To calculate the local density and temperature profile gradients, the rotation gradient, and the effective collisionality for each shot at various radial locations, an IDL routine lsgradienttest.pro was written to perform these tasks and store the output into .sav files stored in the gradienttest directory. To perform the multi-variable linear regression analysis and plotting, another IDL routine, combinedfiletest.pro, was written. These IDL routines and the location of the gradienttest directory can be found in the Appendix.

5.1 Correlations between u' vs. local profile gradients

It can be seen from Figure 33 and Figure 34b that the electron density gradient is strongly correlated to the rotation gradient u' in ohmic L-mode plasmas in ASDEX Upgrade. At $\rho_\phi = 0.35$ in Figure 34b, as the normalized density gradient $\frac{R}{L_{n_e}}$increases and the density profile becomes more peaked, the rotation gradient goes from positive to negative, signifying the switch of the rotation direction from co-current to counter-current. As the rotation gradient and Mach number transition from co-current to counter-current and then back from counter-current to co-current, a phenomenon referred as a double reversal, the electron density gradient changes simultaneously with the reversals, as shown in Figure 33e.

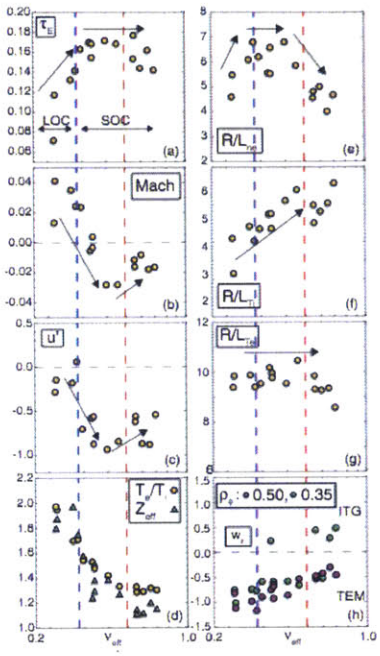

Figure 33: Plot of (a) energy confinement, (b) Mach number, (c) normalized toroidal velocity gradient, (d) temperature ratio and ion effective charge, (e) normalized electron density gradient, (f) normalized ion temperature gradient, (g) normalized electron temperature gradient, (h) dominant turbulent mode vs. effective collisionality of ASDEX Upgrade time slices of one ohmic L-mode plasma discharge at various collisionalities [17].

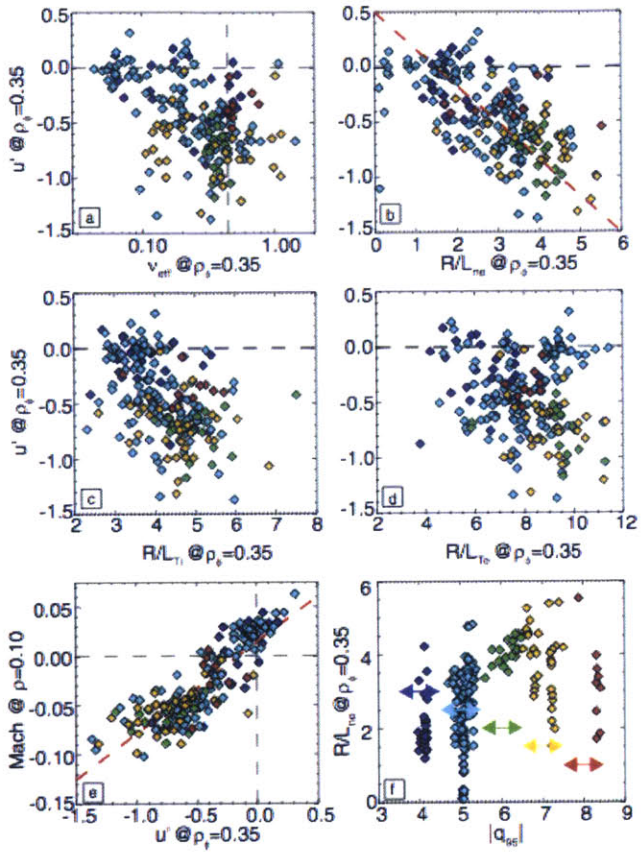

Figure 34: Plots of ASDEX Upgrade ohmic L-mode profiles at $\rho_\phi = 0.35$ of (a) u' vs. ν_{eff}, (b) u' vs. $\frac{R}{L_{n_e}}$, (c) u' vs. $\frac{R}{L_{T_i}}$, (d) u' vs. $\frac{R}{L_{Te}}$, (e) Mach number vs. u', and (f) $\frac{R}{L_{n_e}}$vs. q_{95}. Colors of shots are used to refer to specific q_{95} as shown in (f) [17].

In Figure 34c and 34d, it can be seen that the ion temperature gradient $\frac{R}{L_{Ti}}$ has a weak correlated with the rotation gradient but no strong correlation can be identified between the electron temperature gradient $\frac{R}{L_{Te}}$ and the rotation gradient. This is supported by the single shot plots in Figure 33f and 33g, as these gradients do not change significantly with the two rotation reversals. To test these correlations, the normalized density gradient for electron density, electron temperature, and ion temperature were calculated for all of the C-Mod ohmic L-mode intrinsic rotation and rotation reversal shots at three spatial locations ($\rho_\phi = 0.35$, 0.5, 0.7) and then plotted to the rotation gradient u'. The plots of u' vs. the normalized electron density gradient $\frac{R}{L_{n_e}}$ is shown below in Figure 35.

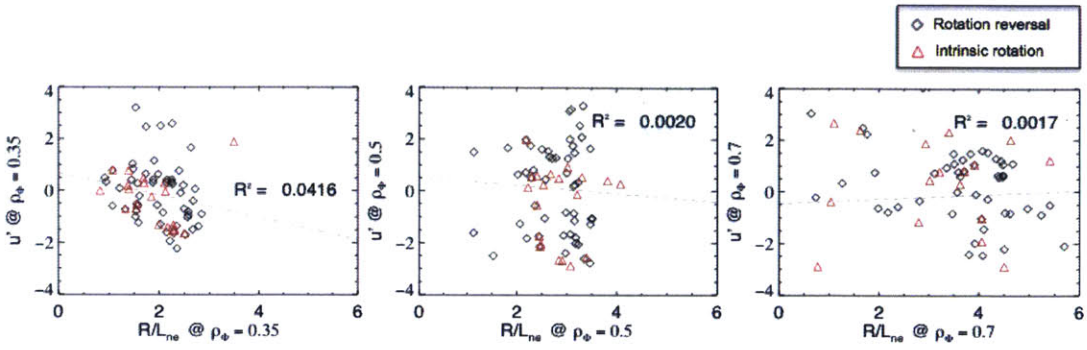

(a) (b) (c)

Figure 35: Trends between rotation gradient u' and the normalized electron density gradient $\frac{R}{L_{n_e}}$ using the C-Mod ohmic L-mode intrinsic rotation/ rotation reversal database at (a) $\rho_\phi = 0.35$, (b) $\rho_\phi = 0.5$, and (c) $\rho_\phi = 0.7$ with linear fits (dashed) and R^2values.

A linear regression of the form y = Ax + B was performed on each plot and the fits are shown in dashed lines with the coefficient determination, R^2, calculated for each fit to determine how well the data matches the linear fit. The slope A and constant B from the linear regression of all of the trends for the density and temperature profile gradients tested are listed in Table 6. It can be seen from Figure 34 that at $\rho_\phi = 0.35$, there is a weak correlation between the rotation gradient u' and electron density gradient $\frac{R}{L_{n_e}}$ between 0 and 4 . As the electron density gradient increases and the profile becomes more peaked, the rotation gradient goes from positive to negative, signifying a rotation reversal from the co-current rotation direction to the counter-current. This is evident by the linear fit and the negative slop of A = -0.427. However, the R^2value is extremely low, at 4.2%, indicating that the data do not strongly match the linear fit. Qualitatively, it can be seen from the figure that within the limited range in $\frac{R}{L_{ne}}$ of 0.5-3.5, the data are scattered and a strong correlation cannot be found. This is even more noticeable in Figure 35b and 35c, at farther distances from the core. At $\rho_\phi = 0.5$, the linear fit has a negative slope, albeit weaker than that of the plot at $\rho_\phi = 0.35$. However for the data at these locations, with an R^2value of 0.2% and 0.17% and the high degree of scatter, it can be seen that no strong correlation between u' and $\frac{R}{L_{n_e}}$ can be identified at either of these locations. These findings from ohmic L-mode C-Mod profiles are inconsistent with those from ASDEX Upgrade, which identified a strong correlation between u' and the density gradient, as shown in Figure 34b. However, as indicated by the low R^2values, serious doubt is cast upon whether these linear fits have any statistical significance.

Although it can be said that no strong correlation exists between rotation and electron density gradients in this C-Mod database, the range of the electron density gradient is fairly limited in comparison to the ASDEX Upgrade database. In C-Mod, data only exist with a $\frac{R}{L_{n_e}}$ range between 0.5 and 3.5. From Figure 34b, it can be seen that the ASDEX Upgrade database of rotation profiles has a $\frac{R}{L_{n_e}}$ range between 0 and 5.5, almost twice as large. With this limited gradient range in C-Mod shots, it may be difficult to find a strong correlation that may become more apparent at much steeper electron density gradients. If

C-Mod rotation gradients tended to decrease at density gradient $\frac{R}{L_{ne}}$ values of 4 to 6, the linear fit would show a stronger correlation. Therefore, the limit of the range of electron density gradients prevents a complete comparison of the correlation between u' and $\frac{R}{L_{ne}}$ as seen from the ASDEX Upgrade database. Nonetheless, Figure 35 shows that within the $\frac{R}{L_{ne}}$ range provided, only a weak correlation between the rotation gradient u' and electron density gradient $\frac{R}{L_{ne}}$ can be found in C-Mod as indicated by the low R^2value of 4.2%. This suggests that for the C-Mod data set, the electron density gradient $\frac{R}{L_{ne}}$ is not a strong dependency of the rotation reversal, which is inconsistent from findings at ASDEX Upgrade.

As mentioned previously, the rotation reversal (black diamond) and intrinsic rotation (red triangle) shots were separated just in case certain trends were specific only to reversal shots or intrinsic rotation shots. However, it can be seen that both types of shots behave similarly, with no pattern or behavior that is idiosyncratic to either reversal or intrinsic rotation only shots. Another notable observation from these plots is the spread of the gradient range at various spatial locations. Closer to the core at $\rho_\phi = 0.35$, the electron density gradient remains tightly within the range of 0.5 to 3.5. Closer to the edge at $\rho_\phi = 0.7$, the gradient ranges widely between 0 and 6.

From Figure 34b, it can be seen that the rotation gradient u' ranges from -1.5 to 0.5 for the ASDEX Upgrade database. For the C-Mod data set, shown in Figure 35, the u' ranges is twice as large, ranging primarily from -2.0 to 2.0 and even exceeding -3.0 and 3.0 for a few shots. The exact reason for these large differences cannot be identified but the disparity suggests that the rotation profile in C-Mod might be more peaked or hollow than those at ASDEX Upgrade. Another possible explanation is that the ion thermal velocity v_{thi} for C-Mod is less than that of ASDEX Upgrade, resulting in greater u' values. Despite these differences in the absolute values of u', the rotation reversal can still be easily identified with the sign change of the rotation gradient.

Table 6: Slope A and constant B of linear fit (y = Ax+B) of the trend between rotation gradient u' and the normalized electron density gradient $\frac{R}{L_{ne}}$, normalized electron temperature gradient $\frac{R}{L_{Te}}$, and normalized ion temperature gradient $\frac{R}{L_{Ti}}$using the C-Mod ohmic L-mode intrinsic rotation/ rotation reversal database.

Parameters (y vs. x)	$\rho_\phi = 0.35$	$\rho_\phi = 0.5$	$\rho_\phi = 0.7$
u' vs. $\frac{R}{L_{ne}}$	A = -0.427	A = -0.159	A = 0.085
	B = 0.694	B = 0.548	B = -0.450
u' vs. $\frac{R}{L_{Te}}$	A = -0.245	A = -0.183	A = -0.148
	B = 0.979	B = 1.545	B = 2.093
u' vs. $\frac{R}{L_{Ti}}$	A = -0.038	A = -0.371	A = -0.110
	B = -0.017	B = 2.657	B = 1.034

In addition to $\frac{R}{L_{ne}}$, it can be seen from Figure 35c and 35d and the coefficients of the multi-variable regression expression that the ion and electron temperature gradients play non-negligible roles in determining the strength and direction of the intrinsic rotation in ASDEX Upgrade. The normalized electron temperature gradient $\frac{R}{L_{Te}}$ and the normalized ion temperature gradient $\frac{R}{L_{Ti}}$are plotted against u' at the same 3 spatial locations ($\rho_\phi =$

0.35, 0.5, 0.7) and are shown in Figure 36 and 37, respectively. The coefficient A and constant B of their linear regression expressions from the plots are listed above in Table 6.

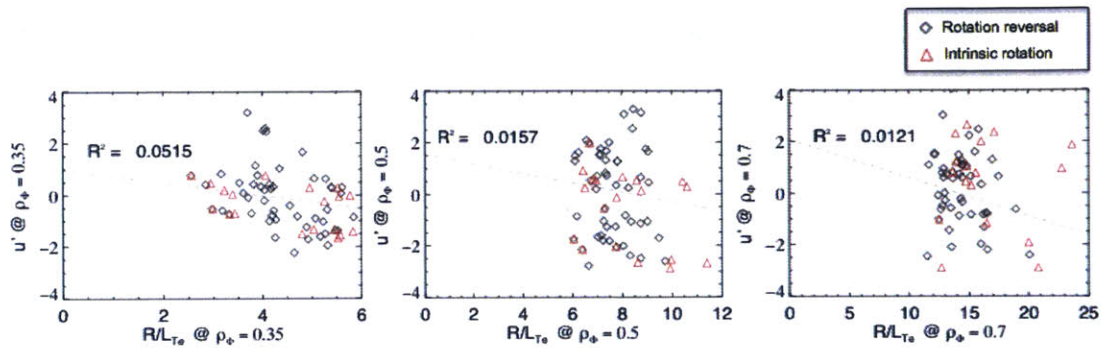

(a) (b) (c)

Figure 36: Trends between rotation gradient u' and the normalized electron temperature gradient $\frac{R}{L_{T_e}}$ using the C-Mod ohmic L-mode intrinsic rotation/ rotation reversal database at (a) $\rho_\phi = 0.35$, (b) $\rho_\phi = 0.5$, and (c) $\rho_\phi = 0.7$ with linear fits (dashed) and R^2values.

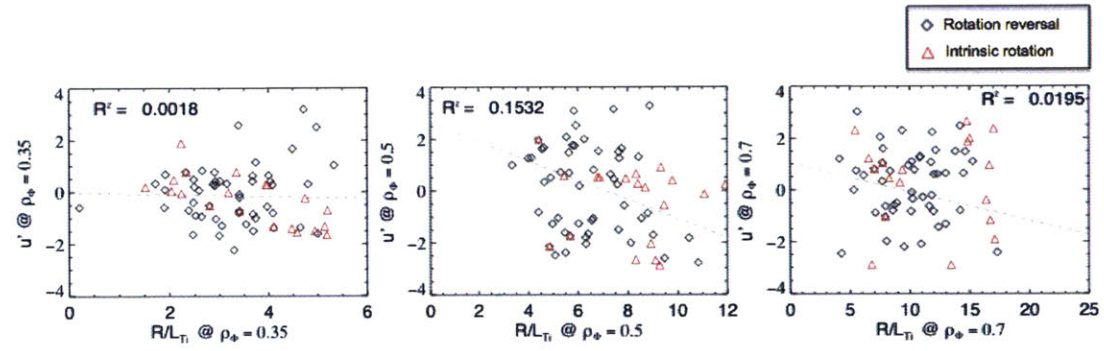

(a) (b) (c)

Figure 37: Trends between rotation gradient u' and the normalized ion temperature gradient $\frac{R}{L_{T_i}}$ using the C-Mod ohmic L-mode intrinsic rotation/ rotation reversal database at (a) $\rho_\phi = 0.35$, (b) $\rho_\phi = 0.5$, and (c) $\rho_\phi = 0.7$ with linear fits (dashed) and R^2values.

At $\rho_\phi = 0.35$, it can be seen from Figure 36a that $\frac{R}{L_{T_e}}$ shows a correlation with u', which decreases as the electron temperature gradient becomes more peaked as indicated by the slope A = -0.245. The R^2 value for this linear fit is 5.2%, which is similar to the 4.2% for the linear fit between u' and $\frac{R}{L_{n_e}}$. This suggests that the electron temperature gradient has a similar correlation with the rotation gradient as the electron density, but both correlations are relatively weak, as indicated by their low R^2 values. Farther from the core, the R^2 value

drops significantly for these correlations near 1%, indicating an even weaker match with the linear fit.

For $\frac{R}{L_{T_i}}$, no strong correlation is found for u' at $\rho_\phi = 0.35$ and $\rho_\phi = 0.7$. However, at $\rho_\phi = 0.5$ in Figure 37b, it can be seen that between the wide range in $\frac{R}{L_{T_i}}$ of 3 to 12, the rotation gradient decreases as the ion temperature gradient increases. The match of this data over the large gradient range to the linear fit is quantified by the R^2 of 15.3%, much higher than that of other profile gradients at the three spatial locations. This may suggest that a correlation may exist between the ion temperature gradient and u'. However, more shots at lower and greater ion temperature gradients need to be analyzed to verify this finding.

From Figure 36 and 37, it can also be observed that both electron and ion temperature gradient ranges for this database of shots increase with radius. At $\rho_\phi = 0.35$, both temperature gradients range from 2 to 6 but farther from the core, the gradients from 4 to 12 and then 5 to 25. Two possible explanations for these observations the three profile gradient plots is that the gradients can vary more widely near the edge for intrinsic rotation/reversal shots, and the other is that the edge is more prone to measurement errors, effectively creating a wider scatter for the gradients in the x-axis. Also, similar to Figure 35, little difference can be observed between the rotation reversal and intrinsic rotation shots when plotting the u' vs. the local profile gradients, except for u' vs. $\frac{R}{L_{T_i}}$at $\rho_\phi = 0.35$, where a strong decrease in the rotation gradient can be observed with increasing $\frac{R}{L_{T_i}}$. This trend can also be seen in the ASDEX database analysis shown in Figure 34c.

Error analysis was performed on these parameters using the methodology and error propagation expression mentioned in Appendix A.6 and Appendix E and assuming a HIREXSR measurement error of 30% for the toroidal rotation velocity and 20% for the ion temperature. Figure 38 below shows the plots from Figure 35, 36, and 37 with error bars.

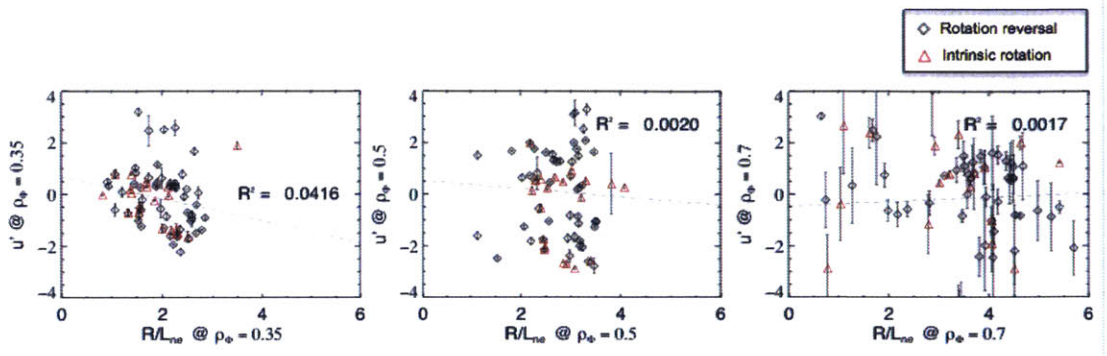

(a)

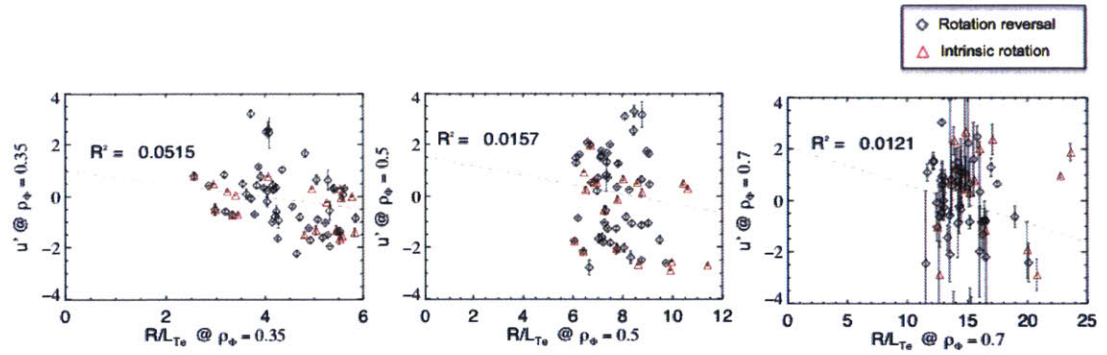

(b)

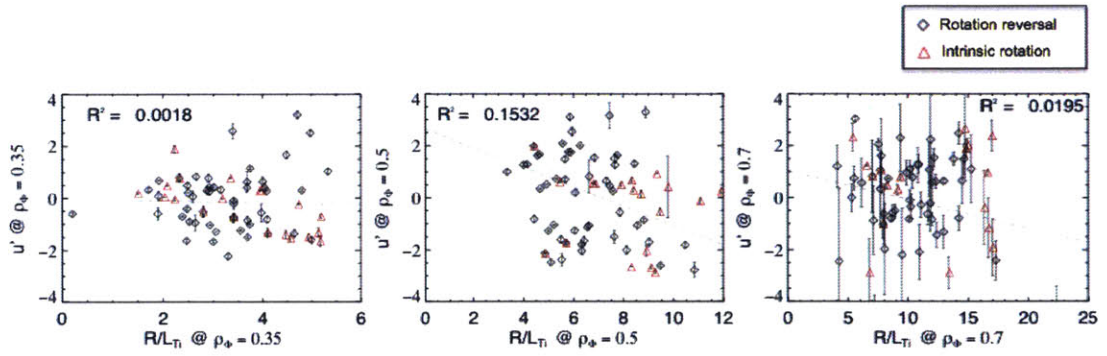

(c)

Figure 38: Plots with u' error bars of (a) u' vs. $\frac{R}{L_{n_e}}$(Figure 35), (b) u' vs. $\frac{R}{L_{T_e}}$(Figure 36), and (c) u' vs. $\frac{R}{L_{T_i}}$(Figure 37)

From Figure 38, it can be seen that near the core at $\rho_\phi = 0.35$, the error bars remain relatively small except for a few data points with large (>40%) errors. Most error bars are barely noticeable relative to the symbols used to mark the data points and both rotation reversal and intrinsic rotation shots have similar errors. The average of these errors for u' at

this spatial location was calculated to be approximately 30%. The mean errors of the local profile gradients at this location are 8% for $\frac{R}{L_{ne}}$, 12% for $\frac{R}{L_{Te}}$, and 16% for $\frac{R}{L_{T_i}}$, much less than the u' errors. The largest errors for these density and temperature profile gradients were from $\frac{R}{L_{T_i}}$, which is expected as $T_i$measurements from the HIREXSR diagnostic system tend to have the greatest experimental errors out of the three parameters.

At $\rho_\phi = 0.5$, the error bars also remain relatively small except at a few points, and the mean is calculated to be 15%. However, at $\rho_\phi = 0.7$ closer to the edge, the u' error bars become very significant and range u' values of 1 to even 4 for several data points. The mean of the u' errors at this location was calculated to be 281% and indicates the significant errors at this location, far from the core. Because the measurement error was assumed to be 30% for the entire rotation profiles and independent of the spatial location, the large u' errors shown in Figure 38 is a direct result of the large fitting errors. The larger u' errors behind observed at $\rho_\phi = 0.35$ and 0.7 combined with a spatially independent measurement error suggests that the rotation profile fitting using the Monte Carlo stochastic method is inaccurate at the edges. This could be due to the lack of accurate data points at the edges of the profiles that result in poor fitting or due to the fitting method itself. Because of the relatively small error bars for the C-Mod parameters at $\rho_\phi = 0.35$, even accounting for the measurement and fitting errors, the correlations between u' and the local profile gradients remain very weak.

Analysis of a large number of ohmic L-mode intrinsic rotation and rotation reversal shots at ASDEX Upgrade have identified the electron density gradient as the primary parameter for determining the magnitude and direction of the rotation for reversals. It also has observed the weaker but non-negligible correlation between the rotation gradient and the electron and ion temperature gradients as shown in the linear regression and Figure 34. However, analysis of C-Mod intrinsic rotation and reversal shots show that the electron density gradient $\frac{R}{L_{ne}}$, electron temperature gradient $\frac{R}{L_{Te}}$, and the ion temperature gradient $\frac{R}{L_{T_i}}$are not strongly correlated with u' even when incorporating the possible errors in u', as shown in Figure 38. The linear regression fit in Table 6 shows that for the most part, the u' decreases with increasing gradients, but the correlations are too weak for the fits to be statistically significant. Additionally, the linear regression and R^2 calculations showed that the electron density and temperature gradients have similar levels of correlation with the rotation gradient. However, at $\rho_\phi = 0.35$, the gradient range is limited relative to that of the ASDEX Upgrade, which might be prevent strong correlations from being identified. Regardless, in the ohmic L-mode C-Mod dataset, the strong correlations between u' and the local profile gradients were not found, which is inconsistent with the experimental observations in ASDEX Upgrade.

5.2 Correlations with ν_{eff}

Along with correlations between u' and the local density and temperature profile gradients, the ASDEX Upgrade database analysis identified a strong correlation between u' and the effective collisionality ν_{eff}, as shown in Figure 34a and Figure 33. As the collisionality increases, the rotation gradient was observed to decrease, signifying that the intrinsic rotation velocity was changing from co-current to counter-current. Additionally, it was observed that past a critical collisionality $\nu_{eff} \sim 0.45$, u' increases again, a phenomenon referred to as

a "double reversal" in the literature [13, 17]. To test the correlation between u' and the effective collisionality and the existence of a double reversal, the u' is plotted as function of ν_{eff}. The expression used to calculate ν_{eff} is given by

$$\nu_{eff} = 0.00279(15.94 - 0.5log\frac{n_e}{T_e^2}) \times \frac{n_e}{T_e^2} R\sqrt{m_A} Z_{eff}$$

where m_A is the mass of the main ion, assumed to be 50% D/50% T and Z_{eff} is the effective nuclear charge, assumed to be 12 for this study. These plots at the three spatial locations ($\rho_\phi = 0.35,\ 0.5,\ 0.7$) are shown below in Figure 39.

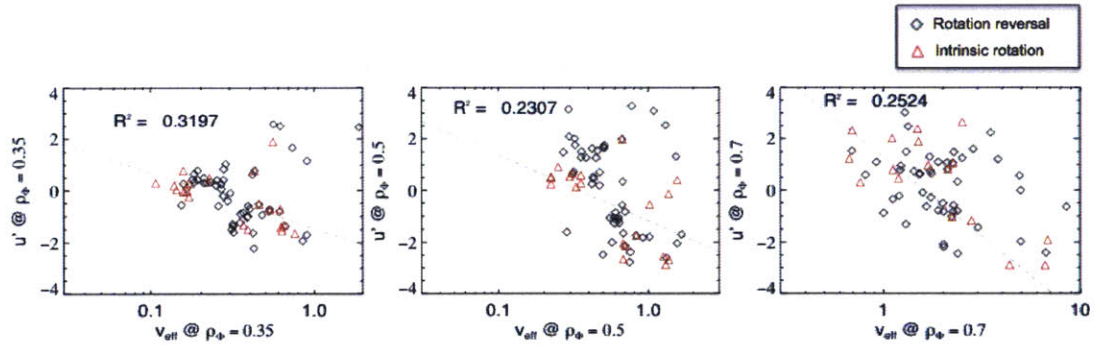

Figure 39: Trends between rotation gradient u' and the effective collisionality ν_{eff} in log using the C-Mod ohmic L-mode intrinsic rotation/ rotation reversal database at (a) $\rho_\phi = 0.35$, (b) $\rho_\phi = 0.5$, and (c) $\rho_\phi = 0.7$ with linear fits (dashed) and R^2 values.

From Figure 36a, it can be seen that a noticeable correlation exists between u' and ν_{eff} at $\rho_\phi = 0.35$ - as the collisionality increases, the plasma becomes increasingly counter-current. This is also seen in the C-Mod data shown in the figure above. The strongest correlation can be seen at $\rho_\phi = 0.35$, where the R^2 is almost 32%. Except for 6 data points near the top right corner of the plot, the rest of the shots seem to indicate a strong correlation between u' and the ν_{eff} . Qualitatively, the data seem to indicate a correlation stronger than what is seen in ASDEX Upgrade in Figure 36a. As for the shot types, both reversal and intrinsic rotation data sets display similar behavior.

This correlation can also be found in the data at $\rho_\phi = 0.5$ and 0.7 as shown in Figure 39b and 39c. The R^2values are 23% and 25% respectively, which indicate relatively significant correlations. At $\rho_\phi = 0.5$, u' decreases with increasing effective collisionality from 0.2 to 2. At $\rho_\phi = 0.7$, the effective collisionality range is much greater, from 0.6 to 10, but the correlation between u' and ν_{eff} can be seen over this larger range. No specific trend is noticeable between the reversal and intrinsic rotation data sets as well. As seen in earlier figures comparing u' and the local profile gradients, it can also be seen that for data sets farther from the core, the range of the independent variable, the effective collisionality, increases. Although the ranges seem similar in the plots, the log x-axis and the intervals show that the range of the collisionality measurements increase dramatically. This could be due to greater differences

in the actual temperature and density measurements near the edge or larger errors in the measurements themselves.

The u' seems to correlate strongly with ν_{eff}, but no sign of the double reversal can be identified from Figure 39. The double reversal occurs past a critical collisionality in which the rotation gradient goes from negative to positive, but, no such second reversal is found with increasing collisionality. One might disagree as there are several points that are positive at the higher collisionalities, possibly a sign of a double reversal. However, from Figure 33 and 34a, it can be seen that the second reversal occurs incrementally with increasing collisionality and u' does not exceed the initial value at low collisionality. This second reversal is not what is seen from the C-Mod data. At higher ν_{eff} between 0.7 and 1.0, most of the u' values are negative and there are a handful at u' of between 2 -3, which is much higher than the initial u' at a ν_{eff} of 0.1. Additionally, from Figure 34a, it can be seen that the second reversal occurs within a ν_{eff} range between 0.45 and 1.0 with most of the u' past ν_{eff} = 0.45 to be increasing back to 0. However in C-Mod, between ν_{eff} of 0.45 and 1.0, most of the data points continue to decrease in u' and only a few are positive. These data points with u' values much greater than those before the 1st reversal and the fact that they are the exception to the overall trend suggest that they might simply be outliers from inaccurate measurements or fitting rather than indicative of a double reversal. Analysis with more data points will be necessary to make a conclusion.

Incorporating error analysis for these parameters, the plots from Figure 39 are replotted with error bars and shown below.

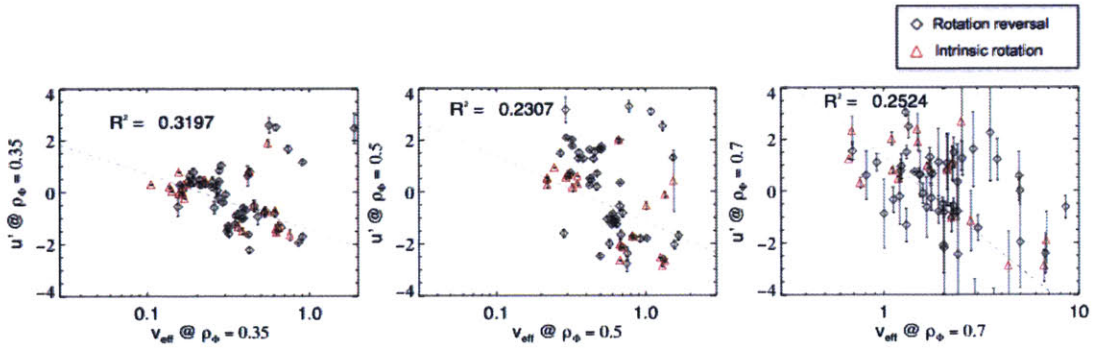

Figure 40: Plots shown in Figure 39 with u' error bars of u' vs. ν_{eff} calculated using the stochastic Monte Carlo method.

From the figure, it can be seen that at $\rho_\phi = 0.35$ and 0.5, the errors are relatively small except for several points. As mentioned previously, the average error bars of u' in this data set are 30%, 15% and 281% for $\rho_\phi = 0.35$, 0.5, and 0.7 respectively. It can be seen that closer to the edge, the errors becomes very large and could be due to inaccurate measurements or due to the fitting routine. With the errors, it can still be seen that there are strong correlations between u' and ν_{eff} at these three spatial locations. Especially at $\rho_\phi = 0.7$, it can be seen that the linear fit (dashed line) falls within most of the error bars of the data. This can also be seen for $\rho_\phi = 0.35$. Because these error bars are representative of 1-sigma errors or 1 standard deviation from the mean, it is expected that even the best linear fit cannot

be expected to match every data point within error bars. Nonetheless, it can be seen from Figure 39 and 40 that there is a strong correlation between u' and ν_{eff} as the linear fits fall well into the errors of most of the data set.

A strong correlation has been identified between u' and ν_{eff}, but it has not been found between u' and $\frac{R}{L_{ne}}$, $\frac{R}{L_{Te}}$, and $\frac{R}{L_{Ti}}$. To investigate the possible correlations between ν_{eff} and the profile gradients, the local profile gradients should not be strongly correlated with ν_{eff}. To check, the normalized electron density, electron temperature, and ion temperature profile gradients are plotted vs. ν_{eff} and is shown below in Figure 41.

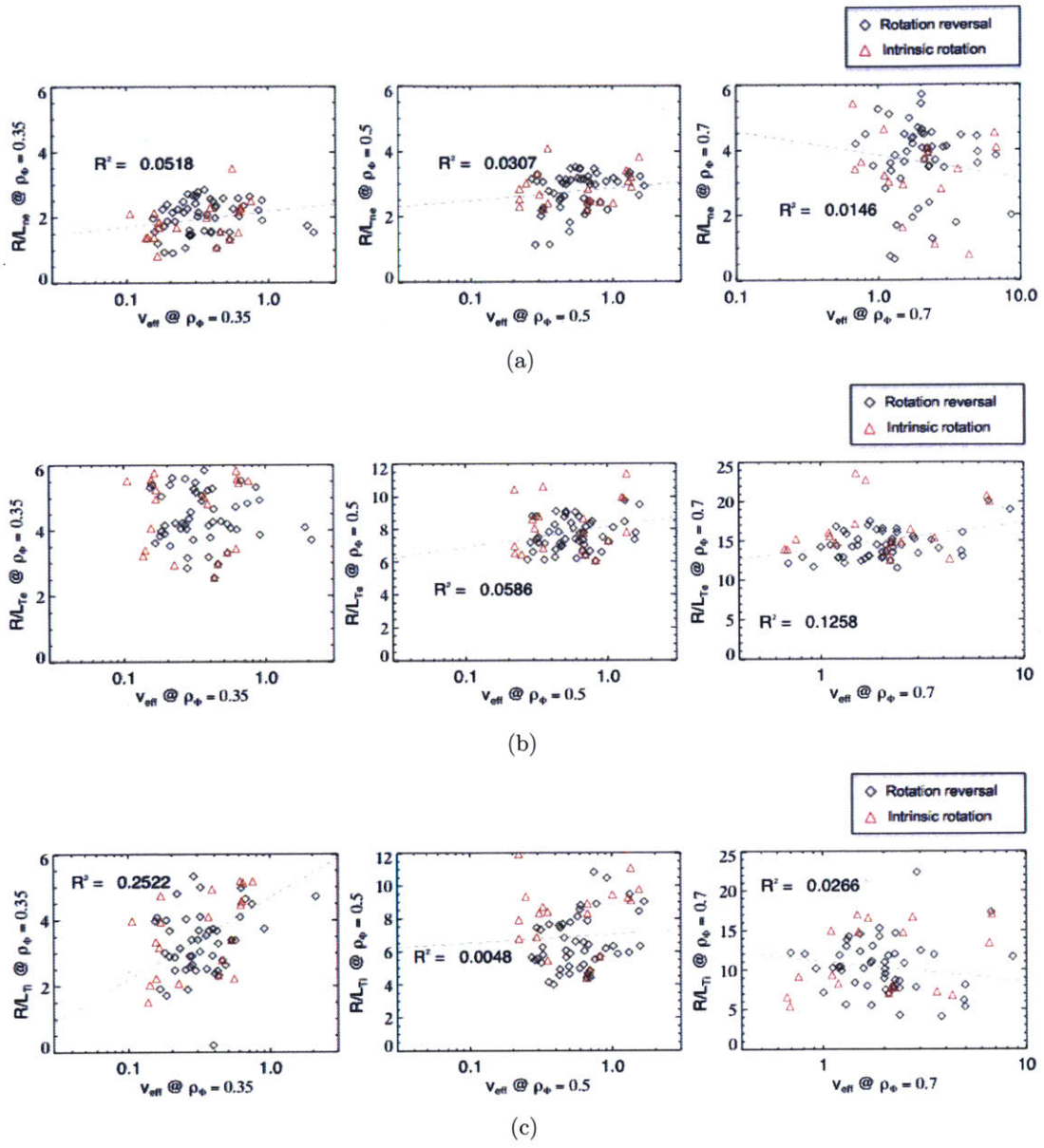

Figure 41: Trends between (a) the normalized electron density gradient $\frac{R}{L_{n_e}}$, (b) the normalized electron temperature gradient $\frac{R}{L_{T_e}}$, and (c) the normalized ion temperature gradient $\frac{R}{L_{T_i}}$ vs. ν_{eff} using the C-Mod ohmic L-mode intrinsic rotation/ rotation reversal database at $\rho_\phi = 0.35$, 0.5 and 0.7 with linear fits (dashed) and R^2values.

A weak correlation was identified between u' and $\frac{R}{L_{n_e}}$ and for $\frac{R}{L_{T_e}}$at $\rho_\phi = 0.35$, but a strong correlation was identified between u' and ν_{eff} . To get a better understanding of these parameters and the underlying physics behind rotation reversals, u' and ν_{eff} are compared as well. Identifying trends between certain parameters is helpful in discerning how

each parameter influences another and in this study, testing multiple correlations among u', profile gradients, and collisionality can provide a better picture of how each are connected.

A weak correlation between the density and temperature gradients and ν_{eff} is observed and shown in the plots shown in Figure 41a and b. At $\rho_\phi = 0.35$, the R^2 value for the linear fit between $\frac{R}{L_{n_e}}$ and ν_{eff} is 5% and for $\frac{R}{L_{T_e}}$, the linear regression analysis yielded an almost perfectly vertical slope and thus was not plotted. It can be seen for the other spatial locations that the correlations are very weak as well, as expected. However, two notable observations were made in this analysis in the correlation between $\frac{R}{L_{T_e}}$ and ν_{eff} at $\rho_\phi = 0.7$ and $\frac{R}{L_{T_i}}$ and ν_{eff} at $\rho_\phi = 0.35$. These two plots show relatively high R^2 values relative to those of other correlations and were unexpected results. From Figure 36c and 37a, it can be seen that these parameters do not display strong correlations to u' with R^2values of 1.2% and 0.2% respectively, yet display strong correlations with ν_{eff} . Additionally, the strong correlation between $\frac{R}{L_{T_i}}$ and ν_{eff} has also been observed ASDEX Upgrade, as shown in Figure 33h. However, what mechanism causes this strong correlation is not known. These observations need to be investigated further before any conclusions can be made.

These findings suggest that ν_{eff} is a good parameter for determining the rotation gradient u', which is consistent with the observations from ASDEX Upgrade [17]. Although the underlying physics behind the strong correlation between these two parameters and the one between u' and $\frac{R}{L_{T_i}}$ is unknown, the correlation and its agreement with the observations in ASDEX Upgrade underscores the importance of ν_{eff} as a key parameter for rotation reversals.

5.3 Multi-Variable Linear Regression

To test the statistical importance of the density and temperature profile gradients and the effective collisionality to the rotation gradient and thus intrinsic rotation, a multi-variable linear regression of u' was performed at two spatial locations ($\rho_\phi = 0.35$ and 0.5). As seen from the results above, the errors of the parameters at $\rho_\phi = 0.7$ are so large that a regression analysis would not yield any accurate results. The results of the regression analysis is expressed as

$$u' = (0.675\pm0.005)\frac{R}{L_{n_e}} - (0.998\pm0.007)ln(\nu_{eff}) + (0.143\pm0.004)\frac{R}{L_{T_i}} - (0.435\pm0.003)\frac{R}{L_{T_e}} - 1.522$$

at $\rho_\phi = 0.35$ with a root mean square error (RMSE) value of 0.764 and

$$u' = (1.065\pm0.014)\frac{R}{L_{n_e}} - (2.567\pm0.009)ln(\nu_{eff}) + (0.174\pm0.003)\frac{R}{L_{T_i}} - (0.154\pm0.005)\frac{R}{L_{T_e}} - 3.129$$

at $\rho_\phi = 0.5$ with a RMSE value of 1.70. From these regression results, the statistical significant of each parameter can be calculated and compared to one another. The statistical significance is calculated by the regression coefficient divided by the variable's standard deviation. For the regression analysis at $\rho_\phi = 0.35$, the absolute values of these significance values are 1.30 for $\frac{R}{L_{ne}}$, 0.45 for $\frac{R}{L_{Te}}$, 0.12 for $\frac{R}{L_{Ti}}$, and 1.931 for $ln(\nu_{eff})$. Therefore, the collisionality is is the most significant parameter, followed by the electron density gradient, the electron temperature gradient, and the ion temperature gradient. This is consistent with previous analysis using linear regression analysis in comparing these parameters to u'. According to this statistical analysis, electron density gradient is more significant in comparison to the electron temperature gradient, even though they had similar R^2 values for their linear fits. This suggests that the linear fits for these two parameters differ significantly in accuracy, such that the R^2 is not an accurate measure of the correlation and significance between these gradients and u'. For the expression at $\rho_\phi = 0.5$, the absolute values of these significance values are 1.96 for $\frac{R}{L_{ne}}$, 0.10 for $\frac{R}{L_{Te}}$, 0.085 for $\frac{R}{L_{Ti}}$, and 4.264 for $ln(\nu_{eff})$. The order of the significance of these parameters is the same as that of the regression analysis at $\rho_\phi = 0.35$ and is consistent with the analysis shown in Figure 35, 36, 37, and 38.

The results of the multi-variable linear regression from the C-Mod data set differ from those of the ASDEX Upgrade data in the regression coefficients, statistical significance of the parameters, and the regression error. The coefficients in the regression results from ASDEX Upgrade at $\rho_\phi = 0.35$ are between -0.12 and 0.028 in comparison to the range of 0.675 to -0.998 for C-Mod at the same location. One partial explanation for the larger coefficients is that the u' range for C-Mod is twice that of ASDEX Upgrade. However, the all of the regression coefficients for ASDEX Upgrade are negative, indicating that the u' decreases with increasing all of the parameters. However, in C-Mod, $\frac{R}{L_{ne}}$ and $\frac{R}{L_{Ti}}$ have positive regression coefficients, such that keeping all of the other parameters fixed, an increase in either the electron density or ion temperature gradient would result in an increase in u', which was not observed in the direct single variable linear regression analysis. The exact reason for this counterintuitive result is unknown. In C-Mod, the variables in decreasing significance are ν_{eff}, $\frac{R}{L_{ne}}$, $\frac{R}{L_{Te}}$, and $\frac{R}{L_{Ti}}$, but in ASDEX Upgrade, the rank in decreasing significance is $\frac{R}{L_{ne}}$, ν_{eff}, $\frac{R}{L_{Ti}}$, and $\frac{R}{L_{Te}}$. Although both suggest that the temperature gradients play the smallest roles out of these parameters in determining u', the data show a disagreement over which parameter is the most significant. From Figure 35 and 38, it can be seen that the correlation between u' and ν_{eff} is stronger than that between u' and $\frac{R}{L_{ne}}$, but for ASDEX Upgrade, the observations are the exact opposite. Lastly, the RMSE of the regression analysis for the ASDEX Upgrade data set at $\rho_\phi = 0.35$ is 0.27, but for C-Mod, it is calculated to be 0.76, almost a factor of 3 larger. One partial explanation for this difference is that the RMSE is an absolute measure of error, such that the larger u' ranges in C-Mod shots can result in a larger RMSE even if the errors are similar percentage-wise between C-Mod and ASDEX Upgrade. However, this does not explain such a larger disparity. The larger RMSE indicates that the regression results for C-Mod does not match the experimental measurements as well as that of ASDEX Upgrade. This could be partly driven by the low correlations observed between u' and the density and temperature profile gradients in C-Mod. A regression analysis with a larger dataset could help in determining a more accurate multi-variable regression expression for u' and identify the causes for the issues and unexpected observations in this study.

5.4 Summary

The C-Mod database of ohmic L-mode intrinsic rotation/reversal shots was used to test the local profile gradient hypothesis. Based on experimental studies at ASDEX Upgrade, this hypothesis identified the local electron density, electron temperature, and ion temperature profile gradients ($\frac{R}{L_{ne}}$, $\frac{R}{L_{Ti}}$, and $\frac{R}{L_{Te}}$) as important parameters in determining the rotation gradient and thus, the rotation velocity magnitude and direction, with the electron density gradient being the most significant parameter out of the three. A strong correlation between u' and the effective collisionality ν_{eff} was also observed. To test this hypothesis and the correlations, the density, temperature, and rotation gradients and effective collisionality were calculated for each C-Mod shot in the data set and then plotted against each other to identify any possible correlations and to compare them to the results from ASDEX Upgrade. In addition to these comparisons, linear regression analysis, Pearson correlation analysis via R^2 calculations, and error analysis were also performed to fit the data, quantify the correlation and goodness of fit, and incorporate experimental and fitting errors, respectively.

First, the rotation gradient u' was plotted against $\frac{R}{L_{ne}}$, $\frac{R}{L_{Ti}}$, and $\frac{R}{L_{Te}}$ at three spatial locations (ρ_ϕ = 0.35, 0.5 and 0.7) to identify any correlations between the gradients. Only a weak correlation was found between u' and $\frac{R}{L_{ne}}$at $\rho_\phi = 0.35$ and the R^2 of the linear fit of 4.2% was similar to the 5.2% of the fit between u' and $\frac{R}{L_{Te}}$. No other correlation was able to be identified for the other profile gradients at the three locations. These findings are inconsistent with the results at ASDEX Upgrade. However, the C-Mod data have a limited range of density and temperature gradients of 0 to 4 at $\rho_\phi = 0.35$ in comparison to the range of 0 to 6 for the gradients at ASDEX Upgrade, such that any strong correlations that may appear for larger density and temperature gradient ranges would not be able to be identified in C-Mod.

To identify any correlations between u' and ν_{eff}, these two parameters were plotted at the same three spatial locations (ρ_ϕ = 0.35, 0.5 and 0.7). It was seen that there is a strong correlation between them as indicated by an R^2 value of 43% at $\rho_\phi = 0.35$ - as the collisionality increased, the rotation gradient became increasingly negative, signifying a counter-current rotation. This correlation was also observed at $\rho_\phi = 0.5$ and 0.7, albeit they were weaker. This strong correlation between u' and ν_{eff} is consistent with the results at ASDEX Upgrade. As a check for self-consistency, $\frac{R}{L_{ne}}$, $\frac{R}{L_{Ti}}$, and $\frac{R}{L_{Te}}$ were plotted against ν_{eff} and the results were as expected, except for two plots. $\frac{R}{L_{Te}}$ vs. ν_{eff} at $\rho_\phi = 0.7$ and $\frac{R}{L_{Ti}}$ vs. ν_{eff} at $\rho_\phi = 0.35$ showed very strong correlations although these gradients did not show correlations with u'. The reason or mechanism behind these results is unknown, but the same strong correlation between $\frac{R}{L_{Ti}}$ vs. ν_{eff} at $\rho_\phi = 0.35$ is observed in ASDEX Upgrade.

To identify the most significant parameters and to quantify the effects each parameter has on u', a multi-variable linear regression was performed on u'. The results showed that the parameters in order of decreasing statistical significance are ν_{eff}, $\frac{R}{L_{ne}}$, $\frac{R}{L_{Te}}$, and $\frac{R}{L_{Ti}}$, which is inconsistent with the regression results from ASDEX Upgrade. Additionally, the regression coefficients for C-Mod showed that u' increases with increasing $\frac{R}{L_{ne}}$and $\frac{R}{L_{Ti}}$in comparison to the coefficients for ASDEX Upgrade that showed u' decreasing for an increase in any of

the four parameters. The root mean square error (RMSE) value for the regression results for C-Mod were almost a factor of 3 greater than that of ASDEX-Upgrade, suggesting that using the effective collisionality and the density and temperature gradients to predict u' is not very accurate and does not fully capture the physics of rotation reversals.

One key limiting factor in testing this hypothesis was the limited density and temperature ranges, especially closer to the core at $\rho_\phi = 0.35$. A larger range of these parameters is important in verifying the existence or lack of correlation between these parameters and u'. Analyzing a larger number of ohmic L-mode shots would also be useful in determining the existence or lack of correlations in various parameters and reduce the effects of outliers in the linear regression analysis. Incorporation of a better error analysis routine, perhaps by using actual measurement errors from HIREXSR diagnostic system for the ion temperature and toroidal rotation velocity, can help in observing trends and correlations that may fall within the error of the data.

6 Testing the Neoclassical Hypothesis and the 1-D Intrinsic Rotation Model

The neoclassical hypothesis posits that neoclassical corrections to the equilibrium ion distribution function modify the turbulent transport and thus cause the rotation reversals [56, 57]. These non-Maxwellian corrections depend heavily on the plasma collisionality and current, which are also important parameters for determining the strength and direction of the intrinsic rotation [56]. Therefore, this hypothesis suggests that these neoclassical corrections, rather than linear turbulence drive, is the primary mechanism for rotation reversals, which makes collisionality a primary parameter for determining reversals and intrinsic rotation. Past work have shown that neither the ITG/TEM transition nor the local density and temperature profile gradients are highly correlated with rotation reversals for ohmic L-mode plasmas [13, 17, 19]. However, the strong correlation between collisionality and rotation has been observed in this study and others [14, 17]. To capture the underlying physics of neoclassical effects on reversals, a 1-D analytical model has been presented and suggests that the rotation reversal occurs when the collisionality passes a threshold value [57]. The model and the comparison to experiments from the Mega Amp Spherical Tokamak (MAST) is presented in detail in Chapter 1 and the 1-D analytical expression is given as

$$\frac{v_{ti}}{R_\psi}\frac{\Pi_{int}}{Q_i} = \frac{B}{B_\theta}\frac{\rho_i}{L_{T_i}}\tilde{\Pi}(\nu_\star)$$

where $v_{ti} = \sqrt{\frac{2T_i}{m_i}}$is the ion thermal speed, $R_\psi = \sqrt{< R^2 >}$is the flux surface averaged major radius, $Q_i$is the turbulent energy flux, ρ_i is the ion gyroradius, and $L_{T_i}$is the ion temperature gradient scale length, and$\tilde{\Pi}$is the order unity function dependent on the normalized collisionality and is expressed as

$$\tilde{\Pi}(\nu_\star) = \frac{\tilde{\Pi}_0(\nu_\star/\nu_c - 1)}{1 + (\nu_\star/\nu_c)(\tilde{\Pi}_0/\tilde{\Pi}_\infty)}$$

which clearly shows that the function changes sign when the normalized collisionality $\nu_\star = \frac{qR_\psi\nu_{ii}}{(v_{ti}\epsilon^{1.5})}$ meets the critical collisionality threshold ν_c where ν_{ii} is the ion to ion collision frequency . $\tilde{\Pi}_0$ and $\tilde{\Pi}_\infty$are constants determined through turbulence simulations of cyclone base cases and the critical value $\nu_c$is determined experimentally to be ~ 1.

Π_{int} is the intrinsic momentum flux. Without external momentum injection, the momentum flux must balance out to be zero, and ignoring pinch terms, the intrinsic momentum flux term must be balanced by the turbulent diffusion. This can be seen in the equation for the Reynolds stress in Chapter 1, which shows the Reynolds stress term balanced by the sum of the diffusive term, convective pinch term, and the residual stress term. Therefore,

assuming that only the diffusive term and the intrinsic momentum flux term exist and must balance, Π_{int} is given as

$$m_i n_i \chi_\phi R_\psi^2 \frac{\partial \Omega_\phi}{\partial r} = \Pi_{int}$$

as shown in Equation 7. This renders the rotation gradient to be directly proportional to the normalized collisionality. By combining these expressions, the rotation gradient u' can be given as a function of the normalized collisionality

$$u' = -\frac{q}{2}\left(\frac{R}{L_{T_i}}\right)^2 \frac{\rho_i}{r}\frac{\chi_i}{\chi_\phi}\tilde{\Pi}(\nu_\star) \tag{9}$$

and this expression is used to calculate the theoretical u' using C-Mod data. It can be seen from these equations that u' only changes sign if the unity function $\tilde{\Pi}(\nu_\star)$ changes sign, as the other terms are always positive or are held fixed. From the expression of $\tilde{\Pi}(\nu_\star)$, it can be seen that the sign can only change if the normalized collisionality $\nu_\star$ exceeds the critical threshold term ν_c . When this occurs, the $\tilde{\Pi}(\nu_\star)$ becomes positive, thus making u' negative and changing the intrinsic rotation direction to counter-current. Physically, the threshold signifies to transition process from the low collisionality "banana" regime to the intermediate collisionality "plateau" regime, changing the turbulent transport and the diamagnetic direction of the turbulence [56, 57].

The theoretical u' values calculated from Equation 9 are compared directly to the experimental u' values to test the 1-D theory and study how the model behaves with increasing collisionality. Table 7 shows the constants and the values assumed to calculate the theoretical u' values.

Constant	Value
$\tilde{\Pi}_0$	0.3
$\tilde{\Pi}_\infty$	1
ν_c	1.7
$P_r = \frac{\chi_\phi}{\chi_i}$	0.7
R_ψ	$(R_{out} + R_{in})/2$

Table 7: List of constants used in calculating the theoretical u' using the 1-D neoclassical model [57]

Two IDL routines, combinedfiletest.pro and hillesheimtestfig2.pro, were written to perform the calculations and generate the plots. The location of these routines can be found in the Appendix B.

6.1 Testing the 1D Intrinsic Rotation Model

Using ohmic L-mode intrinsic rotation and reversal C-Mod shots, the theoretical u' was calculated using Equation 9 and compared to the experimental u'. The plots of the model and experimental values of u' as a function of the normalized collisionality, $\nu_\star$, sometimes denoted as ν_i*, at three spatial locations (ρ_ϕ= 0.35, 0.5, and 0.7) are shown below in Figure 42.

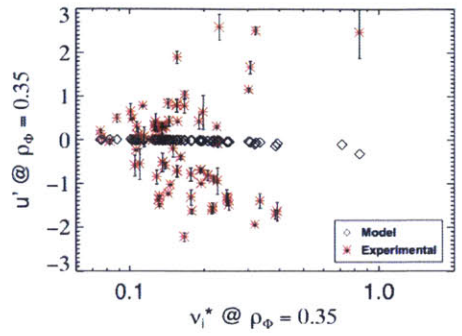

(a)

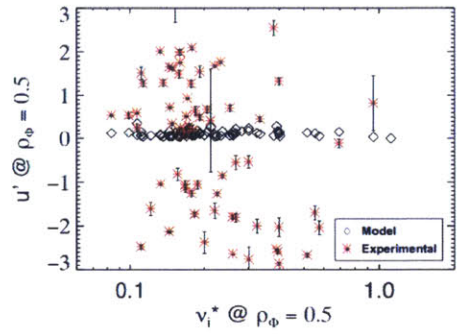

(b)

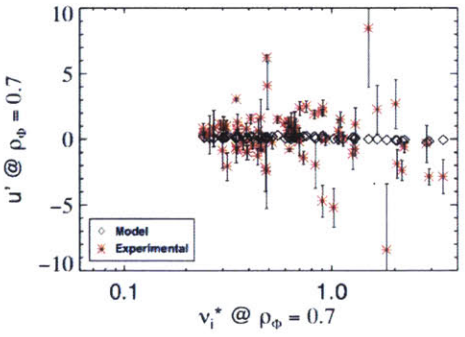

(c)

Figure 42: Plots of theoretical rotation gradient u' (black diamond) calculated from Equation 9 and experimentally measured u' (red star) vs. the normalized collisionality ν_i* for ohmic L-mode C-Mod shots at (a) ρ_ϕ= 0.35, (b) ρ_ϕ= 0.5, and (c) ρ_ϕ= 0.7 with experimental u' error bars.

From Figure 42, it can be seen that the experimental u' values (red stars) show strong co-current and counter-current rotation and the theoretical values are relatively constant throughout the collisionality at u' ~ 0.05. Close to the core at ρ_ϕ= 0.35, it can be seen that the magnitude of u' for both co-current and increase with increasing collisionality while the model values do not change noticeably with collisionality. At all three locations, the

experimental and model u' values do not match, even accounting for error bars. Because the model u' values depend significantly on constants that are estimated empirically from simulations and can vary by a factor of 2-3, the model u' error bars are not statistically meaningful and thus are not shown in Figure 42 and in future plots.

The C-Mod findings shows that the C-Mod data are not consistent with the 1-D analytical model and the assumptions used. This has also seen in ASDEX Upgrade data. The same u' vs. ν_i* plots using ASDEX Upgrade intrinsic rotation and reversal shots are shown below in Figure 43.

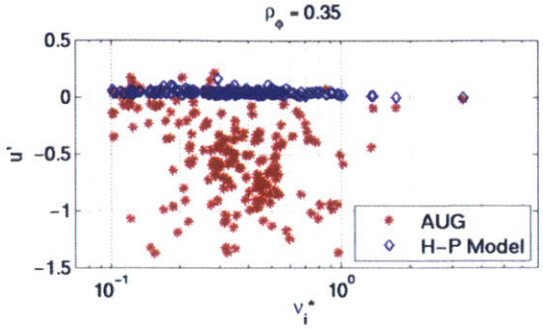

(a)

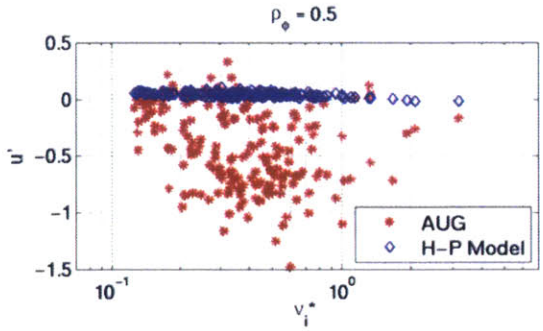

(b)

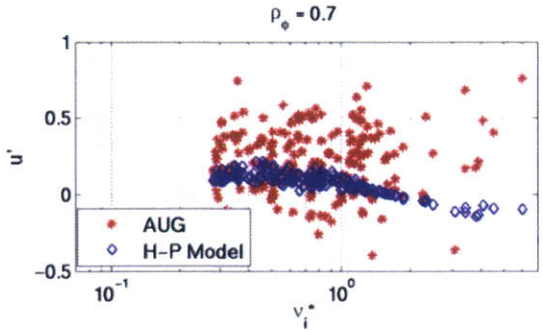

(c)

Figure 43: Plots of theoretical rotation gradient u' (blue diamond) calculated from Equation 9 and experimental u' (red star) vs. the normalized collisionality ν_i* for ohmic L-mode ASDEX Upgrade shots at (a) ρ_ϕ= 0.35, (b) ρ_ϕ= 0.5, and (c) ρ_ϕ= 0.7 [Courtesy of C. Angioni, R.M. McDermott, and ASDEX Upgrade team] using same assumptions given in Table 7.

Although different shots with varying u' and parameters were used, Figure 43 shows a disagreement between experimental and theoretical results. Similar to C-Mod results, the model predicted u' value stays near 0.05-0.1 and varies little with ν_i*. However, the experimental values are centered near u' ~ -0.5 close to the core and ~ 0.5 farther from the core, at ρ_ϕ= 0.7. The theoretical u' values were calculated using the same constant values as

listed in Table 7 and at ν_c= 1.7, it can be seen that the model u' begins to decrease, indicating the occurrence of a rotation reversal in Figure 43c. However, the experimental results do not show a strong correlation between u' and ν_i* in ASDEX Upgrade. The comparisons from both Alcator C-Mod and ASDEX Upgrade show strong disagreement between experimental data and the predicted u' values from the 1-D analytical.

6.2 Testing a Modified 1-D Model

In addition to this direct comparison, another method of testing the 1-D intrinsic rotation model is used. Because the 1-D analytical model is heavily dependent on its constants and especially the value of ν_c, the theoretical u' was recalculated using a ν_c of 0.15 and increasing u' by a factor of 100. From Figure 42a, it can be seen that a large number of experimental values of u' begin to grow increasingly counter-current at $\nu_i* \sim 0.15$. Therefore, to ensure the model also predicts this reversal, the critical threshold value ν_c was set to 0.15. Also, it can be seen that the experimental values of u' range from -3 to 3 near the core at ρ_ϕ= 0.35 and 0.5 but model u' values are much smaller at approximately 0.05. With such small values, a rotation reversal will be difficult to see in these plots and the model cannot be compared accurately. Therefore, the theoretical u' values were increased by a factor of 100, such that the behavior of u' as a function of ν_i* can be compared to experimental u' behavior without worrying about the exact magnitudes of each value. Decreasing the ν_c to 0.15 is not realistic as the transition in the collisionality from the "banana" regime to the "plateau" regime does not happen at collisionalities that low. Also it can be seen from Equation 9 that increasing u' by a factor of 100 is an artificial modification to ensure any reversals are observed on the plot as the constants in the expression are relatively constant and none can be expected to increase by such a large amount without significantly changing the physics. Although this test and the values assumed are not realistic and manufactured, it allows for a more accurate comparison of the underlying physics behind the 1-D model and how well it can predict the intrinsic rotation and reversals. Additionally, if the experimental and theoretical results do not agree even with unrealistic and artificial assumptions, it strongly supports the findings from Section 6.1.

These artificially manufactured test plots are another way to study the model. The test plots at three spatial locations (ρ_ϕ= 0.35, 0.5, and 0.7) are shown in Figure 44.

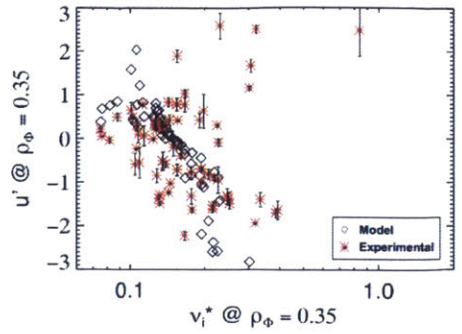

(a)

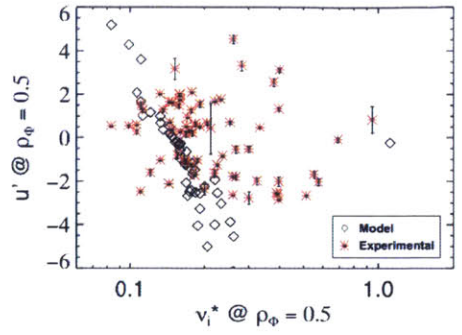

(b)

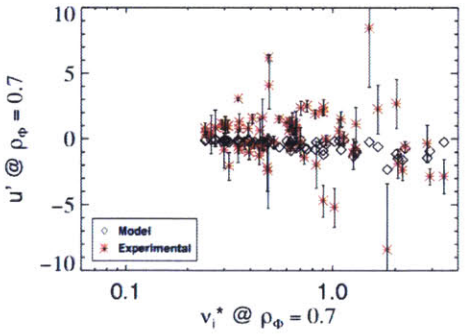

(c)

Figure 44: Plots of the modified theoretical rotation gradient u' (black diamond) calculated from Equation 9 with $\nu_c = 0.15$ and increased by a factor of 100 and experimentally measured u' (red star) vs. the normalized collisionality ν_i* for ohmic L-mode C-Mod shots at (a) $\rho_\phi = 0.35$, (b) $\rho_\phi = 0.5$, and (c) $\rho_\phi = 0.7$ with experimental u' error bars. For $\rho_\phi = 0.7$, model values of u' were not increased by a factor of 100.

At $\rho_\phi = 0.35$, it can be seen from Figure 41a that there is agreement between the experimental and theoretical u' values. However, the model predicts u' to continue decreasing with increasing collisionality, although the experimental u' does not exhibit this behavior. At $\rho_\phi = 0.5$, there is no strong correlation between experimental and model results. The model predicts u' to decrease from co-current to counter-current rapidly with increasing collisionality

continuously, but this behavior is not shown in the experimental data. The experimental u' values show a similar behavior as seen in Figure 41a which is a plot of u' vs. ν_{eff}, in which u' decreases with increasing collisionality and then stays relatively fixed at a negative value with some points showing an increase in u' back to the co-current direction with increasing collisionality. This phenomenon, referred to as the double reversal, is somewhat observed in Figure 44b, as some shots show increasing u' with collisionality past $\nu_i* \sim 0.3$. However, the model does not match neither the double reversal nor the relatively fixed behavior of u' past a certain threshold. These two plots show that even with these manufactured test plots, the experimental data is inconsistent with the theoretical model results and the underlying physics based on normalized collisionalityν_i*. At $\rho_\phi = 0.7$, the u' was not increased by a factor of 100 as the test u' values would have been too large to compare to experimental values. Due to the large measurement errors farther from the core, there is a lack of correlation between u' and ν_i*, which is also seen in previous plots, such as in Figure 41c. From these plots of modified test values of u', it can be seen that this simplified 1-D model does not accurately match the experimental data and the correlation between u' and collisionality, suggesting that the physics is more complex.

6.3 Summary

A 1-D intrinsic model is presented in a previous study that posits the neoclassical corrections to the equilibrium ion distribution function modifies the turbulent transport and drives the rotation reversal. Rather than the linear turbulence drive or the local profile gradients, the neoclassical corrections is suggested to be the primary parameter for determining the strength and sign of the intrinsic rotation. This model uses the normalized collisionality ν_i* as the collisionality term and states that when ν_i* exceeds a critical threshold, the plasma transitions from a low collisionality "banana" regime to an intermediate collisionality "plateau" regime, which is responsible for modifying the turbulence and causes a reversal. Although earlier work have shown that neither the TEM/ITG transition nor the profile gradients are the primary parameters, no work has shown neoclassical corrections and the collisionality to be the primary parameter behind rotation reversals and this model has not been tested outside of experiments in MAST, a spherical tokamak.

Using C-Mod data, the experimental results are compared to the predicted rotation by this 1-D analytical model, which as shown to disagree. ASDEX Upgrade has also shown strong disagreement between experiment and the 1-D model, suggesting that the model does not fully capture the complex mechanisms causing reversals or neoclassical corrections are not the primary driver. For both tests, as shown in Figure 42 and 43, the theoretical u' values stay relatively constant at 0.05 with increasing collisionality ν_i* at all spatial locations but the experimental u' values show significant scatter. Near the core, u' decreases with increasing collisionality, but this was not predicted by the model using the assumptions presented in the literature.

Another comparison was made increasing u' by a factor of 100 and using a different critical threshold value of 0.15 instead of 1.7. The aim was to isolate the reversal mechanism predicted by the model by ensuring the magnitudes of the theoretical u' matched the experimental values to some degree. The results, shown in Figure 43, indicate that the model predicts the u' to increase in the co-current direction with increasing ν_i*, although u' actually

seems to increase back in the co-current direction or stay constant with increasing ν_i*. Even with these test cases, the 1-D model did not show strong agreement with the experimental results, suggesting that the model is too simple to capture the complex behavior observed in C-Mod and ASDEX Upgrade.

Because the 1-D model is a simplified expression that uses ν_i* and a critical threshold value ν_c, it may not accurately predict the rotation reversal, which is the result of a complex set of transport mechanisms. This is evident by the lack of agreement in the modified test cases where significant unrealistic changes were made to the expression to match the experimental data and theoretical values. Another reason for the disagreement is that the model is affected heavily by the constants and the critical threshold value, which have only been derived from simulations. Without accurate values for these constants, the model will not be able to predict the u'. Therefore, a necessary future work would be to calculate more accurate values of these constants or create an expression that uses constants and values that can be more easily defined and estimated. Additionally, the 1-D analytical expression has shown agreement with MAST after modifications were made to its constants, which suggests that this model may not hold with tokamaks with larger aspect ratios, such as C-Mod and ASDEX Upgrade. Using experimental data from another spherical tokamak, such as NSTX, to test this 1-D model is necessary to verify whether this model is device specific and does not accurately capture the physics in larger tokamaks. Nonetheless, it can be seen that C-Mod and ASDEX Upgrade experimental data disagrees with the 1-D intrinsic rotation neoclassical model.

7 Conclusion

The viability and performance of magnetic confinement fusion devices depends a better understanding of the underlying physics and mitigating the effects of mechanisms that degrade confinement, such as instabilities, turbulence, and disruptions. It has been observed that velocity shear resulting from plasma rotation is known to improve confinement by suppressing turbulence [1, 2, 3, 4, 5, 6] and plasma rotation can also increase stability against a variety of MHD instabilities, such as resistive wall modes [6, 7, 8] and neoclassical tearing modes [9, 10]. However, in future devices, such as ITER, sufficient plasma rotation cannot be generated from external injection methods. Rotation not only helps suppress and reduce turbulence and harmful plasma instabilities in these larger devices but also helps prevent locked modes, in which the plasma rotation velocity is too low resulting in major disruptions [81, 45].

Fortunately, a phenomenon known as intrinsic rotation has been observed in multiple tokamak devices throughout the world [11, 14] in which the plasma rotates toroidally without any external momentum input. From a practical standpoint, the intrinsic rotation will be valuable for preventing locked modes and mitigating turbulence and instabilities in future devices and academically, it is an opportunity to gain further understanding of momentum transport. Intrinsic rotation in H-mode plasmas is relatively well defined by the Rice scaling but in ohmic L-mode plasmas, the phenomenon exhibits complex, multi-faceted behavior. Therefore, rotation linked to ohmic L-mode plasmas is the focus of this study. In addition to intrinsic rotation, spontaneous reversals of the intrinsic rotation direction have been observed [14] without a significant change to the global plasma parameters, a phenomenon referred to as a rotation reversal. Such a large displacement of momentum triggered by an unknown mechanism has driven research with aims of identifying the key dependencies linked to reversals and ultimately finding the mechanism or mechanisms responsible for them. Many hypotheses have been presented in past experimental and theoretical work and this thesis aims to test three of them through analyzing a large set of intrinsic rotation and reversal shots in Alcator C-Mod. Each hypothesis identifies different parameters to be the key dependency linked to rotation reversals: dominant turbulence regime [40], local density and temperature profile gradients [13, 17], and neoclassical effects [56, 57].

The first hypothesis, referred to as the dominant turbulence regime hypothesis, posits that the dominant turbulence regime, more specifically the TEM/ITG transition, is linked to rotation reversals based on experimental observations in Alcator C-Mod of the transition in the turbulent mode and rotation direction occurring simultaneously. The second hypothesis, named the local profile gradient hypothesis, identifies the local electron density, electron temperature, and ion temperature profile gradients to have significant roles in determining the magnitude and direction of the intrinsic rotation, especially the electron density profile gradient. This hypothesis has been developed based on experimental observations in ASDEX Upgrade of the electron density gradient having a strong correlation with the rotation gradient u'. The first two hypotheses focus on the linear turbulence drive and turbulent modes as the main drivers of rotation reversals. However, the third hypothesis, named the neoclassical hypothesis, states that neoclassical corrections to the equilibrium ion distribution function, rather than the turbulence drive or fluctuations, modifies the turbulent transport and causes the reversals and presents a 1-D analytical model predicting the u' as a function

of the plasma collisionality.

Similar to the database of intrinsic rotation profiles built in ASDEX Upgrade, a dataset of 76 intrinsic rotation profiles in Alcator C-Mod is constructed and used to test the three hypotheses. Such a large dataset driven study has not been performed in C-Mod to study intrinsic rotation and reversals, so an analysis workflow, a semi-autonomous process of shot analysis routines used at the MIT PSFC, has been built to perform the required profile, linear stability, sensitivity, and error analysis.

7.1 Summary of Results

76 ohmic L-mode profiles exhibiting strong intrinsic rotation velocities ($>$ 5km/s) were collected for the database. To test whether the dominant turbulent mode transitions from TEM to ITG with the rotation reversal, linear stability analysis was performed using GYRO to identify the dominant, or fastest growing, turbulent mode and its growth rates. By comparing u' the normalized rotation gradient, a proxy variable used in place of the toroidal rotation velocity, and the real frequency of the turbulence ω_r, it has been shown that both co-current and counter-current plasmas remain ITG-dominated rather than TEM-dominated for co-current and ITG-dominated for counter-current. The ω_r of the turbulence fluctuations at three specific wavenumbers $k_\theta \rho_s$and at the wavenumber corresponding to the fastest growing fluctuations were used in this comparison, both of which showed the plasma to be strongly ITG-dominated, regardless of the rotation direction. These findings are consistent with previous C-Mod linear gyrokinetic simulations [19]; however, it has been observed in ASDEX Upgrade that both co-current and counter-current plasmas remain TEM-dominated. When directly compared, the results from the two devices are inconsistent with one another but still suggest that the TEM/ITG transition is not a key reversal dependency as the resulting bifurcation of the dominant turbulence regime with the rotation direction was not observed.

To test the local profile gradient hypothesis, the normalized profile gradients $\frac{R}{L_{n_e}}$, $\frac{R}{L_{T_e}}$, and $\frac{R}{L_{T_i}}$ were calculated using fitting routines and plotted against the rotation gradient u'. In contrast to the strong correlation found between u' and the electron density gradient, $\frac{R}{L_{n_e}}$, no noticeable correlation was found between u' and these three local profile gradients, as quantified by the linear regression fit on every plot that had R^2correlation values lower than 3% for most plots. A noticeable correlation was found between u' and the ion temperature gradient $\frac{R}{L_{T_i}}$ was found at ρ_ϕ= 0.5, but no explanation could be found for this result. In addition to the local profile gradients, u' was plotted against the effective collisionality ν_{eff}, which had previously shown strong correlation in ASDEX Upgrade. Similarly, a strong correlation was found between u' and the collisionality near the core. Near the edge, the measurements and fitting errors were too large to make a statistically significant fit. A phenomenon called a double reversal is stated to be observed in ASDEX Upgrade, in which the rotation switches direction to counter-current and then changes again to the co-current direction with increasing collisionality. Two reversals are not found in the results but more shots are required. To test the statistical significance of the local profile gradients and the effective collisionality, a multi-variable linear regression is performed and shows that the effective collisionality has the greatest significance out of the four parameters, which is inconsistent with the regression results from ASDEX Upgrade that showed the electron

density gradient to be the primary term. However, errors of the C-Mod regression analysis results are three times greater than that of ASDEX Upgrade, suggesting that the regression analysis is not a good measure of the statistical significant of these parameters for C-Mod.

The neoclassical hypothesis suggests that neoclassical corrections cause non-Maxwellian terms to dominate and cause the rotation reversal. Earlier work supporting this hypothesis states it to be the explanation for the high correlation between u' and collisionality. One specific work presents a 1-D analytical model that suggests that when the normalized collisionality $\nu_\star$or ν_i*, the ratio of the ion-ion collision frequency to the bounce frequency, crosses a critical threshold, the plasma transitions from the low collisionality banana regime to the intermediate collisionality plateau regime, driving neoclassical effects that modify the turbulent transport and thus, the rotation direction. The test this hypothesis, the 1-D expression, as given in Equation 9, is used to calculate the theoretical u', which is compared to the experimentally measured u' in C-Mod. The experimental and theoretical results have shown strong disagreement in C-Mod and an independent ASDEX Upgrade comparison using the same method has yielded the same disagreement. Even modifying the 1-D model with an unrealistically low $\nu_\star$to trigger a rotation reversal and increase in magnitude of the theoretical u' by a factor of 100 did not result in a strong agreement with experimental results. These findings suggest multiple possibilities, such as the model being too simple, the driving mechanism of reversals not being related neoclasiscal effects, the empirically derived constants being very inaccurate, and/or the neoclassical effects triggering different mechanisms, of which more than one could be the contributors.

7.2 Discussion and Future Work

Using a database of ohmic L-mode shots in C-Mod, it has been shown that the data and analysis are inconsistent with previous results from ASDEX Upgrade and earlier studies in C-Mod. Linear stability analysis, profile fitting, and experimental measurements from C-Mod have not shown strong correlations between the rotation gradient u' and the TEM/ITG transition, local density and temperature profile gradients, and neoclassical effects based on the 1-D analytical model. Although the data and error analysis clearly show that the correlations are not existent or weak at best, no conclusive explanation can be provided as to the discrepancy between the results of this study and those of other studies and the disagreements among the earlier works themselves.

Two findings that have found agreement with previous results - the ITG-dominance in co-current and counter-current plasmas and the correlation between u' and the effective collisionality ν_{eff}. Similarly, these empirical results do not provide any insight into the exact mechanisms that are responsible for intrinsic rotation and reversals, so further work is necessary. Because only three hypotheses were tested, other parameters and ideas need to be focused upon to identify any significant factors that affect intrinsic rotation.

In addition to identifying or eliminating other parameters as rotation reversal dependencies, it is also important to explore the physics behind intrinsic rotation apart from experimental observations. The three hypotheses tested in this thesis focus or identify a single parameter or set of closely related parameters in hopes of getting closer to finding the transport mechanism that causes the reversal and intrinsic rotation. However, this method may not work if the physics is incredibly complex, such that multiple mechanisms and there-

fore, many variables may play a significant role but are not required to change to drive the reversal. If multiple mechanisms are at play such that certain parameters related to one can remain unchanged as the other mechanisms drive the rotation reversal, those dormant parameters may be incorrectly eliminated from the list of potential reversal dependencies. Although developing various hypotheses based on experimental observations and studies, such as these, that test those hypotheses are important and the necessary starting point, if the physics behind this phenomenon has multiple layers, various plasma parameters may come in and out of play based on which mechanisms are active and inactive. In this case, simple linear regressions or correlations would not be able to determine the key dependencies. Nonetheless, this study suggests that ,based on the C-Mod profiles and analysis, the dominant turbulence regime, local density and temperature profile gradients, and neoclassical corrections as framed in the 1-D analytical model cannot be the sole and only key dependencies of rotation reversals. Many mechanisms and parameters may be involved, but this study has shown that those suggested by the three hypotheses show weak correlations with rotation and its direction.

Even before the complex physics can be explored, future work can be done to ensure that the testing of the three hypotheses is more direct. Experimental measurements of the turbulent mode propagation direction instead of linear stability analysis can be a more reliable method of testing the dominant turbulence regime hypothesis. Additionally, nonlinear gyrokinetic simulations could be helpful, especially accounting for mode to mode coupling and sub-dominant modes that may play important role in intrinsic rotation and reversals. Even linear stability analysis using different variables or sensitivity cases can be helpful in uncovering more information about possible trends between the rotation and the dominant turbulent modes.

Testing of the local profile gradient hypothesis has shown the limitations of the gradient ranges in testing their correlations with the rotation gradient u'. The limitation in the local profile gradient for the electron temperature, ion temperature, and electron density prevent conclusive comparisons to be made with the results from ASDEX Upgrade, which has much larger range of gradients in its database. Therefore, utilizing more shots and shots with more peaked profiles near the core will be useful in verifying whether certain features and trends seen in ASDEX Upgrade are also seen in C-Mod.

C-Mod experimental data did not agree with the 1-D analytical neoclassical model, but this could be due to a variety of reasons. Therefore to identify the cause of the disagreement between experimental and the model, more comparisons must be performed, such as using data from another spherical tokamak similar to MAST rather than ASDEX Upgrade or C-Mod or evolving the equation to a 3-D level to more accurately capture the tokamak physics. Without eliminating these possible causes, the disagreement between experiment and the model cannot be rooted to a specific mechanism.

Beyond these three hypotheses, other work, such as more complex regression analysis, can be used with larger databases of shots and plasma parameters as potential variables to identify any complex behavior that may exist that is not able to be captured with simple linear comparisons. Additionally, the use of a scaling that accounts for device-specific parameters would allow for inter-device data comparisons. The collection of intrinsic rotation profiles from various tokamaks for analysis is also an important next step, as whether various results and trends seen in this study and others are device-specific, shot-specific, or truly based on the underlying physics cannot be determined without an inter-device study. By improving

current analysis methods and incorporating creative approaches to looking through the data from various devices, future work will ultimately converge upon the exact mechanism(s) that drive intrinsic rotation and rotation reversals.

APPENDIX

A Detailed Methodology

The methodology described in Chapter 2 of this thesis focuses on three steps carried out for this study:

1) **A database of shot numbers will be used as inputs for the workflow, which will use this list to locate and read data from the C-Mod database using MDSplus.**

2) An analysis workflow is created, a semi-autonomous set of routines with a single user interface that takes the C-Mod shots numbers as inputs, processes and performs linear stability analysis using GYRO, and outputs the type, frequencies, and growth rates of the dominant turbulent mode for each shot. To calculate gradients, the same workflow is used to fit profiles to estimate the gradients at various spatial coordinates. The workflow will also perform error and sensitivity analysis on linear stability results and fitting.

3) The results will then be analyzed using a simple multi-variable regression and qualitatively to find possible strong correlations for comparing against the primary dependencies suggested by the hypotheses as well as identifying new possible rotation reversal dependencies.

To address how the methodology will achieve these steps as well as explain how this methodology differs from the current process, this chapter, broken into 6 sections, will describe the process, workflow, IDL routines, GYRO, etc. in detail. Users who wish to utilize the analysis workflow or parts of it or modify it will find this chapter useful as it provides a step by step guide into how the analysis workflow was formed and how it is used.

Section A.1 describes the original method of analyzing a C-Mod shot for linear stability analysis using GYRO and the possible improvements that can be made with the process. Section A.2 presents a brief summary of GYRO, the Eulerian gyrokinetic-Maxwell solver, the code used for linear stability analysis for turbulent modes. Section A.3 explains the modified database process used before the analysis workflow to collect C-Mod intrinsic rotation and reversal shots (Step 1). Sections A.4 focuses on the analysis workflow (Step 2) and how it is modified form the traditional system. Section A.6 covers the error and sensitivity analysis mentioned in Step 2 that will be performed on the results.

A.1 Traditional Method

To process, fit, and perform linear stability analysis using the current method utilized by researchers at the MIT Plasma Science and Fusion Center, numerous routines and programs must be used in a specific order. This series of routines must be called and used individually for each shot. The large number of different routines and analyses that must be run for a single shot can be time-consuming and the entire process requires too many micromanagement from the user. The issues related to carrying one shot through a series of shot

analysis tools pose an opportunity to create a workflow that automatically performs each step of the vertical for a large set of shots, which is one of the key motivations for creating a data analysis workflow. This section presents a basic overview of the traditional process from start - identifying a shot to end - analyzing the linear stability analysis results outputted from GYRO. The section also addresses the issues of this method in the context of this study of rotation reversals. The entire process can be divided into four different steps:

1) Identifying and characterizing C-Mod rotation reversal shots
2) Profile-fitting
3) Running TRANSP
4) Running GYRO

in which each step has a different tasks and therefore requires a different set of routines. A sample diagram of this structure is shown below in Figure 45.

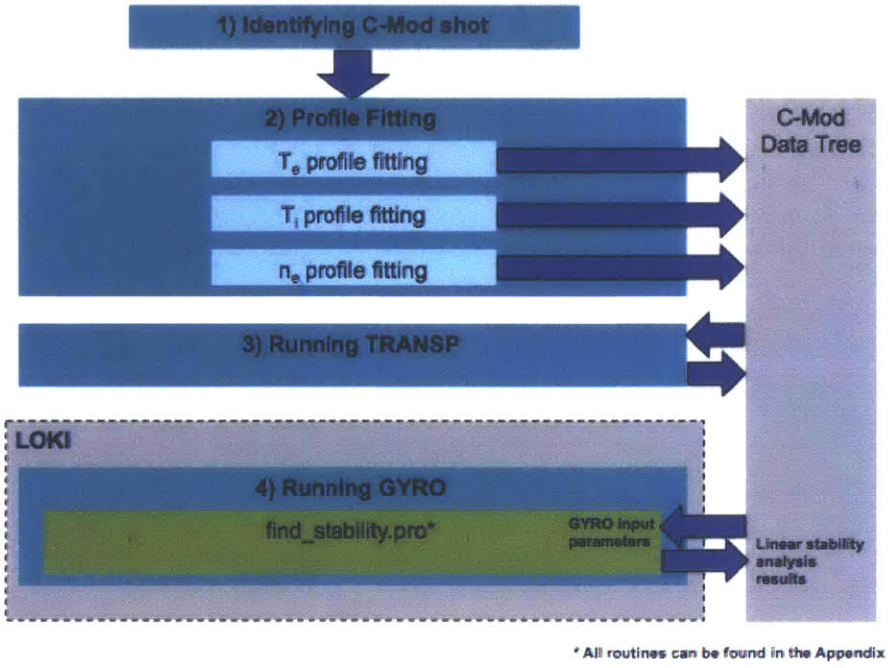

Figure 45: Diagram of the traditional workflow structure using the C-Mod data tree as the storage system.

It can be seen that as each step of the process is run, it must upload and download information into the C-Mod data tree or another data storage medium. Each step is compartmentalized and separate from the others. How this traditional process works and the improvement areas with this method is explained in this section.

A.1.1 Identifying and Characterizing C-Mod Rotation Reversal Shots (Step 1)

A shot is simply the process of generating a plasma within a tokamak for experimental purposes. For Alcator C-Mod, each shot, or plasma discharge, lasts anywhere from a few hundred milliseconds to one to two seconds and is characterized by various diagnostics listed in Section A.2 that measure the many plasma parameters throughout the duration of the shot. These shots are the sources of experimental rotation reversal data for Alcator C-Mod and fortunately, thousands of shots have already been compiled and checked by the Plasma Science and Fusion Center and have been acquired through John E. Rice, Anne White, and other at the MIT PSFC. However, to find the relevant data for this thesis, rotation reversal shots will have to be identified, evaluated, and grouped.

Given a shot number, a 10-digit identification number for each shot that corresponds to the date of the run, the user must ensure that the shot has the traits that he/she is looking for and specify the time range within the shot that the user wants for linear stability analysis. Secondly, the user must verify the existence of high-quality data from the diagnostic measurements before carrying on with the rest of the shot analysis. For studying rotational reversals, the user must verify that the rotation reversal does indeed occur and that it is a significant and large change in sign of the toroidal rotational velocity. To check the change in plasma parameters throughout the shot and to verify its behavior, dwscope is used, an analysis tool that displays line-averaged diagnostic time traces for various parameters such as plasma current, internal energy, and temperature. Information regarding this tool and others can be found in the C-Mod Wiki. A sample of the dwscope interface showing time traces is shown below in Fig. 46.

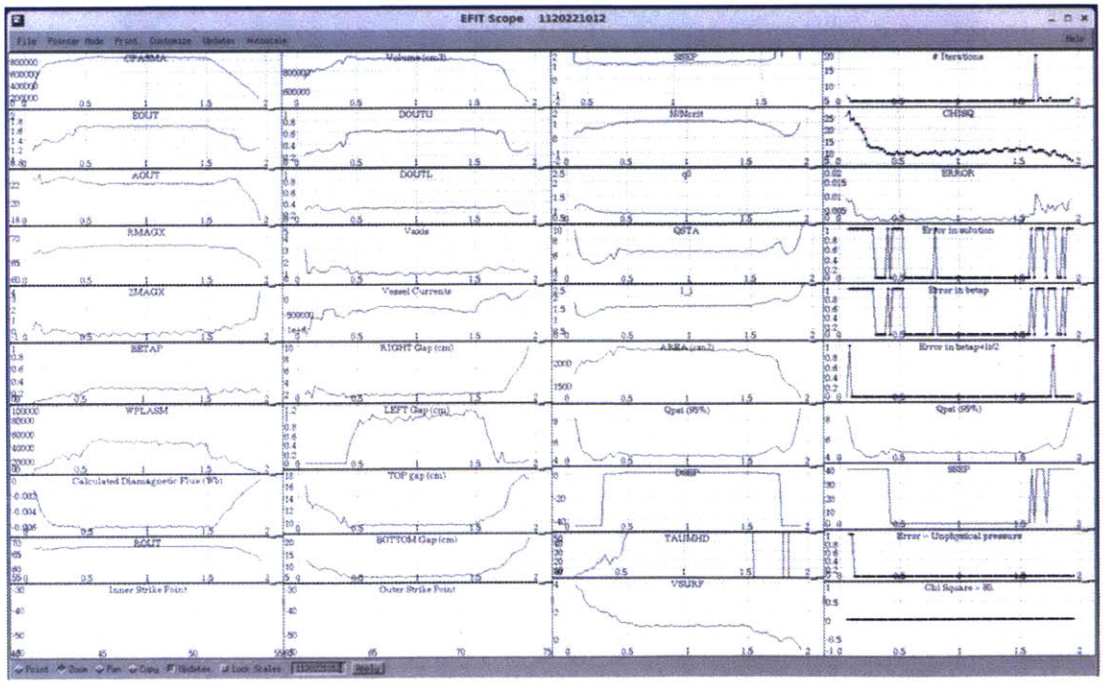

Figure 46: Sample dwscope time traces for Alcator C-Mod shot 1120221012.

It can be seen from the figure that there are a very large number of measurements that characterize each C-Mod shot and the user can customize which time traces are displayed thought dwscope. This program allows the user to specify the time ranges of interest for linear stability analysis because ideally, the user would want a long enough time range to maximize the number of measurement data but short enough to capture steady-state plasma behavior. For example, if the user wanted to record a time range for co-current intrinsic rotation, he/she would look at the time traces to find an adequately long enough time range with a steady and strongly positive toroidal rotation velocity. Additionally, if one or more of the time traces for a key diagnostic used to characterize the shot were missing, the user knows which of the data are missing from the C-Mod database or were not measured for that shot.

To check the existence and quality of measurement data outside of dwscope, various routines can be used. For electron temperature and density measurements, MDS plus, a data acquisition and storage software, can be used to check the C-Mod database or EFIT results can be checked, which create the temperature and density profiles [C-Mod wiki]. For ion temperature and velocity profiles, THACO (The HIREXSR Analysis COde) can be used to check the quality of the profiles and whether the measurements have been processed, in which the data are analyzed via a tomographic inversion process [71]]. Other measurements can be checked through MDS plus or the research group responsible for managing and operating the diagnostics and its data. To evaluate the quality of the data, the user can perform a quick qualitative analysis, checking for any apparent outliers or poor measurements and conferring with the specific research group that would be able to provide a better assessment.

A.1.2 Profile Fitting (Step 2)

One of the most critical aspects of this process is the fitting for the electron density, electron temperature, ion temperature, and rotational velocity profiles. Local gradients of these parameters are significant drivers of dominant turbulence in linear stability analysis [72] and are key variables in testing the three hypotheses; therefore, accurate profile fitting is important and many different tools have been developed for this purpose. Additionally, the toroidal rotational velocity gradient, which will be covered in-depth in future sections, is directly related to the residual stress term for intrinsic rotation. Therefore, to test these hypotheses, especially the analytical model presented by Hillesheim, an accurate estimate of the rotation gradient as well as the profile is important.

For most density and temperature profiles in Alcator C-Mod, the two popular fitting methods are the least-squares polynomial and the least-square b-spline methods. Because density and temperature profiles are usually peaked,monotonically decreasing in radius, and usually predictable in terms of their forms, they are the ideal type of profiles for polynomial and spline fits. Figure 47 shows sample electron density and temperature measurement profiles. The least-squares polynomial method seeks to fit one polynomial equation given by $Y = a_0 + a_1x + a_2x^2 + ... + a_mx^m$,where m is the degree of the polynomial, to experimental data given by $(x_1, y_1), (x_2, y_2).....(x_n, y_n)$ where n $\geq$ m+1. The constants a are chosen to minimize the sum of squared residuals S, given by $S = \sum_{i=1}[y_i - \hat{y}_i]^2$ where $\hat{y}_i = a_0 + a_1x_i + a_2x_i + .. + a_mx_i^m$. Depending on the specific fitting tool used, the order of the polynomial m

is chosen by the user or can be optimally chosen by the fitting tool after trial and error to minimize the S. A sample least squares polynomial fitting is shown below in Figure 47.

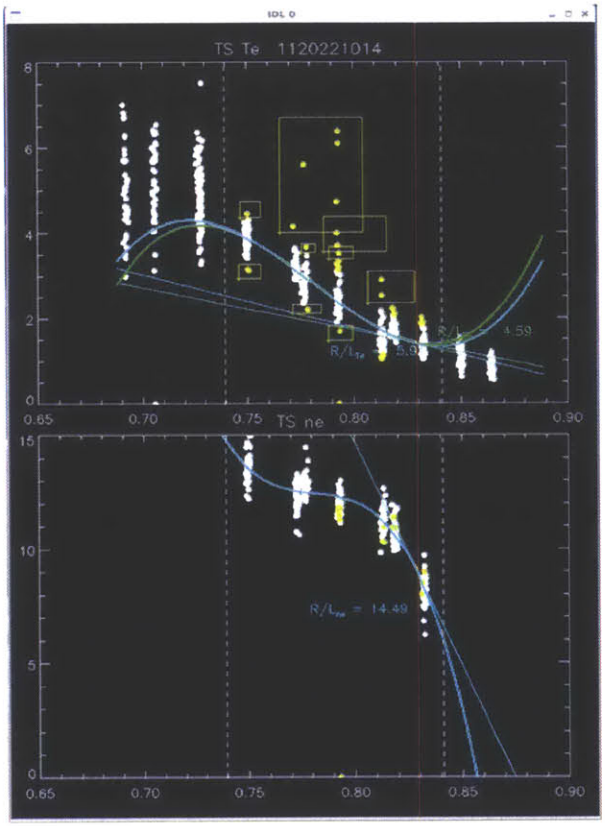

Figure 47: Polynomial fitting for order = 3 using gyro_inputs.pro.

As shown in Figure 47, this method is primarily used for electron density and temperature and provides an analytical fit for typical electron density and temperature profiles in Alcator C-Mod. For ion temperature fitting, the b-spline method is used. The b-spline method is an alternative to the spline method, which uses splines, piecewise functions made up of multiple polynomial expressions. Similar to the polynomial method, the polynomial expressions are chosen to minimize the sum of squared residuals S for a given region and are connected to form a collection of analytical equations to fit the profile. The b-spline method takes advantage of the fact that any spline fit can be expressed as a linear combination of b-splines, or basis splines. Therefore, these splines can be represented by $\sum_{j=1} a_j B_j(x)$ where $B_j(x)$ is the j-th b-spline function and a is determined by the fitting tool to minimize S [98]. A sample b-spline fitting for electron temperature is shown below in Figure 47.

Both electron temperature and electron density profile fitting is done by the same routine as they are similar in structure and are both usually measured the Thompson Scattering diagnostic in Alcator C-Mod. For electron temperature, a second diagnostic, the electron cyclotron emission (ECE) is also used. The fitting tools available at MIT PSFC are fiTS

[73], quickfits [76], basic fitting routines, and Gaussian process regression (GPR) [74]. Each tool has its own advantages and disadvantages in different situations.

fiTS is an IDL-fitting tool for electron temperature and density measurements using least squares data fit and gives the user control over many of the fitting parameters and ability to customize the fit. The tool divides up each profile into three regions: core region, intermediate region, and the edge region. In the core region, the b-spline method is used, the polynomial or tanh [75] method is used for the edge region, and cubic interpolation is used in the zone between the core and edge region, labelled the intermediate region. By allowing the user to modify many of the fitting parameters and constantly change the fit, the "best" profile fitting is guaranteed. However, the definition of "best" is ambiguous in terms of profile fitting as too much user customization can allow for user bias and can lead overfitting the fit to the profile to simply minimize S without extracting any useful information about the underlying physics. Also, one of the seemingly major advantages for fiTS, its ability to allow user customization and interfacing, is actually a disadvantage when creating an automated analysis workflow for analyzing a large number of shots.

Quickfits [76], developed by Yunxing Ma, addresses these concerns by fitting electron density and temperature profiles automatically and quickly (within 1~2 seconds), which is critical when the analysis stream must process over a hundred shots without the constant user input and evaluation. The tool utilizes a polynomial fitting at the core and tanh fitting at the edge. Additionally, quickfits allows inputs for the time interval rather than analyzing the entire shot, as in fiTS, which is essential when fitting data points for pre-reversal and post-reversal halves of each shot. Quickfits also uses a Monte Carlo error analysis method to estimate the error on both the fit and gradient.

The term "basic fitting routines" refers to the generic fitting routines already incorporated into the code, such as or polynomial fitting or basic b-spline fitting available in IDL via bspline_iterfit. These routines are the simplest choice but offer little to no option to customize fits and may lead to low accuracy. Additionally, these routines in IDL do not have error analysis features and must be added separately.

GPR is a new fitting tool in Python developed by Mark Chilenski at MIT PSFC and is unlike traditional least squares fitting. Using a nonparametric regression technique, the tool attempts to eliminate user bias and overfitting, which are common problems when attempting to estimate the density and temperature gradients with any of the first three tools. At its most basic form, GPR focuses on a specific point and assumes that nearby points are more strongly correlated than those farther away rather than assuming an equal weighting for all data points. By doing so, an objective of the tool is to provide an additional level of statistical rigor in an automated form. Because GPR has the potential to reduce user errors in gradient estimates, it could be very attractive when performing linear stability analysis, which is highly sensitive to the density and temperature gradients [77].

For ion temperature and rotational velocity profile fitting, basic IDL fitting routines or the HIREXSR b-spline fitting routine is used, created by Matt Reinke at MIT PSFC and a brief overview can be found in the C-Mod Wiki. In contrast to a majority of temperature and density profiles, which are peaked profiles and monotonically decreasing, rotation velocity profiles can have widely varying shapes as shown in Fig. 10 in Chapter 1 of this thesis depending on direction of the intrinsic rotation and various other factors. No specific routine or tool is used at MIT PSFC for rotation fitting, so this is performed completely separately from temperature and density fitting, which simply requires using one of the pre-

made tools available. The lack of both a consistent profile shape and a tool that accurate fits it makes rotation velocity fitting a significant issue of this current method for studying intrinsic rotation.

Because profile fitting can result in large errors, estimating the error of fits is a critical area as they are used as inputs for other analysis routines. However, many fitting tools work by minimizing the fitting error but do not actually estimate this value. These errors tend to be roughly estimated rather than calculated. The importance of error analysis will be stressed and explained in future sections. After the fitting step, the methods in which this data is stored vary depending on the routines used. Two options that are primarily used are to store the profiles and data in the C-Mod database through MDS-plus and to create save files in IDL that can be reopened when needed. Again, the choice depends on user preference and purpose.

A.1.3 Running TRANSP (Step 3)

TRANSP is a time-dependent transport analysis code developed at the Princeton Plasma Physics Laboratory used to simulate confinement and heating in tokamak geometries and is used to create the input data required for gyrokinetic simulations [78]. By taking the inputs and various control variables, TRANSP can simulate how the plasma behaves in time via the hundreds of scalar and profile variables that evolve throughout the shot. Documentation on the underlying physics of tokamak transport and how the code is used is provided in the TRANSP PPPL site and manuals. Because TRANSP is entirely maintained by PPPL to access and use the code, the user needs preTransp to prime the experimental data for the routine and choose certain control parameters. Then PostTransp and MultiGraph must be used , to manage each TRANSP run and to view its outputs. Due to these tools and how the routine is structured and accessed, TRANSP runs for each shot must be handled separately and managed to ensure accurate results. For linear stability analysis in this study, TRANSP is not required as the fitted profiles and various parameters extracted from the first two steps are adequate inputs for GYRO. Therefore, it will be assumed that the typical user will not use TRANSP for performing linear stability analysis on rotation reversal shots at Alcator C-Mod.

A.1.4 Running GYRO (Step 4)

GYRO, the gyrokinetic-Maxwell solver developed at General Atomics, is used to perform linear gyrokinetic stability analysis, which provides the frequency and growth rates of the dominant turbulent mode of the plasma. These two parameters allow the user to determine whether the dominant turbulent mode is TEM or ITG as well as how quickly it is growing. Because how the TEM/ITG transition correlates with rotation reversals is a key focus of this thesis, it is essential to perform linear stability analysis on a large number of reversal shots to test the first hypothesis in this field of research. Because GYRO and linear stability analysis as a whole will be covered in-depth in Section A.2, this section will focus primarily on how GYRO is traditionally run for linear stability analysis.

After fitting, the necessary data is extracted from the database or save files, written into input files, and sent to GYRO, which will be run on Loki , a 520 core cluster at MIT PSFC. profiles_gen.pro is the GYRO preprocessor that performs these tasks, which extracts data written by TRANSP. Another routine, find_stability.pro, can also be used, which reads data written into the C-Mod data tree and writes the GYRO input files. Once submitted, each GYRO run is expected to take anywhere from 1 to 10 minutes but can take much longer. A possible cause of a long run time is a discharge being very close to both ITG and TEM modes for a large fraction of the wave numbers. In this situation, GYRO must run until one modes dies off and the dominant turbulence regime can be determined, which may take a long time. Therefore, by slightly modifying the gradient inputs or increasing the time skips, the run can be performed quicker, but the effects of these changes on the accuracy of the results must also be considered. Once the run is complete, the code will output the real frequency ω and growth rate γ as functions of the wave number $k_\vartheta\rho$ and save the data into the corresponding shot data tree. The GYRO outputs for a shot with sensitivity analysis through varying the ion temperature gradient $\pm 20\%$ is shown in Figure 48.

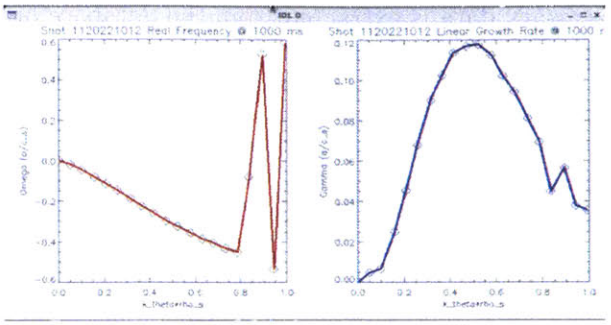

a)

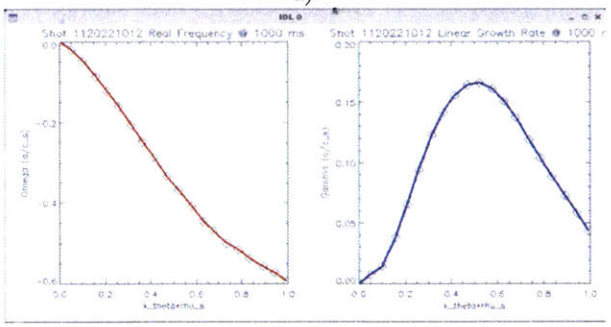

b)

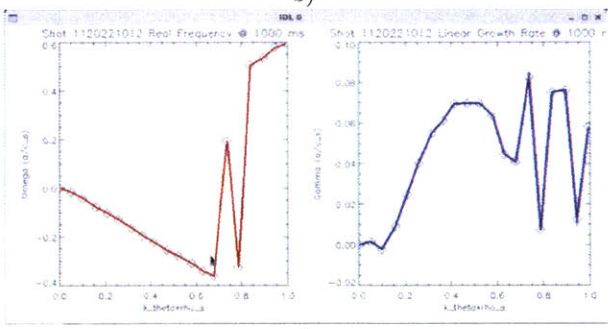

c)

Figure 48: Real frequency and growth rates of dominant turbulent mode for rho = 0.5 for (a) no modification, (b) ion temperature gradient increased by 20%, and)c) ion temperature gradient reduced by 20% using GYRO.

The plots on the left show the real frequency of the turbulence for various wave numbers at r/a = 0.5. Real frequencies < 0 represent the ITG-dominated regime and frequencies $>$ 0 represent the TEM-dominated regime. Therefore, from Fig. 48a, it can be seen that this plasma is ITG-dominated for the most part except toward high wave numbers around 0.8. These sudden changes can occur because the TEM mode is slightly more dominant than the ITG mode for that specific wave number, as explained earlier. However, because ion temperature measurements have significant errors of approximately 20%, sensitivity analysis is required to get a more complete view of the gyrokinetic results. Consequently, Fig. 48b shows a completely ITG-dominated plasma with a 20% increased in the ion temperature gradient, which is expected as the ITG-mode dominates with a more peaked ion temperature

profile [79]. With a reduction in the ion temperature gradient by 20%, the TEM mode appears to be dominant for a larger fraction of the wave number, as expected. GYRO can also be used for a myriad of other purposes i.e. for non-linear gyrokinetic simulations and the code will be explained in greater detail in Section A.2.

A.1.5 Areas of Improvement

The current method explained above is essentially a long chain of processes that must be performed sequentially by the user and is sub-optimal for this study for a variety of reasons. These reasons, which are potential areas of improvement, can be divided into those related to the entire process itself and those related to specific steps within the process. By identifying the reasons and issues, the changes made to create the analysis workflow that is heavily used in this thesis is better understood.

The entire process, a vertical of separate routines, is structured to allow for a user to analyze one shot from start to finish. Historically, most studies on identifying intrinsic rotation/reversal dependencies have only performed linear stability analysis on a handful of shots. Although that may be desired by many users that want to look at a small number of shots or study each shot in detail at each step, the goal of this thesis is to analyze tens to hundreds of C-Mod rotation reversal shots. This large sample size may reduce the effect of errors and provides a fuller picture of possible trends and correlations. Therefore, the process must be streamlined into one robust routine that takes a large number of shot numbers as an input and outputs the linear stability results, parameters, and other important variables. Also, these inputs and outputs must be organized in a way such that the user can easily manipulate and use them for further analysis. However, the current process does not offer the necessary intermediary processes to carry the large volume of shots to and from each routine or a structured method of organizing and storing the data through each step. Additionally, the variety of options for analyzing and fitting data present the risk that different tools are used to fit profiles for various shots. The lack of uniformity in shot analysis can render the end result useless when observing the outputs of many shots. These issues have driven the need for an analysis workflow that connects all of the necessary routines and provides the logistical structure required to analyze large data sets. The workflow precludes the user from constantly micro-managing the data and frees him/her from the inefficiencies related to manually working through the current process.

A key problem with the current method lies within the profile fitting step. Profile fitting is a critical step in the current process that poses two potential issues - overfitting risk and lack of error analysis. Various fitting tools require varying degrees of assumptions and decisions to be made by the user. For example, quickfits requires the user to specify the order of the splines and a range of splines to fit a certain profile and fiTS actually allows users to manually move and modify the fit. Although more areas of control for profile fitting may seem advantageous, there is the risk of overfitting, in which the fit is matches the data too perfectly and actually may negatively affect analysis to reveal the underlying physics. Because each data point of temperature, density, and velocity actually represents a range possible values due to measurement and data processing errors, matching a profile fit to every single point can distort the actual pattern the user is seeking.

In addition to effectively minimizing the error, calculating it is just as important. Error

analysis, which is used to calculate the fitting error, is not available for the data tools listed except for quickfits and HIREXSR b-spline. Although a fitting tool may not be accurate for some shots, calculating the fitting error of the profile provides transparency into the process. This allows the user to quantify fitting errors due to both the tool and measurement errors, which is valuable when comparing a large number of results. Additionally, because the gradients of these parameters are important inputs for linear stability analysis, the fitting error is necessary to study how much results can vary within the experimental and analysis errors resulting from this current process. Error analysis is especially important for ion temperature and toroidal rotational velocity, which can be susceptible to 20-30% experimental errors from HIREXSR. Such significant measurement errors emphasizes the need for mitigating overfitting risk and for proper error analysis.

All of these issues are motivations for the analysis workflow created to autonomously process and analyze a large number of shots to output various variables required to test the three hypotheses. The modifications made and routines created to create the workflow and to resolve the issues stated in this section will be covered in detail in Sections A.3 and A.4. However, before one can appreciate the changes made to the current process of routines that makes the workflow novel, GYRO, the tool used for linear stability analysis must be explained more in detail. How this code works and how it fits into the analysis workflow is essential in understanding the specific changes and improvements made to the current process.

A.2 GYRO

Nonlinear gyrokinetic theory is currently the most advanced and accurate theory for describing plasma turbulence [83, 88]. Because turbulence controls the momentum and energy transport in magnetically confined plasmas, such as the ones in tokamaks, gyrokinetic simulations are valuable in studying plasma behavior [81]. GYRO, a Eulerian gyrokinetic-Maxwell solver, is used to model turbulent transport in fusion plasmas and is frequently used at PSFC. [80]. GYRO validation has been extensive in comparing simulations with measurements of turbulent fluctuations[18, 19, 77, 79]. In this thesis, one hypothesis suggests that the dominant turbulent mode (ITG/TEM) is connected to rotation reversals. Therefore, GYRO is used to perform linear stability analysis, which identifies the dominant turbulent mode, or the fast growing mode,, for many shots to test this hypothesis.

Because GYRO is a key component of both the analysis workflow and the physics required to answer the questions in this thesis, various modifications to the traditional process were made primarily to optimize the way the user utilizes GYRO and extracts as much information from the simulations as possible. Therefore, to understand exactly what changes were made and how these are improvements to the current system, one must first have a general grasp of what GYRO does , how it works, and issues and/or possible areas of improvements. By understanding GYRO's abilities and limitations, one can more easily see the rationale behind the the analysis workflow's design as well as gain a basic understanding of gyrokinetic theory. Therefore, this section aims to provide the backdrop necessary to understand GYRO, gyrokinetic simulations, and the analysis workflow.

A.2.1 Background

GYRO is an Eulerian solver of the gyrokinetic-Maxwell equations, which model the bulk plasma behavior and more importantly, plasma turbulence. Developed at General Atomics by Jeff Candy and Ronald E. Waltz and first introduced in 2002, GYRO was created as an attempt to utilize the numerical methods used in two predecessor nonlinear gyrokinetic solvers gks and gs2 for a wider array of geometries and to test various methods of optimizing the solver. With the ability to perform simulations with plasma equilibrium, electromagnetic effects, and rotation and E x B shearing effects, GYRO can be useful for in modeling intrinsic rotation and reversals, which may be partly driven by these effects [80]

Gyrokinetic theory is based on the simplifications made to the six dimensional Vlasov (or Fokker-Planck) equations for ions and electrons that describe plasma turbulence behavior in time. Rather than tracking all particle motion for each species, the Vlasov equations describe collective behavior by characterizing the plasma as a distribution function of particles in evolving phase space rather than a group of individual particles. The Vlasov equation, also called the collisionless Boltzmann equation, is expressed as

$$\frac{dF}{dt} \equiv \frac{\partial F}{\partial t} + \mathbf{v} \cdot \frac{\partial F}{\partial \mathbf{x}} + \frac{q}{m}\left(\mathbf{E} + \frac{1}{c}\mathbf{v} \times \mathbf{B}\right) \cdot \frac{\partial F}{\partial \mathbf{v}} = 0 \tag{10}$$

where F(**x**,**v**,t) is the distribution function in 6 dimensional phase space of space and velocity, x is the spatial coordinate, t is time, **v** is the velocity, $\mathbf{E} = -\nabla\phi$is the electric field vector , c is the speed of light, and **B** is the magnetic field.

Even with this distribution function assumption, this six dimensional kinetic problem is incredibly difficult to solve and provides a large number of difficulties in both plasma theory and computational methods that seek to create methods to solve the equations efficiently . One major simplification that can be made is to ignore the fastest time scale phenomenon - the cyclical gyrations each particle exhibits due to the presence of a magnetic field. The plasma can effectively be treated as a collection of particles, exhibiting numerous behaviors and characteristics throughout a range of time scales of microseconds to seconds. To study low frequency plasma turbulence such as ITG and TEM, the fastest phenomenon in the plasma, which occurs at the cyclotron frequencies of the particles, can be removed to simplify the equations [80, 81]. However, many instabilities actually depend on finite gyroradius effects such that the gyrations cannot simply be eliminated from the equations . Fortunately, both conditions can be achieved by a guiding-center transform and gyro-averaging, in which the cyclical gyrations of each particle is ignored and each particle is simply treated as a ring of distributed charge centered at the center of its gyrations, known as its guiding center. This precludes the need for tracking the particles in their repetitive cyclical motions yet maintains the particles' gyroradius effects on turbulence in the lowest order. If the time scales of the turbulence of interest are much longer than that of the gyrofrequency and the gyroradius is small compared to the unperturbed scale lengths in the plasma, this method simplifies the equations while preserving kinetic and gyroradius effects, as desired. These scaling assumptions made in gyrokinetic theory are more explicitly expressed as

$$k_\perp \rho_i \sim 1$$

$$\frac{\omega}{\Omega} \sim \frac{\rho_s}{L_n} \sim k_{\|}\rho_i \sim \frac{e\phi}{T_e} \sim \frac{\delta B}{B_0} \sim O(\epsilon)$$

where ω is the characteristic frequency of the microturbulence, $\Omega_s = \frac{e_s B_0}{m_s c}$is the cyclotron frequency of species s, $\rho_s = \frac{v_\perp}{\Omega_s}$is the Larmor radius for specie s, $L_n = \mid \nabla ln n_0 \mid^{-1}$is a characteristic scale length of the density, $k_{\|}$is the parallel wavenumber, $k_\perp$i is the perpendicular wavenumber φ is the electrostatic potential, and δB is the first order magnetic field perturbation. Therefore, the gyrokinetic ordering assumes a microturbulence that are much slower than the cyclotron gyrations, a gyroradius much smaller than the density scale lengths, long wavelength turbulence relative to the gyroradius, negligible electrostatic potential, and small magnetic field perturbations. This scaling has been shown to be ideal for modeling turbulence [82, 83].

By performing the guiding-center transform, the new spatial coordinates $\mathbf{R}$ are of the form

$$\mathbf{R} = \mathbf{r} - \mathbf{b} \times \frac{\mathbf{v}_\perp}{\mathbf{\Omega_s}} \tag{11}$$

where, $\mathbf{r}$ is the position of the particle, $\mathbf{b} = \frac{\mathbf{B_0}}{B_0}$ is the unit vector of the magnetic field and $\mathbf{v}_\perp$ is the parallel component of the velocity calculated by

$$\mathbf{v}_\perp = v_\perp(cos\varphi\hat{e_1} + sin\varphi\hat{e_2}) \tag{12}$$

where $\hat{e}_1$and $\hat{e}_2$are the two unit vectors perpendicular to the magnetic field unit vector $\hat{\mathbf{b}} = \mathbf{B}_0/B_0 = \hat{e}_1 \times \hat{e}_2$ and $\varphi$is the gyrophase. The gyrations are effectively subtracted from $\mathbf{r}$ to yield a coordinate system only focusing on the guiding center. Therefore, rather than tracking each particle as it moves slowly in space, rapidly gyrating perpendicular to the magnetic field, the equation simply treats the particle's position as indicated by its guiding center and effectively blurs out its rapid gyrations through separating these fast dependent components and gyro-averaging them. Derivations of both nonlinear and linear gyrokinetic equations are well documented and can be found in the literature [82, 83, 84, 85, 86, 87, 88].

By dividing the distribution function F into two components where $F = f + \varepsilon g(\varphi)$ where f is independent of the gyrophase, we have the equation

$$\left\{\frac{\partial f}{\partial t} + (U\hat{\mathbf{b}} + \frac{c\mathbf{E}\times\hat{\mathbf{b}}}{B}) \cdot \frac{\partial f}{\partial \mathbf{R}} + \frac{q}{m}\mathbf{E}\cdot\hat{\mathbf{b}}\frac{\partial f}{\partial U}\right\}_1 + \left\{\mathbf{v}\cdot(\frac{\partial p}{\partial x}\cdot\frac{\partial f}{\partial \mathbf{R}} + \frac{\partial \mu}{\partial x}\frac{\partial f}{\partial \mu} + \frac{\partial U}{\partial x}\frac{\partial f}{\partial U})\right\}_2$$
$$- \left\{\Omega\frac{\partial}{\partial\varphi}(g - \frac{q\Phi}{mB}\frac{\partial f}{\partial \mu})\right\}_3 = 0 \tag{13}$$

where $\mu \equiv \frac{v_\perp^2}{2B}\left(1 - \frac{mc}{e}\frac{U}{b}\hat{\mathbf{b}}\cdot\nabla\times\hat{\mathbf{b}}\right)$ is the magnetic moment, R is the spatial location in guiding center coordinates given by Equation 2, $\hat{\mathbf{b}}$ is the magnetic field unit vector, x is spatial

coordinate of the particle, m is the mass of the particle, Φis the magnetic potential related to the electrostatic field by $\mathbf{E} = -\nabla\mathbf{\Phi}$,and U is parallel velocity component. The equation can be broken into three components, each demarcated by brackets. The first set represent the drift-kinetic-like terms, the second represent the toroidal geometry terms for the tokamak, and the third represent the fast gyromotion terms. By performing a gyro-average of all of the terms across the gyrophase, the equation can be simplified into a compact form of the gyrokinetic Vlasov equation given by

$$\frac{Df}{Dt} \equiv \frac{\partial f}{\partial t} + \frac{d\mathbf{R}}{dt} \cdot \frac{\partial f}{\partial \mathbf{R}} + \frac{dU}{dt}\frac{\partial f}{\partial U} = 0 \tag{14}$$

where the spatial evolution of the guiding center is governed by

$$\frac{d\mathbf{R}}{dt} = U\hat{\mathbf{b}} + \frac{c}{B}\bar{\mathbf{E}} \times \hat{\mathbf{b}} + \hat{\mathbf{b}} \times \left[\frac{U^2}{\Omega}(\hat{\mathbf{b}} \cdot \frac{\partial}{\partial \mathbf{R}})\hat{\mathbf{b}} + \frac{v_\perp^2}{2\Omega}\frac{\partial lnB}{\partial \mathbf{R}}\right]$$

and the parallel velocity evolution is expressed as

$$\frac{dU}{dt} = \left(\frac{q}{m}\bar{\mathbf{E}} - \frac{v_\perp^2}{2\Omega}\frac{\partial lnB}{\partial \mathbf{R}}\right) \cdot \left[\hat{\mathbf{b}} + \frac{U}{\Omega}\hat{\mathbf{b}} \times \left(\hat{\mathbf{b}} \cdot \frac{\partial}{\partial \mathbf{R}}\right)\hat{\mathbf{b}}\right]$$

where $\bar{\mathbf{E}}(\mathbf{R}) \equiv \oint \mathbf{E}(\mathbf{x})d\varphi/2\pi$is the electrostatic field averaged across the gyrophase of 2π. This expression tracks how the plasma distribution function for each species evolves in phase space. With the equation set to zero assuming no collisionality and is self-contained in terms of energy, particle number, and momentum, the equation can be seen as forcing the balancing of the development of the particle distributions in time (1st term) with the orbits and rotations the particles undergo in the magnetic field (2nd and 3rd terms). Therefore, although seeming like a simple equation, Equation 5 is actually a combination of numerous ordinary differential equations that are coupled together to accurately account for the many different phenomena that occur in the plasma. Turbulence is modeled using this equation by introducing small perturbations into the system by expanding the distribution function $f = f_0 + f_1 + \bar{f}_2 + ...$ where the first term represents the steady-state or equilibrium distribution function and the others correspond to the various perturbations.

The key nonlinear term is given by $\frac{d\mathbf{R}}{dt}$ which describes how the guiding center develops in time and is determined by the parallel motion and perpendicular drift motion associated with plasma perturbations as well as the curvature and gradient of the magnetic field [81] Therefore, this term takes into account the coupling of multiple unstable modes that introduce various drift motions as well as self-generated turbulence suppression. The guiding center transformation changes the Vlasov equation into a 5D gyro-kinetic equation, which still presents a significant challenge to solve, especially for complex geometries and conditions, but is much less burdensome to solve and can be handled by currently viable computational methods.

To account for the effects of particle charge and current density as well as the electric and magnetic field perturbations, the gyrokinetic equation is coupled to Maxwell's equations to

produce the gyrokinetic-Maxwell (GKM) equations [81]. TAs a result, the particle in gyro-center coordinates are effectively evolved in time through the gyrokinetic Vlasov equation and the resulting fields from this movement are accounted for by Maxwell's equations, most notably Poisson's equation that accounts for the spatially evolving electric fields.

Specific modifications must be made to the equations for specific geometries and situations, for example, rather than an isolated space, tokamak plasmas must be treated as surrounded by a number of sources and sinks. Nonetheless, the GKM equations have become the standard kinetic model for studying micro-turbulence in the plasma core of tokamaks and solving them computationally has driven the creation of many gyrokinetic solvers, such as GTC [81, 89], GT3D [90, 91], GS2 [92], GKW [93], and GYRO.

Because GYRO is a δf code, it divides the distribution function into equilibrium, f_0,and perturbed δf components, as explained above. Then numerical methods are utilized to develop the perturbed electron and ion distribution functions in time until a steady-state or pseudo-steady-state solution is reached. GYRO uses the Eulerian method to solve the GKM equations, one of the three classes of numerical methods used to solve GKM equations with the other two being the Lagrangian and semi-Lagrangian methods [81]. The Eulerian approach discretizes the phase space on a fixed grid and applies finite differences, finite volume, and/or Fourier transforms for the differential and integral operators. Once the values of the distribution function f at grid points of the phase space are calculated for the next time step, the field equations are solved and applied to the phase space. This method is repeated until the solution is found. The exact computational methods used in GYRO is explained in-depth in the original paper written by the developers [80]. A clear diagram of this solver method is present in literature and shown in Figure 49.

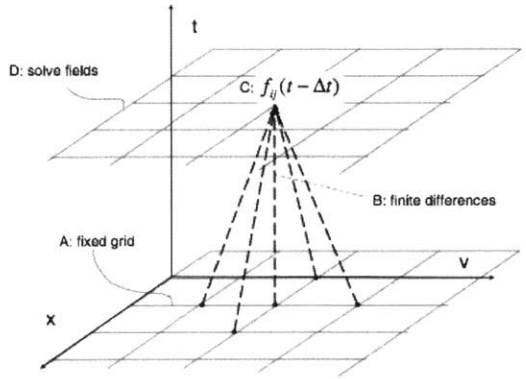

Figure 49: In Eulerian methods, a fixed grid is defined in phase (A). Finite difference are used (B) in order to obtain the value of f at grid points at the next time step (C). Field equations are then solved (D) after integration over velocity space [81].

Conversely, the Lagrangian method, widely known as the particle-in-cell (PIC) method, uses markers, which are super-particles that account for a large number of actual particles in the plasma. These markers are placed in phase space pseudo-randomly. Then, these markers are evolved in time or "pushed" through phase space by the gyrokinetic Vlasov equation to the next time step. Then accounting for the marker movements, the charge, fields, and

current perturbations are projected onto real space. Lastly, the field equations are solved to alter the fields in real space accordingly. Then, the markers are pushed again in phase space with respect to the sightly altered fields. This process is repeatedly iteratively until a solution is reached. Rather than focusing on a phase space grid and how the distribution function and fields evolve at grid points via the Eulerian method, the PIC approach follows the markers that represent particles, altering the background of field, charge, and current perturbations accordingly, that in turn, affects the markers. A simplified diagram of the PIC method is also found in literature shown below in Figure 50.

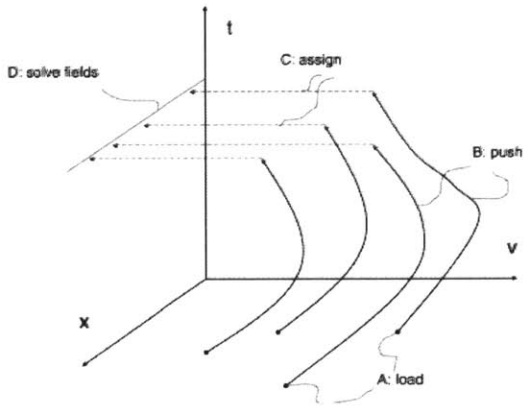

Figure 50: In Lagrangian-PIC methods, marker initial positions are loaded pseudo- (or quasi-) randomly in phase space (A). Markers are evolved along their orbits (B). Charge and current perturbations are assigned (projected) to real space (C). Field equations are solved (D) [81].

The GYRO inputs that are important in the GKM equations for modeling low-frequency turbulence are those that are the primary drivers of the underlying physics - momentum and energy transport and particle orbits that describe the flow and entrapping of particles in the plasma. Table 8 below shows a list of the basic units and parameters used as inputs for GYRO and values corresponding to linear GKM simulations at C-Mod. One can correctly guess that physical global parameters such as the magnetic field (B), device size (R and a), particle temperatures ($T_e$and T_i), densities ($n_e$and n_i), magnetic field geometry ($\varkappa$, β, q), and current (I_p) play important roles in determining how the plasma behaves. Another set of important inputs are the temperature and density gradients, which drive the energy and particle fluxes within the plasma, respectively. These fluxes, which can vary significantly throughout the plasma, are essential in how the particle distribution functions develop in space and velocity. As a result, these gradients are a critical aspect of GYRO simulations. Rather than as spatial gradients, these quantities are frequently expressed in terms of the normalized gradient scale lengths $\frac{a}{L_X}$, where a is the minor radius of the device and $L_X = -\frac{X}{\nabla X}$. These temperature and density gradient normalized scale lengths are calculated by fitting their spatial profiles, which are performed by the various tools mentioned in Section A.1.

GYRO and similar codes require a large number of inputs to solve the gyrokinetic equations. One fundamental component of gyrokinetic equations in the context of tokamak plasmas is the geometry of the magnetic field configuration in which these equations are

solved in. The flux surfaces of the tokamak plasma, the size,shape, and boundary conditions of the plasma domain, and the coordinate system used by GYRO are important aspects of the code that must be determined before the simulation can be run.

A.2.2 GYRO Geometry

As opposed to modeling turbulence in a neutral fluid, for magnetic confined plasmas, the basic geometry of the magnetic field configuration plays an important role in gyrokinetic simulations. The field configuration creates the confinement of the plasma and introduces strong anisotropies of the low frequency perturbations that are of interest. Additionally, these anisotropies actually can be taken advantage of to improve the performance of numerical methods. The role of geometry and how it comes into play in GYRO will be explained in this section.

GYRO uses a right-handed (positively oriented), field-aligned coordinate system to refer to its flux surfaces and flux coordinates. The magnetic field and flux surface are related using the Clebsch field representation given by

$$B = \nabla\alpha \times \nabla\psi(r)$$

where $\alpha = \varphi + \nu(r,\theta)$is the Clebsch angle and $\psi(r)$ is the poloidal flux divided by 2π. $\varphi$is the toroidal angle, θ is the poloidal angle, which increases moving counterclockwise along the flux-surface, and ν is the magnetic field stream function, a variable used to map the magnetic field in space [94]. A flux surface S with normal $\vec{n}$ is a smooth surface in which the magnetic field $\vec{B}$ does not cross it anywhere, such that $\vec{B} \cdot \vec{n} = 0$. A diagram of a magnetic flux surface is shown below in Figure 51. From the figure, it can be seen that the flux surface outlined in blue is set up as such so that no poloidal magnetic field that circles in the Z-R plane crosses it.

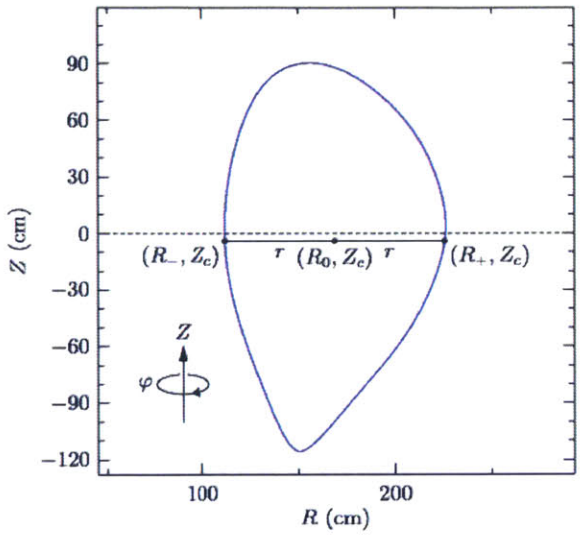

Figure 51: Diagram of flux surface in tokamak field geometry with the centroid coordinate marked with (R_0, Z_C).

The flux surface is representative of a flux surface seen in tokamak experiments. Rather than a perfect circle or symmetrical oval, a D-shaped magnetic configuration is used, as it has been experimentally tested to lead to the highest performance due to the magnetic shear resulting from the asymmetry that help break up turbulent eddies in the plasma. Instead of the (R, Z, φ)coordinate system that resembles that of Cartesian system with R as the x-axis and height Z as the y, GYRO uses the field aligned (r, θ, φ)coordinate system that resembles the polar coordinate system. r acts as the minor radius originating from the centroid (R_0, Z_C), the poloidal angleθrotates around the surface, and toroidal angle φrotates in and out of the page.

The generalized spatial coordinates, $r = \frac{R_+ - R_-}{2}$ and $R_0 = \frac{R_+ + R_-}{2}$ are calculated based on the coordinates (R_-, R_+) of the flux surface at the height $Z_C$of the centroid. The effective field strength $B_{unit}$of the flux surface is expressed as

$$B_{unit} = \frac{1}{r}\frac{d\chi_t}{dr}$$

where $\chi_t$is the toroidal flux divided by 2π, a rough equivalent if the flux surface were a perfect circle. The spatial grids expressed in both minor radius r and major radius R are assumed by GYRO to be on the plane at height Z_C. Additionally, all of the geometry parameters, such as triangularity, squareness, and elongation that will be mentioned in later sections are calculated form the centroid coordinate (R_0, Z_C) unless specified otherwise.

GYRO can use three types of equilibrium models for its magnetic configuration: circular equilibrium, shaped Grad-Shafranov (Miller-type) equilibrium, and general equilibrium (general geometry). The circular equilibrium model, is the simplest and assumes a symmetric, perfectly circular equilibrium where the flux surfaces are expressed as,

$$R(r,\theta) = R_0 + rcos\theta$$

$$Z(r,\theta) = rsin\theta$$

$$\nu(r,\theta) = -q(r)\theta$$

The second equilibrium model, the Grad-Shafranov, or Miller-type, model use flux surfaces that are local Grad-Shafranov equilibria. The Grad-Shafranov equilibria are flux surfaces that account for the Grad-Shafranov shift such that equilibrium is reached [94]. This shift is a result of two factors related with the toroidal and axisymmetric characteristics of tokamak plasmas and magnetohydrodynamic (MHD) equilibrium. Firstly, the cylinder of plasma bent into a torus, as in a tokamak, results in plasma expanding in the radially outward (increasing R) direction. In a perfect cylinder of plasma, the pressure is distributed about the axis symmetrically. However, in a torus, there is a larger amount of surface area on the outward radial, or outboard, side, such that assuming uniform pressure, the net force is larger in the outward radial direction. Secondly, anti-parallel currents repel each other. The poloidally rotating current in the plasma in the R-Z plane at a specific poloidal angle θrepels the opposite flowing current at $\theta + \pi$ due to the magnetic field running perpendicular to the current. As a result, this repulsive force, known as the Lorentz force, creates a force in the direction $J \times B$ which is in the radially outward from the center of the plasma. Because the magnetic field on the inboard side of the torus is stronger as the surface area is smaller, the repulsive $J \times B$ force onto the outboard side is greater than the force on the inboard side by the weaker outboard field. This creates a net force in the radially outward direction of increasing R. Both factors cause an outward expansion of the plasma in the outboard direction. To account for the asymmetry resulting from the toroidal configuration, a new equilibrium can be reached that results in the axis of the flux surfaces to be shifted radially outward. This results in a higher flux density on the radially outward side, thus increasing the magnetic pressure to combat these two effects. A diagram of the Shafranov shift is shown below in Figure 52.

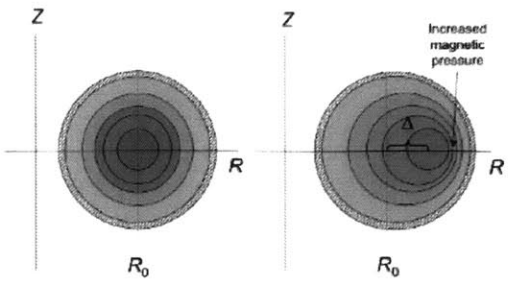

Figure 52: Sample magnetic flux diagram illustrating the outward Grad-Shafranov shift resulting from toroidal MHD equilibrium [Courtesy of University of Wisconsin-Madison Physics Department].

The Δ indicates the magnitude of the Grad-Shafranov shift to required to establish a new equilibrium of the magnetic configuration. As the flux surfaces are closer together on the outboard side of the plasma, the increased magnetic pressure balances with the net force outward to reach the Grad-Shafranov equilibria. Therefore, accounting for these effects, the Grad-Shafranov equilibrium model is expressed as

$$R(r,\theta) = R_0(r) + rcos(\theta + arcsin[\delta(r)]sin\theta)$$

$$Z(r,\theta) = Z_0(r) + \kappa(r)rsin(\theta + \varsigma(r)sin2\theta)$$

where $\delta$is the triangularity of the plasma, κ is the plasma elongation, and ς is the plasma squareness. $\nu(r,\theta)$is computed numerically by the Grad-Shafranov solver. It can be seen how the degree of the Grad-Shafranov shift depends on the shape of the plasma, as expected.

The third equilibrium model assumes a general equilibrium that allows the user to customize the magnetic configuration. The flux-surface shape is governed by an expansion of these two expressions

$$R(r,\theta) = \frac{a_0^R(r)}{2} + \sum_{n=1}^{N}\left[a_n^R(r)cos(n\theta) + b_n^R(r)sin(n\theta)\right]$$

$$Z(r,\theta) = \frac{a_0^Z(r)}{2} + \sum_{n=1}^{N}\left[a_n^Z(r)cos(n\theta) + b_n^Z(r)sin(n\theta)\right]$$

where $\theta = 0$ is the poloidal angle that refers to the rightmost (outboard) point of the flux-surface and N is the value of the order of expansion the user desires for the magnetic flux shape which is set to 16 by default. $\nu(r,\theta)$is also computed numerically.

Another aspect of geometry in GYRO deals with the numerical methods and area of interest of gyrokinetic solvers. GYRO performs two types of simulations: flux-tube and global. As low frequency perturbations exhibit strong anisotropy in tokamak plasmas due to the magnetic configuration, geometry strong affects microinstabilities and turbulence of interest. The long wavelength perturbations parallel to the field lines $\left(k_\parallel\rho_s \sim \rho_* \ll 1\right)$and short perpendicular wavelength perturbations on the scale lengths of the Larmor radius can be taken advantage of in numerically solving the gyrokinetic equations. By using field-aligned coordinates, the solving speed of gyrokinetic solvers are improved by an order of magnitude by focusing on the long wavelength perturbations of interest close to the field lines [81]. The flux-tube code takes this approach one step further by focusing only on the areas in the vicinity of a field line, thus focusing only on a cylindrical tube of plasma surrounding a field line. By doing so, the code expands the GKM equations assuming that various coefficients, such as $f_0, \frac{\partial f_0}{\partial x}, T_{e,i}, \frac{dT_{e,i}}{dx}, \frac{dn_0}{dx}$ and all tensor elements such as q and s, magnetic shear, will remain constant. Therefore, no profile variations are allowed and the radial gradients are frozen. Because flux-tube simulations only look at a cylinder of plasma, its boundary conditions are specified to be radially periodic, which is only possible with

an infinite system size such that $\rho_\star = \frac{\rho_s}{a} \rightarrow 0$. These simulations offer a great amount of simplicity in solving the gyrokinetic equations but may be too simplified for some types of studies. For simulations that need to account for profile shearing, profile variation, or large scale relaxations, flux-tube simulations are not adequate as they assume frozen profiles.

In contrast to the narrow focus of flux-tube simulations, global simulations use the entire plasma as the domain without radial boundary conditions. Most notably, the profiles are allowed to vary self-consistently with the physics. Therefore, global codes can be used to study profile shearing, profile relaxation, and avalanche propagation [95]. Because these phenomena are not of particular interest for this study and speed is important, flux-tube simulations and periodic boundary conditions are used. This can be seen in Table 9 and the value for parameter BOUNDARY_METHOD, which determines whether the boundary conditions are periodic (1) or non-periodic (2).

Although the type of simulation that is used determines whether the profiles vary or remain constant during the simulation, GYRO has another parameter for deciding which type of profiles to use as inputs. The parameter RADIAL_PROFILE_METHOD not only selects which profiles to use but also determines the plasma equilibrium geometry. There are 6 types of methods in GYRO and they are (with the corresponding number):

1: flux-tube, s-α geometry
2: power-law
3 experimental
4: variable shear
5: flux-tube, Miller shaped geometry
6: GTC-style profiles

The three that are primary used are 1, 3, and 5. Method 1 corresponds to profile parameters taken from the default values in a GYRO input file input.gyro rather than experimental data. Additionally, this method uses the circular equilibrium model. Method 3 results in GYRO using input.profiles, another type of GYRO input file, to use the experimental profile data. If this method is chosen, the user can then decide whether to use a model geometry or the general geometry through choosing 0 or 1, respectively, for the NUM_EQUIL_FLAG parameter. For Method 5, the profile parameters are taken from default input.gyro parameters and the Grad-Shafranov, Miller-type, equilibrium model is used. Once the geometry is determined for a simulation, GYRO requires a large amount of input parameters ranging from physical parameters to control and output parameters with regard to the numerical scheme being used and the resolution of its simulations. Further explanation of the input.gyro and input.profiles files as well as the parameters used in GYRO is provided in Section A.2.3.

GYRO and other GKM solvers are used to study low-frequency plasma turbulence but exactly what outputs are generated can vary depending on the goals of the user. Although the GYRO simulates the development of plasma perturbations in time to observe how turbulence and various instabilities evolve, the user can also specify what type of turbulence and exactly what quantities are to be calculated. For this thesis, GYRO will be used to solve the linear GKM equation to study the development of microinstabilities, instabilities on scale lengths comparable to ion and electro gyroradii and much smaller than equilibrium scales [81]. They have been observed to be responsible for driving the anomalous transport of particles, momentum, and energy in tokamak plasmas. This type of simulation, also known

as linear stability analysis, focuses on ITG and TEM, also known as drift wave instabilities [62, 96].

A.2.3 Linear Stability Analysis

Solving the GKM equations, even with current numerical methods and computational power, is a very demanding and complex. Although non-linear GKM simulations are the most comprehensive, the process and optimization of solving them is still a relatively open problem in research [81]. Fortunately, linear stability analysis is a computationally inexpensive process of obtaining information about the dominant, or the most rapidly growing, turbulent modes at localized regions of the plasma. Although it does not account for nonlinear interactions between different modes or the saturation of the resulting turbulence that its nonlinear counterpart does, linear stability analysis does provide adequate information about the plasma turbulence to test one of the hypothesis presented in this thesis and is a good first step in studying the relation between rotation reversals and turbulent transport.

Linear stability analysis solves the linear components of the GKM equations to generate either general eigenvalue solutions or initial value solutions. If the proper initial conditions and parameters are provided, the initial value solutions provide the real frequency and growth rate of the most unstable linear mode vs. normalized wavenumber $k_\theta \rho_s$where $k_\theta = \frac{nq(r)}{r}$is the poloidal wave number of the turbulence where n is the toroidal mode number shown in Equation 10 and q is the safety factor as a function of r and $\rho_s = \frac{c_s}{\Omega_{ci}}$ is the ion-sound Larmor radius where $c_s$is the acoustic ion speed and $\Omega_{ci}$is the ion cyclotron frequency. Because these frequencies and growth rates are used to identify the dominant turbulent mode (TEM/ITG) for testing the first hypothesis and its relation to rotation reversals, the stability analysis will be used to generate initial value solutions. Using this method, GYRO solves the linear GKM equations. It treats the $f_0$component as the equilibrium portion and assumes the perturbed quantities to be of the form

$$\delta\phi_n(r,\theta,t) = \phi_n(r,\theta)e^{-i\omega t+\gamma t} \tag{15}$$

where n is the toroidal mode number, ω is the real frequency, and γ is the growth rate of the most unstable turbulent mode.

Once the user provides the specific rho, the square root of the normalized toroidal flux, corresponding to the spatial location within the tokamak and the necessary inputs, GYRO uses the Eulerian method to solve the linear GKM equations to generate the real frequency and growth rates of the most unstable modes at a range of wavelengths. Before this step, various GYRO input files must be created that determine how GYRO will be run, what solution is sought after, and what parameters and profiles to use.

GYRO has 4 types of input files:

1) input.gyro
2) input.profiles
3) input.profiles.geo
4) input.geo

input.gyro is the input file that must exist regardless of the type of gyrokinetic simulation being run as it stores many of the critical plasma parameters and GYRO specifications needed to run the simulations. The parameters included in the file can be grouped into 13 sections:

1) Plasma shape/geometry
2) Plasma profiles
3) Particle mass and charge
4) Numerical resolution
5) Control parameters
6) Rotation physics
7) Source and buffer parameters
8) Data output
9) HDF5 Data output
10) Gyrokinetic eigenvalue solver parameters
11) Field eigenvalue solver parameters
12) General geometry parameters
13) Experimental profile control parameters

However, because there are over 100 different parameters and many of them are not useful for linear stability analysis. For example, because experimental profiles are stored in input.profiles, many of the plasma profile parameters of the input.gyro file has default, standardized parameter profiles that are not be used. Additionally, some parameters regarding data output, source and buffer parameters, and eigenvalue solver parameters are either not used or do not provide the reader with any insight into GYRO. Therefore, it is not necessary to exhaustively list and explain every parameter. Nonetheless, Table 8 lists the major parameters of interest to the reader used as inputs in the input.gyro file. A complete alphabetical list of the parameters in this file can be found in the GYRO website (https://fusion.gat.com/theory/Gyroinput#Parameters).

Table 8: Incomplete list of parameters included in input.gyro input file for GYRO.

a) Plasma shape/geometry

input.gyro parameter	Interface parameter	Description	Default
ASPECT_RATIO $\left(\frac{R_0(r)}{a}\right)$	gyro_aspect_ratio_in	Normalized major radius	3.0
DELTA (δ)	gyro_delta_in	Triangularity measured at the radial box center	0.0
DZMAG $\left(\frac{\partial Z_0(r)}{\partial r}\right)$	gyro_dzmag_in	Gradient of elevation	0.0
KAPPA (κ)	gyro_kappa_in	Elongation measured at radial box center	1.0
RADIUS $\left(\frac{r_0}{a}\right)$	gyro_radius_in	Normalized minor radius	0.5
SAFETY_FACTOR $\left(q=\frac{rB_\phi}{RB_p}\right)$	gyro_safety_factor_in	Safety factor at center of radial simulation domain	2.0
SHEAR $\left(s=\frac{r}{q}\frac{\partial q}{\partial r}\right)$	gyro_shear_in	Magnetic shear at center of radial simulation domain	1.0
SHIFT $\left(\triangle=\frac{\partial R_0(r)}{\partial r}\right)$	gyro_shift_in	Shafranov shift at center of radial simulation domain	0.0
BTCCW	gyro_btccw_in	Orientation of the toroidal magnetic field B_ϕ relative to the toroidal angle φ	-1.0
IPCCW	gyro_ipccw_in	Orientation of the plasma current $I_p$relative to toroidal angle φ	-1.0
S_DELTA $\left(s_\delta=r\frac{\partial\delta}{\partial r}\right)$	gyro_s_delta_in	Triangularity shear at center of radial simulation domain	0.0
S_KAPPA $\left(s_\kappa=\frac{r}{\kappa}\frac{\partial\kappa}{\partial r}\right)$	gyro_s_kappa_in	Elongation shear at center of radial simulation domain	0.0
S_ZETA $\left(s_\varsigma=r\frac{\partial\varsigma}{\partial r}\right)$	gyro_s_zeta_in	Squareness shear at center of radial simulation domain	0.0
ZETA (ς)	gyro_zeta_in	Squareness	0.0
ZMAG $\left(\frac{Z_0(r)}{a}\right)$	gyro_zmag_in	Elevation of the flux surface	0.0

b) Plasma profiles

input.gyro parameter	Interface parameter	Description	Default
AMPERE_SCALE	gyro_ampere_scale_in	Electromagnetic scaling factor used in Ampere equation	1.0
BETAE_UNIT $\left(\beta_e=\frac{8\pi n_e T_e}{B^2_{unit}}\right)$	gyro_betae_unit_in	Electron beta at center of radial simulation domain	0.0
COLLISION_METHOD	gyro_collision_method_in	1: Traditional method. Incompatible with compressional perturbations 2: New scheme. Ignores field evolution. Compatible with compressional perturbations	2
LAMBDA_DEBYE $\left(\lambda_D=\sqrt{\frac{T_e}{4\pi n_e e^2}}\right)$	gyro_lambda_debye_in	Debye length at center of radial simulation domain	0.0
NU_EI (ν_{ee})	gyro_nu_ei_in	Electron-electron collision frequency with in electron and ion pitch-angle-scattering operators	0.0
NU_EI_SCALE	gyro_nu_ei_scale_in	Electron-ion collision frequency scale factor	1.0
NU_II_SCALE	gyro_nu_ii_scale_in	Ion-ion collision frequency scale factor	0.0
RHO_STAR$\left(\rho_\star=\frac{\rho_s}{a}\right)$	gyro_rho_star_in	Ion-sound gyroradius to minor radius at center of radial simulation domain	0.0025

c) Plasma mass and charge

input.gyro parameter	Interface parameter	Description	Default
MU $\left(\mu = \sqrt{\frac{m_D}{m_i}}\right)$	gyro_mu_in	Inverse root of main ion mass to deuterium mass	1.0
MU_ELECTRON $\left(\mu_e = \sqrt{\frac{m_D}{m_e}}\right)$	gyro_betae_unit_in	Inverse root of electron mass to deuterium mass	60.0
Z	gyro_collision_method_in	Main ion charge	1.0

d) Rotation Physics

input.gyro parameter	Interface parameter	Description	Default
DOPPLER_SCALE	gyro_doppler_scale_in	Doppler shearing rate scaling factor	1.0
GAMMA_E (γ_E)	gyro_gamma_e_in	Doppler shearing rate in units of c_s/a	0.0
MACH(M)	gyro_mach_in	Rotation speed	0.0
MACH_SCALE	gyro_mach_scale_in	Scale factor for Mach	1.0
PGAMMA (γ_p)	gyro_pgamma_in	Rotation (parallel velocity) shearing rate	0.0
PGAMMA_SCALE	gyro_pgamma_scale_in	Rotation shearing rate scaling factor	1.0
ROTATION_THEORY_METHOD	gyro_rotation_theory_method_in	Method of treating plasma rotation 1: Standard model $\gamma_E = -\frac{r}{q}\frac{\partial \omega_0}{\partial r}$ $\gamma_p = -R_0\frac{\partial \omega_0}{\partial r}$ $M = \frac{\omega_0 R_0}{c_s}$ 2: Waltz model $\gamma_E = -\frac{r}{q}\frac{\partial \omega_0}{\partial r}$ $\gamma_p = (BTCCW)R_0\frac{\partial}{\partial r}\left(\frac{U_\parallel}{R_0}\right)$ $M = \frac{v_\parallel}{c_s}$	1

As expected when solving an ordinary differential equation describing a time-evolving system, the inputs consist of the dimensions and physical parameters such as speed, mass, temperature, and density as well as the background magnetic field from the safety factor q. In addition to physical parameters, the input also have various theory method choices for profile analysis and rotation analysis. The default values correspond to the values that GYRO will use if left unspecified by the user.

The second type of input file input.profiles is only required when performing simulations with experimental profiles rather than assuming circular, monotonically decreasing profiles. Because these are critical for accurate linear stability analysis, this input file is used for GYRO simulations. Because the file contains the entire dataset of experimental profiles and has to default values, GYRO will halt if data is missing. The data can be grouped into 1 scalar block and 8 separate vector blocks. The vector blocks can loosely be grouped into: geometry and electron parameters (1,2), moments, flux, and power (3,4), ion density (5), ion temperature (6), ion toroidal rotation (7), and ion poloidal rotation (8). As vector blocks 5-8 only hold the profile data corresponding to the stated parameters, the data is from experimental data and self-explanatory in terms of their descriptions. For the scalar block and vector blocks 1-4, Table 9 below lists the various parameters included for input.profiles. If the general magnetic field geometry is desired and the simulations are based on experimental profiles, an input.profiles.geo input file is required. input.geo is used for general geometry simulations in local mode. More information about these input files can be found in the GYRO input website (https://fusion.gat.com/theory/Gyroinput).

Table 9: List of parameters included in input.profile input file for GYRO in the scalar block and vector blocks 1-4.

a) Scalar data

input.gyro parameter	Description
N_EXP	Number of experimental data gridpoints
BT_EXP (B_{ref})	Reference magnetic field (vacuum toroidal field)
ARHO_EXP ($\rho(a)$)	Parametrization function for the toroidal flux

b) Vector data, block 1

input.gyro parameter	Description
rho $\left(\hat{\rho} = \frac{\rho(r)}{\rho(a)}\right)$	Dimensionless areal variable
rmin (r)	Generalized minor radius
rmaj ($R_0(r)$)	Generalized major radius
q $\left(q = \frac{rB_\phi}{RB_p}\right)$	Safety factor
kappa(κ)	Plasma elongation

c) Vector data, block 2

input.gyro parameter	Description
delta(δ)	Plasma triangularity
te (T_e)	Electron temperature (keV)
ne (n_e)	Electron density ($10^{19}/m^3$)
z_eff (Z_{eff})	Effective ion charge
omega0 $\left(\omega_0 = \frac{cE_r}{RB_p}\right)$	Rotation frequency (rad/s)

d) Vector data, block 3

input.gyro parameter	Description
flow_mom	Total integrated angular momentum flow (torque) (Nm)
pow_e	Total integrated electron power (MW)
pow_i	Total integrated ion power (MW)
pow_ei	Integrated electron-ion energy exchange power (MW)
zeta (ς)	Plasma squareness

e) Vector data, block 4

input.gyro parameter	Description
flow_beam	Total integrated angular momentum flow (torque) (Nm)
zmag (Z_0)	Flux-surface elevation
ptot	Total plasma pressure (Pa)
polflx	Poloidal flux over 2π

Two values shown in Table 9a, BT_EXP and ARHO_EXP are essentially arbitrary values that are remnants from a previous version of the code. Therefore, the user should not pay too much attention as to the exact values assigned to these two parameters. Although Table 9 shows the default values of parameters in input.gyro, the user may specify parameter values that differ significantly. The actual values for the input.gyro input file created for this study will be listed in Table 13.

Using these two input files, input.gyro and input.profiles, linear stability analysis can be performed using GYRO. Plots of sample results from linear stability analysis are shown above in Figure 48. The real frequency plot indicates the dominant turbulent mode as $\omega > 0$ signifies modes rotating in the electron diamagnetic drift direction, indicative of TEM and $\omega > 0$ signifies modes rotating in the ion diamagnetic drift direction, indicative of ITG modes. The growth rates then be used to identify at the wavelengths in which these modes are the fastest growing and most unstable.

By identifying the drift direction of these unstable waves, the dominant turbulent mode can be identified. By performing linear stability analysis for co-current and counter-current rotation shots, the user can use the frequency and growth rates to test the hypothesis regarding the supposed connection between rotation reversals and the ITG/TEM transition. If the hypothesis is correct, the user should observe a clear bifurcation in which shots with co-current intrinsic rotation all have positive real frequencies and the counter-current rotation shots have negative real frequencies, indicating a clear transition from TEM to ITG along with a change in rotation direction.

A.2.4 Areas of Improvement

The two major concerns regarding GYRO and more specifically, linear stability analysis, involve the shot-by-shot process of the analysis and the lack of a sensitivity analysis option. To perform linear stability, the user must use an IDL routine to provide GYRO the proper inputs and conditions for each shot at one specific radial location. Therefore, if the user wanted to perform linear stability analysis at a range of spatial coordinates for one shot, many shots at one radial location, or a mix of the two, he/she would have to perform the analysis one by one, which is very time-consuming. For example, to analyze five shots at five radial locations each, the user would have to perform 25 individual linear stability analyses. Therefore, for analyzing at 5-10 radial locations for tens to hundreds of shots, the number of linear stability analysis runs that must be performed gets out of hand very quickly. One significant inefficiency is that even though a single C-Mod shot has the same global parameters and profiles, there is no system that allows a streamlined way of performing linear stability analysis for the shot at many radial locations using the same data. The user must input the data for each shot-radial location pairing. By creating a process that can iteratively perform linear stability and save the outputs would greatly simplify this step and make it possible for one user to analyze hundreds of shots at many radial locations.

Secondly, as stated previously, GKM equations are strongly dependent on the various temperature and density gradients. However, electron and ion temperature and electron density measurements can have significant experimental errors ranging from 3-5% to 10-20% for ion temperature measurements from HIREXSR. Inputs that are critical to GYRO with large inputs casts doubt on the accuracy of the linear stability analysis results. To exacerbate

the problem, the temperature and density gradients are estimated from profile fitting and then calculating the derivative at the specified radial location. This process can result in significant analysis errors that cannot be roughly estimated as the quality of the fits can vary widely. To remedy this problem, sensitivity analysis needs to be performed on the linear stability analysis for the main drivers of the GKM simulations in studying rotation reversals. This method creates transparency and reveals the effects of these errors on the stability analysis. However, GYRO does not have this capability and even if it did, there is currently no single routine that calculates the experimental and analysis errors of the various input parameters. Without the proper sensitivity analysis, the results of stability analysis cannot be fully trusted and how strongly each input parameter affects the results cannot be revealed.

A.3 Modified System - Database

The methodology of this study is divided into three steps, as listed in Section A.1:

1) Identifying and characterizing
2) Profile-fitting
3) Running GYRO

Because TRANSP is not used, as explained in Section A.1.3, the step is unnecessary and thus, removed. The structure of the analysis workflow is re-shown in Figure 53 below.

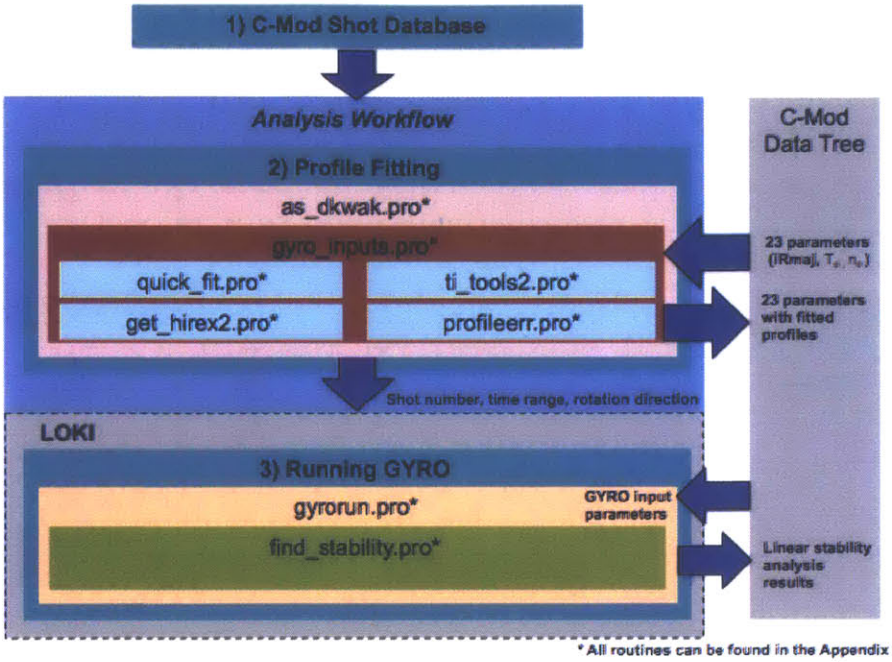

Figure 53: Diagram of the analysis workflow structure developed for this study including the IDL routines used.

This diagram shows how these steps are organized within the context of this study and what routines are used. To perform the various steps, a large number of Alcator C-Mod ohmic L-mode rotation reversal and intrinsic rotation shots are needed to form a database similar to the one used at ASDEX [12, 17]. However, traditionally, linear stability analysis and profile fitting is performed on a shot-by-shot basis on a handful of shots. In addition to the shot number, each shot needs to be characterized by the appropriate time range for analysis, the rotation direction, heating method, confinement regime, and any other material information required by the user in the analysis. To keep track of all of this information for a large number of shots, the thesis breaks from the status quo and uses a modified system via a database that contains all of this information throughout the analysis workflow.

The general process of identifying and characterizing a shot is described in Section A.1.1. For this thesis, the focus is on C-Mod shots with only ohmic heating and in the low-confinement regime displaying strong rotation reversals and intrinsic rotation [42]. The list of shots were provided by John Rice, Chi Gao, Anne White, and Choongki Sung at the MIT PSFC. Additional shots were also found in the literature from PSFC and all shots are listed in the Appendix C. To observe a shot's time trace, dwscope was used and seniormom.dat was used as the specific scope, which determines what diagnostic measurements and what processed data is shown in the display interface. Figure 54 below shows time traces of a sample shot (1120626027) using the seniormom.dat scope.

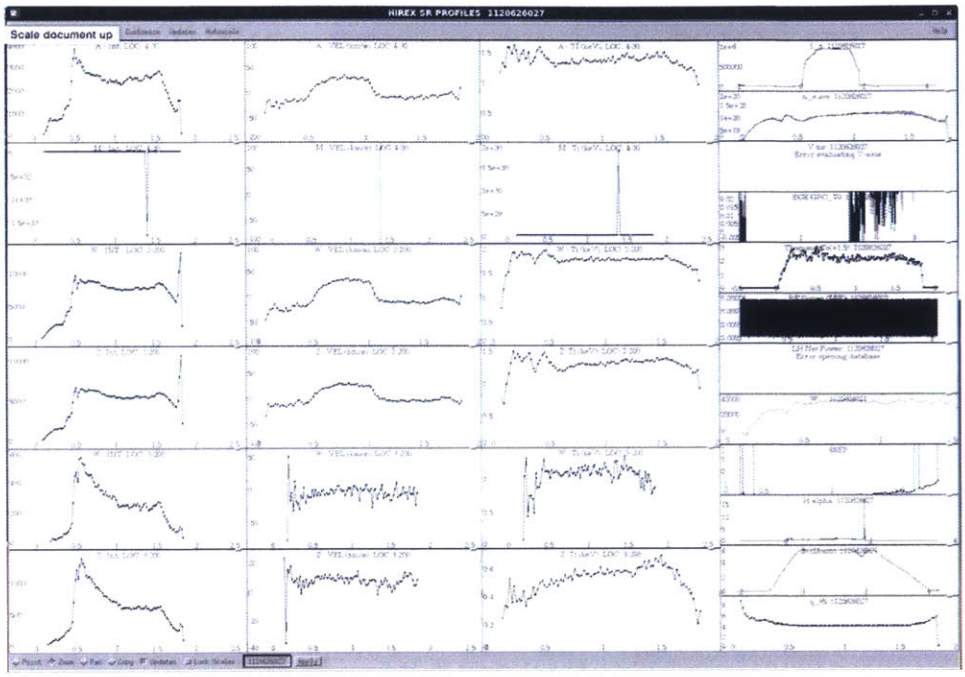

Figure 54: dwscope time trace using seniormom.dat for rotation reversal shot 1120626027.

seniormom.dat was chosen as it displays the various toroidal velocity measurements of the four different HIREXSR lines [71], plasma current, plasma density, safety factor, electron and ion temperature, and RF power. Because the density, temperature, and velocity measurements are line-averaged values across the minor radius of the tokamak, they do not provide explicit localized values, but are useful in characterizing shots prior to analysis and determining the time ranges for analysis.

The velocity time traces, shown in the second column of Fig. 54, are used to observe a strong change in rotation direction ($\Delta V > 10$ km/s). The seniormom.dat scope shows emissions from four HIREXSR channels: A, M, W, and Z. Because HIREXSR is a passive diagnostic that uses emissions from the plasma, the letter correspond to the different emission wavelengths that are detected. Three correspond to the emission lines from argon, which is puffed into the plasma. Once the argon is ionized by the plasma, it exists primarily in two states, Ar^{16+} (He-like) and Ar^{17+}(H-like) and as the electrons jump between states, emissions are generated which are detected. The A channel corresponds to the Lyman-alpha emission from H-like Ar and W and Z correspond to the w and z emission lines from He-like Ar using the standard Gabriel notation. M corresponds to the emission from molybdenum (Mo^{38+}). Most often, the Z and W lines of the toroidal velocity are used. However, for higher core electron temperatures ($T_e > 3$ keV), the strength of these emissions drop significantly and the A line is more reliable for identifying reversals. More information about the HIREXSR diagnostic, emission lines, and how it measures toroidal velocity and ion temperature can be found in the literature by Matt Reinke [71].

The RF power (titled "RF POWER (MW)" in the right-most column in Fig. 54) is used to identify the heating mode of the shot, as a lack of significant power input from ICRF heating

during the shot is indicative of an ohmically heated plasma. The density and current are used in determining the critical density at which the reversal occurs and as a characterization of the shot. Additionally, the current is used to determine whether the rotation is co-current or counter-current. If the current and rotation velocity are both the same sign, this indicates a co-current rotation and vice versa for counter-current rotation. When using another scope for time-traces, the user must be aware that the seniormom.dat is specifically modified to create this alignment between the current and toroidal rotation velocity and that this method of determining the rotation direction might not be applicable with other scopes.

In seniormom.dat, $I_p > 0$ signifies a counterclockwise plasma current from a top-down laboratory frame of the tokamak and $V_\Phi > 0$ signifies a counterclockwise rotation velocity. In most C-Mod shots, the current is in the counterclockwise direction, such that a plasma rotating counterclockwise has co-current rotation direction. Therefore, $V_\Phi > 0$ signifies a co-current rotation and $V_\Phi < 0$ signifies a counter-current rotation. However, in some shots, the current is in the clockwise direction and shown as negative in the seniormom.dat dwscope. With these shots, the exact opposite of the aforementioned relationship is true, such that $V_\Phi < 0$ signifies a co-current rotation and $V_\Phi > 0$ signifies a counter-current rotation. The analysis workflow assumes that $V_\Phi > 0$ signifies a co-current rotation and $V_\Phi < 0$ signifies a counter-current rotation, such that the rotation velocities of the shots with clockwise current ($I_p < 0$ in seniormom.dat) are flipped to address this issue. The shots that have clockwise currents are listed in the Appendix C.

The H-alpha section (right-most column in Fig. 54) is used to determine the confinement regime as it drops suddenly upon entering the H-mode regime from L-mode [97]. Only L-mode shots without this sudden drop in H-alpha are used in this analysis.

To determine the appropriate time range, a time period of steady-state velocity and other parameters, such as density and current, is chosen for each intrinsic rotation direction. Each rotation reversal shot produces two rotation shots (one co-current and one counter-current). A time duration of anywhere from 0.02-0.2 s is chosen for each shot. Because all of the data is time-averaged, an extremely long or short time range is avoided for consistency in the number of data points for each shot. A detailed description of the shots used in the study and how they are classified is provided in Chapter 3 of the thesis.

After checking the time traces using dwscope, the rotation and ion temperature profiles are checked using THACO as described in Section A.1.1. If high-quality velocity or temperature profiles are not available or if the profiles have not been processed, the HIREXSR data must be processed [71]. This is a result of the HIREXSR data from each shot needing to be calibrated to a baseline as over time, the detectors can become inaccurate. Therefore, it requires finding a locked mode, or baseline, shot, and then simply using it as a benchmark for the data for calibration. The steps to actually perform this inversion process is listed in the Appendix F. Once the data is verified to be processed and is not poor quality, the shot can successfully be added into the database as a shot for the analysis workflow.

The shot number, time range, rotation direction, heating method, and confinement regime are all listed down in an Excel spreadsheet. The list of the information recorded for the shot database is shown below in Table 10.

Table 10: List of information and parameters recorded and used to characterize each rotation shot

Information	Description
C-Mod Shot Number	10 digit shot identifier corresponding to date and number of the shot
Time Range	Time range of interest for profile-fitting and linear stability analysis - limited to 0.1-0.2 s
Rotation Direction	Co-current or counter-current intrinsic rotation
Heating Method	Ohmic or RF-heated plasma
Confinement Regime	L-mode, H-mode, I-mode, etc.
Comments	Any significant information about the shot data

If anything about a shot is noticeable, such as a significant spike in RF heating, drop in density, etc. then it is recorded as a comment. The Excel spreadsheet is preferable for dealing with large data sets and a screenshot of it and the list of shots and time ranges are shown in the Appendix. The shot numbers, time ranges, and directions are then copied into a simple ASCII .txt file, which is read by the profile-fitting routines. A screenshot of the .txt file, named shotlist.txt, is shown below in Figure 55.

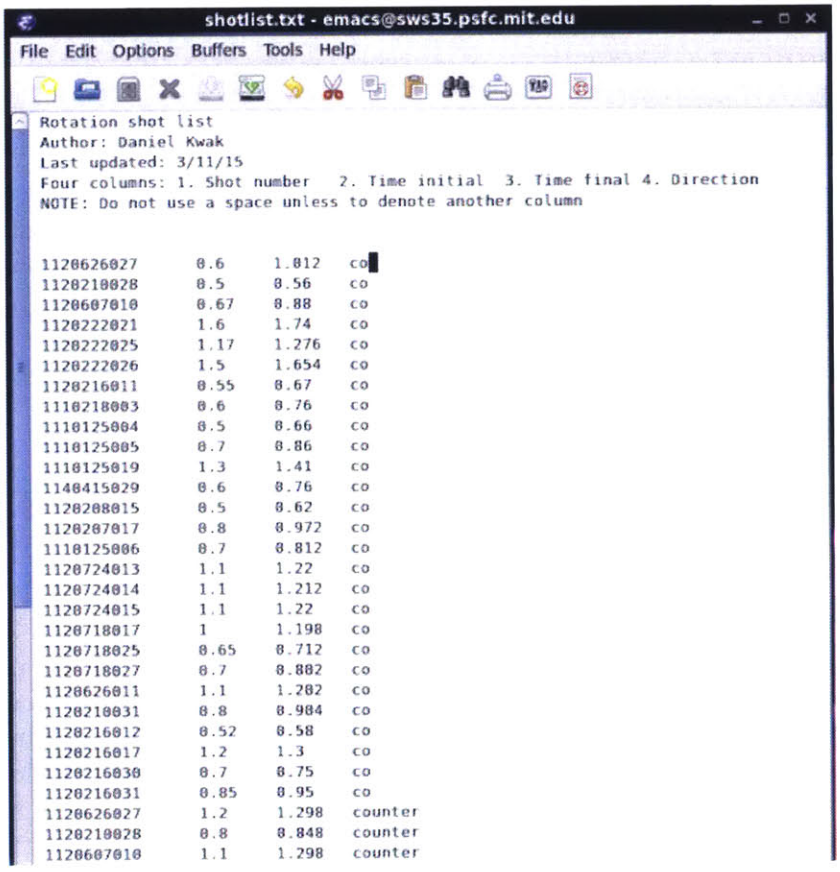

Figure 55: shotlist.txt displayed in EMACS

In terms of the types of shots that are sought after, the first choice are shots with strong rotation reversals. Each reversal shot not only effectively produces two shots (one co-current and one counter-current) but also generates two shots with very similar global plasma parameters. These similarities allow those parameters to be eliminated as rotation dependencies as they do not change significantly between the change in rotation direction.

However, other types of shots can be added to the database as well, especially for testing a certain hypothesis. For the dominant turbulence regime hypothesis, the only significant parameter is the dominant mode, such that many Ohmic co-current and counter-current shots, regardless of whether they were part of a reversal or not, can be added for linear stability analysis. In this case, C-Mod shots displaying strong intrinsic rotation via significant rotation velocities can be used. Another type of shots that are added are RF shots, which are analyzed to supplement the results from Ohmic shots. Whether the heating mode has a significant effect on the results can provide valuable insights into the underlying drivers of intrinsic rotation and rotation reversals and this comparison of the heating modes is recommended work in the future.

By creating a simple database that stores the key information of each shot, a large number of shots can be collected, classified, and prepared for the analysis workflow. Because a large number of shots must be identified and characterized, using the simple combination of dwscope for the time traces to determine the time ranges and THACO for checking the HIREXSR rotation data allows the user to build a collection of many shots with ease. With the database, the shotlist.txt file is used as the input for analysis workflow.

A.4 Modified System - Analysis Workflow

The analysis workflow comprises of a composition of routines and tools that fits profiles, performs error analysis, generates GYRO inputs, and performs linear stability analysis using GYRO for a large number of shots without constant user input and oversight. The structure of the workflow is shown in Figure 53. In addition, the workflow must deal with storing, saving, and uploading all of the inputs and output files of the various routines. The aim of this workflow is to remove the burdensome process of shot-by-shot analysis traditionally performed by users interested in performing linear stability analysis and to provide the structure to handle large data sets required for identifying intrinsic rotation and reversal dependencies from many plasma parameters. Therefore, the analysis workflow grew out of necessity for this thesis to balance speed, simplicity, and accuracy in the analysis required to generate results and to promote full transparency in the tools and models that are used. To create the analysis workflow, various pre-existing routines are used, some routines are modified, and others are created from scratch. The full list of routines used, modified, and created can be found in the Appendix B.

The workflow is comprised of three steps as shown in Figure 53: profile-fitting, input generation, and linear stability analysis and is presented in this section as it is built - into two separate components. One component, operated on the PSFC workstations, uses a modified version of gyro_inputs, the fitting and data-saving routine written by Martin Greenwald at PSFC. Another routine, as_dkwak.pro, iteratively runs these routines along with error analysis for the list of shots. The second component, run on the MIT PSFC cluster, LOKI, uses an IDL routine, find_stability.pro, written by Nathan H. Howard at PSFC, which generates and submits GYRO input files using the data stored by gyro_inputs. A second IDL routine, gyro_run.pro, iteratively runs this routine to perform linear stability for each shot at 5 different spatial locations (ρ = 0.3, 0.4, 0.5, 0.6, 0.7) with 7 sensitivity analysis cases at each location, thus performing 35 different runs for each shot. Section A.4.1 describes the non-LOKI components comprising gyro_inputs.pro and as_dkwak.pro. Section A.4.2 describes the LOKI component comprising find_stability.pro and gyro_run.pro.

A.4.1 Profile Fitting (gyro_inputs.pro & as_dkwak.pro)

As explained in previous sections, accurate temperature, density, and rotation velocity profile fitting is essential in testing the hypotheses presented in this study. Temperature and density gradients are some of the primary drivers in linear stability analysis using GYRO, which is used to determine the dominant turbulent mode of the plasma. Density gradients are important for testing the hypothesis stating that intrinsic rotation and reversals are correlated with increasing density gradients. In testing the theory suggesting that collisionality is the primary dependency of intrinsic rotation, temperature and rotation velocity gradients are used to test the validity of the 1-D analytical model presented in the paper [57]. Therefore, fitting profiles of a large amount of shots using fast and simple routines while maintaining consistency and accuracy is a core element of the analysis workflow. To accomplish this task, gyro_inputs.pro written by Martin Greenwald at MIT PSFC is used as a skeleton in which various profile fitting routines were added and as_dkwak.pro is used to iteratively run gyro_inputs for all of the shots required. As shown in Figure 53, profile-fitting is the second step of the analysis workflow. A diagram of how this step of the workflow is structured in detail is shown below in Figure 56.

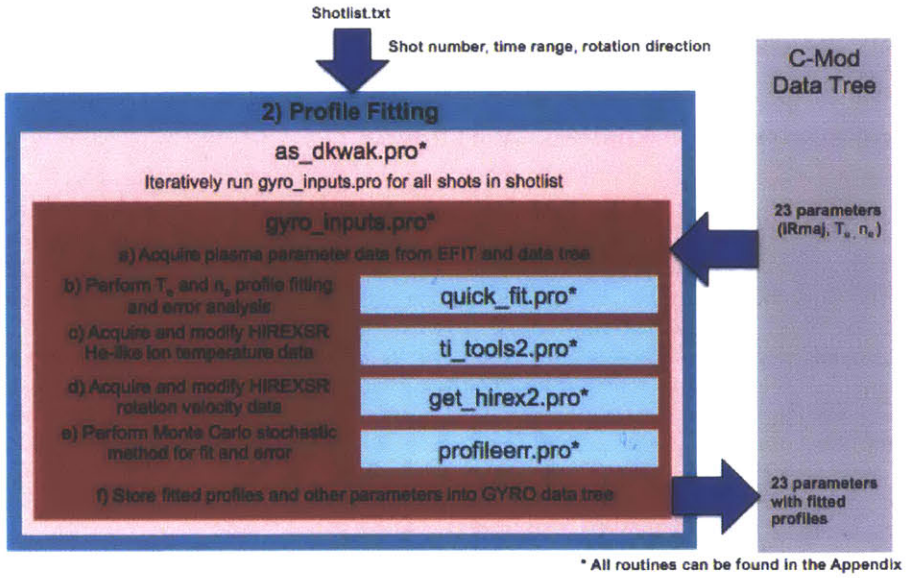

Figure 56: Detailed diagram of the structure of the Profile Fitting (Step 2) step in the analysis workflow as shown in Figure 53.

It can be seen that the profile-fitting is accomplished by using the quick_fit.pro, ti_tools2.pro, get_hirex2.pro, and profileerr.pro routines, which are called within gyro_inputs.pro. Because gyro_inputs.pro can only perform the fits for one shot and one time range, as_dkwak.pro was written to run gyro_inputs.pro iteratively for all of the shots and time ranges, specified by shotlist.txt, the list of shot numbers, times, and directions from the shot database created

in the previous step. Each routine will be described in the order it is used in the workflow, as shown in Figure 56.

Originally designed for quick in-between shot profile fitting for Alcator C-Mod, gyro_inputs.pro is an IDL routine that fits electron temperature and density profiles and ion temperature profiles and stores this data into the PSFC database tree for the corresponding shot using MDS-plus. This routine was chosen as it already had the structure to upload the raw experimental data from the database, perform the required fits, and then save the results back into the data tree. However, some components were removed and many others were modified to accomplish four tasks:

- decrease user input
- increase fitting accuracy
- add rotation velocity fitting
- add fitting error analysis.

Therefore, used as a "skeleton", the modified gyro_inputs.pro acts as a shell for various other IDL routines. (The directories to both the unmodified and modified gyro_inputs.pro routine can be found in the Appendix B) After the unmodified routine is described, the modifications that were made and their purpose are explained in detail.

a) Unmodified gyro_inputs.pro

The unmodified gyro_inputs.pro routine is comprised of four steps that focus on the radius, electron temperature and density, ion temperature, and data tree. The user specifies the shot number, time range, and rho, the squareroot of the normalized toroidal flux coordinate. gyro_inputs uses this information to identify and access the plasma parameter data from EFIT and the database. Then, the routine plots delta, kappa, the major radius, and the safety factor q as a function of the rho spatial grid. Although the radius of the minor axis shifts in time, gyro_inputs time-averages this quantity over the specified time range. Sample plots of this first step in gyro_inputs.pro is shown below in Figure 57.

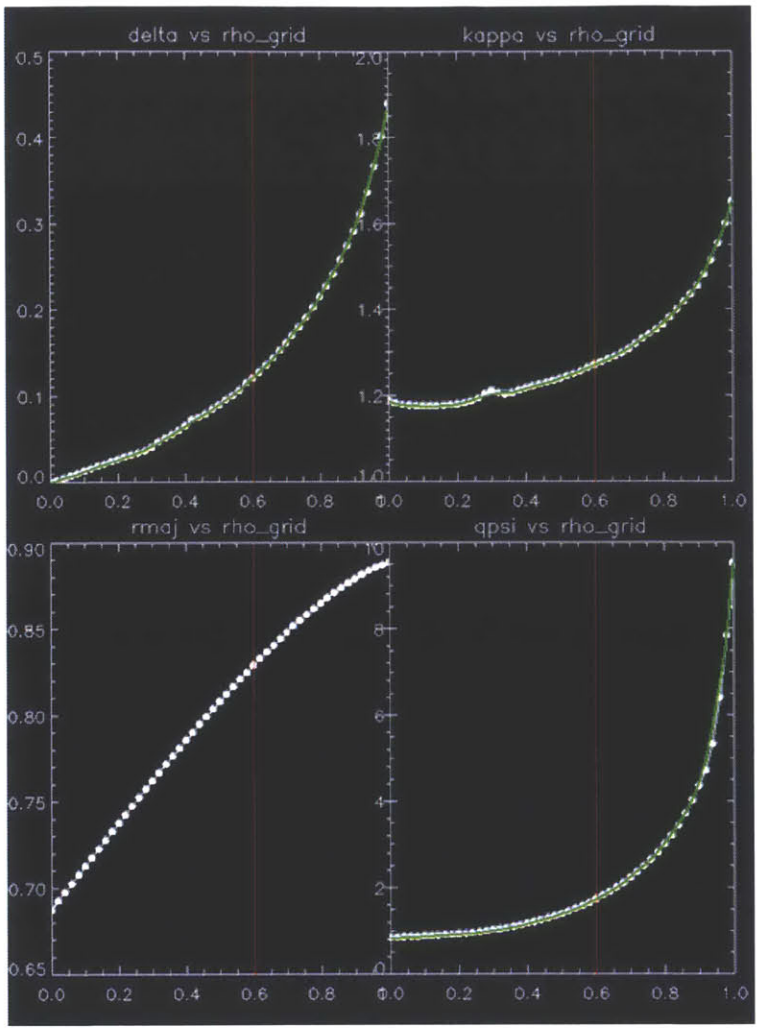

Figure 57: Rho grid plot from unmodified gyro_inputs.pro routine for C-Mod shot = 1120221014.

After this step, gyro_inputs.pro performs electron temperature and density profile fits. Then, the routine get_ts.pro is run within the routine, which displays the TS and ECE electron temperature measurements for the time range specified. These measurements and all of the others are mapped to the r/a spatial coordinate system. The user is then given the option of manually eliminating outlier data points via an interface and upon completion of this removal process, the user is given the option of running an IDL polynomial (poly_fit) or bspline fit (bspline_iterfit) routine and can specify the order of the fit. The interface of the data removal step is shown below in Figure 58.

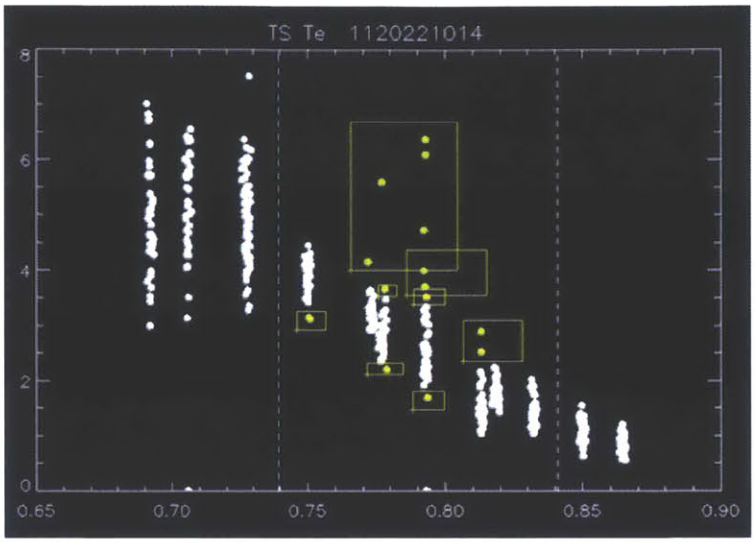

Figure 58: Electron temperature data removal step from unmodified gyro_inputs routine.pro for C-Mod shot = 1120221014.

After the user removes the unwanted outliers and decides what type and order of fit is desired, get_ts runs the same profile fitting process for both electron temperature and density profiles, as they are similar in form. Then, the user is given the option to remove data points with standard deviations greater than 2 and re-run the fitting. After this process, the final electron temperature and density fit is displayed, as shown in Figure 59 below.

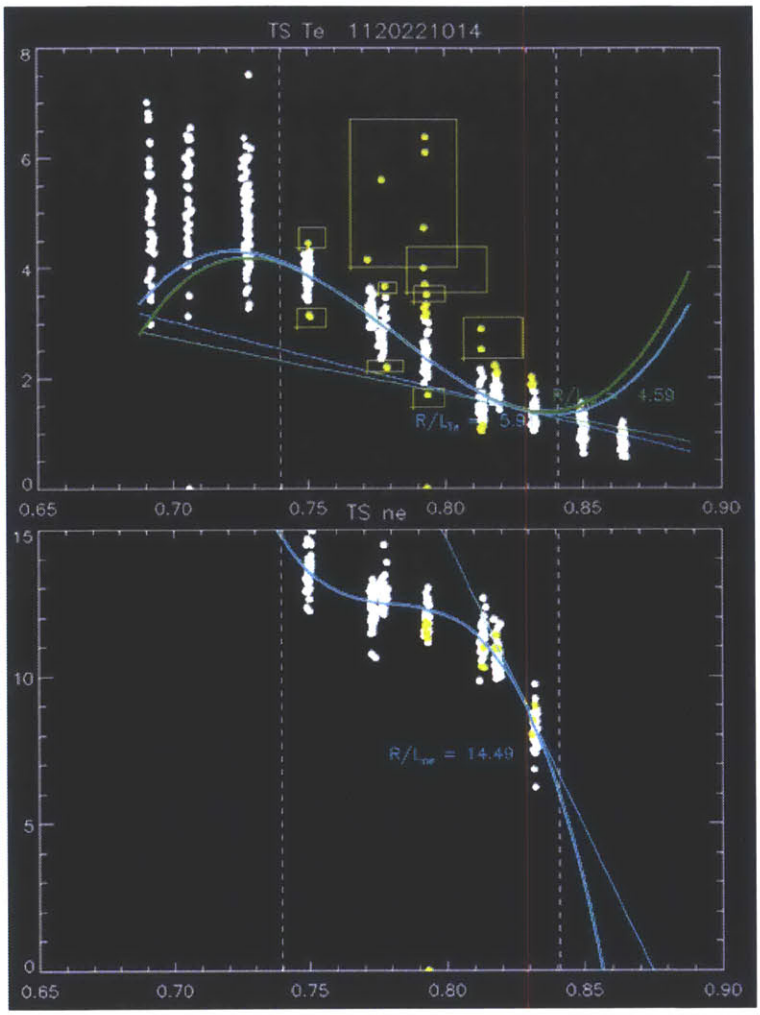

Figure 59: Electron density and electron temperature profile fitting from unmodified gyro_inputs.pro routine for C-Mod shot = 1120221014.

Because the data points that are used correspond to many time slices, it is essential that the user specify a time-range of steady-state plasma behavior to ensure that the temperature and density profiles are relatively stable in time.

Upon user approval, gyro_inputs runs the ti_tools.pro routine to pull ion temperature measurements and get_hirex.pro to fit the ion temperature data. The user must specify the HIREXSR measurements for ion temperature profile fitting. The HIREXSR data is divided into H-like and He-like measurements, as explained in Section A.3. The H-like measurements are present near the core of the plasma (rho = 0.1 - 0.3) while He-like measurements are present everywhere else (rho = 0.3 - 1.1). However, near the fringes of each measurement at rho = 0.3 where they intersect, they become less accurate. Therefore, the user chooses the data by choosing the outermost H-like data point to contain in its fit and then the innermost He-like data point. Like electron temperature and density data, the HIREXSR

measurements used are those taken within the time range specified by the user. Once the data is specified, the same IDL bspline routine (bspline_iterfit) is used by get_hirex.pro.. The interface of this data selection and the resulting profile fit for this process is shown in Figure 60.

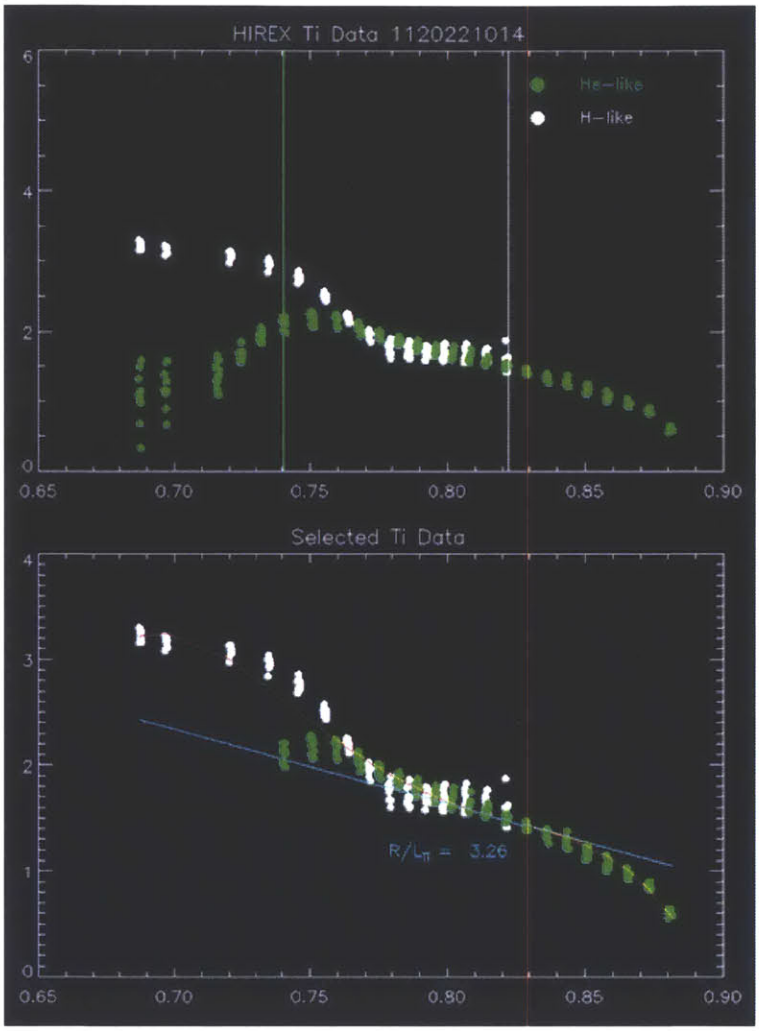

Figure 60: Choosing H-like and He-like data for ion temperature fitting from unmodified gyro_inputs.pro routine for C-Mod shot = 1120221014.

Once the data is specified, the same IDL bspline routine (bspline_iterfit) is used by get_hirex.pro and the fit is shown, as seen in Fig. 61 below.

Once the fitting is completed for electron temperature and density and ion temperature, gyro_inputs saves the data into the shot's transport data tree using MDS plus. If a data tree does not exist, it creates one. If it does exist, the routine creates a name or t_node for the node in which the data is stored using the average of the time range specified (i.e.

t_initial = 1000 ms and t_final = 1600ms results in t_node = 't1300'). If this node already exists, the routine exits rather than overwriting the data. If the node is empty, all of the parameters and fits are stored. Table11 lists all of the values stored in the transport data tree using the gyro_inputs routine.

Table 11: List of all of the variables stored in the transport data tree using the unmodified gyro_inputs.pro

Scalar Variables	Description
krange	Range of $k_\theta \rho_s$ values for GYRO (default = 0 - 1.0)
nk	Number of grid points for GYRO (default = 20)
ngrid	Number of radial grid points in normalized flux (default = 20)
rho ($\rho = \sqrt{}$)	Radial coordinate of the normalized toroidal flux
zeff	Effective nuclear charge (default = 2.0)
zav	Average ion charge (default = 12)

Profile Variables	Description
kappa ($\kappa = \frac{b}{a}$)	Elongation of plasma
delta ()	Average triangularity
q ($q = \frac{rB_\phi}{RB_\theta}$)	Safety factor
zeta	Plasma squareness (default = 0)
zmag	Height of center of each flux surface (default = 0)
rho_grid	Spatial grid in normalized toroidal flux
rmin	Spatial grid in minor radius
rmaj	Spatial grid in major radius
te	Electron temperature
ne	Electron density
ti	Ion temperature

The scalar variables and several of the profile variables related to the plasma geometry are outputs of EFIT. The b used to calculated kappa is the height measured from the equatorial plane of the plasma. The profile variables are mapped onto both the major radius and rho grids as they are both used by the various fitting routines.

b) Modified gyro_inputs.pro

The modifications to gyro_inputs.pro were made to accomplish four tasks listed above: to decrease user input, increase fitting accuracy, add rotation velocity fitting, and add error analysis. After gyro_inputs.pro pulls the input files form EFIT, the measurement data is mapped to rho, the spatial coordinate of the normalized toroidal magnetic flux (equation shown in Table 11), as that is the spatial grid used by GYRO and several other tools. Therefore, to preclude the need to constantly convert profiles between the r/a and rho grid system, rho grid was chosen as the spatial coordinate system.

For electron temperature and density fitting, get_ts.pro was replaced with quickfits, which pulls TS and ECE data and fits them using a combination of fitting methods at various regions of the profile. Because quickfits allows for user-free fitting, it was decreased the level

of user input needed for removing outliers, choosing between polynomial and spline fitting, and deciding what order to fit the profiles [76]. Additionally, quickfits performs Monte Carlo error analysis on its fits. Therefore, the use of this routine greatly simplifies electron temperature and density fitting while removing guess work regarding the best type of fit. A sample plot of the electron temperature and density fits with error bars are shown below in Figure 61.

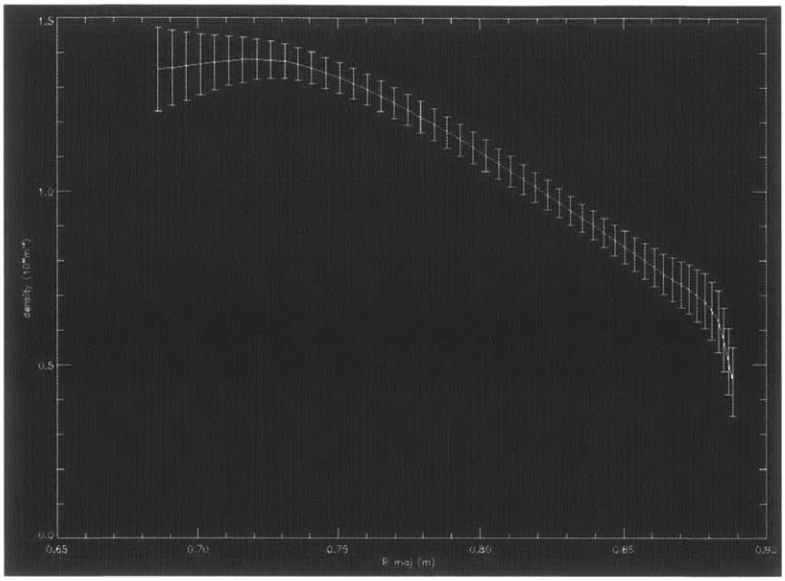

Electron Density

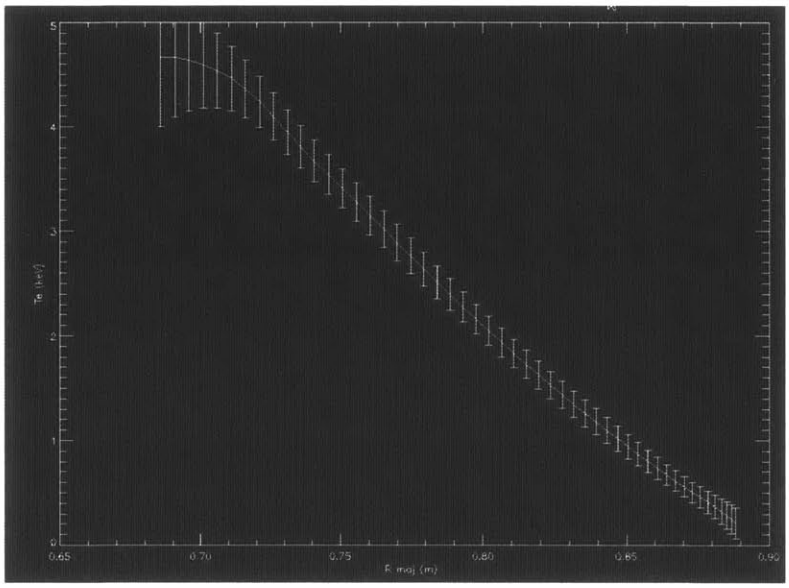

Electron temperature profile fit

Figure 61: Electron density (10^{20}m^{-3}) and electron temperature (keV) profile fitting with MC error analysis from modified gyro_inputs.pro routine for C-Mod shot = 1120221014.

For ion temperature, one common issue when analyzing a large number of shots was that many shots did not have the H-like rotation data. Additionally, the need for the user to specify the outermost H-like data point and the inner-most He-like data point for fitting had

to be removed to reduce the need for user input. Therefore, ti_tools.pro, which is called by get_hirex, was modified into ti_tools2.pro to remove H-like data entirely and for the user to simply choose the innermost He-like data point to use in the fitting. get_hirex.pro was modified into get_hirex2.pro to account for fitting only He-like data. Therefore, rather than choosing the outermost data point for H-like measurements and the innermost data point for He-like measurements as done in the unmodified gyro_inputs.pro routine, the user only choose the innermost He-like data to use. This allows the user to exclude ion temperature measurements near the core, as they can be very inaccurate for some shots. This modified interface is shown below in Figure 62.

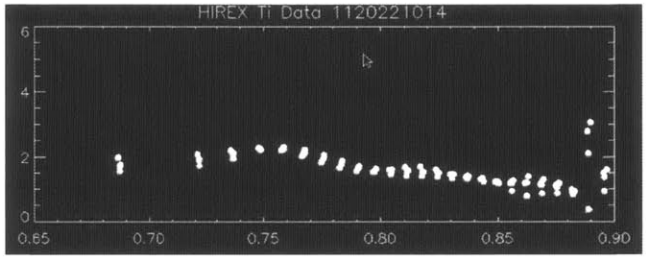

Figure 62: He-like ion temperature (keV) data selection process from modified gyro_inputs.pro routine for C-Mod shot = 1120221014.

To get the rotation velocity data from HIREXSR and fit it, gyro_inputs calls hirexsr_load_result.pro, which pulls the velocity data from the data tree. Because the velocity measurements tend to be very inaccurate near the core and at the edge, 1 data point from the core and 9 data points from the edge are removed. To account this reduction in data, a new spatial coordinate system with 41 spatial points called vrmaj that also has these spatial coordinates removed, is used for mapping the velocity profile. Then gyro_inputs performs a time-averaging of the data and then uses the IDL bspline routine to fit the data. The exact order and spacing of the bspline fit can be found through gyro_inputs.pro. The location of the routine is listed in the Appendix. Because the rotation velocity does not exhibit a simple monotonically decreasing profile like temperature and density, the bspline routine can result in inaccurate fitting with large errors. In this case, the user can re-run the fitting with different bspline ordering, bspline spacing, or change the time interval to increase or decrease the number of data points used in the fit. These changes can be made by modifying the source code of gyro_inputs.pro.

For the profile fitting and fit error calculations, a Monte Carlo stochastic method was added. An IDL routine, profileerr.pro, was written to perform this method and is called within gyro_inputs.pro once the ion temperature and velocity data have been acquired. The routine takes the 1-sigma experimental error for all of the data points as the input and uses the error to create a normalized distribution of the values for each of the 51 spatial points. Through a Monte Carlo sampling of the values from the distribution, another data set is created that is fitted using IDL's bspline routine (bspline_iterfit). After 10,000 runs, the profile is taken to be the mean of the new distribution of the 10,000 spline fits and the standard deviation of these distributions is taken as the fitting error. 20% is assumed to be the 1-sigma experimental error for ion temperature and toroidal velocity measurements

as mentioned in literature [71]. This Monte Carlo method will be described more in detail in Section A.6 and the exact characteristics of the bspline_iterfit routine used for ion temperature fitting can be found through gyro_inputs in the Appendix. The plot of the ion temperature and toroidal rotation velocity fitting and error is shown below in Figure 63.

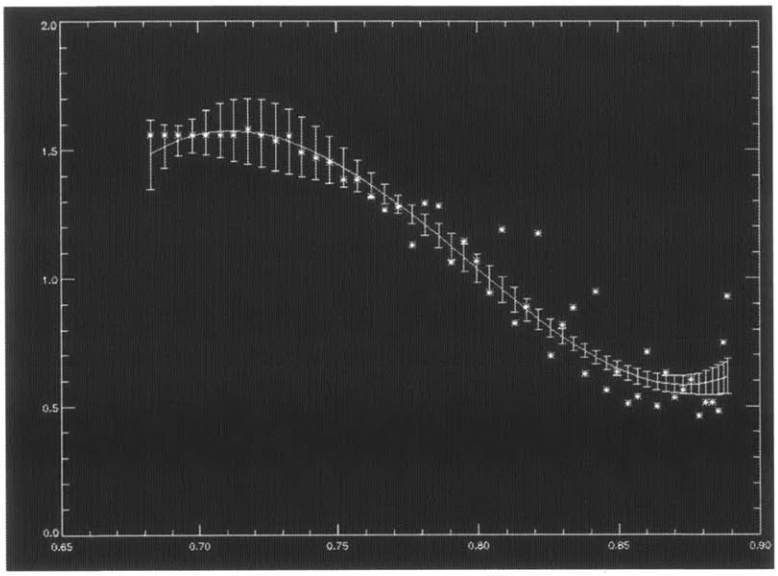

(a) Ion temperature profile fit

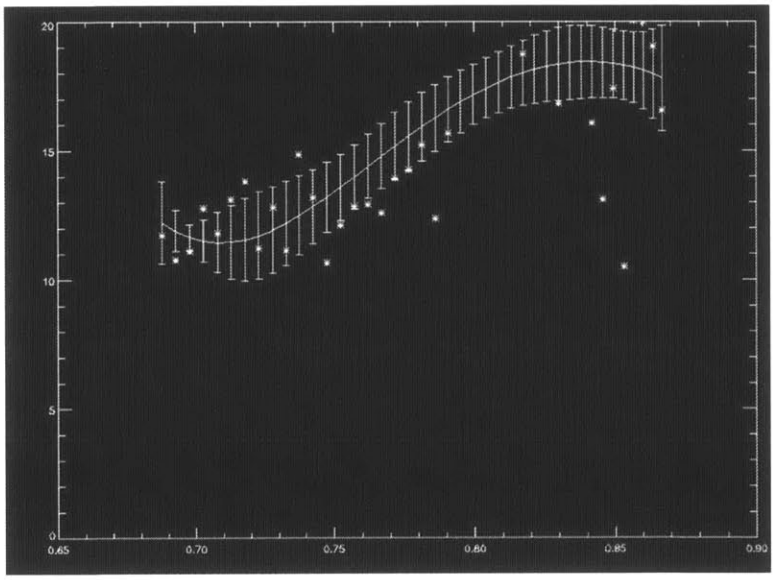

(b) Rotation velocity profile fit

Figure 63: (a) Ion temperature (keV) and (b) toroidal rotation velocity (km/s) profile fitting with MC error analysis from modified gyro_inputs.pro routine for C-Mod shot = 1120221014.

These 1-sigma errors from the MC stochastic method are used for calculating the errors of the results and is also explained in detail in Section A.6. After all of these profiles are fit and the errors are calculated, the data is stored into the GYRO data tree using MDS-plus. Because error analysis and toroidal velocity was added to gyro_inputs, these new parameters are added into the tree. Table 12 lists the additional profile variables added to the modified gyro_inputs.pro code.

Table 12: List of new profile variables added in the transport data tree from the modified gyro_inputs.pro

Profile Variables	Description
teperr	Electron temperature profile fit error
neperr	Electron density profile fit error
tperr	Ion temperature profile fit error
velocity_out	Toroidal rotation velocity profile fit
vperr	Toroidal rotation velocity profile fit error
vrmaj	41 point spatial coordinate system for velocity data in major radius

By replacing the electron temperature and density fitting routine get_ts.pro with quick-fits, modifying get_hirex.pro and ti_tools.pro to remove H-like ion temperature data, and using get_hirex_results.pro to fit velocity data, gyro_inputs.pro was improved to require less user input and more accurate bspline fitting. Through Monte Carlo error analysis, the fitting error can be calculated, taking the measurement errors into account, which is vital for sensitivity analysis in linear stability analysis using GYRO. Although more accurate fitting routines can be used that is more tailor-made for each type of profile fitting, using the common bspline routine throughout gyro_inputs reduces the risk of overfitting each profile and is a simple IDL fitting routine that can be easily understood and is highly transparent to the user.

gyro_inputs.pro is a one-shot routine, which means it only performs the profile fitting and saving for a given time range. However, this analysis must be performed for a database of shots without manual user input. Therefore, a simple IDL routine, as_dkwak.pro, was written that reads the .txt file with the shot number, time range, and whether the shot is co-current or counter-current. Although knowing whether the shot is co-current or counter-current isn't required for gyro_inputs, because some shots have hollow velocity profiles but are still co-current because the current is also in the opposite direction, it helps the user to flip the velocity profiles in these instances for rotational velocity analysis later on. The routine also provides the user the option to create a .sav file of the scalar and profile variables for each shot and will output a different .sav file with the list of all of the .sav files it generated. The directory to find as_dkwak.pro is listed in Appendix B. With the combination of the modified gyro_inputs and as_dkwak.pro, the user only needs to maintain a database of shot numbers, time ranges, and rotation direction to generate data trees filled with the parameters necessary to create GYRO input files for linear stability analysis, an improvement to the traditional system when analyzing a large number of shots with little oversight required.

A.4.2 Input Generation and Linear Stability Analysis (find_stability.pro & gyro_run.pro)

The second and third steps of the workflow, GYRO input generation and linear stability analysis, are performed primarily by two IDL routines: find_stability.pro and gyro_run.pro. These routines are stored and run on LOKI, the MIT PSFC cluster, which is used to run GYRO simulations. Because files and routines run on LOKI are stored within its own network rather than on PSFC's, the workflow had to be bifurcated into a PSFC and LOKI component for simplicity and ease of use. This is shown in the structure of the workflow in Figure 64 . However, because LOKI routines can still read parameters stored onto the PSFC database, the outputs of gyro_inputs can be used. For other files, such as shotlist.txt, they are copied into LOKI to be used.

The primary concerns surrounding these two steps involve the manual shot-by-shot process required for GYRO input file generation and the lack of a sensitivity analysis option. Both profiles_gen and find_stability, the GYRO input file generating routines, only can perform shot-by-shot processing. Therefore to analyze a large number of shots, the user must submit a shot number and time range, wait as the input files are generated and the linear stability analysis is completed, and then submit another shot. Additionally, for each shot, only one linear stability analysis is performed without any sensitivity cases. However, as stated previously, the temperature and density gradients are critical drivers of linear gyrokinetic simulations and are also prone to significant errors. As a result, a single linear stability analysis on a shot cannot be taken at face value as there may be large errors that would've drastically affected the results. A sensitivity analysis is needed that performs multiple linear stability analyses with slightly varied density and temperature gradients to account for the measurement and fitting errors calculated by the Monte Carlo error analysis implemented to the gyro_inputs.pro routine. This sensitivity test also shows the primary drivers of the most unstable linear modes that is important for understanding turbulent transport. To address these two concerns of single shot processing and lack of sensitivity analysis, find_stability.pro was chosen to be used as the GYRO input generator, which performs sensitivity cases, and gyrorun.pro was written to perform sensitivity cases for each shot and store the linear stability analysis results into .sav files. The structure of this step of the workflow is shown below in Figure 64.

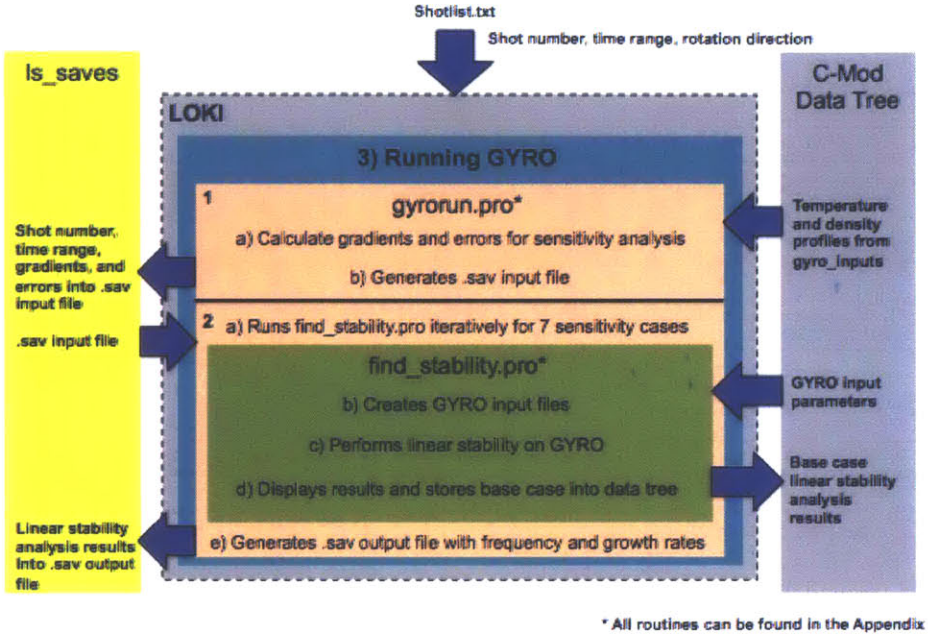

Figure 64: Diagram of Step 3 of the analysis workflow structure including the IDL routines used.

It can be seen from the figure that gyrorun.pro is run, which calls find_stability.pro. These routines frequently upload and use data stored in the C-Mod data tree and the ls_saves directory. How this process works and the individual routines will be explained. The location and codes of these routines are listed in the Appendix.

a) find_stability.pro

Written by Nathan H. Howard at the MIT PSFC, find_stability.pro was written for quick, in-between shot GYRO simulations. Therefore, it was created to generate GYRO input files without user oversight and to upload these files into GYRO for linear stability analysis. Also, find_stability allows for running different sensitivity cases by increasing or decreasing the normalized electron temperature and density and ion temperature gradients. Because of these two reasons, find_stability.pro is chosen to be used.

Once the user specifies the shot number, time range, and rho, find_stability pulls the necessary parameters from the data tree previously filled by gyro_inputs.pro. These input parameters are used to generate a GYRO input file, more specifically, input.gyro and input.profiles. The structure of a sample GYRO input file can be found in the Section A.2. From the samples in Table 8 and 9, it can be seen that various assumptions regarding the geometry, solution method, time steps, and blending functions need to be made. For input.gyro, find_stability specifies values for multiple parameters rather than using GYRO's default values. The parameters that are modified from their default values and the specified values are listed in Table 13 below and arranged by their sections. The sections with no modified parameters are also listed in the table.

Table 13: Values of input.gyro parameters directly specified by find_stability classified by parameter type.

1) Plasma shape/geometry

input.gyro parameter	Interface parameter	Description	Default	Specified
RADIUS $\left(\frac{r_0}{a}\right)$	gyro_radius_in	Normalized minor radius	0.5	User specified

2) Plasma profiles

input.gyro parameter	Interface parameter	Description	Default	Specified
AMPERE_SCALE	gyro_ampere_scale_in	Electromagnetic scaling factor	1.0	0.0

3) Particle mass and charge

input.gyro parameter	Interface parameter	Description	Default	Specified
MU_ELECTRON $\left(\mu_e = \sqrt{\frac{m_D}{m_e}}\right)$	gyro_mu_electron_in	Inverse root of electron mass to deuterium mass	60	60.6

4) Numerical resolution

input.gyro parameter	Interface parameter	Description	Default	Specified
INTEGRATOR METHOD	gyro_integrator_method_in	Time-integration scheme	1	2
RADIAL_GYRO_BAND	gyro_radial_gyro_band_in	Gyroaverage stencil width	3	User specified
TIME_MAX	gyro_time_max_in	Simulation time	15.0	User specified
TIME_STEP	gyro_time_step_in	Timestep	0.2	0.008
TOROIDAL_MIN	gyro_toroidal_min_in	Lowest mode number	30	User specified
TOROIDAL_SEP	gyro_toroidal_sep_in	Mode spacing	10	6

5) Control parameters

input.gyro parameter	Interface parameter	Description	Default	Specified
ELECTRON METHOD	gyro_electron_method_in	Electron treatment 1: GK ions, adiabatic electrons 2: GK ions, drift-kinetic electrons 3: GK electrons, adiabatic ions 4: All species GK	1	2
RADIAL_PROFILE_METHOD	gyro_radial_profile_method_in	Profile/geometry selector 1: Flux-tube, s-α equilibrium geometry 2: Power-law 3: Experimental (input.profiles used) 4: Variable shear 5: Flux-tube, Miller geometry 6: GTC-style profiles	1	3

6) Rotation physics

input.gyro parameter	Interface parameter	Description	Default	Specified
DOPPLER_SCALE	gyro_doppler_scale_in	Doppler shearing rate scaling factor	1.0	0.0
MACH_SCALE	gyro_mach_scale_in	Scale factor for Mach	1.0	0.0
PGAMMA_SCALE	gyro_pgamma_scale_in	Rotation shearing rate scaling factor	1.0	0.0
ROTATION_THEORY_METHOD	gyro_rotation_theory_method_in	Method of treating plasma rotation 1: Standard model $\gamma_E = -\frac{r}{q}\frac{\partial \omega_0}{\partial r}$ $\gamma_p = -R_0\frac{\partial \omega_0}{\partial r}$ $M = \frac{\omega_0 R_0}{c_s}$ 2: Waltz model $\gamma_E = -\frac{r}{q}\frac{\partial \omega_0}{\partial r}$ $\gamma_p = (BTCCW)R_0\frac{\partial}{\partial r}\left(\frac{U_\parallel}{R_0}\right)$ $M = \frac{v_\parallel}{c_s}$	1	2

7) Source and buffer parameters

input.gyro parameter	Interface parameter	Description	Default	Specified
EXPLICIT_DAMP_GRID	gyro_explicit_damp_grid_in	Width in number of radial grid points of the artificial damping region at boundaries	8	16

8) Data output

input.gyro parameter	Interface parameter	Description	Default	Specified
TIME_SKIP	gyro_time_skip_in	Number of timesteps to skip between data output to large files (like field output)	5	125
THETA_PLOT	gyro_theta_plot_in	Number of output gridpoints for plotting	1	32

(For 9-12: no modifications to default parameter values)

13) Experimental Profile Control Parameters

input.gyro parameter	Interface parameter	Description	Default	Specified
EPS_DLNNDR_ELECTRON	gyro__eps_dlnndr_electron_in	Rescale $\frac{a}{L_{n_e}}$ by (1-ε)	0.0	Sensitivity case
EPS_DLNTDR	gyro_eps_dlntdr_in	Rescale $\frac{a}{L_{T_i}}$ by (1-ε)	0.0	Sensitivity case
EPS_DLNTDR_ELECTRON	gyro_eps_dlntdr_electron_in	Rescale $\frac{a}{L_{T_e}}$ by (1-ε)	0.0	Sensitivity case

In Table 13, the parameters that have values that the user directly or indirectly specifies, such as by choosing a spatial location for the linear stability analysis, were labeled with "User specified". For the Experimental Profile Control Parameters, the changes made to the gradient scale lengths are dependent on the specific sensitivity case being run. The list of sensitivity cases is shown in Table 14 below. Because these simulations are relatively quick in comparison to other GYRO simulations, the resolution of the output was increased and the time steps decreased. To utilize the experimental profiles, the experimental radial profile method was chosen. Also, because the linear stability analysis is performed to determine whether the plasma is dominated by ITG/TEM, the electron method that treats electrons as drift-kinetic components and ions as gyrokinetic. To find the complete list of parameter values specified by find_stability.pro, the location of the code can be found in the Appendix.

After an input file is created, find_stability submits it to GYRO, using the nodes of the LOKI cluster to perform the linear stability analysis. The run with nk = 20 is separated into 20 separate files that are each run on a different node and then compiled again to generate the ω vs. $k_\vartheta \rho_s$and γ vs. $k_\vartheta \rho_s$ plots as shown in Figure 48. These plots along with other output parameters from the linear stability analysis is saved into the transport data tree using MDSplus. How the file is separated using the openPBS batch system, how the queue for running on LOKI works, or how to get access to LOKI can be found through the LOKI PSFC website (loki.psfc.mit.edu).

For sensitivity analysis, the alti, alte, and alne, corresponding to the normalized ion temperature, electron temperature, and electron density gradients, respectively, can be specified. The user can set one or more of the variables to a value between -1.0 and 1.0. Because of the value specified by the user is taken from the initial value, to increase the gradient scale length, the user must specify a negative value for that variable and vice versa to decrease the gradient scale length. For example, alti = -0.2 would result in linear stability analysis with a 20% increase in the normalized ion temperature gradient $\frac{a}{L_{T_i}}$. Although the option to perform the sensitivity analysis exists, there are two problems - the exact value of the increase/decrease in normalized gradients are not known and the runs with modified gradient scale lengths are not stored in the data tree for future analysis. Therefore, an IDL routine, gyrorun.pro, was written to calculate these normalized gradients and to save these sensitivity cases.

b) gyro_run.pro

Rather than altering the find_stability.pro source code, an IDL routine called gyrorun.pro was written to calculate density and temperature gradients, iteratively run find_stability.pro for a specific shot at the 5 different radial locations (ρ = 0.3, 0.4, 0.5, 0.6, 0.7) with 7 different sensitivity analysis cases, and to save all of these cases for future analysis. Similar to as_dkwak.pro for profile fitting, gyrorun.pro reads the shotlist.txt file for the list of shots, time ranges, and intrinsic rotation direction. Then, the routine divides each shot into 5 different rhos (ρ = 0.3, 0.4, 0.5, 0.6, 0.7) and then seven sensitivity cases at each spatial location, resulting in a total of 35 linear stability runs for each C-Mod shot. gyrorun.pro gives the user the option of running through the 35 cases for one specific shot or at one rho or sensitivity case for all shots, but if not, the routine runs through all of the shots in the database at all of the locations for every sensitivity case. The location and source code of the routine can be found in the Appendix B.

Table 14 shows the exact changes made to the normalized gradients for each of the seven sensitivity cases performed on gyro_run.pro.

Table 14: Descriptions of the sensitivity cases on gyro_run.pro for linear stability analysis using GYRO

Case Number	Description
1	No changes to normalized gradients (Base case)
2	Increase $\frac{a}{L_{T_i}}$ by 1-sigma error
3	Decrease $\frac{a}{L_{T_i}}$ by 1-sigma error
4	Increase $\frac{a}{L_{T_e}}$ by 1-sigma error
5	Decrease $\frac{a}{L_{T_e}}$ by 1-sigma error
6	Increase $\frac{a}{L_{n_e}}$ by 1-sigma error
7	Decrease $\frac{a}{L_{n_e}}$ by 1-sigma error

This accounts for all of the various gradient scale length modification options presented by find_stability.pro. Each of the seven sensitivity cases vary one normalized gradient by its 1-sigma error. This error is calculated using error propagation and the fitting errors calculated by the various fitting routines used in gyro_inputs. The exact equations and methods used to calculate these gradient errors is explained in Section A.6. In essence, the fitting errors incorporates the errors from the diagnostic systems and the bspline fitting routines, so it captures the experimental and analysis errors used up to this point. By accounting for all of the sources of errors and then using them to vary the gradients in the sensitivity analysis, the user can see the effects of the experimental and analysis errors on the linear stability analysis and identify the key drivers in determining the most unstable linear mode in this study. Although other input parameters could be modified in the sensitivity analysis, because the density and temperature gradients are the key drivers for linear gyrokinetic simulations, a simple sensitivity test by only modifying the gradients is sufficient for the goal of this study.

gyrorun.pro is divided into two components as shown in Figure 64. Each component can be run separately or together depending on the situation. The first component (1) calculates the input plasma parameters used by find_stability.pro to create the GYRO input file and saves them into one .sav file for each rotation shot. The second component (2) then iteratively calls find_stability.pro, which uses these .sav input files to create the GYRO input files, runs the linear stability analysis, and then saves the results in a .sav file for each case (C-Mod shot, rho, sensitivity case). gyrorun.pro reads the shot number, time range, and the rotation direction from a shot list. The first component (1) then imports data from the tree and calculates the normalized electron temperature, electron density, and ion temperature gradients and their errors. This process is explained in Section A.6. Because find_stability.pro requires that the sensitivity variables alte, alne, and alti be entered as percentage changes rather than absolute magnitudes, the gradient errors are divided by the gradients to calculate the errors as ratios (alte_ratio, alne_ratio, alti_ratio). These ratios and the electro temperature, electron density, and ion temperature errors are calculated at the five spatial coordinates (rho = 0.3, 0.4, 0.5, 0.6, 0.7) and saved into a .sav file with the shot number and time range. The .sav file is named according to the C-Mod shot number and rotation direction. Because many shots in the database are rotation reversal shots, a

C-Mod shot number can refer to both a co-current and counter-current. As a result, the direction is identified. The format for the name of each input .sav file is

lsinput_(C-Mod shot number)_(1 for co-current/ 2 for counter-current).sav.

For example, for shot 1234567890 with counter-current rotation, the input file is named lsinput_1234567890_2.sav. All input files are stored in the ls_saves directory and its location is listed in Appendix B. Because each input file has the gradient ratios required for the sensitivity cases at all of the spatial locations, it can then be used by the second component of gyrorun.pro to perform all 7 sensitivity cases at each spatial location.

The second component (2) uses the same shotlist used by the first component to identify and open the correct .sav input file from the ls_saves directory. Then, using the gradient error ratios, the code iteratively runs find_stability.pro for all seven sensitivity cases, unless specified otherwise by the user. For each linear stability run for a specific shot, rho, and sensitivity case, the results are stored in a .sav output file. Therefore, for each .sav input file, 35 .sav output files will be generated, for each of the seven sensitivity cases (1-7) and each rho (0.3, 0.4, 0.5, 0.6, 0.7) . The data in the .sav input file, wave number $k_\theta \rho_s$, real frequency ω_r, growth rate γ, and the frequency and growth rate errors are stored into each .sav output file. The naming format for each .sav output file is

lsout_(C-Mod shot number)_(1 for co-current/ 2 for counter-current)_(rho*10)_(sensitivity case number).sav.

For linear stability analysis results for shot 1234567890 with counter-current rotation at rho = 0.6 for the 4th sensitivity case (Table 14), the output file is named lsout_1234567890_2_6_4.sav. This name includes all of the information required to identify a particular linear stability run. All output files are also saved in the ls_saves directory. Each set of linear stability analysis results is saved into an individual .sav file for simplicity and ease of use. Because various linear stability runs can fail due to errors or inaccurate input parameters, using a .sav file that collected the results for many different cases and/or rhos results in many .sav files with incomplete data arrays. At this point,t he user would have to identify for which specific case the simulation failed and then attempt to re-run the linear stability analysis or skip the failed case when analyzing the GYRO results. Although feasible, when dealing with hundreds of linear stability runs for many C-Mod shots, this process can be time-consuming and overly complicated. By isolating each linear stability run to its own .sav file, the data becomes much easier to create, identify, and use.

By observing how the dominant turbulent mode and its growth rate varies with respect to the changes in specific gradient scale lengths, the primary drivers of linear stability analysis for studying rotation reversals and intrinsic rotation can be identified. Additionally, sensitivity analysis accounting for the fitting and experimental errors gives a more complete and reliable answer to draw conclusions from. Once all of shots are run through gyro_run.pro, the data in the .sav files can then be compiled for further analysis. Additionally, for certain types of analysis that require only looking a specific subset of shots (i.e. ohmic shots for testing the ITG/TEM hypothesis), the user can choose to compile the data from certain .sav files rather than dealing with large, cumbersome data arrays of all linear stability analysis outputs. This system of partitioning the linear stability results by each shot by each case is

simple to understand and easy to work with.

The separation of the gyrorun.pro routine into two components is useful when find_stability.pro stops due to errors or when new shots are added to the shotlist. gyrorun.pro iteratively calls find_stability.pro to perform linear stability analysis for 35 total cases for each shot. For a variety of reasons, such as missing input parameters or inaccurate data, the linear stability analysis cannot be performed and find_stability.pro stops and exits without running linear stability analysis for all of shots in shotlist.txt. In this case, the issue can be fixed and gyrorun.pro can be rerun. As the .sav input files for each shot have already been created in the previous run of gyrorun.pro, the user can simply skip to the second component (2) of the routine and skip the redundant process of recreating the .sav input files. If new shots are added to shotlist.txt, the .sav input files will need to be created. Rather than generating the .sav input files for all of the shots in the shotlist, the user can simply run the first component (1) for the list of new shots and then run the second component (2) of gyrorun.pro for the complete list of shots.

Although the analysis work flow is designed to minimize user oversight, one step of the process that still requires user input is the quality check and output evaluation at various steps of the profile fitting and linear stability analysis. Because poor data, analysis, or a combination of other factors can yield unrealistic outputs that would unfairly skew the end results, the user must still evaluate the accuracy of each shot and/or case using a pre-determined set of criteria. However, rather than taking minutes, this check takes a matter of seconds for each shot/case, relieving the user of much of the time-consuming aspects of the work flow.

A.5 Quality Check

At certain points of the analysis workflow, the user must routinely check the results to evaluate the outputs of the various steps to guarantee accuracy. Although the workflow is created to minimize the user input required, this quality check is essential in ensuring the accuracy of the analysis done in the study and the future work done with the same data. Various parameters, such as density and temperature profiles, exhibit similar behaviors, but idiosyncrasies and characteristics specific to a handful of shots can produce unrealistic or inaccurate outputs when using these automated routines. As a result, the quality check by the user precludes these inaccuracies from significantly affecting the end results. The main points for evaluating the data are marked below in red circles in Figure 65.

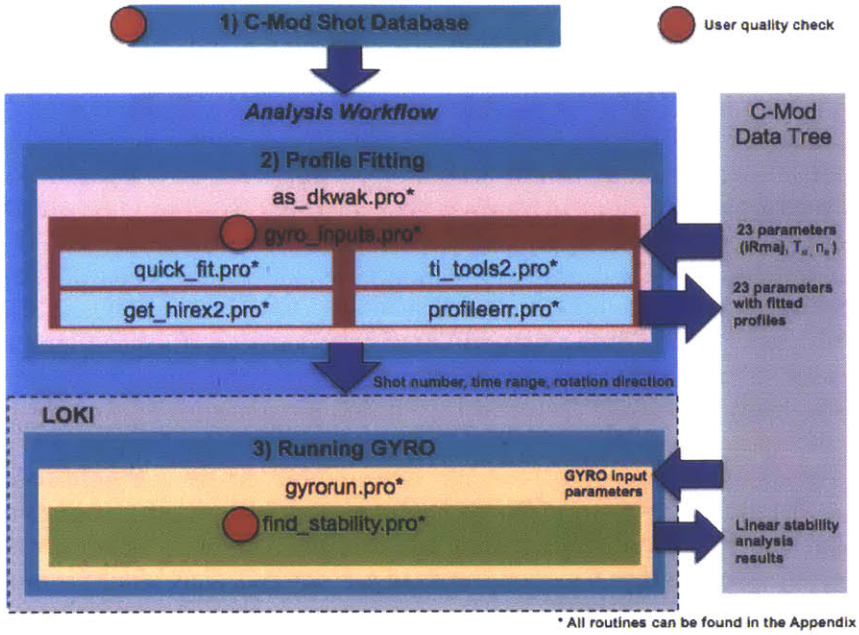

Figure 65: Essential checkpoints for user evaluation of outputs marked in the workflow structure diagram as shown in Figure 9.

The three checkpoints occur when forming the database, fitting profiles using gyro_inputs, and performing the linear stability analysis using find_stability.pro. After the shot number is found and the user has verified that the shot shows a strong rotation reversal or other characteristics he/she is looking for, the user uses THACO to check the ion temperature and toroidal rotation velocity data. The threshold for determining strong rotation was chosen to be 5 km/s for this study. Therefore, each shot must have an intrinsic rotation velocity greater than or equal to 5 km/s in terms of absolute magnitude for the entire specified time range. This value was chosen as the error for HIREXSR measurements after processing could result in errors of 1-2 km/s, so 5 km/s precludes the risk of inaccurately categorizing a shot as having co-current or counter-current rotation. Additionally, many shots displayed velocities of 5-10 km/s, such that increasing the threshold would've significantly reduced the number of shots that could be used for this study.

By launching w_hirexsr_profiles from THACO, the user can verify that the toroidal rotation data has been processed through the inversion method and evaluate the quality of the line-integrated velocity data. Although an exact quantitative evaluation cannot be performed, the user must scan through the relevant time ranges of the shot to ensure the existence and quality of the experimental data and to verify that the toroidal rotation velocity meets or exceeds the 5 km/s threshold. Two common issues that arise at this step are outliers in ion temperature and velocity data near the core and edge that are many factors greater or smaller than the rest of the data and rotation data that show a profile that does not match the time traces from dwscope. The first issue can be resolved by removing certain data points from the dataset in the same method used for the inversion process described in the Appendix F. The latter issue can be solved by determining the cause of the inaccurate

profile, most likely from poor execution of the inversion process or problems with the locked mode shot used for calibration. If the issue cannot be resolved, the shot can be removed from the database until the issue can be addressed.

The second checkpoint involves evaluating the data and the profile fitting in gyro_inputs.pro. Within as_dkwak.pro and gyro_inputs.pro, the electron density and temperature are fitted using Quickfit and the ion temperature and rotation velocity are fitted using the IDL bspline fitting routine and the Monte Carlo stochastic method. gyro_inputs.pro plots the fit, experimental data points, and the calculated error bars such that the user can evaluate the quality of the fit for each shot immediately. Although this process is qualitative and can be subjective, the user can quickly identify inaccurate and unrealistic fits if the fit does not match the data points and the monotonic behavior as expected for most density and temperature profiles. As the temperature and density profiles are peaked and rarely have any off-axis peaks or rapid drops, the user can quickly check each fit for any major mistakes.

If the user decides that the fit is inaccurate, the time range and the fitting routine can be altered. Because the data is time-averaged, if the time range is too large, there is a risk of the measurements varying widely within this time duration and resulting in inaccurate and unrealistic time-averaged measurements. In this case, the user can narrow the time range to mitigate the effects of this problem. This issue is frequently seen for HIREXSR ion temperature measurements and can be identified by an inundation of He-like measurements in the data selection interface, as shown in Figure 62. In addition to shortening the range, the user can simply choose a different time range if a specific range contains very inaccurate measurements. Ideally, the time range should be chosen for relatively stable durations as close to the rotation reversal as possible.

If shortening or modifying the time range does not work, the user can also change the spline order and break points of quickfit and the IDL bspline routines. For example, if the profile is being overfitted, reducing the number of break points, which is effectively the number of splines used to fit the data, can simplify the fit. Because electron temperature and density measurements from ECE and Thompson scattering tend to be very reliable and accurate and are simple monotonically decreasing profiles, these parameters usually do not pose problems. For ion temperature and velocity measurements, HIREXSR data tends to have errors of 10-30% and rotation velocity profiles may not exhibit a simple monotonic behavior, as shown in Figure 63b. Toroidal rotation velocity profiles exhibit widely varying profile shapes and magnitudes, which are difficult to capture using a single fitting routine across a large number of shots. In the end, if altering the time and fitting routine does not fix the problem, the user will have to remove the shot from the database.

Additionally, the quality check can be used to ensure that a shot has all of the necessary data. A shot can be missing temperature or density data or various other measurements, so it is important to identify these shots such that the data can be located. As gyro_inputs displays messages if certain data arrays are missing, the user must simply be cognizant of the printed outputs while the IDL routines are being run. The user can also access the data in the tree via MDS plus to verify that correct data has been stored through gyro_inputs. If the data cannot be located, is listed as inaccurate measurements, or does not exist, then the shot must be removed from the database.

Before the linear GYRO results can be analyzed, they must be checked and evaluated to spot possible issues or mistakes created through the analysis workflow. This is marked as the last checkpoint in Figure 65. Each shot and the results of its corresponding sensitivity runs

need to be visually checked to check for any discernible signs of an error, such as an overly dominant regime or growth rate (too high of ω or γ), a flat plot corresponding to no turbulent activity, or a constantly alternating dominant regime in all sensitivity shots. As the frequency and growth rate plots are displayed for each of a shot's 35 runs at its completion, the user can quickly check the results and identify potential issues. If the GYRO run produces unrealistic results or errors, the shot can be re-run manually using the original versions gyro_inputs and find_stability to allow for constant user management. Specific issues that could arise are positive gradients near the core, indicating a non-monotonic profile, which results from inaccurate bspline fitting, and negative values for density and temperature that result from poor fitting or measurements. The user can also open the input.profiles or input.gyro input files to manually check the input parameter values being used. Issues such as typos in the input file or incorrectly placed values can be possible sources of inaccuracies or errors within gyrorun.pro. If the shot still produces faulty results, the shot must be removed from the database and is recorded as yielding poor linear stability results. The rest of the shots that have no noticeable issues or errors and have successful linear stability runs are then recorded in the Excel spreadsheet by the user to be used for the regression analysis and further work.

These three checkpoints are critical for verifying the outputs of the various IDL routines and steps of the workflow, but are in no way a complete sets of quality checks that must be performed by the user. In addition to these checkpoints, the process had to be re-run for various sensitivity cases only after identifying several outliers in the end results with unrealistically high real frequencies and growth rates of the most unstable turbulent modes. The user must be aware of the inputs and outputs with every IDL routine and process being performed, as each shot or case presents its own risk of yielding unrealistic results. With the focus being on analyzing large data sets, it is critical to ensure that high-quality analysis is being performed at each step to guarantee the accuracy of the end results when comparing them to the results of earlier work.

A.6 Error and Sensitivity Analysis

a) Error Analysis

Because this study heavily involves the use of analysis and experimental data to test hypotheses, calculating the fitting and measurement errors is essential in understanding the results and putting them in the right context. Definitive conclusions cannot be drawn without knowing the magnitude of the errors of the results. Therefore, a key aspect of the analysis workflow is the error analysis of the temperature, density, and velocity profile fits. Additionally, the fitting process for these profiles is also performed using the same Monte Carlo method as the error analysis, so explaining this process in detail is important in demonstrating how these fits were calculated.

To perform the profile fitting and error analysis for electron temperature, electron density, ion temperature, and toroidal velocity, the analysis workflow uses a Monte Carlo stochastic profile analysis. This is used internally by quickfits for electron temperature and density and separately by profileerr.pro for ion temperature and velocity. However, the processes

are similar. Given an array of experimental data, new set of values are chosen randomly assuming a normal distribution centered at the experimental value μ and the experimental error to be the 1-sigma error σ. Figure 66 below shows a sample data set of 5 measurements with these assumptions.

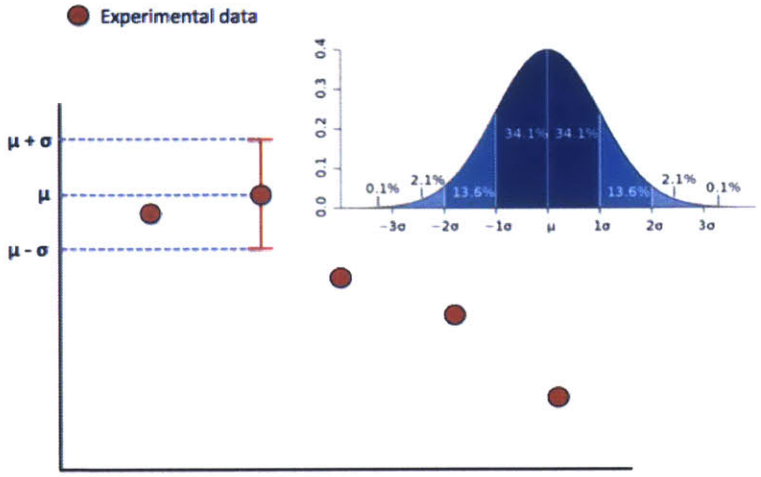

Figure 66: Sample plot of 5 data points with the assumption that 1 standard deviation = experimental error.

The figure also shows the normal distribution that is used when each of the measurement values are sampled. After sampling, a hypothetical data set is generated, which is shown below in Figure 67.

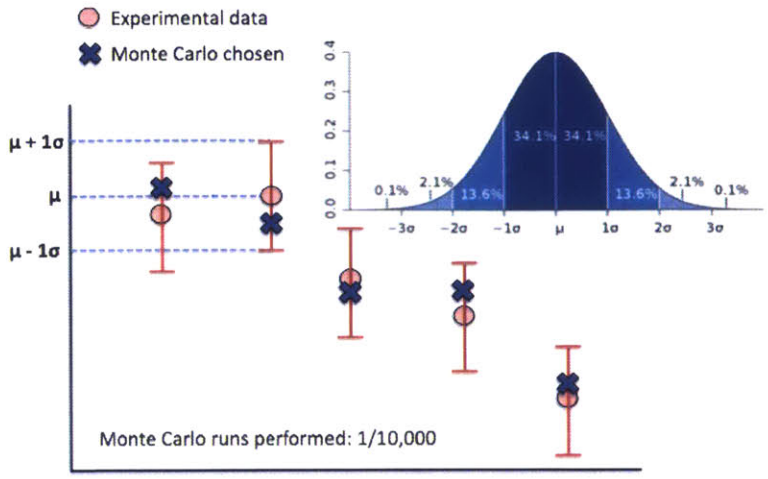

Figure 67: Hypothetical data set generated using random sampling from the normal distribution based on experimental values.

It can be seen that a hypothetical data set (blue X's) is generated based on the probabilities of the normal distribution determined by the experimental value and its errors. Because these hypothetical data sets are chosen randomly, it is possible for these hypothetical values to deviate widely from the original experimental values. However, when many of these data sets are created, the values should map the normal distribution centered at μ with experimental error σ. Each hypothetical data set is then fitted. For electron temperature and density, the hypothetical profiles are fitted using quickfit's partitioned fitting routine. For ion temperature and toroidal rotation velocity, the hypothetical profiles are fitted using the IDL bspline routine bspline_iterfit. The profile fit of the sample hypothetical data set in Figure 67 is shown below in Figure 68.

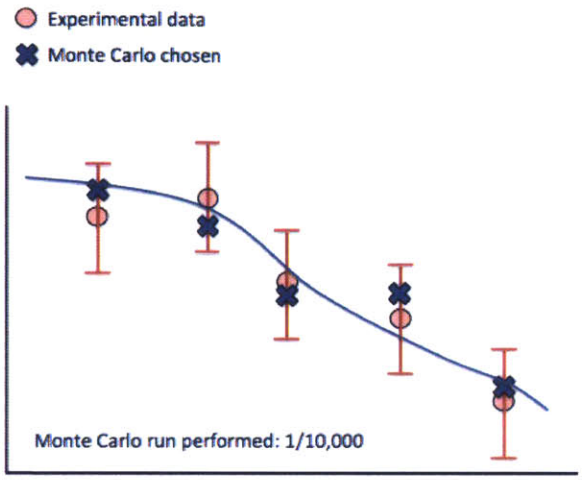

Figure 68: Sample fitted profile of the hypothetical data set shown by the blue line.

The fit shown by the blue line is solely based on the Monte Carlo data points and not the original experimental values (red circles). The values corresponding to the fit is recorded. Then this process is repeatedly many times (N=10,000 for this study) using the same normal distribution and fitting routines that creates a large data set of N profile fits. quickfit then weigh averages the N set of profiles using the probability distribution function of the chi-squared of the fits. In essence, quickfit treats the N data points as N measurements, each with a weight equal to the probability distribution function of its chi-squared value. In profileerr.pro, the routine assumes the N measurements fits a normal distribution centered at a new value μ, which is the mean of the data set. The 1-sigma error σ of the fits is calculated by calculating the standard deviation of the data set of N measurements. This method is illustrated below in Figure 69.

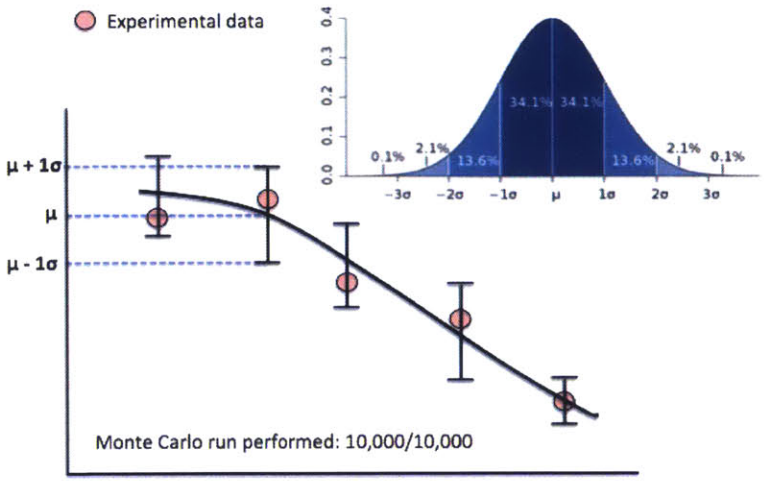

Figure 69: Profile fit calculated by Monte Carlo stochastic method for experimental data.

In the first step of the error analysis process, the standard deviation is used to assume a normal distribution that is used for the random sampling of the hypothetical data values. This is flipped for this last process. Instead, the N fits are assumed to be in a normal distribution at the mean μ and the standard deviation is calculated from this distribution to use as the 1-sigma error of the profile fit.

For the ion temperature and rotation velocity profiles, the arrays of mean values μ are used. Rather than one bspline fitting, the mean value calculated using the Monte Carlo stochastic method for 10,000 hypothetical data sets is a more accurate fit. This method performs both the profile fitting and experimental error analysis that is not possible with 1 simple bspline fitting. This Monte Carlo method accounts for both experimental and bspline fitting errors. These 1-sigma errors are stored in the database along with the other plasma parameters and can then later be used to estimate the errors of various parameters.

Error propagation must be used to calculate the errors of the end parameters used to test the hypotheses. For the gradient and neoclassical hypotheses, errors must be calculated for the temperature and density gradients, rotation gradients, and collisionality. For the dominant turbulence regime hypothesis, the temperature and density gradient errors are required for the sensitivity analysis, as shown in Table 14.

The 1- sigma error for the various parameters is calculated by performing error propagation. The error propagation formula for a function $X = f(a, b, c)$ is given by

$$\sigma_x^2 = \left(\frac{\partial x}{\partial a}\right)^2 \sigma_a^2 + \left(\frac{\partial x}{\partial b}\right)^2 \sigma_b^2 + \left(\frac{\partial x}{\partial c}\right)^2 \sigma_c^2$$

where σ_z is error of variable z and $\frac{\partial x}{\partial z}$ is the partial derivative of the function X with respect to variable z. By using this formula, the expression for error of the normalized gradient scale length $\frac{a}{L_X}$, assuming no error in the minor radius constant a, is given by

$$\sigma_{\frac{a}{L_x}} = a\sqrt{\left(\frac{\nabla x}{x}\right)^2 \sigma_x^2 + \left[\left(\frac{\nabla^2 x}{x}\right)^2 - \left(\frac{\nabla x}{x}\right)^2\right]\sigma_R^2}$$

where x(R) is the temperature or density profile, $\sigma_x$is the 1-sigma error from gyro_inputs for parameter x calculated from the Monte Carlo stochastic method, and $\sigma_R$is the error in the spatial coordinates, estimated to be 5%, a conservative approximation frequently used for calculating radial coordinates for C-Mod. Because the error of the minor radius a is less than a few percent compared to 1-sigma parameter errors on the average of 10-20%, ignoring this error in a in calculating the error of the gradient scale lengths resulted in negligible difference of less than 3%, thus justifying the assumption to set σ_x to 0. This method is used to calculate the gradient error ratios used in the sensitivity analysis explained in Section A.4. The errors of the other parameters used to the test the three hypotheses, such as the rotation gradient, Mach number, and collisionality, are also calculated using error propagation. The error propagation expressions can be found in Appendix E.

b) Sensitivity Analysis

To determine the most unstable linear mode, referred to the dominant turbulence regime in this study, linear stability analysis is performed using GYRO on intrinsic rotation shots in C-Mod. In addition to testing the dominant turbulence regime hypothesis, the analysis is also an opportunity to identify the primary drivers of the linear gyrokinetic equations and study how much the real frequency and growth rates of the most unstable mode vary within experimental error ranges. It has already been shown how important temperature and density gradients are to gyrokinetic simulations, but just how important has not been quantified or explained in detail. By performing a sensitivity analysis by altering the electron temperature, electron density, and ion temperature gradients, the effects of these gradients on the most unstable mode and its growth rates can be observed and quantified for linear gyrokinetic simulations. These results can help improve understanding of linear gyrokinetic simulations for intrinsic rotation shots and identify the key parameters to focus on for future work using linear stability analysis. Figure 70 below shows the sample results of a sensitivity analysis performed by increasing and decreasing the normalized ion temperature gradient $\frac{a}{L_{T_i}}$by 20%.

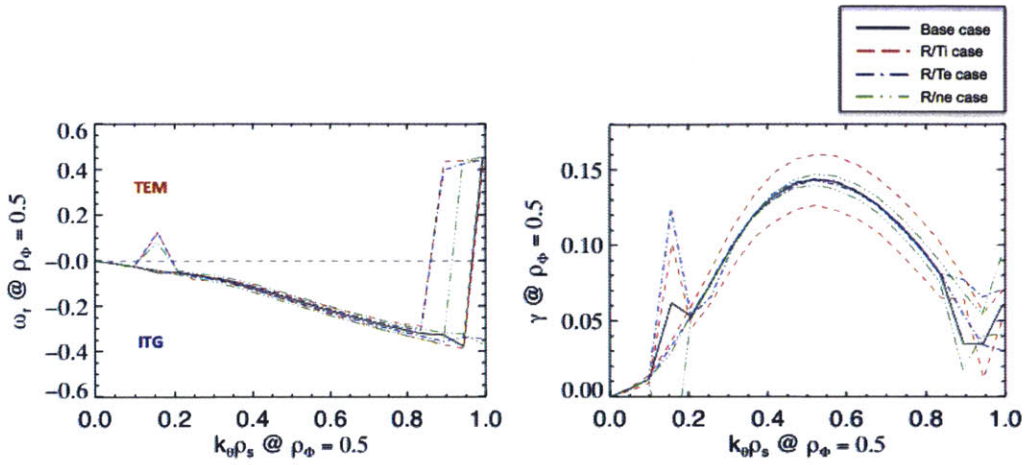

Figure 70: Sample plot of the real frequency ω_r and growth rate γ of the most unstable mode vs. $k_\theta\rho_s$ from linear stability analysis using GYRO at $\rho_\phi = 0.5$ for C-Mod shot 1120222026 with 20% increase/decrease in the normalized ion temperature gradient $\frac{a}{L_{T_i}}$, normalized electron temperature gradient $\frac{a}{L_{T_e}}$, and normalized electron density gradient $\frac{a}{L_{n_e}}$.

It can be seen that a 20% change in the gradients can significant alter the real frequency of the dominant turbulent mode from linear stability analysis. The effects on the real frequency are most noticeable for the red and blue dashed lines, showing that the various gradient increases/decreases can affect the linear stability results to varying degrees. In Figure 70, a 20% increase in the ion temperature gradient (red dashed) resulted in significant changes and the plasma to be TEM-dominated at lower wavenumber than that of the base case. By seeing which gradient changes result in the largest changes from the base case, the most significant driver out of these gradients can can be identified for the linear gyrokinetic simulations. By identifying this driver, a better understanding of intrinsic rotation and turbulent transport is provided.

Table 14 shows the six sensitivity cases that are performed along with the one base case using the routines gyrorun.pro and find_stability.pro. The 1-sigma errors that are used to vary the normalized gradients for the sensitivity analysis are calculated by using error propagation as explained in the previous section. Using the 1-sigma error to vary the gradients rather than increasing/decreasing the gradients by a fixed percentage also allows the sensitivity analysis to be used for seeing the effects of measurement and profile fitting errors. In essence, the sensitivity analysis provides insight into how much the real frequency and growth rates can vary by due to experimental and analysis errors for C-Mod intrinsic rotation data. Consequently, it can also be seen as estimating the error of the linear stability analysis results. This is critical when using the real frequency of the most unstable modes to test the dominant turbulence regime hypothesis.

B IDL Routines and Directories

The analysis workflow and the following analysis is very data-driven. To collect, process, and analyze all of the data, a variety of IDL routines are used and several are modified or created. This section describes the various IDL routines used in this thesis and how they were modified or used. Although not an exhaustive list of the IDL routines and directories, this section covers and most of the routines and their locations in case any reader desires to look at the source code.

a) Files used in Step 1

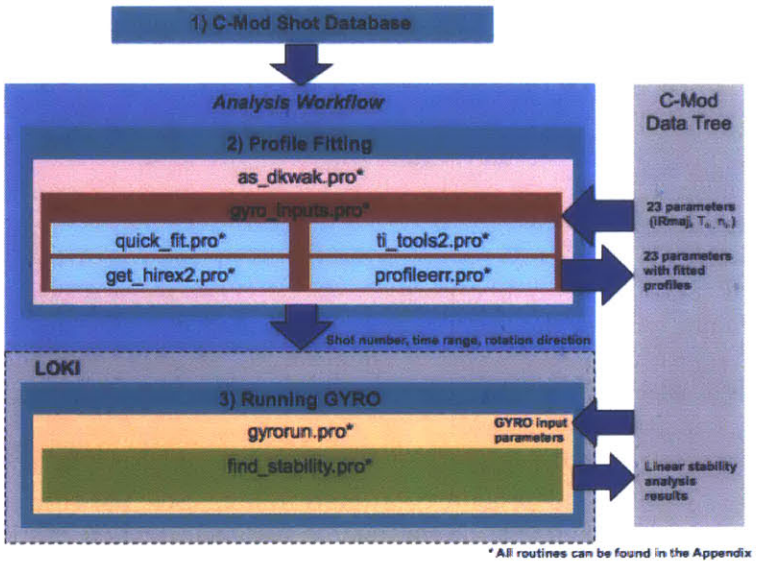

Name: Excel_shotlist.ods
Type: Created by author
Location: dkwak/gyro/excel_shotlist.ods
Description: Excel spreadsheet of all 76 ohmic L-mode rotation reversal and intrinsic rotation profiles, time ranges, current and rotation direction, and comments used to keep track of all shots throughout analysis workflow.

b) Files used in Step 2

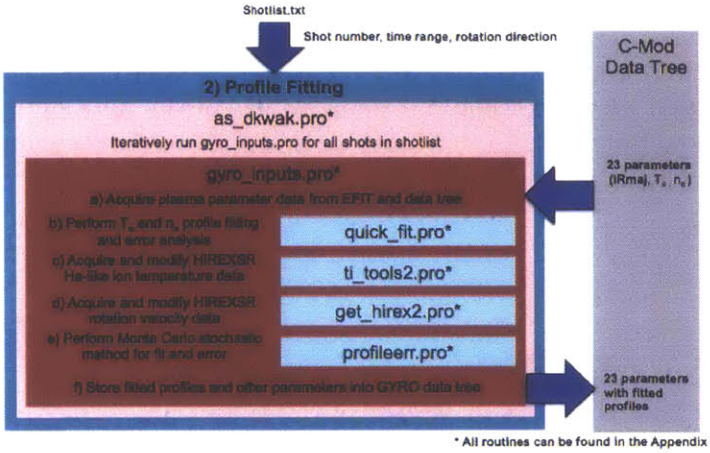

Name: gyro_inputs.pro
Type: Modified
Location: dkwak/gyro/gyro_inputs.pro
Description: Loads plasma parameters and time-averaged profile measurements from a C-Mod shot, fits electron density, electron temperature, and ion temperature profiles, and stores fits and parameters into C-Mod data tree.
Modifications: 7 major changes made:
1) All profile parameters are mapped to the normalized toroidal magnetic flux coordinates $\rho_\phi = \sqrt{(\psi_0 - \psi)(\psi_0 - \psi_{sep})}$ as that is the coordinate system used in earlier studies. Additionally, various parameters throughout the routine are mapped to different spatial coordinates, so mapping everything to $\rho_\phi$forces consistency.
2) For $T_e$and n_e, get_ts.pro is replaced by quick_fit.pro, which loads the profile measurement data, fits the profiles, and calculates the fitting error using the Monte Carlo stochastic method. As a result of quick_fit handling both data acquisition and fitting, bspline and polyfit options for electron temperature and density were removed.
3) For $T_i$data, only He-like Argon emissions from HIREXSR are used as some shots do not have H-like emission measurements, causing errors due to empty data arrays. Therefore, get_hirex2.pro and ti_tools2.pro are used to load only the He-like HIREXSR data and mapping it to the magnetic flux coordinates. Because the profile fitting is done using the Monte Carlo stochastic method in profileerr.pro, the bspline fitting is removed. Additionally, the first 8 points of the ion temperature profile are removed as they tend to be significant outliers. To account for outliers elsewhere, data points with $T_i > 2.0$ keV or < 0 keV are removed as they are not realistic.
4) For velocity data, instead of the local $V_\phi$measurements from HIREXSR, the line-integrated measurements are used from hirexsr_load_result.pro as they tend to provide more accurate profiles for fitting.

5) For T_i and $V_\phi$profile fitting and error analysis, profileerr.pro is used.
6) An option to create a .sav file for the parameters and profile fits for each shot is created in case the user needs to have the data files directly without having to access the data tree.
7) Routine that writes the data to the tree is modified to add the new parameters - V_ϕ and profile fitting errors.

Name: quick_fit.pro
Type: Unmodified
Location: dkwak/quickfit/quick_fit.pro
Description: Loads T_e and n_e measurement data, performs tri-partitioned profile fitting, and Monte Carlo stochastic error analysis.

Name: get_hirex2.pro
Type: Modified from get_hirex.pro
Location: dkwak/gyro/get_hirex2.pro
Description: Calls ti_tools2.pro to load only He-like Ar emission T_i data from HIREXSR and truncates the temperature profile before fitting as shown in Figure 62.
Modifications: Modified to only handle He-like Ar emissions and not perform profile fitting.

Name: ti_tools2.pro
Type: Modified from ti_tools.pro
Location: dkwak/gyro/ti_tools2.pro
Description: Loads HIREXSR T_i data
Modifications: Modified to only load He-like Ar emission data and ignore any H-like Ar emission data.

Name: hirexsr_load_result.pro
Type: Unmodified
Location: dkwak/gyro/hirexsr_load_result.pro
Description: Loads HIREXSR toroidal rotation velocity profile measurements.

Name: profileerr.pro
Type: Created by author
Location: dkwak/gyro/profileerr.pro
Description: Performs T_i and $V_\phi$profile fitting and error analysis sing the Monte Carlo stochastic method described in Section A.6 with N = 10,000 assuming the 1-sigma errors σ_{T_i}= 20% and σ_{V_ϕ}= 30%.

Name: as_dkwak.pro
Type: Created by author
Location: dkwak/gyro/as_dkwak.pro
Description: Reads list of shots and time ranges from shotlist.txt, iteratively runs gyro_inputs.pro for each profile, and creates .sav file with all list of profiles that were processed.

c) Files used in Step 3

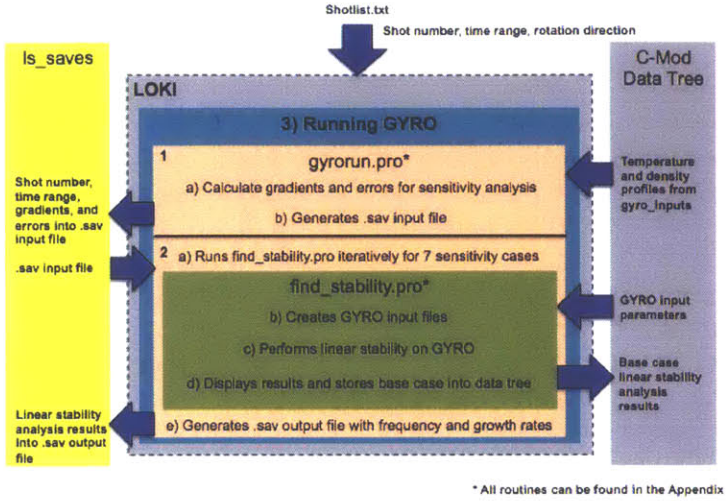

Name: find_stability.pro
Type: Unmodified
Location: dkwak@loki:~/gacode/gyro/sim/find_stability/find_stability.pro
Description: Generates GYRO input files as described in Section A.2., runs linear stability analysis at a specific ρ_ϕ using GYRO, and stores base case results in C-Mod data tree. Also gives option to perform sensitivity cases by altering the local profile gradients $\frac{R}{L_{T_i}}$, $\frac{R}{L_{T_e}}$, and $\frac{R}{L_{n_e}}$.

Name: gyrorun.pro
Type: Created by user
Location: dkwak@loki:~/gacode/gyro/sim/find_stability/gyrorun.pro
Description: Reads list of shots and time ranges from shotlist.txt, loads data from C-Mod data tree stored by gyro_inputs.pro, prepares 1 base case and 6 sensitivity cases as listed in Table 14, calculates the 1-sigma gradient errors at five spatial coordinates (ρ_ϕ= 0.3, 0.4, 0.5, 0.6, 0.7), and iteratively runs find_stability.pro 35 times for each shot (7 sensitivity cases x 5 spatial locations). Each linear stability case result is saved into a uniquely named .sav file as explained in Section A.4.

Name: ls_saves
Type: Directory created by user
Location: dkwak@loki:~/gacode/gyro/sim/find_stability/ls_saves
Description: Contains all of the input and GYRO linear stability analysis output.sav files generated by gyrorun.pro.

d) Files used in Output Data Collection and Plotting

Name: gradienttest
Type: Directory created by author
Location: dkwak/gyro/gradienttest
Description: Holds all plots in Chapter 4, 5, and 6 of the thesis and output processing routines involved in testing of the three hypotheses and identifying correlations between parameters.

Name: lsgradienttest.pro
Type: Created by author
Location: dkwak/gyro/gradienttest/lsgradienttest.pro
Description: Given a $\rho_\phi$by the user and list of shots, the routine loads all parameters from the data tree stored by gyro_inputs.pro and linear stability results from .sav files in ls_saves to form arrays of all of the local parameters for all of the profiles that need to be analyzed. These arrays are then stored into one .sav. file in the gradienttest directory.

Name: combinedfiletest.pro
Type: Created by author
Location: dkwak/gyro/gradienttest/combinedfiletest.pro
Description: Uses the output file generated by lsgradienttest.pro and allows user to plot any combination of parameters together to identify possible correlations and trends. This routine can be used to quickly test for correlations or to generate high-quality EPS plots.

Name: sensesample.pro
Type: Created by author
Location: dkwak/gyro/gradienttest/sensesample.pro
Description: Designed specifically to collect all 35 linear stability output .sav files corresponding to the sensitivity analysis for each C-Mod profile and then plots the results for sensitivity analysis as shown in Figure 70.

C Ohmic L-mode C-Mod Shot Database

a) Rotation reversal profiles

Shot Number	Co-current Time Range	Counter-current Time Range
1120626027	0.800 - 1.120	1.200 - 1.298
1120210028	0.500 - 0.560	0.800 - 0.848
1120607010	0.670 - 0.880	1.100 - 1.298
1120222021	1.600 - 1.740	0.700 - 0.898
1120222025	1.170 - 1.276	0.800 - 0.998
1120222026	1.500 - 1.654	0.900 - 1.098
1120216011	0.550 - 0.670	1.100 - 1.298
1110218003	0.600 - 0.760	1.300 - 1.498
1110125004	0.500 - 0.660	1.300 - 1.498
1110125005	0.700 - 0.860	1.100 - 1.298
1110125019	1.300 - 1.410	1.560 - 1602
1140415029	0.600 - 0.760	1.400 - 1.598
1120208015	0.500 - 0.620	0.850 - 0.948
1120207017	0.800 - 0.972	1.200 - 1.398
1110125006	0.700 - 0.812	1.200 - 1.398
1120724013	1.100 - 1.220	1.450 - 1.500
1120724014	1.100 - 1.212	1.500 - 1.550
1120724015	1.100 - 1.220	1.400 - 1.500
1120718017	1.000 - 1.198	0.600 - 0.648
1120626011	1.100 - 1.202	0.800 - 0.896
1120210031	0.800 - 0.904	1.550 - 1.596
1120216012	0.520 - 0.580	1.200 - 1.250
1120216017	1.200 - 1.300	1.400 - 1.500
1120216030	0.700 - 0.750	1.200 - 1.250
1120216031	0.850 - 0.950	1.300 - 1.400

b) Intrinsic rotation profiles

Shot Number	Time Range	Rotation Direction
1120210002	1.220 - 1.300	Co-current
1120210003	1.200 - 1.300	Co-current
1120210007	1.250 - 1.300	Co-current
1120210015	0.800 - 0.850	Co-current
1120210031	1.050 -1.100	Co-current
1120210032	0.800 - 0.900	Co-current
1120216006	1.400 - 1.500	Co-current
1120216007	1.200 - 1.300	Co-current
1120216008	1.100 - 1.200	Co-current
1120216021	1.000 - 1.110	Co-current
1120626023	1.100 - 1.200	Co-current
1120210011	1.200 - 1.300	Counter-current
1120210012	1.000 - 1.100	Counter-current
1120210016	0.300 - 0.350	Counter-current
1120210021	1.000 - 1.100	Counter-current
1120210026	1.100 - 1.200	Counter-current
1120210028	1.100 - 1.200	Counter-current
1120210029	1.100 - 1.200	Counter-current
1120216013	1.300 - 1.400	Counter-current
1120216020	1.000 - 1.100	Counter-current
1120216028	1.210 - 1.250	Counter-current
1120626028	1.100 - 1.200	Counter-current

1	Rotation Shot Database			senormom.dat reverses current	I > 0 clockwise	V > 0 counter						*Add Choongki's and Anne's ITPA shots in this database (for lu
2	Last Updated: 2/25/15				I < 0 counter	V < 0 clockwise						
3												
4	Cmod_shot	TiInit	Tfinal	Co/Counter	Current Direction	Rotation Direction	Tavg	In MDS?	Heating Method	Confinement	LS	Comments
43	1120626027	1.2	1.298	counter	cc	co	1.249	Yes	OH		L	
44	1120210025	0.8	0.848	counter	cc	co	0.824	Yes	OH		L	Y Tiny co region and large counter (~1s)
45	1120607010	1.1	1.298	counter	cc	co	1.199	Yes	OH		L	N T = 1199
46	1120222021	0.7	0.898	counter	cc	co	0.799	Yes	OH		L	Y T=799
47	1120222025	0.8	0.998	counter	cc	co	0.899	Yes	OH		L	Y
48	1120222026	0.9	1.098	counter	cc	co	0.999	Yes	OH		L	Y
49	1120216011	1.1	1.298	counter	cc	co	1.199	Yes	OH		L	N T = 1199 - poor Ti bspline data at 0.67 and edge - but fit looks
50	1120210026	1	1.184	counter	cc	co	1.092	Yes	OH		L	Y
51	1110218003	1.3	1.498	counter	**co**	cc	1.399	Yes	OH		L	Y T=1399 - **This has POSITIVE VTOR – REVERSE**
52	1110125004	1.3	1.498	counter	cc	co	1.399	Yes	OH		L	N No Te, no fit shown T = 1399
53	1110125005	1.1	1.298	counter	cc	co	1.199	Yes	OH		L	N 4 Ti data points near core = 0
54	1110125019	1.56	1.602	counter	cc	co	1.581	Yes	OH		L	Y 7 Ti data points near core = 0 and poor Ti data
55	1140415029	1.4	1.598	counter	**co**	cc	1.499	Yes	OH		L	Y **POSITIVE VTOR – REVERSE**
56	1120913012	0.43	0.598	counter	**co**	cc	0.514	Yes	OH			Poor Ti data at edge – rises to 2.0 keV – Probably rerun
57	1120517002	1.3	1.5	counter			1.400	No	OH			Processed – no TS
58	1120517003	1.1	1.3	counter			1.200	No	OH			Processed – no TS
59	1120517004	1.1	1.3	counter			1.200	No	OH			Processed – no TS
60	1120517006	1.2	1.4	counter			1.300	No	OH			
61	1120210031	1.55	1.596	counter	cc	co	1.573	Yes	OH		L	Y Check dwscope – awful velocity data
62	1120208015	0.85	0.948	counter	cc	co	0.899	Yes	OH		L	N
63	1120207017	1.2	1.398	counter	cc	co	1.299	Yes	OH		L	Y
64	1110125006	1.2	1.398	counter	cc	co	1.299	Yes	OH		L	Y
65	1110125013	1.2	1.4	counter			1.300	No	OH		L	Processed – no TS
66	1110125020	1.5	1.7	counter			1.600	No	OH		L	Processed – no TS
67	1110125021	1.2	1.4	counter			1.300	No	OH		L	Processed – no TS
68	1110125023	1.2	1.4	counter			1.300	No	OH		L	Processed – no TS
69	1120724013	1.45	1.55	counter			1.500	Yes			L	N High 1.5 KeV tail at edge Ti
70	1120724014	1.5	1.55				1.525	No			L	Bad Ti measurements
71	1120724015	1.4	1.5	counter	cc	co	1.450	Yes	OH		L	N Bad Ti measurements at edge
72	1120718017	0.6	0.648	counter	cc	co	0.624	Yes	OH		L	Y
73	1120718025	0.8	0.902	counter	cc	co	0.851	Yes	OH		L	Y >0.85 - Ti climbs up and distorts Ti fit - probably rerun
74	1120718027	0.4	0.504	counter	cc	co	0.452	Yes	OH		L	Y
75	1120626011	0.8	0.896	counter	cc	co	0.848	Yes	OH		L	Y
76	1120210013						#DIV/0!				L	CC data outside of HIREXSR range
77	1120210014						#DIV/0!				L	CC data outside of HIREXSR range
78	1120210015						#DIV/0!				L	CC data outside of HIREXSR range
79	1120216012	1.2	1.25	counter	cc	co	1.225	Yes	OH		L	RR
80	1120216017	1.4	1.5	counter	cc	co	1.450	Yes	OH		L	RR
81	1120216030	1.2	1.25	counter	cc	co	1.225	Yes	OH		L	RR
82	1120216031	1.3	1.4	counter	cc	co	1.350	Yes	OH		L	RR

E Error Propagation Equations

Equation for error of $\frac{R}{L_X}$ where x is a density or temperature parameter

$$\sigma_{\frac{R}{L_x}} = R\sqrt{\left(\frac{dX}{dR}\frac{1}{X}\right)^2\sigma_X^2 + \left(\frac{1}{X}\frac{d^2X}{dR^2} - \frac{1}{X^2}\left(\frac{dX}{dR}\right)^2\right)\sigma_R^2}$$

Equation for error of v_{thi}

$$\sigma_{v_{thi}} = \frac{\sigma_{T_i}}{\sqrt{2T_i m_i}}$$

Equation for error of experimentally calculated u'

$$\sigma_{u'} = \sqrt{\left(\frac{R}{v_{thi}}\frac{d^2V_\Phi}{dr^2}\right)^2\sigma_r^2 + \left(\frac{1}{v_{thi}}\right)^2\sigma_{V_\Phi}^2 + \left(\frac{R\frac{dV_\Phi}{dr} - V_\Phi}{v_{thi}^2}\right)^2\sigma_{v_{thi}}^2}$$

Equation for error of $\nu_\star$

$$\sigma_{\nu_\star} = \nu_\star\sqrt{\left(\frac{1}{n_e}\right)^2\sigma_{n_e}^2 + \left(\frac{-2}{T_i}\right)^2\sigma_{T_i}^2 + \left(\frac{1}{R}\right)^2\sigma_R^2 + \left(\frac{1}{q}\right)^2\sigma_q^2 + \left(\frac{-1.5}{\epsilon}\right)\sigma_\epsilon^2}$$

where $\epsilon = \frac{r}{R_\psi}$, the inverse aspect ratio.

Equation for error of u' from 1-D analytical neoclassical model

$$\sigma_{u'} = u'\sqrt{\left(\frac{\sigma_q}{q}\right)^2 + \left(2\left(\frac{R}{L_{T_i}}\right)^{-1}\right)^2\sigma_{\frac{R}{L_{T_i}}}^2 + \left(\frac{\sigma_{\rho_i}}{\rho_i}\right)^2 + \left(\frac{1}{r}\right)^2\sigma_r^2}$$

where $\rho_i = \frac{mv_{thi}}{qB}$ is the ion gyroradius.

F HIREXSR Inversion Process on THACO

Before HIREXSR data can be fitted using gyro_inputs, the experimental toroidal rotation velocity measurements must first undergo an inversion process that calibrates the the velocity with a benchmark zero-velocity frame of reference. This frame of reference is a zero-velocity C-Mod shot called a locked mode shot. Therefore, this tutorial walks the user through the steps to perform the inversion process on an unprocessed shot.

1) Verify Shot is Unprocessed

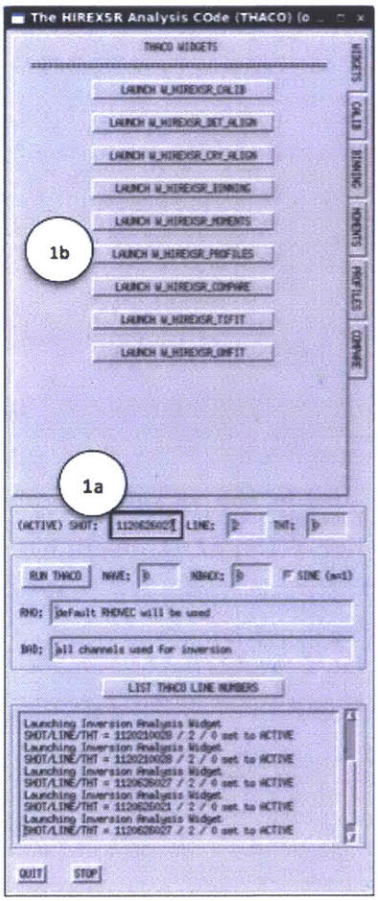

1a) Enter C-Mod shot number and press enter (shot number should appear in comment box below as successfully entered)

1b) Click 'Launch W_HIREXSR_PROFILES' to view velocity and moment profiles
1c) Check to see if profile exists - lack of measurement data (white points) and line-integrated data (red points) means profile has not been processed

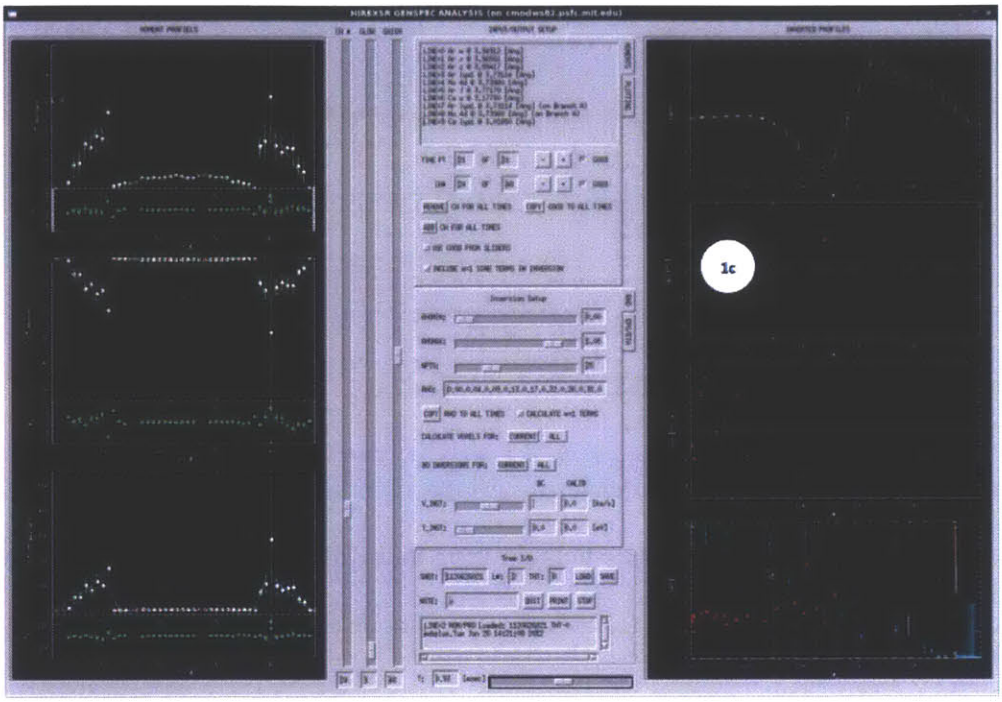

2) Identify Locked Mode Shot

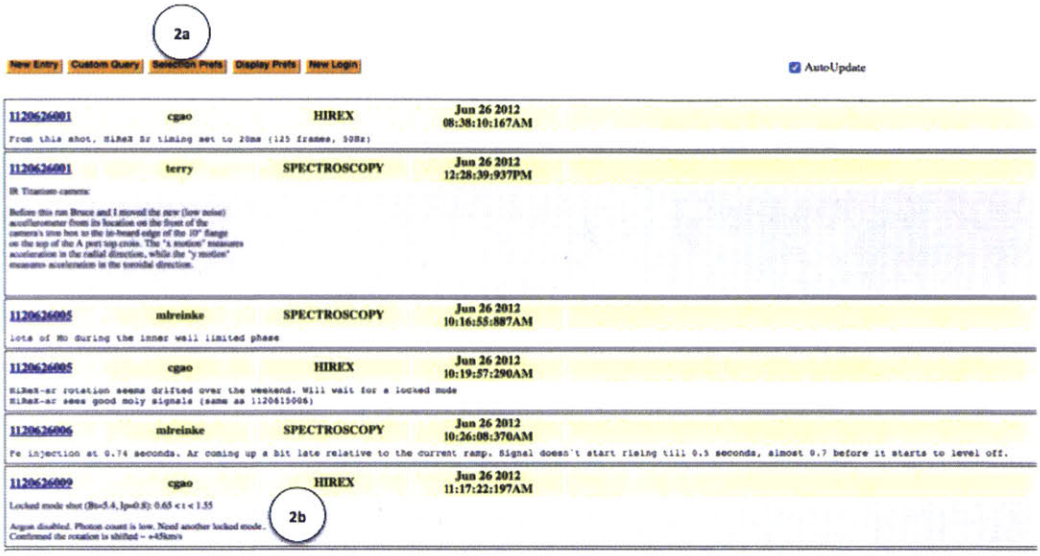

(link: https://www.psfc.mit.edu/research/alcator/logbook.php) - Check CMod Wiki for access account and password
2a) Enter date (first 6 digits of C-Mod shot number) and check HIREX and spectroscopy boxes and press 'Ok'
2b) Check query for locked-mode shot (listed as 'Locked mode shot' in comments) and record shot number and time range

3) Check Locked Mode Shot

3a) Enter locked mode shot number and follow steps 1a-1c
3b) Ensure V = 0 for the time range of the locked mode shot

4) Calibrate Shot

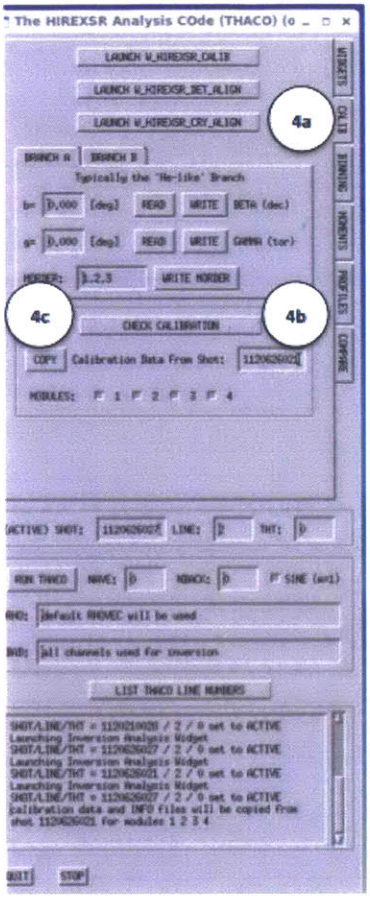

4a) Select Calibration by clicking the 'CALIB' tab
4b) Enter locked mode shot number and click enter
4c) Click 'COPY' - completion should be denoted by the comment box below

5) Check Binning

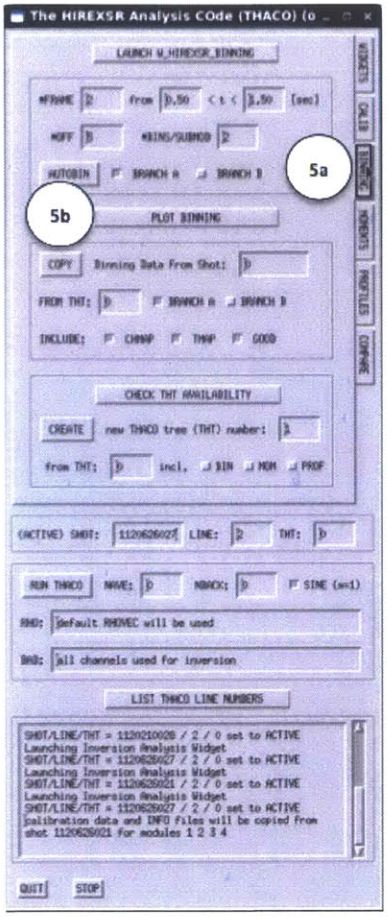

5a) Click 'BINNING' tab
5b) Click 'PLOT BINNING'
5c) Ensure that the spatial binning and time binning are appropriately chosen to ensure acceptable levels of spatial and time resolution (contact John Rice - rice@mit.edu or Chi Gao - cgao@mit.edu about the binning process)

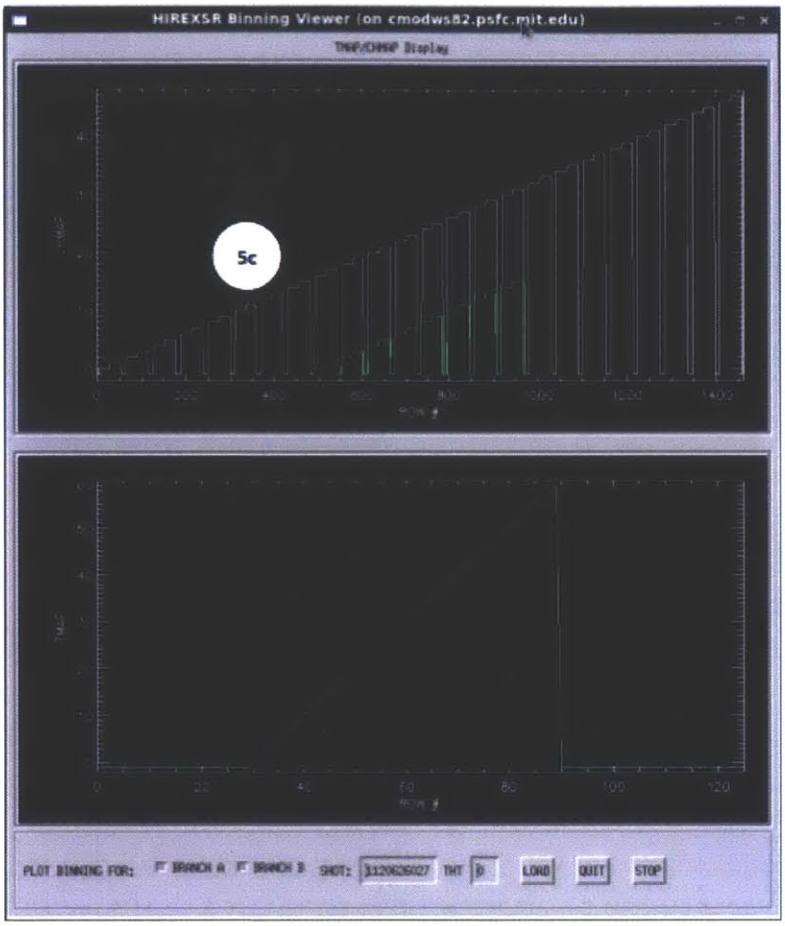

6) Apply Moments

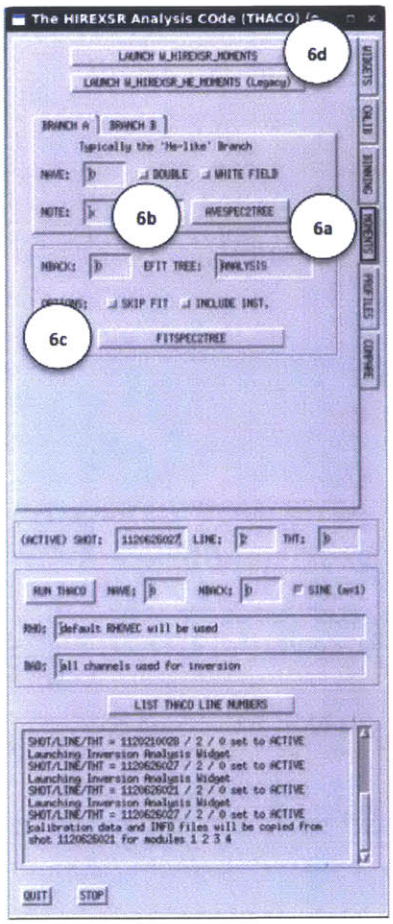

6a) Click 'MOMENTS' tab
6b) Click 'AVESPEC2TREE' and wait until process is complete
6c) Click 'FITSPEC2TREE' and wait until process is complete (takes ~1-2 minutes)
6d) Click 'LAUNCH W_HIREXSR_MOMENTS' to see moments applied to the shot
6e) Scroll through channels and record channel numbers corresponding to poor data (signified by large white error bars on top screen and example shown in figure below)

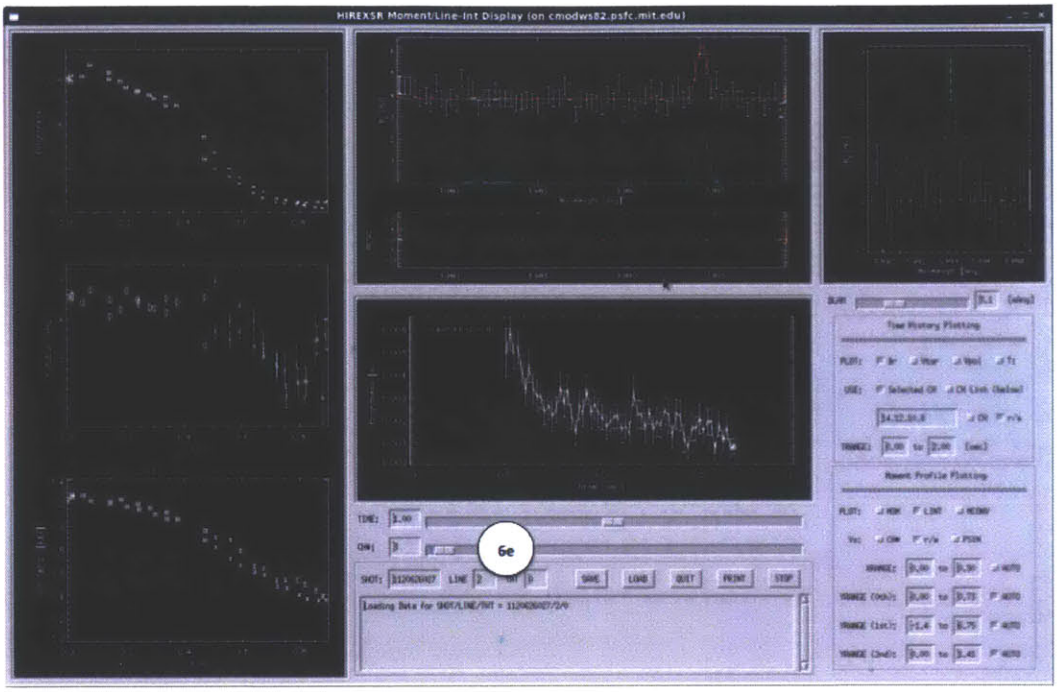

7) Check Profile and Remove Channels

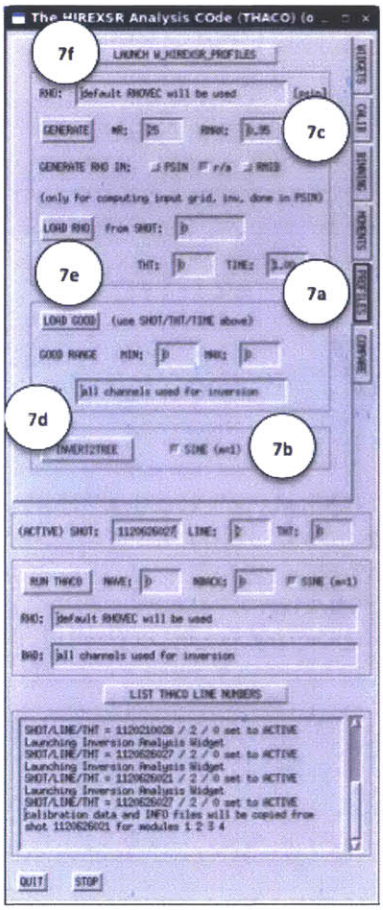

7a) Click 'PROFILES' tab
7b) Uncheck 'SINE (m=1) box
7c) Specify RMAX to 0.95 (outer r/a boundary for processing - outside of this range, measurements get wildly inaccurate)
7d) Press 'INVERT2TREE' and wait until completion
7e) Enter Shot and press 'LOAD RHO' and 'LOAD GOOD' (chooses spatial coordinates and channels to be removed)
7f) Press 'LAUNCH W_HIREXSR_PROFILES'
7g) Scroll through channels and remove bad ones from 6e
7h) Remove Channel 27 and 28 (poor calibration in the core) - Channel 28 highlighted in figure below
7i) Press 'VOXELS' and 'INVERSION' for 'ALL'
7j) Ensure ion temp. measurements near edge are consistent - if not, remove the corresponding channels
7k) Set $T_i$to 150.0 keV
7l) Click 'SAVE' - successful save should be stated in comment box below

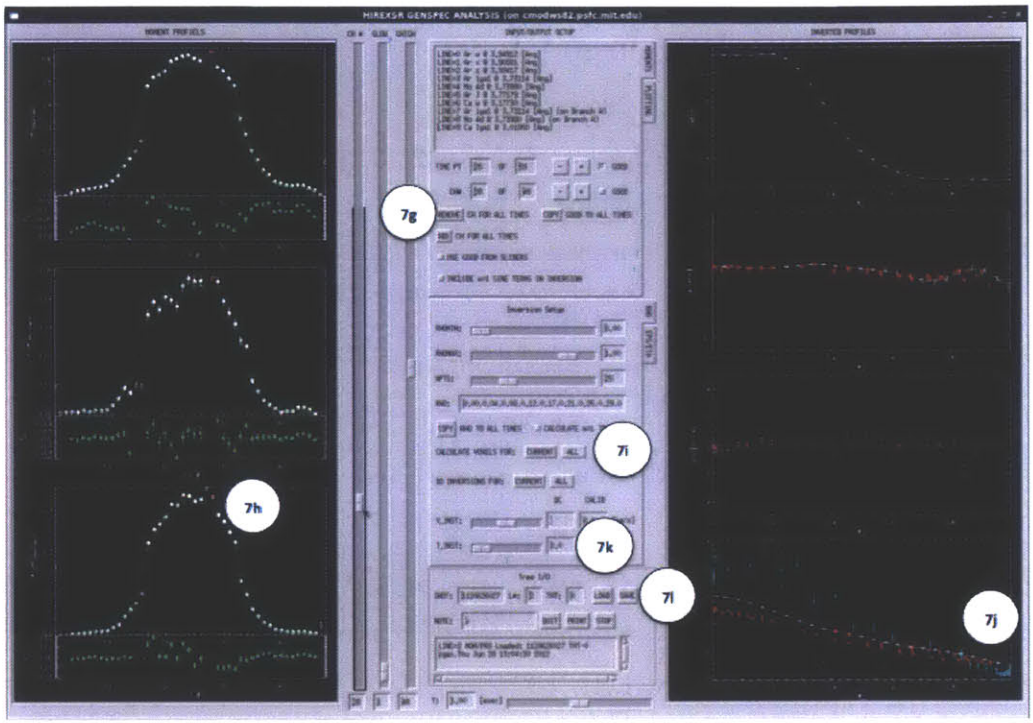

After these steps, the shot should be processed and ready for profile fitting. However, if any issues arise, the user should contact the HIREXSR team - John Rice (rice@mit.edu) or Chi Gao (cgao@mit.edu) in PSFC. If the user wants to create multiple processed version of the HIREXSR data, it is possible to create new THTs that only have the unprocessed data and binning. This can be done in the 'BINNING' tab where the user can get THT availability and then create new THT is it is available.

References

[1] Biglari H. *et al* 1990 Phys. Fluids B **2** 1

[2] Hahm T.S. 1994 Phys. Plasmas **1** 2940

[3] Hahm T.S. and Burrell K. H. 1995 Phys. Plasmas **2** 1648

[4] Burrell K.H. 1997 Phys. Plasmas **4** 1499

[5] Terry P.W. 2000 Rev. Mod. Phys. **72** 109

[6] Strait E. *et al* 1995 Phys. Rev. Lett. **74** 2483

[7] Garofalo A.M. *et al* 2002 Phys. Rev. Lett **89** 235001

[8] Reimerdes H. *et al* 2008 Phys. Rev. Lett. **98** 055001

[9] Buttery K.J. *et al* 2008 22nd IAEA Fusion Energy Conf. (Geneva, Switzerland)

[10] Politzer P.A. *et al* 2008 Nucl. Fusion **48** 075001

[11] Rice J.E. *et al* 2007 Nucl. Fusion **47** 1618

[12] McDermott R.M. *et al* 2011 Plasma Phys. Control. Fusion **53** 124013

[13] Angioni C. *et al* 2011 Phys. Rev. Lett. **107** 215003

[14] Rice J.E. *et al* 2011 Nucl. Fusion **51** 083005

[15] Bortolon A. *et al* 2006 Phys. Rev. Lett. **97** 235003

[16] Rice J. E. *et al* 2012 Phys. Plasmas **19** 056106

[17] McDermott R.M. *et al* 2014 Nucl. Fusion **54** 043009

[18] White A.E. *et al* 2013 Phys. Plasmas **20** 056106

[19] Sung C. *et al* 2013 Nucl. Fusion **53** 083010

[20] Marmar E. *et al* 2007 Fusion Sci. Technol. **51** 261

[21] Whyte D.G. *et al* 2010 Nucl. Fusion **50** 105005

[22] Ince-Cushman A. *et al* 2008 Rev. Sci. Instrum. **79** 10E302

[23] Basse N.P. *et al* 2007 Fusion Sci. Technol. **51** 476

[24] Hughes J.W. *et al* 2003 Rev. Sci. Instrum. **74** 1667

[25] O'Shea P.J. *et al* 1995 Proc. 9th Joint Workshop on ECE & ECRH (Borrego Springs, CA)

[26] Ida K. *et al* 1995 Phys. Rev. Lett. **74** 1990

[27] Luce T.C. *et al* 1992 Phys. Rev. Lett. **68** 52

[28] Nagashima K. *et al* 1994 Nucl. Fusion **34** 447

[29] Rice J.E. *et al* 1997 Nucl. Fusion **37** 421

[30] Rice J.E. *et al* 2004 Nucl. Fusion **44** 379

[31] DeGrassie J.S. *et al* 2003 Nucl. Fusion **43** 142

[32] Duval B.P. *et al* 2007 Plasma Phys. Control. Fusion **49** B195

[33] Rice J.E. *et al* 2001 Nucl. Fusion **41** 277

[34] Rice J.E. *et al* 2002 Nucl. Fusion **42** 510

[35] Rice J.E. *et al* 2003 Nucl. Fusion **43** 781

[36] Fiore C.L. *et al* 2012 Phys. Plasmas **19** 056113

[37] Rice J.E. *et al* 1999 Nucl. Fusion **39** 1175

[38] Hubbard A.E. *et al* 2011 Phys. Plasmas **18** 056115

[39] Lee W.D. 2003 Phys. Rev. Lett. **91** 205003

[40] Rice J.E. *et al* 2011 Phys. Rev. Lett. **107** 265001

[41] Nave M.F.F. *et al* 2010 Phys. Rev. Lett. **105** 105005

[42] Rice J.E. *et al* 2005 Nucl. Fusion **45** 251

[43] Rice J.E. *et al* 2008 Plasma Phys. Control. Fusion **50** 124042

[44] Erikkson L.,-G. *et al* 2009 Plasma Phys. Control. Fusion **51** 044008

[45] Diamond P.H. *et al* 2009 Nucl. Fusion **49** 045002

[46] Itoh S.I. 1992 Phys. Fluids B **4** 796

[47] Peeters A.G. *et al* 2011 Nucl. Fusion **51** 0924027

[48] Ida K. and Rice J.E. 2014 Nucl. Fusion **54** 045001

[49] Peeters A.G. *et al* 2007 Phys. Rev. Lett. **98** 265003

[50] Garbet X. *et al* 2002 Phys. Plasmas **9** 3893

[51] Hahm T.S. *et al* 2007 Phys. Plasmas **14** 072302

[52] Gurcan O.D. *et al* 2007 Phys. Plasmas **14** 042306

[53] Camanen Y. *et al* 2009 Phys. Rev. Lett. **102** 125001

[54] Casson F.J. *et al* 2009 Phys. Plasmas **16** 092303

[55] Camanen Y. *et al* 2011 Nucl. Fusion **51** 073039

[56] Barnes M. *et al* 2013 Phys. Rev. Lett. **111** 055005

[57] Hillesheim J.C. *et al* 2015 Nucl. Fusion **55** 032003

[58] Wagner F. and Stroth U. 1993 Plasma Phys. Control. Fusion **35** 1321

[59] Rettig C.L. *et al* 2001 Phys. Plasmas **8** 2232

[60] Angioni C. *et al* 2005 Phys. Plasmas **12** 040701

[61] Rice J.E. *et al* 2012 Phys. Plasmas **19** 056106

[62] Horton W. 1999 Rev. Mod. Phys. **71** 735

[63] Fable E. *et al* 2010 Plasma Phys. Control. Fusion **52** 015007

[64] Angioni C. *et al* 2009 Plasma Phys. Control. Fusion **51** 1240417

[65] Parra F.I. *et al* 2012 Phys. Rev. Lett. **108** 095001

[66] Parra F.I. *et al* 2010 Plasma Phys. Control. Fusion **52** 045004

[67] Parra F.I. *et al* 2011 Nucl. Fusion **51** 113001

[68] Lee J.P. *et al* 2014 Nucl. Fusion **54** 022002

[69] Lee J.P. *et al* 2014 Phys. Plasmas **21** 056106

[70] Watterson R.L. *et al* 1985 Phys. Fluids **28** 2857

[71] Reinke M.L. *et al* 2012 Rev. Sci. Instrum. **83** 1135004

[72] Tynany G.R. *et al* 2009 Plasma Phys. Control. Fusion **51** 113001

[73] Ely D. 2014, 'fiTS v. 1.4.0 User's Manual'

[74] Chilenski M.A. *et al* 2015 Nucl. Fusion **55** 023012

[75] Kallenbeach A. *et al* 2003 Nucl. Fusion **43** 573

[76] Ma Y. 2010 'A quick profile fitting code and some issues in Monte Carlo profile analysis', C-Mod Wiki

[77] Holland C. *et al* 2009 Phys. Plasmas **16** 052301

[78] 1990, 'Accessing TRANSP Output: A User's Guide', Princeton Plasma Physics Laboratory

[79] Howard N.T. *et al* 2013 Nucl. Fusion **53** 123011

[80] Candy J. and Waltz R.E. 2003 J. Comput. Phys. **186** 545

[81] Garbet X. *et al* 2010 Nucl. Fusion **50** 043002

[82] McKee G.R. *et al* 2001 Nucl. Fusion **41** 1255

[83] Rutherford and Frieman 1968 Phys. Fluids **11** 569

[84] Brizeard A. *et al* 1989 J. Plasma Phys. **41** 541

[85] Jenko F. *et al* 2000 Phys. Plasmas **7** 1904

[86] Frieman 1982 Phys. Fluids **25** 502

[87] Lee W.W. *et al* 1983 Phys. Fluids **26** 556

[88] Catto P.J. *et al* 1977 J. Plasma Phys. **20** 719

[89] Lin Z., Hahm T.S., Lee W.W. *et al* 1998 Science **281** 1835

[90] Idomura Y. *et al* 2003 Nucl. Fusion **43** 234

[91] Jolliet S. *et al* 2007 Comput. Phys. Commun. **177** 409

[92] Kotschenreuther M. *et al* 1995 Comput. Phys. Commun. **88** 128

[93] Peeters A.G. *et al* 2004 Phys. Plasmas **11** 3748

[94] Friedberg J.P. 2008, *Plasma Physics and Fusion Energy*, Cambridge Press

[95] McMillan B.F. *et al* 2009 Phys. Plasmas **16** 022310

[96] Lee W.W. *et al* 2008 Comput. Sci. Disc. **1** 015010

[97] Snipes J.A. *et al* 1998 Plasma Phys. Control. Fusion **40** 765

[98] de Boor C. 1978, *A Practical Guide to Splines*, Springer Press